Development of *in vitro* 3D model systems for screening non-viral neurotrophic factor gene therapies for the retina

by

Ding-Wen Chen

A thesis
presented to the University of Waterloo
in fulfillment of the thesis requirement
for the degree of
Doctor of Philosophy
in
Pharmacy

Waterloo, Ontario, Canada, 2018

Examining Committee Membership

The following served on the Examining Committee for this thesis. The decision of the Examining Committee is by majority vote.

External Examiner	Dr. Heather Sheardown Professor (Chemical Engineering, McMaster University) Canada Research Chair in Ophthalmic Biomaterials and Drug Discovery
Supervisor	Dr. Marianna Foldvari Professor (Pharmacy, University of Waterloo)
Internal Member	Dr. Michael Beazely Associate Professor (Pharmacy, University of Waterloo)
Internal Member	Dr. John G. Flanagan Dean and Professor (Optometry and Vision Science, University of California, Berkeley) Adjunct Professor (Pharmacy, University of Waterloo)
Internal Member	Dr. Jonathan Blay Professor (Pharmacy, University of Waterloo)
Internal-External Member	Dr. Vivian Choh Associate Professor (Optometry and Vision Science, University of Waterloo)

Author's Declaration

I hereby declare that I am the sole author of this thesis. This is a true copy of the thesis, including any required revisions, as accepted by my examiners.

I understand that my thesis may be made electronically available to the public.

Abstract

Glaucoma is a neurodegenerative disease that can lead to a complete loss of vision due to retinal ganglion cell (RGC) death. Therapies that have the capacity to protect and rescue stressed RGCs remain a critical unmet need in glaucoma management. Neurotrophic factor (NF) gene therapy is a promising therapeutic approach that can address this current clinical deficiency by providing damaged RGCs with extrinsic neurotrophic support as a means of protection and repair. Moreover, a non-viral approach to the delivery of NF-encoding plasmid DNA (pDNA) confers many advantages over a viral approach for its improved immunogenicity and mutagenesis risks, patient compliance and large-scale manufacturing cost and feasibility. In this research, the main objective was to address the challenges facing non-viral NF gene therapy field for the retina, through development of three *in vitro* model systems that aim to facilitate the preclinical screening and identification of promising NF gene delivery systems. The first model system developed was a versatile co-culture model that simulates cellular interactions between "healthy" and "stressed" cells in the retina. Furthermore, through incorporation of techniques including enzyme-linked immunosorbent assay (ELISA), immunofluorescent imaging, and neurite tracing into the co-culture setup, the model system enables a systematic evaluation of the therapeutic potential of gene delivery systems through assessment of bioavailability and bioactivity of therapeutic proteins produced from transfected cells. The second model system was a new potential RGC cell line, termed XFC series of cells, that express key RGC characteristics and suitable for the evaluation of RGC-aimed gene therapies. Derived from multipotent retinal stem cells (RSCs), XFC cells express multiple RGC markers including *Map-2*, *Rbpms*, and *Tubb3,* and exhibit RGC-like neurite extension capacity in response to brain-derived neurotrophic factor (BDNF), ciliary neurotrophic factor (CNTF), and rho-kinase inhibitor (RKI) Y-27632 activation. The feasibility of the cell model was further validated in the described co-culture setup as XFC cells were able to validate

the bioactivity of the BDNF proteins released by transfected cells. The third model system developed was a stem cell-derived 3D "mini-retina" culture model (termed MiEye series of retinal neurospheres) that contains multiple retinal cell types and enables *in vivo-like* gene delivery assessment. Derived from differentiating multipotent RSCs in 3D culture, MiEye retinal neurospheres with different retinal biomarker expressions can be generated using different protocols. Moreover, by harnessing the tissue-like arrangement of retinal cells in MiEye retinal neurospheres, it enables the assessment of infiltration and transfection capacity of gene delivery systems in tissue-like structure, towards the establishment of a more representative *in vitro-in vivo* correlation and prediction of *in vivo* gene delivery feasibility.

Concurrent to model system development, aspects that focus on the development of non-viral gene delivery systems for the retina were also explored. The first aspect involved the optimization of gemini surfactant (GS) lipid nanoparticle systems (GL-NPs) physicochemical properties by evaluating the roles of minicircle plasmid (MC), sonication processing, and total NP component concentration (TNPC). Through dynamic light scattering and fluorescent correlation spectroscopy physicochemical characterizations, it was found that the size, particle size distribution, and zeta potential could be effectively optimized through sonication processing and TNPC. Moreover, the number of pDNA per particle homogeneity can be improved by formulating GL-NPs with MCs. The second aspect involved an investigation on the application of carbon nanotubes (CNTs) as a gene delivery vehicle to retinal cell types. More specifically, GS-functionalized SWNT gene delivery system (f-ptSWNT) was developed and demonstrated the ability to deliver pDNA to a retinal astrocyte cell line. The results demonstrate the feasibility of utilizing f-ptSWNT to deliver pDNA to retinal cells and serves as a starting point for future f-ptSWNT retinal gene delivery system development.

The development of the three *in vitro* model systems in this thesis collectively aims to facilitate the preclinical screening and development of non-viral NF gene therapies in a synergistic manner, covering key areas of assessments that are critical to *in vivo* therapeutic success. Furthermore, concurrent developments in non-viral gene delivery systems through GL-NP optimization and CNT exploration also advance the knowledge towards the development of better non-viral gene delivery systems.

Acknowledgement

First and foremost, I would like to express my most sincere gratitude and appreciation to my supervisor and mentor, Dr. Marianna Foldvari, for her guidance and support. Thank you for believing in me with the opportunities that you have provided me and thank you for constantly encouraging me to push the boundaries to become better. I will remain forever grateful for all you have done. I would also like to thank my thesis committee members Dr. Michael Beazely and Dr. John G. Flanagan, for your valuable input and support of my thesis research. To examiners Dr. Heather Sheardown, Dr. Vivian Choh, and Dr. Jonathan Blay, thank you for reviewing my thesis and for your valuable suggestions and comments.

To lab mates from the past to present whom I have had the privilege of working with at the Foldvari Research Group, thank you for your companionship, intriguing scientific discussions, and invaluable technical advices, with special thanks to Lokesh Narsineni, Daniella Calderon, Marina Jalal, Chilbert Dong, Samih Alqawlaq, and Dr. Nafiseh Nafissi.

To colleagues of the School of Pharmacy from the past to present, thank you for your kindness, encouragements, conversations, and friendship throughout the years, with special thanks to Eric Lee, Monica Hoang, Deep Patel, Samantha Shortall, Jessica Nicastro, and Nyasha Gondora.

To my parents and grandparents, thank you for your unconditional support and wisdoms that continuously provide me with guidance through the journeys of life. None of this would be possible without you. Finally, to my partner and my best friend, Amber Li, thank you for your love, care, and support. I am eternally grateful to have you in my life.

Table of Contents

List of Figures

List of Tables

List of Abbreviations

f-ptSWNT	Gemini-functionalized single-walled carbon nanotube
f-ptSWNT-pDNA	Gemini-functionalized single-walled carbon nanotube complexed with pDNA
2.5D	Two and half dimensional
2D	Two-dimensional
3D	Three-dimensional
4PL	Fourth party logistics
A7/oxSH-SY5Y	A7 co-cultured with oxidatively stressed SH-SY5Y
AAV	Adeno-associated virus
AAV1	Adeno-associated virus 1
ACC	Autocorrelation curve
AD	Adenovirus
ADA	Adenosine deaminase
ADA-SCID	Adenosine deaminase deficiency severe combined immunodeficiency
AH	Aqueous humour
AMD	Age-related macular degeneration
ANOVA	Analysis of variance
API	Active pharmaceutical ingredient
ATP	Adenosine triphosphate
BDNF	Brain-derived neurotrophic factor
bFGF	Basic fibroblast growth factor
Brn3	Brain-specific homeobox / pou domain protein 3
CAR-T	Chimeric antigen receptor T-cell
CE	Ciliary epithelium
CFDA	China Food and Drug Administration
CMV	Cytomegalovirus
CNS	Central nervous system
CNTF	Ciliary neurotrophic factor
CRS	Cytokine release syndrome
DLBCL	Diffuse large B-cell lymphoma
DLS	Dynamic light scattering
DMEM	Dulbecco's modified eagle's medium
DNA	Deoxyribonucleic acid
DOPE	1,2-dioleoyl-sn-glycero-3-phosphoethanolamine
ECM	Extracellular matrix
EGF	Epidermal growth factor
EHS	Engelbreth-holm-swarm
ELISA	Enzyme-linked immunosorbent assay
EMA	European Medicines Agency

ESC	Embryonic stem cell
FACS	Fluorescence-activated cell sorting
FBS	Fetal bovine serum
FCS	Fluorescence correlation spectroscopy
FDA	Food and Drug Administration
GDNF	Glial-derived neurotrophic factor
GFP	Green fluorescent protein
GL-NP	Gemini surfactant phospholipid np
GS	Gemini surfactant
f-CNT	Gemini surfactant functionalized carbon nanotube
GTP	Guanosine triphosphate
hBDNF	Human brain-derived neurotrophic factor
hiPSC	Human induced pluripotent stem cell
HSC	Human schlemm's canal
IOP	Intraocular pressure
IV	Intravenous
K2	K2® transfection reagent
K2-NP	K2® nanoparticle
LC	Lamina cribrosa
LCA	Leber congenital amaurosis
LGN	Lateral geniculate nucleus
LHON	Leber hereditary optic neuropathy
LPL	Lipoprotein lipase
LV	Lentivirus
MACS	Magnetic-activated cell sorting
MC	Minicircle plasmid
MMP	Matrix metalloproteinases
mRNA	Messenger ribonucleic acid
ND1	Nadh dehydrogenase-1
ND4	Nadh dehydrogenase-4
ND6	Nadh dehydrogenase-6
NF	Neurotrophic factor
NFL	Nerve fiber layer
NGF	Nerve growth factor
NP	Nanoparticle
NT-3	Neurotrophic factor 3
NT-4/5	Neurotrophic factor 4/5
NTG	Normal-tension glaucoma
ONH	Optic nerve head
oxSH-SY5Y	Oxidatively stressed SH-SY5Y cells

PACG	Primary angle-closure glaucoma
PALS	Phase analysis light scattering
PBS	Phosphate buffered solution
PCG	Primary congenital glaucoma
pDNA	Plasmid DNA
PEG	Polyethylene glycol
PET	Polyethylene terephthalate
PFA	Paraformaldehyde
PLGA	Poly(lactide-co-glycolide)
PLO	Poly-L-ornithine
PNS	Peripheral nervous system
POAG	Primary open-angle glaucoma
ptSWNT	Puretubes™ carbon nanotube
RGC	Retinal ganglion cell
ROS	Reactive oxygen species
RP	Regular plasmid
RPE	Retinal pigmented epithelium
RSC	Retinal stem cell
RSCDM-1	Retinal stem cell differentiation medium 1
RSCDM-2	Retinal stem cell differentiation medium 2
SC	Schlemm's canal
ScN	Sciatic nerve
SMI-32	Anti-neurofilament H
TE	Transfection efficiency
TIMP1	Metallopeptidase inhibitor 1
TIMP2	Metallopeptidase inhibitor 2
TIMP4	Metallopeptidase inhibitor 4
TNPC	Total nanoparticle component concentration
TM	Trabecular meshwork
trA7	Transfected A7 cells
trXFC-3	Transfected XFC-3 cells
TrkB	Tropomyosin receptor kinase B

Chapter 1 Introduction

1.1 Gene therapy: status to date

Gene therapy is a novel form of therapeutic approach that utilizes genetic materials as the therapeutic agent, providing the possibility of addressing diseases and conditions at the molecular level through various methods of genetic augmentation, inhibition or deletion. As of July 2018, there are seven human gene therapy products that are approved worldwide (Table 1.1), demonstrating the feasibility of three main types of gene-based therapeutic approaches directed for seven different disease interventions.

Gendicine™ and Oncorine™ were the first two gene therapies that entered the market globally, through their approval in China by the Chinese State Food and Drug Administration (CSFDA) in 2003 and 2005, respectively [1, 2]. Both therapies are viral-based gene therapies indicated for the treatment of head and neck squamous cell carcinoma through genetic augmentation of a tumor suppressor gene. More specifically, these therapies are designed for intratumoral injection of adenoviruses carrying the p53 gene, a pro-apoptotic tumor suppressor gene, aimed to induce apoptosis in cancer cells through the p53-mediated pathway which is otherwise suppressed [3]. The p53 gene is a well-studied anti-tumor gene for its role in the induction of pro-apoptotic cascades, which have been shown to play a promising role in tumor suppression. Development of Gendicine™ and Oncorine™ carries two major significances: 1) it enables a novel treatment option for patients with head and neck squamous cell carcinoma beyond existing pharmacological, radiological, and surgical interventions; and 2) it demonstrates the clinical feasibility of a human gene therapy intervention at the bedside for the first time.

One of the most unique advantages of a genetic-based therapy, otherwise inconceivable through traditional pharmacological or surgical interventions, is the ability to treat genetic-based

disease conditions by replacing the mutated dysfunctional gene(s) responsible. Currently, treatment options available for patients suffering from acquired or hereditary genetic diseases focus on either symptom reduction or delay disease progression as there are no effective means of treating the root genetic causative factor. Recently, new hope emerged for patients suffering from hereditary lipoprotein lipase deficiency (LPLD) and Leber Congenital Amaurosis (LCA) with the approval of Glybera™ and Luxturna™, two first of its class of therapeutic offerings to treat these two hereditary monogenic diseases by replacing the causative mutated gene with a functional version. Glybera™ is the first gene therapy approved by the European Medicines Agency (EMA) for the treatment of a rare monogenic disease known as LPLD, which is a hereditary disease caused by a mutation of the lipoprotein lipase (LPL) gene that results in the inability to breakdown triglycerides and leads to excessive accumulation of chylomicrons throughout the body. High levels of chylomicrons accumulation lead to elevated risk of developing acute pancreatitis and other complications. Glybera™ treatment regimen aims to restore triglyceride metabolism function through intramuscular injection of the AAV1 virus carrying functional LPL^{s447x} gene, which would be taken up by monocytes and subsequently facilitate the production of LPL [4, 5]. On the other hand, Luxturna™ is the first direct-administered gene therapy product approved by the United States Food and Drug Administration (FDA), indicated for the replacement of an inherited defected gene that causes vision loss. More specifically, the approved gene therapy is a RPE65 replacement gene therapy, designed for the treatment of a rare form of inherited vision loss known as the biallelic RPE65 mutation-associated retinal dystrophy or LCA. Patients who suffer from such inherited retinal dystrophy have a mutated RPE65 gene that consequently leads to progressive loss of vision and eventual blindness [6, 7]. Luxturna™ is formulated using AAV-based viral vector carrying a functional RPE65 gene, which is administered through subretinal injection to replace

the defective RPE65 gene in retinal pigment epithelial cells in the retina. The approval of the two gene therapy products, Glybera™ and Luxturna™, is significant in multiple aspects. From gene therapeutic development perspective, it marks a major breakthrough in demonstrating the feasibility of gene therapy for the treatment of monogenic diseases through replacement of a defective gene. From a monogenic disease management perspective, the two products demonstrated the clinical feasibility to treat hereditary diseases using gene therapy.

Another novel genetic-based therapeutic approach involves the integration of cell therapy and gene therapy, where genetic manipulation of somatic cells is performed *ex vivo* for subsequent reintroduction into the patient body. While involving numerous sophisticated steps from harvesting patient cells to *ex vivo* genetic manipulation and cellular expansion, the series of *ex vivo* steps allow for high degree of controlled genetic manipulation, maximizing synergistic therapeutic potential between the two therapeutic principles. Strimvelis™, an *ex vivo* hematopoietic stem cell gene therapy approved by EMA in 2016 was the first approved human gene therapy product of its kind, developed for the treatment of a rare disease known as adenosine deaminase deficiency severe combined immunodeficiency (ADA-SCID) [8]. ADA-SCID is a monogenic immunodeficiency disease caused by the mutation of the adenosine deaminase (ADA) gene. Mutation of ADA results in dysfunctional deoxyadenosine clearance, which incurs toxicity primarily towards monocytes that leads to the development of severe immunodeficiency. Strimvelis™ is composed of retroviruses carrying functional ADA genes designed to treat ADA deficiency through the integration of functional ADA genes into CD34+ hematopoietic stem cells harvested from the patient, which are then intravenously infused back to the patient upon successful ADA augmentation of the stem cells for engraftment and restoration of ADA expression [9]. Successful treatment through this therapy provides a possibility for sustained long-term

engraftment of ADA-expressing CD34+ hematopoietic stem cells, restoring immune system development through lymphocyte generating capacity. The combination cell and gene therapy approach was also shown to be a promising therapeutic approach in cancer therapy with the approval of Kymriah™ and Yescarta™ by the FDA in 2017. Both Kymriah™ and Yescarta™ are human gene therapy products indicated for cancer therapy through the mechanism of chimeric antigen receptor T-cells (CAR-T), which is a novel therapeutic approach that utilizes and combines the patient's own immune system and gene therapy for the treatment of lymphocytic leukemia. More specifically, Kymriah™ not only was the first approved CAR-T gene therapy, but also the first gene therapy approved for two indications by the FDA. The first approved indication of Kymriah™ was for the treatment of a B-cell precursor acute lymphoblastic leukemia (ALL), an aggressive type of leukemia most commonly found in children that stemmed from B-cell malignancy. More recently in May 2018, a second indication of Kymriah™ was approved by the FDA, for the treatment of relapsing or refractory large B-cell lymphoma including diffuse large B-cell lymphoma (DLBCL), high grade B-cell lymphoma and DLBCL arising from follicular lymphoma. DLBCL is one of the most common form of non-Hodgkin's lymphoma that is also a result of B-cell malignancy [10]. Approval of Kymriah™ for the second indication is in direct competition with Yescarta™, another CAR-T gene therapy approved by the FDA to treat DLBCL. Majority of the B-cell malignancies are associated with elevated level of CD19 expression, thus it is the major receptor target in CAR-T therapy. CAR-T genetically modifies patient's own T-cells to express anti-CD19 antigen receptors, which act as targeting molecules assisting T-cells in recognizing CD19 expressing cancerous B-cells and terminating the growth of the cancerous B-cells in B-cell ALL and DLBCL. Approval of the two CAR-T based gene therapies further demonstrates the potential of gene therapy as the new therapeutic paradigm for utilizing patient's

own immune system as scavengers for cancer cells, offering alternative means of effective cancer management.

The approval of the seven gene therapy products to date demonstrates the feasibility of bringing gene therapy products to the bedside despite the hurdles and challenges. Moreover, it opens new dimensions to disease management that are not possible through traditional pharmacological, radiological, and surgical interventions.

Table 1.1 Human gene therapy products approved worldwide as of July 2018

Name	Company	Agency	Year Approved	Indication	Therapeutic Approach	Administration Method	Mechanism of Action	Gene	Vector base
Luxturna™ (voretigene neparvovec-ryzl)	Spark Therapeutics	FDA	2017	Biallelic RPE65 mutation-associated retinal dystrophy	Direct administration of AAV-RPE65 gene therapy for RPE65 replacement	Subretinal injection	• Injection of adeno-associated serotype 2 viruses carrying RPE65 gene for replacement of mutated RPE65 in the retinal pigmented epithelium cells	RPE65	Adeno-associated virus serotype 2
Yescarta ™ (axicabtagene ciloleucel)	Kite Pharma / Gilead	FDA	2017	DLBCL non-Hodgkin lymphoma	Cell-based gene therapy Anti-CD19+ T-cells for elimination of CD19+ B-cells	Intravenous injection	• Harvest T-cells from patient, genetically modify to express Anti-CD19 • Anti-CD19+ T-cells infused back to patient to eliminate CD19+ B-cells	Anti-CD19 antigen receptor	Retrovirus
Kymriah™ (tisagenlecleucel)	Novartis	FDA	2017 First indication	B-cell precursor acute lymphoblastic leukemia up to 25 years of age. Refractory or in second or later relapse	Cell-based gene therapy Anti-CD19+ T-cells for elimination of CD19+ B-cells	Intravenous infusion	• Harvest T-cells from patient, genetically modify isolated T-cells to express Anti-CD19 • Anti-CD19+ T-cells infused back to patient to eliminate CD19+ B-cells	Anti-CD19 antigen receptor	Lentivirus
			2018 Second indication	Relapsing or refractory large B-cell lymphoma including DLBCL, high grade B-cell lymphoma and DLBCL arising from follicular lymphoma					
Strimvelis™	GlaxoSmith Kline	EMA	2016	Adenosine deaminase deficiency severe combined immunodeficiency	Cell-based gene therapy ADA gene replacement	Intravenous infusion	• CD34+ hematopoietic stem/progenitor cells are harvested from patient • Harvested CD34+ cells are transduced with retroviruses carrying ADA gene • ADA-expressing CD34+ hematopoietic cells are administered for bone marrow engraftment	ADA	Retrovirus
Glybera™	UniQure	EMA	2012 (with-drawn from renewal in 2017)	Hereditary lipoprotein lipase deficiency	Direct administration for LPL^{s447x} gene replacement	Intramuscular injection	• Injection of LPL-carrying adeno-associated serotype 1 viruses into muscle, to mediate production of LPL proteins in myoctes	LPL^{s447x}	Adeno-associated virus serotype 1

Name	Company	Agency	Year Approved	Indication	Therapeutic Approach	Administration Method	Mechanism of Action	Gene	Vector base
Oncorine™ (ONYX-015)	Shanghai Sunway Biotech	CSFDA	2005	Head and neck squamous cell carcinoma	Direct administration for p53 gene replacement	Intratumoral injection	• Injection of p53-carrying conditionally replicative adenoviruses to tumor for selective replication within cancer cells to express p53 proteins for induction of cancer cell apoptosis	p53	Condition-ally replicative adenovirus (E1B-55 deficient)
Gendicine™	Shenzhen SiBiono GeneTech	CSFDA	2003	Head and neck squamous cell carcinoma	Direct administration for p53 gene replacement	Intratumoral injection	• Injection of p53-carrying adenoviruses allow p53-transuced cancer cells to express p53 proteins for induction of cancer cell apoptosis	p53	Recombin-ant adenovirus

1.1 Non-viral gene therapy nanomedicine: key component of gene therapy maturation

Approval of multiple human gene therapy products in recent years marked significant milestones in genetic-based therapeutic development across the globe. Despite the recent momentum, many important questions still need to be investigated and properly addressed in order to bring forth the full therapeutic potential of gene therapy. In addition to the approved treatments, the majority of gene therapies undergoing pre-clinical and clinical investigations are currently dominated by viral-based gene therapies. With the intrinsic ability designed by nature to specifically carry out the task of gene transfer through dedicated transduction machinery on human host, viral-based gene delivery vectors derived from various types of viruses such as adeno-associated virus (AAV) [11], adenovirus (AD) [12], and lentivirus (LV) [13] are indisputably prime candidates for gene delivery applications. While advantageous for gene delivery applications, viruses are naturally an impediment to the human immune system owing to the intrinsic host immune response that actively responds to the presence of viral particles in human body [14-16]. Innate immune response may eliminate viral vectors before they arrive at target sites

or cells, thereby eliminating the viral particles before therapeutic activity could take place [17], or limiting therapeutic efficacy at low viral titre [18]. However, using elevated levels of viral vector titre may subsequently increase the risks of systemic immune response and mutagenesis. To address these concerns, immunomodulators, corticosteroids or antihistamines, such as methylprednisolone, cyclosporin, mycophenolate mofetil, busulfan, and prednisone are recommended as part of the prescribing guidelines for pre-treatment and post-treatment conditioning of the immune system. Of note on CAR-T therapy, tocilizumab is recommended for managing cytokine release syndrome (CRS) [19], a major risk associated with excessive T-cell based therapy [20]. Aside from immune response-related risk factors, other factors such as viral mobility and cost of manufacturing are also important factors to be considered. Viral mobility is a major concern when administered viral vectors travel beyond the intended target due to the risk of initiating undesirable immunogenicity or introducing genetic interventions beyond the intended therapeutic region. As shown in a comparative study between nanoparticles (NPs) and AAVs, subretinally injected AAVs were found to have exited the eye and travelled to parts of the brain, while NPs remained within the subretinally injected eye [21]. Another reflective point revolves around the pricing associated with these novel gene therapy products. Currently approved gene therapies such as Glybera™ (€990,000 EUR), Strimvelis™ (€594,000 EUR), Yescarta™ ($373,000 USD), Kymriah™ ($475,000 USD), and Luxturna™ ($850,000 USD) all are associated with a hefty treatment cost. New models of payment have been proposed to reduce the financial burdens of the treatments such as the incorporation of risk-sharing approaches and long-term payment plans [22]. On the other hand, better pricing models have also been called upon to better assign the value and pricing of gene therapy through finding a common ground between R&D investment, drug manufacturing cost, company profitability, patient accessibility and affordability

[23]. From the perspective of gene therapy development, one of the key cost contributors in viral-based gene therapy lies in the high cost of large-scale manufacturing of viral vectors. Since vectors are a substitutable component in a gene therapy system, utilization of non-viral vector is a promising approach for providing gene therapy treatments with higher safety profile and at a more affordable cost. Collectively, the risks of virus associated immunogenicity, mutagenicity, mobility, and manufacturing costs are all reasonable grounds to consider alternatives to deliver the full potential of gene therapy.

Non-viral gene therapy is an alternative approach to viral-based gene therapy that utilizes nanomaterials for the construction of gene-carrying vectors instead of packaging therapeutic genes within a viral capsid [24, 25]. Using synthetic and naturally derived nanomaterials as the basic building blocks of gene delivery vectors, they offer a better safety profile with lower cost of production. However, the advancement of non-viral vectors to the bedside is hindered primarily by low gene delivery efficiencies. In contrast to viral vectors, non-viral vectors are not equipped with the biological machinery designed to initiate gene delivery through transduction mechanisms. As a result, non-viral gene delivery systems need to overcome several major barriers to achieve successful transfection. Currently, there are at least 40 liposomal and polymeric gene delivery systems at various stages of clinical trials (Table 1.2).

Table 1.2 Lipid- and polymer- based non-viral gene therapies as of July 2018

Indication	Gene Therapy Drug	Phases				
		Phase I	Phase I/II	Phase II	Phase II/III	Phase III
Liposome						
Advanced Cancer Solid Tumor	siRNA-EphA2-DOPC	NCT01591356 (Active)				
Advanced Metastatic Cancer	Pbi-shRNA STMN1	NCT01505153 (Complete)				
Advanced Oral Squamous Cell Carcinoma	DC-Chol liposome	NCT00009841 (Complete)				
Advanced Pancreatic Cancer	Atu027		NCT01808638 (Complete)			
Advanced Solid Tumor	Atu027	NCT00938574 (Complete)				
Children with Refractory or Recurrent Solid Tumor	SGT-53 Transferrin receptor-targeted cationic liposome	NCT02354547 (Active)				
Cystic Fibrosis	pGM169/GL67A [GL67A/DOPE/ DMPE/PEG]		NCT00789867 (Complete)	NCT01621867 (Complete)		
	pGT-1 DMIRE/DOPE liposome	NCT00004471 (Complete)				
Elevated LDL-Cholesterol	ALN-PCS02	NCT01437059 (Complete)				
Fibrotic Diseases	ND-L02-S20201	NCT01858935 (Complete)				
Glioblastoma	SGT-53 Transferrin receptor-targeted cationic liposome			NCT02340156 (Active)		
Metastatic Pancreatic Cancer	SGT-53 Transferrin receptor-targeted cationic liposome			NCT02340117 (Active)		

Indication	Gene Therapy Drug	Phases				
		Phase I	Phase I/II	Phase II	Phase II/III	Phase III
Muscular Dystrophy	GNE Lipoplex (DNA plasmid/DOTAP/ Cholesterol)	Unknown				
Neuroendocrine Tumors, Adrenocortical Carcinoma	TKM-08301	NCT01262235 (Complete)				
Non-small Cell Lung Cancer or Small Cell Lung Cancer	DOTAP:Chol-fus1	NCT00059605 (Complete)	NCT01455389 (Active)			
Solid Tumor	SGT-53 Transferrin receptor-targeted cationic liposome	NCT00470613 (Complete)				
Stage III or IV Head and Neck Cancer; Squamous Cell Carcinoma of the Head and Neck	DOTMA/Cholesterol			NCT00006033 (Complete)		
Transthyretin Amyloidosis	Patisiran ALN-TTR02	NCT01148953 (Complete)		NCT01617967 (Complete)		
		NCT01559077 (Complete)		NCT01961921 (Complete)		
		NCT02053454 (Complete)				
Transthyretin Cardiac Amyloidosis	Revusiran ALN-TTRSC	NCT01814839 (Complete)		NCT01981837 (Complete) NCT02292186 (Complete)		
Transthyretin mediated Familial Amyloidotic Cardiomyopathy	Revusiran ALN-TTRSC					NCT02319005 (Complete)
Transthyretin mediated Familial Amyloidotic Polyneuropathy	Patisiran ALN-TTR02					NCT01960348 (Complete)
Polymer						
Advanced Pancreatic Adenocarcinoma	CYL-02/ Polyethyleneimine	NCT01274455 (Complete)				

Indication	Gene Therapy Drug	Phases				
		Phase I	Phase I/II	Phase II	Phase II/III	Phase III
Bladder Carcinoma	BC-819/PEI BioCanCell Therapeutics	NCT01878188 (Unknown)				
CMV Vaccine for Patient with CMV-Seropositive and CMV-Seronegative Dialysis Patient	ASP0113	NCT02103426 (Complete)				
Colorectal Cancer	EGEN-001 [IL-12 pDNA/PEG-PEI-Cholesterol]		NCT01300858 (Terminated)			
Cytomegalovirus Vaccine for Patient under Allogenic Hematopoietic Cell Transplant	ASP0113			NCT01903928 (Complete)		NCT01877655 (Active)
Cytomegalovirus Vaccine for patient with CMV-seronegative receiving kidney transplant from CMV-seropositive donor	ASP0113			NCT01974206 (Active)		
Multiple Myeloma, B-cell Lymphoma, Plasma Cell Leukemia	SNS01-T/pDNA/PEI		NCT01435720 (Unknown)			
Ovarian Neoplasma	EGEN-001 [IL-12 pDNA/PEG-PEI-Cholesterol]	NCT00473954 (Complete)				
Persistent Ovarian Epithelial Cancer, Fallopian Tube Cancer, or Primary Peritoneal Cancer	EGEN-001 [IL-12 pDNA/PEG-PEI-Cholesterol]	NCT01489371 (Active)		NCT01118052 (Complete)		
Superficial Bladder Cancer	DTA-H19/PEI			NCT00595088 (Unknown)		
Tetravalent Dengue Vaccine	Tetravalent Dengue Vaccine	NCT01502358 (Unknown)				

1.2 Gemini Surfactant NP System: A Promising Nanomedicine Solution to Gene Therapy

GL-NPs are a novel class of gene delivery system that could play a significant role in the development of non-viral gene delivery systems. GS is an amphiphilic surfactant molecule first described by Menger and Littau consists of a dimeric structure composed of two amphiphilic moieties linked by a modifiable hydrocarbon spacer in a *m-s-m* configuration [26]. The structure offers a diverse possibility of GS variations, which can be achieved through hydrocarbon length modifications of the spacer and alkyl chains. Further functionalization of GS can be achieved through conjugation of various functional moieties to either the spacer or the alkyl chain [27]. In addition to the self-assembling amphiphilic properties, another hallmark of GS is the two polar head groups. In particular, the family of GS that contains two positively-charged quaternary nitrogen head groups provide an important electrostatic-based physicochemical property that enables the compaction of nucleic acids and initiation of cellular membrane interactions, properties that are essential in gene delivery applications [28-30]. In the past 18 years of research in this laboratory, several advancement of GS were made through generation of novel GS compounds [31-34], and their therapeutic applications have also been explored heavily in transdermal delivery [31, 35-38]. In some of the more recent work, developments of GS in the areas of pulmonary [39] and ocular delivery have shown promise [40, 41]. Previous work by Alqawlaq and colleagues demonstrated GL-NPs are thermodynamically stable in the posterior segment of the eye, capable of evenly distributing across the nerve fiber layer of the retina upon intravitreal injection administration. On the other hand, GL-NPs have also shown to localize in the anterior segments of the eye upon topical eye drop administration [42].

1.3 Gene therapy in ophthalmology

The eye can greatly benefit from genetic-based therapeutic interventions as major degenerative diseases of the macula, retina, and choroid all have either acquired or inherited genetic basis. As of July 2018, there is one approved human gene therapy product and more than forty-five ocular gene therapies in clinical trials for ocular disease interventions (Table 1.3). Gene therapy of LCA is in the forefront of ocular gene therapy development, with the approval of Luxturna™ by the FDA as described in the previous section. In addition to LCA, Leber Hereditary Optic Neuropathy (LHON) is another disease in the forefront with three phase III clinical trials currently in progress. LHON is a rare inherited retinal dystrophy that results in the degeneration of RGCs caused by mitochondrial gene mutation in NADH dehydrogenase-1 (ND1), NADH dehydrogenase-4 (ND4), or NADH dehydrogenase-6 (ND6) enzymes [43-45]. Previous studies have shown that a replacement of functional ND4 in a rat model of LHON containing G11778A mutated ND4 protected RGCs and prevented associated visual field loss [46, 47]. GS010, an AAV gene therapy system that carries functional ND4 gene is currently in phase III clinical trials for the treatment of LHON. Concurrently, promising advancement in ocular gene therapy is also observed throughout a spectrum of other ocular diseases such as achromatopsia, age-related macular degeneration (AMD), choroideremia, giant axonal neuropathy, gyrate atrophy, retinitis pigmentosa, Stargardt disease, and x-linked retinoschisis, where active clinical trials are currently taking place for the treatment of these ocular diseases (Table 1.3). One of the ocular diseases that has not been mentioned but could greatly benefit from gene therapy is glaucoma. Glaucoma is a neurodegenerative disease and the second leading cause of blindness globally. While there is yet any gene therapy for glaucoma, substantial research and development efforts are in progress towards clinical trials.

Table 1.3 Gene therapies for various ocular diseases currently evaluated in clinical trials as of July 2018

Indication	Gene Therapy Drug	Phases				
		Phase I	Phase I/II	Phase II	Phase II/III	Phase III
Achromatopsia	AAV - CNGB3		NCT03001310 (Active) NCT03278873 (Active)			
	AGTC-402		NCT02935517 (Active)			
	rAAV2tYF-PR1.7-hCNGB3		NCT02599922 (Active)			
Age-Related Macular Degeneration	AAV2-sFLT01	NCT01024998 (Active)				
	AAVCAGsCD59	NCT03144999 (Active)				
	rAAV.sFlt-1		NCT01494805 (Complete)			
	RetinoStat	NCT01678872 (Active) NCT01301443 (Complete)				
	RGX-314	NCT03066258 (Active)				
Choroideremia	AAV2-hCHM		NCT02341807 (Active)			
	AAV2-REP1			NCT02553135 (Active)		
	AAV-REP1			NCT02407678 (Active)		
	rAAV2.REP1		NCT02077361 (Active) NCT01461213 (Active)	NCT02671539 (Active)		
Giant Axonal Neuropathy	scAAV9/ JeT-GAN	NCT02362438 (Active)				
Gyrate Atrophy	Unspecified - Gene therapy	NCT00001735 (Complete)				

Leber Congenital Amaurosis	AAV OPTIRPE65		NCT02946879 (Active)			
	AAV RPE65		NCT02781480 (Active)			
	AAV2-hRPE65v2	NCT00516477 (Active)	NCT01208389 (Active)			NCT00999609 (Active)
	QR-110 (RNA antisense)		NCT03140969 (Active)			
	rAAV2/4.hRPE65		NCT01496040 (Complete)			
	rAAV2-CB-hRPE65		NCT00749957 (Active)			
	rAAV2-CBSB-hRPE65	NCT00481546 (Active)				
	rAAV2-hRPE65	NCT00821340 (Unknown)				
	tgAAG76 (rAAV 2/2.hRPE65p.hRPE65)		NCT00643747 (Complete)			
Leber Hereditary Optic Neuropathy	GS010		NCT02064569 (Active)			NCT03293524 (Active)
						NCT02652780 (Active)
						NCT02652767 (Active)
	rAAV2-ND4				NCT03153293 (Active)	
	scAAV2-P1ND4v2	NCT02161380 (Active)				
Retinitis Pigmentosa	AAV2/5-hPDE6B		NCT03328130 (Active)			
	AAV-RPGR		NCT03252847 (Active)			
			NCT03116113 (Active)			

	GS030-DP		NCT03326336 (Active)			
	rAAV2tYF-GRK1-RPGR		NCT03316560 (Active)			
	rAAV2-VMD2-hMERTK	NCT01482195 (Active)				
	RST-001		NCT02556736 (Active)			
Stargardt Disease	SAR422459		NCT01736592 (Active)			
X-Linked Retinoschisis	rAAV2tYF-CB-hRS1		NCT02416622 (Active)			
	RS1 AAV Vector		NCT02317887 (Active)			
	Unspecified - Gene therapy		NCT02317354 (Active)			

1.4 Glaucoma

1.4.1 Glaucoma pathophysiology & disease management

From *glaukos*, to *gutta serena,* to *glaucoma,* the evolving nomenclature of the optic neuropathic disease reflects our progressive understanding from a disease described by the changing opacity and color of the pupils in the 8th century BC, to a multifactorial neurodegenerative disease of the optic nerve today [48]. Presently, glaucoma is considered the world's second leading cause of blindness with an estimated 111.8 million people to be affected by the disease by 2040 [49].

Glaucoma can be broadly categorized based on the clinical presentation of the iridocorneal angle, the passage between iris and lens that channels aqueous humour outflow from the ciliary body, into two main types: *open-angle* and *angle-closure*. A primary open-angle glaucoma (POAG) refers to a glaucomatous eye with an "open" iridocorneal angle, which consists of an open passage that enables aqueous humour outflow to subsequent drainages in the trabecular meshwork and Schlemm's canal [50]. However, aqueous humour drainage resistance from the trabecular meshwork and Schlemm's canal was shown to play an important role in IOP elevation, which is deemed as a major risk factor for POAG. Despite this correlation, the specific mechanism of IOP-mediated optic nerve degeneration remains unclear as patients can still develop the pathophysiology of POAG even in the absence of elevated IOP such as normal tension glaucoma (NTG). On the other hand, primary angle-closure glaucoma (PACG) refers to glaucomatous eye with a "closed" iridocorneal angle, obstructing the outflow of the aqueous humour that results in its rapid accumulation and subsequent elevation of IOP [51]. Primary congenital glaucoma (PCG) is the third major form of glaucoma that results from deficiencies in the development of drainage canals [52].

Major risk factors of glaucoma are found to have high associations with ethnicity, family history, and age [53]. POAG has the highest prevalence amongst African Americans, while PACG is most prevalent amongst Asians [49]. Individuals who are either over the age of 60, have a family history of glaucoma, or have diabetes are also at higher risk of glaucoma [53]. High IOP remains the most measurable and treatable risk factors amongst the risk factors [54]. Other possible risk factors that may contribute to glaucoma development are factors such as neurotrophin deprivation, glutamate excitotoxicity, oxidative stress, and hypoxia [55].

Early detection plays a key role in the success of glaucoma management as the onset of visual field loss symptom signifying a significant level of optic nerve damage has already been triggered and taken place. Several assessments are important in the diagnosis of glaucoma: tonometry, ophthalmoscopy, perimetry, gonioscopy and pachymetry. The diagnosis of glaucoma is mainly based on the combination of optic nerve fiber layer assessment of the cup-disc ratio and visual field test. Cup-disk ratio is a clinical feature that measures optic nerve health through the comparison of the ratio between the diameters of optic cup and optic disc [56, 57]. An enlarged cup-disc ratio, as a consequence of increased cupping, is the manifestation of optic nerve head widening and posterior movement towards the lamina cribosa [58]. Cupping and thickening of the prelaminar tissues suggests increasing degeneration of the nerve fiber layer and increases the likelihood of glaucoma development [58]. Corneal thickness has also been suggested to be an indicator of POAG development [59]. Current glaucoma management consists of IOP reduction-focused therapeutic regimens, with topical eye drops that facilitate the drainage of the aqueous fluid such as prostaglandin, mitotics, epinephrine, beta-blocker, and carbonic anhydrase inhibitors. Surgically, laser trabeculoplasty and laser iridotomy are common surgical procedures for POAG and PACG, respectively.

Oxidative stress is implicated as one of the factors that contribute to glaucoma disease development and the death of the RGCs [60]. Oxidative stress is a state of intracellular imbalance where high levels of reactive oxygen species (ROS) are present due to insufficient intrinsic cellular ROS scavenging. Moderate levels of ROS are routinely generated and removed through redox modifications in essential metabolic processes from signal transduction to ATP production in the mitochondria [61]. However, excessively high ROS levels can result from mitochondrial dysfunction and insufficient ROS removal in stressed cellular states. Consequently, it can further inflict cellular damages such as lipid peroxidation, mitochondrial membrane damage, and protein oxidation that would subsequently trigger various pathways of cell death [60].

While current glaucoma management can effectively reduce IOP, many patients continue to experience progressive visual field loss. Furthermore, IOP reduction has limited therapeutic benefit to patients with normal-tension glaucoma [62]. More importantly, IOP reduction alone does not address the health of RGCs as damaged RGCs may continue to degenerate even after IOP reduction. RGCs are the main cell types of the retina responsible for the visual communication between the eye and the brain. Thus, a therapeutic approach that aims to improve the health of RGCs is an important unmet need in glaucoma management.

1.4.2 Retinal ganglion cell death: role of neurotrophin deprivation theory

Composed of more than 30 different subtypes that distribute across the ganglion cell layer of the retina, the axons of RGCs extend and converge to form the optic nerve [63]. The optic nerve extends from the retina to the brain, most of which innervates the lateral geniculate nucleus (LGN), with some that innervates superior colliculus [64]. The “neurotrophin deprivation” hypothesis is one of the main theories that attempts to explain the death of RGCs [65].The hypothesis suggests that axonal transport obstruction in glaucoma causes insufficient retrograded transport of collicular

derived neurotrophins to the ganglion cell body, resulting in cellular stress and triggering cell death mechanisms [65]. Neurotrophins, also known as neurotrophic factors, are a family of growth factors that are responsible for neuronal development, growth, maintenance, and survival [66]. Examples of NFs include nerve growth factor (NGF), BDNF, neurotrophin 3 (NT-3), and neurotrophin 4/5 (NT-4/5). Furthermore, NFs were shown to have anti-apoptotic effects in neurons [67, 68]. Evidently, NFs play an important role in the pathogenesis of glaucoma. In particular, BDNF has shown protective effect of RGCs in multiple studies. Direct BDNF protein injection into the retina have shown to enhance RGCs survival in various experimental glaucoma models such as optic nerve crush model in cat [69], spontaneous glaucoma model in DBA2/J mouse [70], acute ocular hypertension model in rat [71], and optic nerve crush and transection in Crl:CD1 mouse model [72]. Combination injections of BDNF protein at sites of superior colliculus and retina resulted in further enhancement of RGC survival after optic nerve crush in cats compared to single site injection, which further demonstrated the therapeutic value that can be achieved with BDNF [73]. BDNF-mediated RGC rescue was achieved through various gene based therapeutic approaches using AAV vector [74, 75], AD vector [76, 77], and electroporation [78] in experimental rat glaucoma models. Furthermore, a study utilizing a transgenic mouse model Thy-1-CreER^{T2}::BDNF^{stop} containing Cre-recombinase inducible system upstream of BDNF has shown that induced BDNF overexpression was able to provide protection to specific type of RGC after optic nerve crush in mouse [79]. Recent studies have also suggested that there is differential tolerance to glaucomatous stress and responsiveness to BDNF treatment between different RGC subtypes. For example, brn3a+ RGCs were more susceptible to acute hypertension-mediated cell death compared melanopsin+ RGCs in an acute hypertension rat model [71]. In addition, the survival of both RGC subtypes were improved with BDNF protein injection [71]. In a separate

study using transgenic mouse, it was shown that SMI-32+ RGCs were less susceptible to optic nerve crush and more responsive to BDNF overexpression mediated rescue compared to large-soma RGCs [79]. Altogether, research to date shows that BDNF is an important therapeutic molecule in the overall objective of protection and rescue of RGCs and subtype-specific efficacy remains to be elucidated to harness its maximum therapeutic potential.

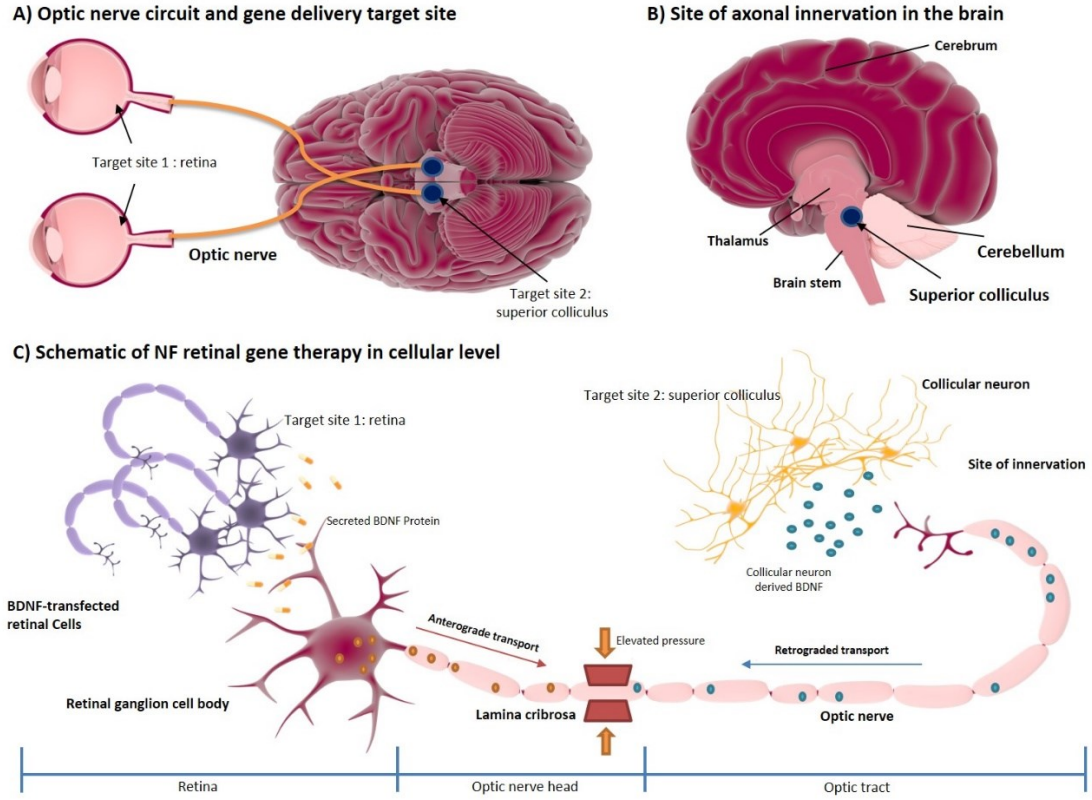

Figure 1.1 NF gene therapy for the protection of RGCs in the retina. (A) Illustration of the two anatomical sites for gene therapy administration: retina and superior colliculus. (B) Superior colliculus, the site at which retinal ganglion cell axons innervate in the brain. (C) Schematic drawing describing the rationale of NF gene therapy and the role of retinal cells and superior collicular cells play in the cellular level.

1.5 Three-dimensional cell culture: enriching the value of in vitro culture models

In vitro cell culture models have been an integral part of scientific research for decades, contributing to discoveries from basic cellular mechanism to drug development. Despite their pivotal roles, the lack of *in vivo-relevant* results derived from *in vitro* models remains a major

hindrance for efficient clinical translation of scientific discovery. A potential solution to this obstacle is to bypass *in vitro* screening and directly perform screening *in vivo* using animal models instead. While possible, direct animal model screening approach is an expensive and complex option for screening libraries of candidate compounds and elucidating complex molecular pathways. Evidently, a solution that bridges the gap between *in vitro* and *in vivo* is needed [80]. The lack of *in vivo* relevance is attributed to the inability for *in vitro* model to yield results that are representative and reproducible in an *in vivo* environment [81]. Cells found *in vivo* exhibit diverse cellular interactions with the extracellular matrices, as well with the neighboring cells from multiple directions. However, cells cultured in 2D plastic surfaces are forced to reside on a flat plane in monolayer, thus cellular contacts are only limited to cells to their sides. The issue of limited cellular interactions under 2D culture particularly restrains our level of understanding in disease models involving complex cellular crosstalk and extracellular matrix interactions in the microenvironment.

Three-dimensional (3D) cell culture is a novel method that was designed to overcome the limitations present in traditional 2D culture methods by allowing cells to be cultured *in vitro*, yet still able to be grown in a microenvironment representative of *in vivo* conditions. Unlike traditional 2D culture where cells are grown on flat plastic surface in monolayers, cells in 3D culture are grown in multilayers in multicellular spheroids or scaffold-dependent multilayer arrangements. The goal of 3D cell culture is to create *in vitro* microenvironment that are representative of *in vivo* cellular architecture and topology to facilitate cells to grow and differentiate in a more *in vivo*-relevant condition. Functional differences in cellular structures [82], gene expression profiles [83], receptor presentation [84], growth factor secretion [85] and stimuli mediated responses [86] have all been reported to have closer resemblance to *in vivo* using 3D cultures.

1.5.1 Structural composition of three-dimensional culture system

Rapid advancements in 3D culture system development have generated a diversity of three-dimensional cell culture methods (Table 1.4). 3D culture systems can be broadly classified into two major types based on the presence of anchors available for cellular attachment into *scaffoldless* and *scaffold-based* systems.

Scaffold-based systems are typically established using naturally derived proteins or synthetic materials for scaffold construction. The scaffold acts as an architecture that enables cells to adhere and grow either above, beneath, within or surrounding the scaffold. *Naturally derived scaffolds* are typically composed of ECM proteins such as collagen, laminin, and proteoglycans in the form of hydrogels [87, 88]. On the other hand, *synthetic scaffolds* are typically prefabricated using synthetic materials with defined shape and architecture. Both naturally derived and synthetic scaffold methods utilize similar principles as they both provide cells with a third dimension that resembles *in vivo* architecture. *Naturally derived scaffold* such as Matrigel™ is an example of complex ECM protein hydrogel system isolated from Engelbreth-Holm-Swarm mouse sarcoma cells consisting of mainly collagen IV and laminin [89]. Other naturally derived systems with a more defined protein content are also available such as purified collagen [90, 91] or fibrin extract [92-94]. Naturally derived proteins from plants such as alginate [95, 96], agarose [97], and chitosan [98, 99] are also compatible biomaterial candidates. *Synthetic scaffolds* are typically prefabricated porous structures of a set shape and size, in which cells could enter the matrices and establish multicellular arrangements with shape and size determined by the scaffold architecture, constructed using synthetic polymeric materials such as polystyrene [100], polyethylene glycol (PEG), and poly(lactic-co-glycolic acid) (PLGA) [101].

Scaffoldless systems are the other main type of 3D culture systems that rely on cells' intrinsic intercellular adhesion properties in the absence of ECM support. The two types of scaffoldless culture systems are *forced-floating* and *hanging-drop* methods. The *forced-floating* method enables the establishment of multicellular spheroidal architecture by prohibiting cellular attachment to the plastic surface functionalized with ultra-low adhesives or micropatterns. On the other hand, the *hanging-drop* method relies on the formation of multicellular architecture in a cell suspension droplet, where cells collects at the bottom of the droplet to form multicellular spheroidal structures [102, 103] .

Table 1.4 Commercially available 3D cell culture systems

Method of 3D construction	Material	3D Culture System	Company
Scaffoldless			
Hanging Drop	Cellular intrinsic adhesion	Perfecta 3D® (Discontinued)	3D Biomatrix
		Gravity Plus®	inSphero
Forced-Floating	Micropatterned Surface	SCIVAX 3D Nanoculture Plate®	Infinite Bio
		CYTOOchips	Cytoo
		Elplasia	Kuraray
		3D Petri Dish®	Microtissue
	Low-Adhesion Surface	Costar Ultra-Low Adhesion Plate	Corning
		Prime Surface	Sumitomo Bakelite
Naturally-derived Scaffold			
Naturally-derived material	Alginate	Algimatrix®	Life Technologies
	Extracted from Engelbreth-Holm-Swarm (EHS) Mouse Sacroma Laminin, Collagen IV, Entactin, Growth Factor	Culturex®	Trevigen
	RGD-Dextran CD-Link (Polyethylene glycol and matrix metalloprotease - cleavable peptides)	3D Life Biomimetic®	Cellendes
	Extracted from Engelbreth-Holm-Swarm (EHS) Mouse Sacroma Laminin, Collagen IV, Entactin, Growth Factor	Matrigel™	BD
	Collagen	RAFT® (Real Architecture for 3D Tissue)	TAP Biosystems (Sartorius Stedium)
	PEG-based molecule	QGel	QGel BIo
	Arginine-Alanine-Aspartic Acid-Alanine monomer repeating amino acid	PuraMatrix	Puramatrix
	Alginate RGD-Alginate Hyaluronan	Novamatrix	FMC Dupont
Synthetic Scaffold			
Synthetic material	Polystyrene scaffold	Alvetex®	Reinnervate (Reprocell)
	Polystyrene, Polycapronolactone, Poly(DL-lactide-co-glycolide)	3D Biotek®	3D Biotek
Hybrid			
Hybrid anchor dependent/independent	Magnetic scaffold and magnetic ECM coupled with levitation	Bio Levitator®	Hamilton Company (Global Cell Solutions)
	Gold, iron oxide, poly-l-lysine to magnetize cells; for levitation	BioAssembler System®	Nano 3D Biosciences

Chapter 2 Research Focus

2.1 Rationale and objective

Current glaucoma management focuses on IOP-reduction using pharmacological and surgical therapeutic interventions. While effective in lowering IOP-mediated risk factors and delaying glaucoma disease progression, direct extrinsic support to RGCs to improve RGC health is lacking. Evidently, therapies that can provide extrinsic support to protect and repair damaged RGCs is an unmet clinical need in glaucoma disease management. NF gene therapy is a therapeutic approach that has the potential to address such clinical deficiency by providing RGCs with NF support. Moreover, using a non-viral approach of gene delivery improvements compared to viral systems may be achieved such as low risk of immunogenicity and mutagenesis, coupled with better patient compliance and production cost. In this research, the objective was to facilitate the preclinical screening and identification of promising NF gene delivery systems through developments of retinal 3D *in vitro* model methodologies and non-viral gene delivery systems for the retina.

2.2 Hypothesis

Main hypothesis:

- A non-viral gene delivery approach can deliver BDNF-encoding pDNA to retinal cells for NF gene therapy in three-dimensional culture.

Sub hypothesis:

I. *Sub-hypothesis #1*: An *in vitro* co-culture modality utilizing BDNF-responsive neuronal cells can serve to evaluate bioactivity of BDNF protein secreted from NP-transfected retinal cells.

Corresponding findings: Developed a neurite outgrowth functional assay to assess the bioavailability and bioactivity of BDNF protein produced and secreted from retinal cells transfected by NPs carrying BDNF encoding pDNA. (Chapter 3)

II. *Sub-hypothesis #2*: A multipotent stem cell-derived RGC-like cell can be isolated and characterized for future screening of non-viral gene delivery systems.

Corresponding findings: Generated and characterized RGC-like cells derived from differentiated multipotent retinal stem cells. The newly isolated cells express RGC biomarkers and exhibit neurite extension and can serve as a model cell line for *in vitro* screening of non-viral gene delivery systems. (Chapter 4)

III. *Sub-hypothesis #3*: A multipotent stem cell-derived 3D retinal neurosphere model can be used to improve the *in vitro – in vivo* correlations of gene delivery system evaluation.

Corresponding findings: Developed a "mini-retina" 3D retinal neurosphere model that can be utilized as a tool for evaluating transfectability, targeting, and infiltration capacity of gene delivery systems. (Chapter 5)

IV. *Sub-hypothesis #4*: GL-NP physicochemical properties can be improved through the replacement of regular plasmid vector with minicircle plasmid and manufacturing considerations.

Corresponding findings: Minicircle plasmid, sonication and formulation concentration can result in generation of GL-NPs with smaller size and higher particle size homogeneity. (Chapter 6)

V. *Sub-hypothesis #5*: SWNTs can complex pDNA and be utilized as gene delivery vehicle for ocular delivery application.

Corresponding findings: SWNTs can complex with pDNA and be utilized as gene delivery carrier for the delivery of pDNA to A7 retinal astrocytes *in vitro.* (Chapter 7)

Chapter 3 Development of an *in vitro* bioassay to evaluate the effect of BDNF expressed and secreted by non-virally transfected retinal cells

Majority of this chapter are reflective of an original manuscript published in the journal Drug Delivery and Translational Research and a book chapter published in Springer Protocols Retinal Gene Therapy Methods and Protocols.

Chen, D.W. and Foldvari, M., 2016. *In vitro* bioassay model for screening non-viral neurotrophic factor gene delivery systems for glaucoma treatment. *Drug Delivery and Translational Research*, *6*(6), pp.676-685.

Author contributions: DWC and MF developed the concept and designed the experiments. DWC performed the experiments. DWC and MF analyzed the data and prepared the manuscript.

Chen D.W., Pauloff K., and Foldvari M., 2018. Three-dimensional co-culture bioassay for screening of retinal gene delivery systems. Methods in Molecular Biology (MiMB) series; In: "Retinal Gene Therapy: Methods and Protocols" ed. Wijnholds J. (Springer) 1715:79-88.

Author contributions: DWC, KP, and MF developed the concept and designed methodologies. DWC and MF prepared the manuscript.

3.1 Rationale and objective

One of the preclinical hurdles in the development of BDNF gene therapy systems for RGC is the lack of representative model for efficient and effective *in vitro* screening. To address this issue, an *in vitro* 3D co-culture model that simulates the "stressed" and "medic" retinal cells interactions *in vivo*, which can be utilized using different combination of cellular candidates was developed. Furthermore, by incorporating ELISA, immunofluorescent imaging, and neurite tracing techniques into the methodology, the therapeutic potential of the "medic" cell secreted BDNF can be assessed based on its bioavailability and bioactivity.

3.2 Background

Gene therapy using NFs is a novel therapeutic approach that could revolutionize glaucoma therapy and provide a means of disease management that beyond risk factor reduction. NFs are a class of proteins that are known to play an important role in the development, maintenance and

survival of neurons in both the central nervous system (CNS) and the peripheral nervous system (PNS) [65, 104]. In particular, BDNF has shown to be a potent NF based on results from several *in vivo* studies, thus is a suitable candidate for gene therapy applications by supporting both protective and regenerative functions [70, 74, 105].

Local support of RGCs within the retina with BDNF could provide neuroprotection if challenges such as maintenance of BDNF levels in the retina for a prolonged period and needle-free administration of the therapeutic plasmid can be safely and effectively addressed. This could be achieved using NPs carrying BDNF-encoding plasmids to the retina, where the expressed BDNF protein could rescue RGCs that are damaged from glaucomatous stress. There are several candidate cells within the retina that could serve as BDNF producers, including non-damaged RGCs, astrocytes [106], Müller glial cells [76], or retinal pigment epithelial cells (RPE). Astroglial cells, located mostly in the innermost retinal layers, are prime candidates because of their close proximity to RGCs within the retina nerve fiber layer (NFL) and optic nerve head (ONH), and their role in structural, metabolic and neurotrophic support, and in sensing hypoxia, immunological damage and neurogenesis [107].

Screening of non-viral gene delivery system carrying pDNA involves the assessment of nucleic acid delivery and protein production efficiency, however, the biological effect of the expressed protein is not typically evaluated. To develop an *in vitro* system that would allow the measurement of the bioactivity of the expressed protein, a co-culture model consisting of two cell populations was utilized. C*ell layer 1* represents the cells to be transfected non-virally with NPs carrying the therapeutic gene of interest, while *cell layer 2* represents the cells responding to the therapeutic protein. In the context of the retina, cell layer 1 represents the potential retinal target cell population (eg. healthy RGCs, astrocytes or Müller cells) and cell layer 2 represents the

neuronal-like test cells for neurite outgrowth measurement. As an initial model, an astrocyte cell line was selected to serve as "medic cells" after non-viral transfection producing and secreting BDNF and SH-SY5Y neuroblastoma cells, routinely used in high throughput neurite outgrowth assays, as BDNF-responsive cells and suitable for the evaluation of BDNF bioactivity [108]. Moreover, SH-SY5Y neuroblastoma cells, exposed to hydrogen peroxide, provide an *in vitro* oxidative stress disease model representing one of the major glaucomatous stresses that contributes to the disease pathogenesis.

Using the described co-culture model, it was demonstrated that transfected astrocytes were able to secrete enough bioactive BDNF and induced neurite outgrowth and extension in both untreated and oxidatively stressed SH-SY5Y cells. The two-layer co-culture model could potentially be used as a versatile system to test the transfectability and protein production of several retinal target cell types. The modality described here shows the feasibility of the approach for rapid screening of non-viral gene delivery systems for retinal gene therapy and provide a proof-of-concept that astrocytes can be genetically transformed into BDNF producing cells using a non-viral transfection method and the level of BDNF produced is sufficient to stimulate neurite outgrowth in a standard SH-SY5Y neuroblastoma cell model.

3.3 Materials and methods

3.3.1 Plasmid construct and NP formulation

The pDNA was prepared by cloning the BDNF (transcript variant 1) sequence (NCBI Reference Sequence: NM_170735) into pCMV6-Entry expression vector (Origene, Rockville, MD, USA) with 5' Sgfl (GCGATCGC) and 3' Mlul (ACGCGT). TAG stop codon was inserted downstream of the BDNF construct, upstream of the Myc-DDK, to prohibit the expression of BDNF-Myc-DDK fusion protein. De novo gene synthesis, construct cloning and DNA purification

was performed by Blue Heron Biotech (Bothell, WA, USA). NPs (NPs) were formulated by complexing either BDNF-encoding plasmid or gWiz™ GFP (green fluorescence protein) reporter plasmid (Aldevron, Fargo, ND, USA) with K2® transfection agent (Biontex Laboratories GmBH, München, Germany) at ratios of either 2 µL of K2® per 1 µg of pDNA (Formulation #1) or 4 µL of K2® transfection reagent per 1 µg of pDNA (Formulation #2). Size and zeta potential of K2-NPs were characterized by DLS using Zetasizer Nano ZS (Malvern Instruments, Malvern, Worcestershire, United Kingdom). Two hours prior to NP transfection, 2.5 µL of K2® Multiplier were added into the culturing medium of A7 astrocytes followed by K2-NPs.

3.3.2 Genetically modified BDNF-expressing astrocyte co-culture model

Co-culture was established using a combination of 0.4 µm polyester (PET) membrane transwell 12-well inserts (Corning) and glass bottom 12-well plates (MatTek Corporation, Ashland, MA, USA). Each well of the glass-bottom plates were pre-coated using recombinant human laminin (EMD Millipore, Billerica, MA, USA) at 0.625 µg/cm^2 overnight at 4°C, followed by seeding 100,000 A7 cells into each transwell insert and 200,000 SH-SY5Y cells into each well of the plates. Oxidative stress was induced in SH-SY5Y cells with 100 µM of hydrogen peroxide for 24 hours prior to co-culturing. A total of four conditions were evaluated, all in triplicates, with two conditions containing non-virally transfected astrocytes trA7/oxSH-SY5Y and trA7/SH-SY5Y; along with two controls such as oxidatively stressed neuroblastoma only (oxSH-SY5Y), and non-transfected A7 astrocyte co-cultured with oxidatively-stressed neuroblastoma cells (A7/oxSH-SY5Y).

3.3.3 Oxidative stress SH-SY5Y model

SH-SY5Y neuroblastoma cells (CRL-2266, ATCC, Manassas, VA, USA) were cultured in in 1:1 ratio of Eagle's Minimum Essential Medium (EMEM, ATCC, Manassas, VA, USA) and

F12 medium (Thermo Fisher Scientific, Waltham, MA, USA) supplemented with 10% fetal bovine serum (FBS) and 1% penicillin/streptomycin antibiotics (Pen/Strep). Cells were cultured in a 37 °C incubator with 95% air/5% carbon dioxide. To establish the oxidatively stressed SH-SY5Y modality, 20,000 SH-SY5Y cells were seeded into each well of black clear-bottom 96-well microplates (Corning, Corning, NY, USA) and hydrogen peroxide at concentrations of 50, 100, 150 or 200 μM was added for 24 hours, each in triplicates. The viability was measured using Presto Blue® viability assay (Thermo Fisher Scientific) at 24 hours with SpectraMax M5 microplate reader (Molecular Devices, Sunnyvale, CA, USA).

3.3.4 Transfection of A7 astrocytes

A7 rat astrocytes (a gift from Dr Jeremy Sivak, University of Toronto; [109, 110]) were cultured in DMEM/high glucose media (Hyclone, GE Healthcare Life Sciences, Logan, Utah, USA) supplemented with 10% FBS and 1% Pen/Strep at 37 °C in a 95% air/5% carbon dioxide. K2-NPs were first evaluated and optimized in monolayer cultures of A7 astrocytes. Cells at 25,000, 50,000 and 100,000/well (n=3 each) were seeded into clear 24-well culture plates (Grenier Bio-One, Monore, NC, USA) and transfected using K2-NPs carrying gWiz™ GFP. The transfection efficiency (TE) was assessed based on the percentage of cells expressing GFP and viability based on MitoTracker® Deep Red (Thermo Fisher Scientific) staining using Attune Flow Cytometer (Thermo Fisher Scientific).

3.3.5 BDNF protein production and neurite outgrowth bioassay

BDNF production in A7 astrocyte supernatants was assayed at 24, 48 and 72 hours using a human BDNF ELISA kit (R&D Systems, Minneapolis, MN, USA). Standards were prepared according to the manufacturer's protocol and standard curve was constructed using the 4 Parameter Logistic (4PL) Non-Linear Regression Model with an r^2 of 0.997. Neurite counts and length

measurements were performed by first fixing SH-SY5Y cells with 4% paraformaldehyde (PFA) in phosphate buffered saline (PBS; 137 mM NaCl, 2.7 mM KCl, 10 mM Na_2HPO_4, 1.8 mM KH_2PO_4) containing 1 mM of $CaCl_2$ and 0.5 mM $MgCl_2$ for 20 minutes at room temperature. Cells were then blocked using PBS containing 10% FBS, 0.1% Triton X-100, and 1% bovine serum albumin at 37 °C for 40 minutes. Post-blocking, 1X NorthernLights™ 493 (NL493)-conjugated mouse monoclonal anti-neuron-specific β-III tubulin antibody (R&D Systems) in PBS was added and incubated for 4 hours at 37°C. After immunostaining, cells were counterstained with 1 μM SYTO™ 61 (Thermo Fisher) for 20 minutes at 37°C. Cells were imaged using Zeiss LSM710 confocal laser scanning microscope (Carl Zeiss AG, Oberkochen, Baden-Wü, Germany) with 63x oil immersion objective. Ten fields of 2048x2048 images were captured from each replicate of each experimental condition with approximately 100 cells per field using Zen 2009 software (Carl Zeiss AG). Acquired images were evaluated for neurite counts and length by tracing the neurites using the Simple Neurite Tracer plug-in from Fiji software (ImageJ, National Institute of Health, Bethesda, MD, USA) [111]. Neurite length was determined by converting the number of pixels in each of the traced neurites to micrometer using a predetermined pixels/micron ratio.

3.3.6 Statistical analysis

The statistical analysis was performed using the Graph Pad Prism software (GraphPad Software, La Jolla, CA, USA). One-way ANOVA and two-way ANOVA in conjunctions Tukey post hoc test were used to analyze neurite distribution for single variable and multi-variable analysis, respectively. A p-value of less than 0.05 was considered as statistically significant.

3.4 Results

3.4.1 Astrocyte-neuroblastoma three-dimensional co-culture model for neurite extension evaluation

A simple contact-independent two-layer (three-dimensional) neuronal co-culture model was developed to test the effect of BDNF, produced by non-virally transfected A7 astrocytes, by evaluating the neurite growth stimulation of a second cell population representing oxidatively damaged retinal cells. The transfected A7 astrocytes were seeded into transwell inserts, while the SH-SY5Y neuroblastoma cells cultured as a monolayer in the bottom of the wells (Figure 3.1)

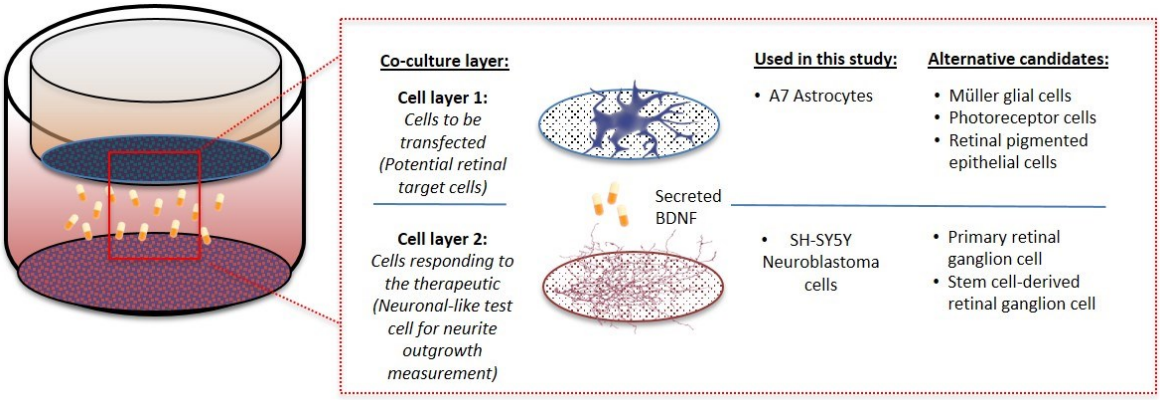

Figure 3.1 Schematic drawing of the two-layer, contact-independent 3D astrocyte-SH-SY5Y co-culture model. SH-SY5Y cells were cultured on laminin-coated glass bottom plates and astrocytes were cultured in transwell inserts that were positioned in the same well separated by the culture medium and membrane. NP-transfected astrocytes carrying BDNF-encoding plasmid express BDNF, stimulating SH-SY5Y cells. The bioactivity and therapeutic potential of the secreted BDNF are evaluated by comparing the neurite counts and the neurite lengths of BDNF-exposed SH-SY5Y versus the SH-SY5Y presented in BDNF-absent controls.

To estimate the LD50, oxidative stress was titrated in separate SH-SY5Y cultures with 50, 100, 150, and 200 µM hydrogen peroxide. The corresponding cell viabilities were 52.0±13.5%, 54.1±5.1%, 12.3±0.9%, and 1.9±2.0% after 24 hours of exposure, respectively. The 100µM concentration was chosen for generating oxidative stress in the co-culture model (Figure 3.2), due to robustness and lower variability compared to 50 µM.

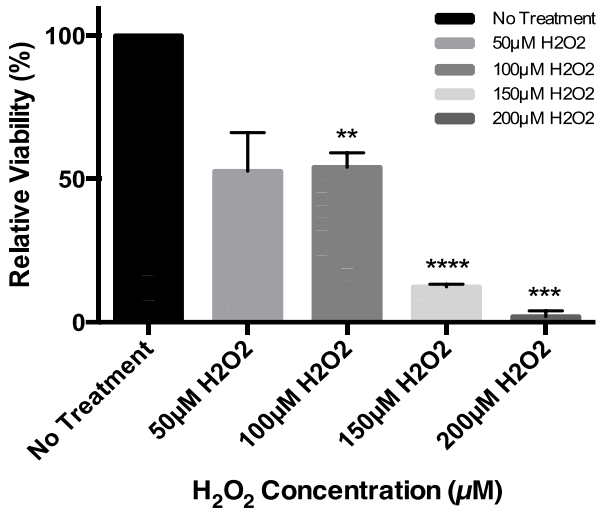

Figure 3.2 Viability of SH-SY5Y cells 24 hours after hydrogen peroxide exposure at concentrations of 50, 100, 150, and 200 µM. Viability was measured based on Presto Blue® assay. Values expressed as mean ± s.d., n=3. Statistical significance was compared to the untreated condition. * $p<0.05$; ** $p<0.01$; *** $p<0.001$; **** $p<0.0001$

3.4.2 Efficient and safe non-viral gene delivery system for astrocyte delivery

K2-NPs are highly cationic NPs with a mean hydrodynamic diameter of 97.0±1.1 and 83.9±0.4 nm, with a polydispersity index (PDI) of 0.22±0.01 and 0.17±0.01, and an average zeta potential of +59.6±1.6 mV and +57.3±2.8 mV with DNA:K2 ratio of 1 µg: 2 µL (Formulation 1) and 1 µg: 4 µL (Formulation 2), respectively (Table 3.1). The TE of A7 astrocytes was optimized using two different compositions of K2-NPs and three different cell seeding densities. The TE was 17.3±5.8%, 15.8±2.6%, and 14.3±5.2% (Formulation 1) and 39.5±4.6%, 31.3±1.6%, and 29.9±1.8% (Formulation 2) after 48 hours with seeding densities of 25,000, 50,000 and 100,000 cells/well, respectively (Figure 3.3). The viability of A7 cells after transfection were 71.40±15.52%, 76.2±1.7%, 86.3±0.4% (Formulation 1), and 72.6±2.3%, 44.8±2.2%, and 54.9±3.9% (Formulation 2) at the indicated cell densities, respectively (Figure 3.3).

Table 3.1 Size (hydrodynamic diameter), polydispersity index and zeta potential of the K2-NPs formulated with different DNA:K2 ratios. Values expressed as mean ± s.d., n=3

NP Formulation	Size (nm)	PDI	Zeta Potential (mV)
DNA : K2 (1 µg : 2 µL) (Formulation #1)	96.9±1.1	0.22±0.01	+59.6±1.6
DNA : K2 (1 µg : 4 µL) (Formulation #2)	83.9±0.3	0.17±0.01	+57.3±2.8

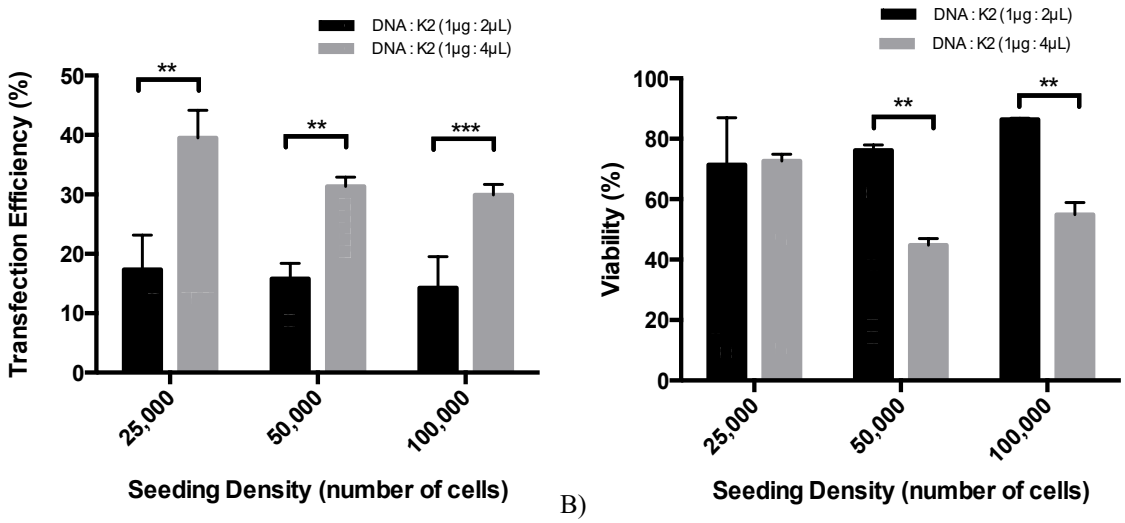

Figure 3.3 Optimization of K2-NPs for optimal transfection condition using two different formulations and three different seeding densities of 25,000, 50,000 and 100,000 A7 astrocytes cells: B) TE was measured based on GFP expression and the viability was evaluated by MitoTracker® Deep Red using flow cytometry. Values expressed as mean ± s.d., n=3 * $p<0.05$; ** $p<0.01$; *** $p<0.001$; **** $p<0.0001$

3.4.3 BDNF-transfected astrocytes can produce and secrete BDNF protein

BDNF was detected in co-cultures containing non-virally transfected astrocytes in increasing concentrations with time. More specifically, 3,750.8±251.1 ng/mL, 9,052.6±1391.2 ng/mL, and 10,367.1±390.8 ng/mL were detected in trA7/oxSH-SY5Y co-culture conditions at 24, 48, and 72 hours, respectively (Figure 3.4). Similarly, BDNF was also detected in the culture medium of trA7/SH-SY5Y co-cultures at concentrations of 3,836.9±595.5 ng/mL, 8,816.8±911.6 ng/mL, and 11,585.3±902.5 ng/mL at 24, 48, and 72 hours, respectively. BDNF protein was not

detectable in control experimental conditions such as oxSH-SY5Y and A7/oxSH-SY5Y, where BDNF-transfected astrocytes were not present in the co-culture.

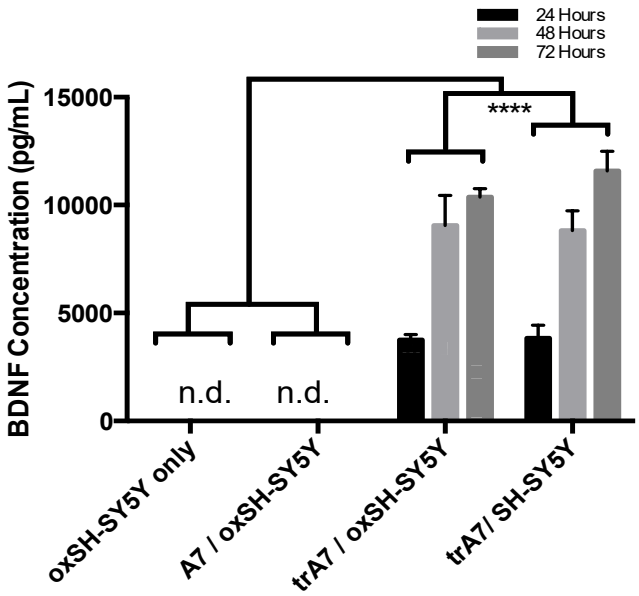

Figure 3.4 Quantification of the secreted BDNF protein using ELISA in the four different experimental conditions at 24, 48, and 72 hours. Values expressed as mean ± s.d., n=3; n.d.= not detectable. * $p<0.05$; ** $p<0.01$; *** $p<0.001$; **** $p<0.0001$

3.4.4 BDNF secreted from non-virally transfected astrocyte are bioactive and sufficient to induce neurite extension in neuroblastoma

The increased number of neurites with higher neurite lengths confirmed the bioactivity of BDNF secreted from the transfected A7 astrocytes over 72 hours (Figure 3.5). Neurite count comparison showed that both trA7/oxSH-SY5Y and trA7/SH-SY5Y consistently produced higher neurite counts compared to A7/oxSH-SY5Y and oxSH-SY5Y only experimental conditions (Figure 3.6). Statistical analysis using one-way ANOVA shows that trA7/oxSH-SY5Y consistently showed higher neurite count compared to oxSH-SY5Y and A7/oxSH-SY5Y at 24, 48, and 72 hours with p-values of at least <0.001. In addition, trA7/SH-SY5Y also demonstrated to

have consistently higher number of neurite counts compared to oxSH-SY5Y and A7/oxSH-SY5Y, the differences peaked at 48 and 72 hours with p-value of at least <0.001.

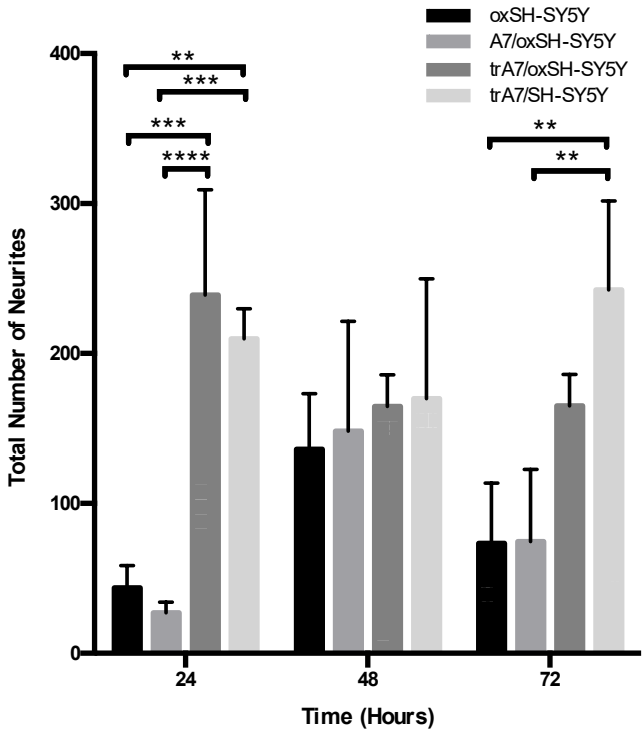

Figure 3.5 Evaluation of BDNF-mediated effect on total neurite count at 24, 48, and 72 hours. * p<0.05; ** p<0.01; *** p<0.001; **** p<0.0001

Neurite length distribution profile was generated to compare the number of neurites in different length categories: <10 μm, between 10 and 20 μm, or > 20μm. Based on the neurite distribution profile, it was shown that trA7/oxSH-SY5Y and trA7/SH-SY5Y consistently had higher number of neurites that were longer than 20 μm compared to oxSH-SY5Y and A7/oxSH-SY5Y over 72 hours (Figure 3.7). The most significant increase in the number of neurites that was longer than 20 μm was observed at 24 and 72 hours. The trA7/oxSH-SY5Y was shown to have 8.2 times and 7.5 times more neurites longer than 20 μm compared to the BDNF-absent controls of oxSH-SY5Y and A7/oxSH-SY5Y at 24 hours with a p-value of <0.001.

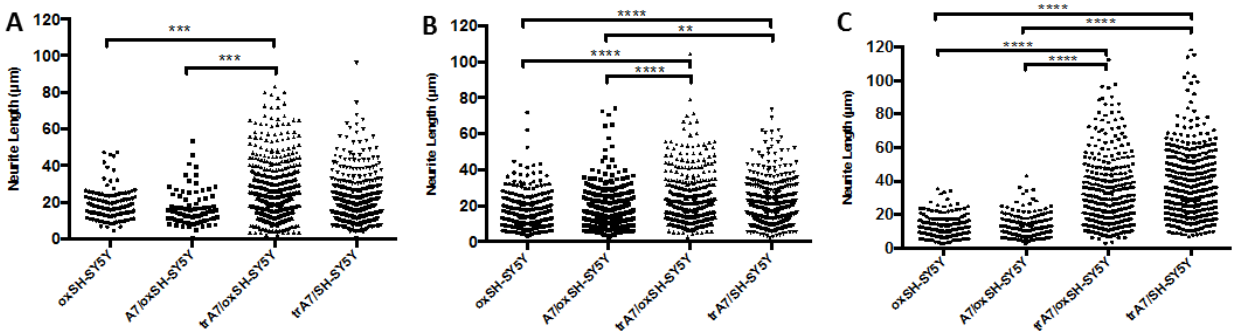

Figure 3.6 SH-SY5Y cells neurite length distribution profile under various experimental conditions at 24 hours (A), 48 hours (B) and 72 hours (C). Each condition was performed in triplicates, and 10 frames were measured for each replicate. * p<0.05; ** p<0.01; *** p<0.001; **** p<0.0001

Furthermore, trA7/oxSH-SY5Y was also shown to have 10.8 times and 10.4 times the number of neurites with longer than 20 µm compared to the BDNF-absent controls of oxSH-SY5Y and A7/oxSH-SY5Y at 72 hours, respectively. Whereas, the extent of neurite extension longer than 20 µm in unstressed SH-SY5Y cells co-cultured with BDNF-transfected A7 (trA7/SH-SY5Y was 22.4 and 21.6 times greater compared to oxSH-SY5Y and A7/oxSH-SY5Y at 72 hours, respectively.

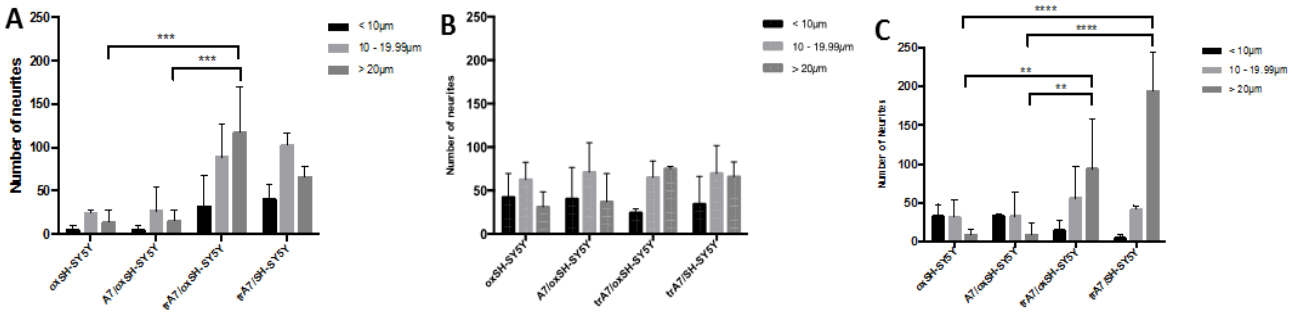

Figure 3.7 Total number of SH-SY5Y neurites in each length categories: less than 10 µm, between 10-20 µm, or greater than 20 µm over 24 hours (E), 48 hours (F), and 72 hours (G). Each condition was performed in triplicates, and 10 frames were measured for each replicate. * p<0.05; ** p<0.01; *** p<0.001; **** p<0.0001

3.5 Discussion

The specific modalities for non-viral gene therapy using NFs to support regenerative functions of the retina are currently under intensive investigations. Several specific aspects of a neuroprotective and neuroregenerative treatment, including the design of non-viral gene delivery systems, best candidate cell types to produce the NF and delivery methods require elucidation.

In this study, the usefulness of a two-layer astrocyte-neuroblastoma co-culture system to test the BDNF production efficiency of non-virally transfected astrocytes and neurite outgrowth stimulation by the secreted BDNF protein was demonstrated. Additionally, the effect of astrocyte-secreted BDNF on oxidatively damaged SH-SY5Y cells as a potential *in vitro* disease model system was also evaluated. This aspect of the co-culture system is useful since it can model oxidative stress in the gene therapy recipient cell line which was implicated to be one of the major contributors to RGC death in glaucoma [60].

The results show that BDNF expressed by trA7 cells increased neurite outgrowth response in both SH-SY5Y and oxSH-SY5Y cells over 72 hours. BDNF-mediated neurite extension increase included both the neurite counts and the proportion of neurites that were longer than 20 μm in neuroblastoma cells compared to cells that were not exposed to BDNF. However, more detailed investigation on the dose-dependency of BDNF-mediated neurite extension will be needed. Furthermore, assessment of total neurite count alone is insufficient in determining the bioactivity and neurite outgrowth potential, and instead, the profiling and comparing of neurite lengths abundancy is a more accurate indicator.

In case of a therapy that aims to rescue retinal ganglion cells in glaucoma, astrocytes appear to be one of the most promising candidates for neurotrophin supplementation gene therapy approach given their distribution in strategic areas of the eye such as in the matrices of lamina

cribrosa, which is strongly associated with the pathogenesis of glaucoma [112]. By targeting the astrocytes in the eye for gene delivery, transfected-astrocytes can be transformed into “medic cells” and become the protein production ‘factories’, particularly in the area close to the lamina cribrosa to provide the retinal ganglion cells with NFs for rescue and potential regeneration capacity.

In terms of the selection of a NF for gene therapy, BDNF continues to be a molecule of interest for therapeutic applications in glaucoma. Findings within the past decade have revealed the increasing importance of BDNF on the health of RGCs. In glaucoma, although BDNF is expressed locally in the retina, it is only expressed at low levels while most of the BDNF is retrogradely transported from the SC, which is blocked in the event of elevated intraocular pressure [113]. BDNF appears to have multiple effects on RGCs as it directly corrects the problem associated with bidirectional transport of NFs, and at the same time indirectly influence other retinal cells in the guidance of damaged axons. For instance, neurotrophin deprivation due to bidirectional axonal transport obstruction within RGCs was shown to result in axonal damage [114]. Orthograde flow at the optic nerve head prevents proteins made by RGCs from reaching their axonal extensions and perturbed retrograde transport of NFs produced in the SC in the brain to reach the RGC soma [115]. BDNF also appears to support axonal path finding to the brain [116, 117]. Given the results in this study showing that transfected astrocyte can produce bioactive BDNF, further research in the development of targeted astrocyte delivery would be advantageous. In this study, BDNF-mediated neurite extension resulted in increased neurite counts and the proportion of extended neurites (>20 μm) in neuroblastoma cells compared to cells that were not exposed to BDNF at 24 and 72 hours, suggesting that BDNF gene therapy is promising for optic nerve repair and regeneration.

Throughout the decades of glaucoma research, a significant obstacle was the lack of a true representative RGC line for *in vitro* research. The RGC-5 virally transformed and known at the time as a rat RGC cell line provided a much needed model for close to a decade [118]. However, recent investigations confirmed that RGC-5 is in fact a mouse photoreceptor cell line, rather than a rat RGC line as it was claimed to be [119]. There is currently no RGC line available, apart from primary RGCs. Indeed, primary RGCs would be the most ideal cells to use, however, RGCs are present in low abundance *in vivo*, which makes it costly to isolate high cell populations for rapid and large-scale drug screenings. Furthermore, primary RGCs undergo spontaneous degeneration upon isolation, which makes it difficult to recreate representative glaucomatous stress model *in vitro* given it is already undergoing degeneration as soon as it is isolated. As a result, an initial model was described in the study for rapid screening of non-viral BDNF gene therapy with astrocytes. The model presented in this study is flexible in terms of the two cell layers; depending on the target "medic cell" of interest, various gene delivery target cells could be selected for evaluation, such as Müller glial cells or healthy RGCs.

3.6 Conclusion

Overall, our results show that the neurite outgrowth quantitation of astrocyte-neuronal co-culture model described in this study can be used to evaluate non-viral gene delivery systems for retinal gene therapy by determining the bioactivity of the secreted BDNF. A schematic describing the systematic flow of bioassay is illustrated in Figure 3.8. Furthermore, it also demonstrates that K2® NPs can efficiently deliver BDNF-encoding pDNA into A7 astrocytes to produce functional BDNF and initiate neurite extension in cell layer 2. Lastly, BDNF supplementation gene therapy using a non-viral gene delivery vector could be a promising approach for the rescue of

glaucomatous-stressed retinal ganglion cells using astrocytes as gene delivery targets with the added possibility of needle-free topical administration of NPs in the future.

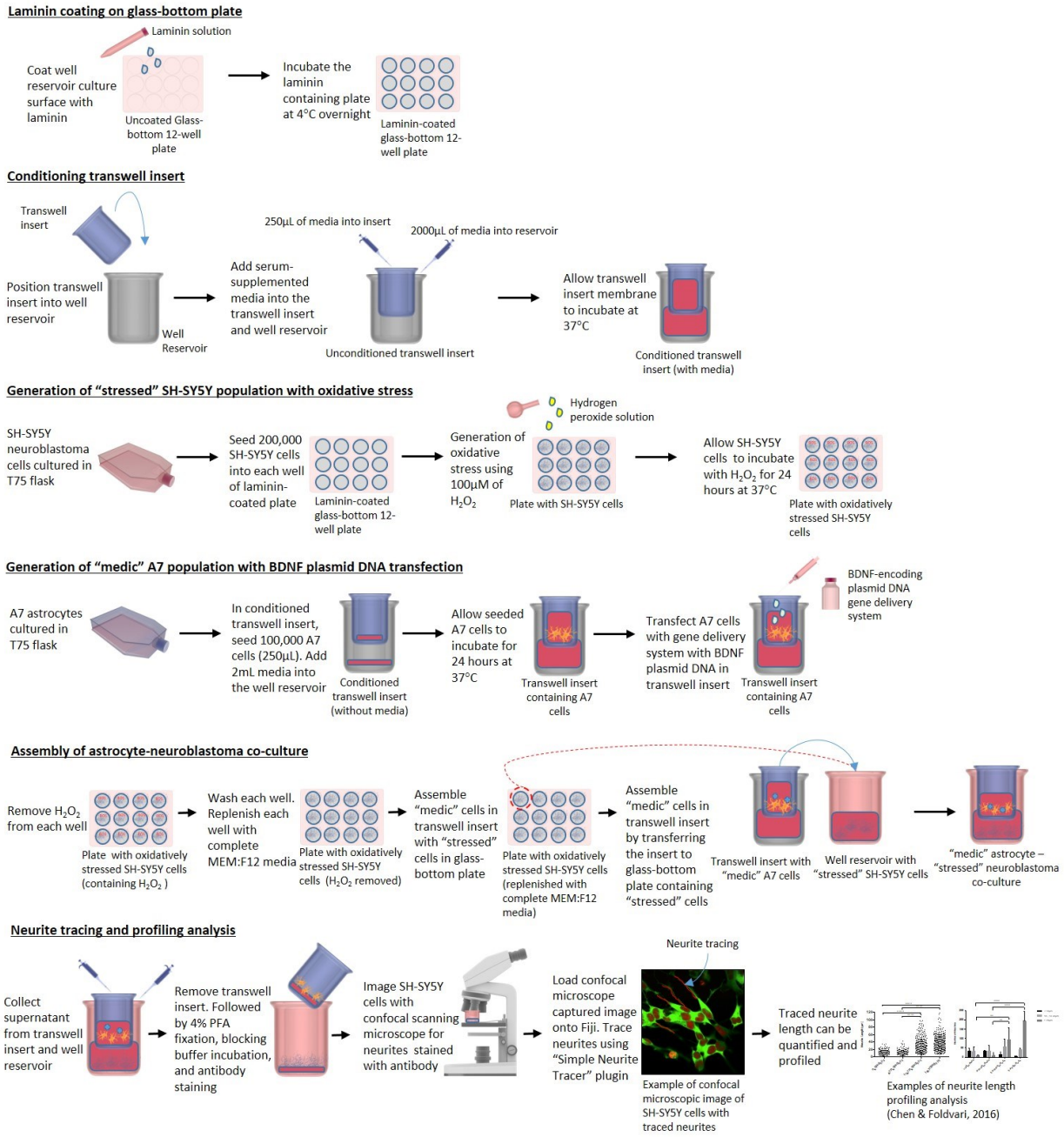

Figure 3.8 Schematic of the systemic bioassay protocol procedure for therapeutic protein bioavailability and bioactivity assessment [120]

Chapter 4 Characterization of RGC-like cells derived from retinal multipotent stem cells

4.1 Rationale and objective

Protection and rescue of RGCs is a pivotal aspect in glaucoma management. The lack of a representative RGC cell model to assess RGC-specific responses of candidate therapeutics is currently a major hindrance to therapeutic discovery of new candidate compounds and delivery systems for downstream development. To address this issue, multipotent retinal stem cell-derived RGCs was generated, termed XFC cells, which can be utilized for preclinical screening of RGC-aimed therapeutics. Multiplexed gene expression profiling and stimuli-mediated neurite extension assessment showed that one of the isolated cell population, XFC-3 cells, express key RGC biomarkers *Map-2*, *Rbpms*, and *Tubb3,* and exhibit neurite extension upon activation by BDNF, CNTF, and Y-27632. The application of XFC-3 cells in therapeutic discovery was demonstrated in the co-culture bioassay model described in previous chapter for screening NF gene therapy systems. By using ELISA, immunofluorescent imaging and neurite tracing techniques, the bioavailability and bioactivity of BDNF secreted from XFC-3 cells transfected by various nanoparticles were evaluated. In summary, this study showed the generation of stem cell-derived XFC-3 cells that express key RGC characteristics that have potential as an RGC cell model for preclinical screening and therapeutic discovery applications.

4.2 Background

Degeneration of RGCs is a key aspect of glaucoma pathogenesis that ultimately results in continued loss of vision despite the current standard of treatment. Gene therapy with NF is a promising approach for neuroprotection of the retina by supporting the functions of damaged RGCs. In order to develop effective gene delivery systems, a reliable and representative RGC cell

model is needed. In light of the misidentification of the RGC-5 cell line [119], used extensively by many research groups for years, currently no cell model is available that can be utilized for *in vitro* preclinical screening of promising therapeutic candidates. While the utilization of primary RGCs as a source of RGCs is a possible option for *in vitro* investigations, their use is limited due to low abundancy *in vivo*, poor isolation efficiency, and spontaneous degeneration upon isolation.

Stem cells are unique cell types characterized by their intrinsic ability to self-renew and to differentiate into multiple different cell types, providing opportunity for generating specific cell types of interest for broad biomedical and research applications. In particular, multipotent retinal stem cells (RSCs) are promising for generating most retinal cell types. Li and colleagues have described successful isolation of CD1-4 multipotent RSCs from CD-1 mouse retina that can differentiate into multiple retinal cell types including rod photoreceptor cells, cone photoreceptor cells, Müller glial cells, bipolar cells, amacrine cells, horizontal cells, and RGCs [121]. Furthermore, they showed that the photoreceptor cells isolated from differentiated retinal populations were able to restore the functionality of the photoreceptors in photoreceptor-deficient *rd1* mutant mouse after transplantation [121].

In this study, we show the isolation and characterization of RGC-like cells from the mixed retinal cell population differentiated from CD1-4 RSCs. Amongst the cells isolated, one of the isolate termed XFC-3 was determined to be RGC-like, expressing key RGC biomarkers *Map-2, Rbpms,* and *Tubb3.* Moreover, XFC-3 cells exhibit neuronal morphology with neurites that can be extended in response to stimuli such as BDNF, CNTF, Y-27632 RKI, and their combinations.

Isolated XFC-3 cells were incorporated into the 3D co-culture bioassay model developed previously in our laboratory for screening retinal gene delivery systems [122]. This 3D co-culture model has two layers of cells where *cell layer 1* represents the transfected cells and *cell layer 2*

represents the cells responding to the expressed therapeutic proteins such as NF. The choice of cells in each layer can reflect the particular research question asked. In the model the astrocyte-neuroblastoma cell combination represented a healthy transfected cells (astrocytes) or "medic cells" producing and secreting BDNF and the recipient SH-SY5Y neuroblastoma cells (routinely used in high throughput neurite outgrowth assays) as BDNF-responsive cells and suitable for the evaluation of BDNF bioactivity. In the current study, the use of XFC-3 cells allow direct evaluation of the transfectability and gene expression by RGC-like cells, both healthy and stressed thereby providing an opportunity to develop it as a 'disease' model [122]. Overall, the results described in this paper demonstrate the generation and characterization of RGC-like cells that may serve as a cell model for the preclinical *in vitro* development and screening of candidate RGC therapeutics.

4.3 Materials and methods

4.3.1 CD1-4 RSC culture

CD1-4 RSCs were kindly gifted by Dr. Ting Xie from the Stower Institute for Medical Research and University of Kansas. CD1-4 RSCs were isolated from the neuroretina, excluding retinal pigmented epithelium (RPE), ciliary body, and posterior tissue surrounding the optic nerve head, of 4-8 weeks old CD-1 mouse as described in published literature [121]. Purified CD1-4 RSCs were cultured in 12-well plates coated with 0.2% gelatin for 3 hours at 37 °C and maintained in advanced DMEM/F12 media (1:1) (Gibco, Thermo Fisher Scientific, Waltham, MA, USA) containing 1.0 g/L glucose (Sigma-Aldrich, St. Louis, MO, USA), 1.0 g/L lactose (Sigma-Aldrich), 1.0 g/L BSA (Sigma-Aldrich), 0.045 g/L proline (Sigma-Aldrich), 2 mM nicotinamide (Sigma-Aldrich), 2 mM L-glutamate (Gibco), 1% penicillin/streptomycin (Hyclone, GE Healthcare Life Sciences, Logan, Utah, USA), 1% insulin-transferrin-supplement (Gibco), 5%

knockout serum replacement (Gibco), 20 ng/mL EGF (Gibco), and 20 ng/mL bFGF (Gibco). Cells were cultured in humidified incubator at 37°C with 5% CO_2.

4.3.2 Differentiation of CD1-4 RSCs into retinal cell types

CD1-4 RSCs were differentiated in 24-well glass-bottom plates (MatTek Corporation, Ashland, MA, USA) coated with 0.015 mg/mL poly-L-ornithine (EMD Millipore, Billerica, MA, USA) overnight at room temperature, followed by subsequent coating of 2 µg/cm^2 laminin (EMD Millipore) overnight at 4 °C. 100,000 cells per well were seeded for differentiation, with differentiation medium containing DMEM/F12 (1:1) (Gibco), B-27 supplement (1:50) (Gibco), 2 mM L-glutamate (base differentiation medium) in addition to 10 ng/mL bFGF for the first 2 days. For the next 4 days, differentiation medium was replaced with advanced DMEM/F12 media (Gibco) containing, 2% B-27 supplement (Gibco), 1% N-2 supplement (Gibco), 2 mM L-glutamate (Gibco), and 10 ng/mL bFGF (Gibco). Isolated *XFC* cells were cultured in laminin-coated 6-well glass-bottom plates (MatTek Corporation) using advanced DMEM/F12 (Gibco) media containing 1.0 g/L glucose (Sigma-Aldrich), 1.0 g/L lactose (Sigma-Aldrich), 1.0 g/L BSA (Sigma-Aldrich), 0.045 g/L proline (Sigma-Aldrich), 2 mM nicotinamide (Sigma-Aldrich), 2 mM L-glutamate (Gibco), 1% penicillin/streptomycin (Hyclone), 1% insulin-transferrin-supplement (Gibco), and 10% FBS (Thermo Fisher Scientific). These cells were named XFC cells representing the new differentiated RGC-like cells, with five different cell line variants of XFC were isolated (XFC-2, XFC-3, XFC_m-2, XFC_m-4, and XFC_{facs}-1).

4.3.3 NP gene delivery systems preparation

Three different types of non-viral gene delivery systems were formulated. GL-NP system were prepared by complexation of 18-7NH-18 GS (synthesized in-house [123]) with gWiz™ GFP plasmid (Aldevron, Fargo, ND, USA) at desired charge ratios for 15 minutes at room temperature,

followed by addition of 1,2-dioleoyl-sn-glycero-3-phosphoethanolamine (DOPE) neutral lipid at desired GS/lipid ratios. SWNT system were prepared by first non-covalently functionalizing PureTube™ SWNT (ptSWNT) with GS as described earlier [124]. Briefly, ptSWNTs (NanoIntegris Inc., Boisbriand, QC, Canada) were dispersed in 1 mg/mL 12-3-12 GS solution at 10 µg/mL, and sonicated using Branson bath sonicator at 40 kHz frequency (Branson Ultrasonics Corporation, Danbury, CT, USA) for 1h at temperature not exceeding 40°C. The functionalized ptSWNTs (f-ptSWNT) were then complexed with gWiz™ GFP pDNA (Aldevron) at specified ratios for generation of f-ptSWNT-pDNA complexes. The third transfection agent, the commercially available K2® lipopolyamine-based proprietary transfection reagent (Biontex Laboratories GmBH, München, Germany) was used. K2-NPs were formulated by the complexation of K2® transfection reagent with either gWiz™ GFP (Aldevron) or BDNF (Blue Heron) pDNA at desired ratios according to the manufacturer's protocol. Either gWiz™ GFP or BDNF pDNA was used depending on the specific goal of the evaluation. A pDNA dose of 1 µg/well was used in each transfection.

4.3.4 Magnetic-activated magnetic cell separation

Immunopanning separation was performed using an RGC isolation kit (Miltenyi Biotec, Auburn, CA, USA) with mouse anti-Thy1.2 microbeads instead of anti-Thy1.1 microbeads for mouse RGC isolation. Briefly, differentiated stem cells were dissociated using Accumax™ cell detachment solution (Innovative Cell Technologies, San Diego, CA, USA) and pelleted at 300 x g for 5 minutes. Cells were then resuspended with 500 µL of Thy-1.2 microbeads (1:10, Miltenyi Biotec) and biotinylated depletion antibody (1:50, Miltenyi Biotec) in 0.5% BSA-containing PBS (with calcium and magnesium) for 15 minutes at room temperature. Cells were then pelleted at 130 x g for 5 minutes and stained with anti-biotinylated antibody (1:5, Miltenyi Biotec) diluted in

500 µL of 0.5% BSA-containing PBS (with calcium and magnesium) for 15 minutes. Endothelial and microglial cells were depleted using the MACSiMAG separator (Miltenyi Bitoec) and Thy-1 positive cells were selected with MACs separator using MS column (Miltenyi Biotec).

4.3.5 Fluorescent-activated cell sorting

The differentiated retinal cell population was blocked with blocking media (10% serum and 1% in PBS) for 15 minutes at room temperature. Cells were then stained with anti-Thy1.2-FITC antibody (1:250) (Miltenyi Biotec) for one hour on ice. Stained cells were sorted using BD FACSAria Fusion Cell Sorter with automated cell deposition unit (BD Biosciences, San Jose, CA, USA). Cells were sorted into advanced DMEM/F12 medium (Gibco) supplemented with 10% FBS (Thermo Fisher Scientific), 2% B-27 supplement (Gibco), 1% L-glutamine (Gibco), and 1% penicillin/streptomycin (Hyclone).

4.3.6 Gene expression profiling analysis

RNA samples were isolated using PicoPure® RNA Isolation Kit (Arcturus, Thermo Fisher Scientific, Waltham, MA, USA), based on the manufacturer's protocol and subjected to retinal biomarker gene expression profiling using NanoString nCounter® Analysis System, through quantification of mRNA targets in the custom retinal biomarker codeset (NanoString, Seattle, Washington, USA). The panel of target genes included biomarkers representing major retinal cell types: *ISL-1, Map-2, Nef-H, Pou4f1, Rbpms, Sncg, Thy-1.2,* and *Tubb3* as representative RGC biomarkers; *Aqp4, Prdx6* and *Slcla3* as representative astrocyte biomarkers; *Abca8a*, *ald1a1*, and *Vim* as representative Müller glia biomarkers; and *Nrl* and *Rom1* as representative photoreceptor biomarkers. *Rpe65, Calb2, Prkca*, and *Lim2* each individually represent RPE, amacrine, bipolar and horizontal cell biomarkers, respectively. Each reaction was performed with 100 ng of RNA in a 5µL loading volume, mixed with capture and reporter probes.

4.3.7 BDNF, CNTF, and Y-27632 treatment

Five thousand cells were seeded into each well of 24-well glass-bottom plates (MatTek Corporation) and allowed for incubation for 24 hours prior to the addition of the stimuli with a media volume of 500 µL. BDNF (PeproTech, Montreal, QC, Canada), CNTF (Peprotech), and Y-27632 (Sigma-Aldrich) proteins were prepared by dissolving the lyophilized proteins in sterile water. Protein treatments were added directly into the appropriate wells at desired concentration.

4.3.8 Immunofluorescent staining for flow cytometry analysis

Cells were fixed with 4% PFA (Alfa Aesar, Tewksbury, MA, USA) for 15 minutes at room temperature and blocked with 10% bovine serum (Thermo Fisher Scientific) and 0.3% Triton X-100 for 45 minutes at room temperature. Cells were then stained with one of the following antibodies: mouse anti-Nestin conjugated with Alexa Fluor® 488 (1:250, EMD Millipore), mouse anti-beta-III tubulin conjugated with Alexa Fluor® 488 (1:250, EMD Millipore), mouse anti-Map-2 conjugated with Alexa Fluor® 488 (1:250, EMD Millipore), or mouse anti-Thy.1.2 conjugated to FITC (1:250, Miltenyi Biotec) for one hour at room temperature. Stained cells were then analyzed using Attune Flow Cytometer (Applied Biosystems, Thermo Fisher Scientific, Waltham, MA, USA).

4.3.9 Immunofluorescent staining for confocal microscopy and neurite tracing

After 24 hours of incubation, equal volumes of 4% PFA (Alfa Aesar) were added directly into the media for 2 minutes at room temperature. After 2 minutes, media were removed and 200 µL of 4% PFA (Alfa Aesar) were added into each well and incubated for 13 minutes at room temperature. After fixation, PFA was removed and each well was washed twice with 200 µL of Wash Buffer (0.1% BSA in PBS), and blocked with 200µL of Blocking Buffer (10% FBS + 0.03% Triton in PBS) for 45 minutes at room temperature. Beta Tubulin III conjugated with Alexa Fluor®

647 (BioLegend, San Diego, CA, USA) staining buffer was prepared in Dilution Buffer (1% FBS + 1% BSA + 0.03% Triton + 0.01% sodium azide) at 1 µg/mL. After 45 minutes of blocking, 200 µL of the antibody was added into each well and incubated overnight at 4°C. Cells were washed with cold PBS (137 mM NaCl, 2.7 mM KCl, 10 mM Na_2HPO_4, 1.8 mM KH_2PO_4) and counterstained with fluorescent nucleic acid stain, Syto™ 16 (Thermo Fisher Scientific), at 500 nM concentration prior to imaging. Each well was imaged using a Zeiss LSM710 laser scanning confocal microscope (Carl Zeiss AG, Oberkochen, Baden-Wu, Germany) with a 20x objective. For each well, nine images with a resolution of 1024x1024 were captured using the tile scan function in the Zen 2009 software (Carl Zeiss AG). Captured images were traced using Simple Neurite Tracer plugin in Fiji software (ImageJ). Neurite length changes were quantified and analyzed using GraphPad Prism software (GraphPad Software, La Jolla, CA, USA).

4.4 Results

4.4.1 Differentiated CD1-4 RSC population expresses biomarkers indicative of retinal ganglion cell

Immunofluorescence results showed that the six-day differentiated CD1-4 RSC population consisted of cells that express β-tubulin III (15.8±6.9%), Map-2 (37.7±5.9%), and Thy-1 (3.9±0.5%), suggesting the presence of RGCs within the differentiated cell population. Stem cell biomarker nestin was also evaluated, and it was found that 56.9% of the differentiated cell population showed this stem cell biomarker expression (Table 4.1).

Table 4.1 Biomarker characterization of differentiated RSC after 6 days of differentiation. Values expressed as mean ± s.d., n=3

Biomarker	Fluorophore	% of Cells Expressing Biomarker
Nestin	Alexa Fluor® 488	56.9±8.3
B-III Tubulin	Alexa Fluor® 488	15.8±6.9
Map-2	Alexa Fluor® 488	37.7±5.9
Thy-1	FITC	3.9±0.5

4.4.2 Isolation and cultivation of XFC cells *in vitro*

Three types of stem cell-derived RGC-like cells (*XFC*, XFC_m, and XFC_{facs}) were generated using different combinations of differentiation protocols and Thy-1 positive cell isolation methods. More specifically, *XFC* cell series (Figure 4.1) are stem cell-derived RGC-like cells isolated from 6-day differentiated stem cell population using MACS isolation method. XFC_m cell series are stem cell-derived RGC-like cells isolated from a 14-day differentiated stem cell population using MACS isolation method. XFC_{facs} cell series are stem cell-derived RGC-like cells isolated from a 6-day differentiated stem cell population using FACS isolation method.

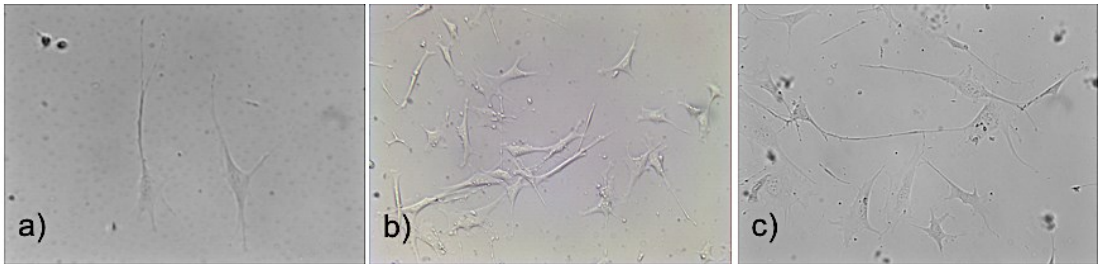

Figure 4.1 Thy-1 positive cell isolated from differentiated RSC cultured on laminin-coated surface over time: A) 2 days after isolation; B) 3 days after isolation; and C) 7 days after isolation. Images were captured with 10x objective using light microscopy

4.4.3 XFC cells express multiple RGC biomarkers

XFC, XFC_m, and XFC_{facs} were characterized using multiplexed gene expression profiling technique, NanoString nCounter® technology, to characterize the cells based on their retinal cell biomarker mRNA expression profile. The nCounter® technology utilizes a mRNA multiplex platform, which can quantify the levels of mRNA expression of the desired gene targets. For this evaluation, we have designed a multiplex gene panel that includes biomarkers representing major cell types found in the retina including RGCs, astrocytes, Müller glia, photoreceptor, RPE, amacrine, bipolar, and horizontal cells. *ISL-1, Map-2, Nef-H, Pou4f1, Rbpms, Sncg, Thy-1.2,* and *Tubb3* are representative RGC markers; *Aqp4, Prdx6* and *Slcla3* are representative astrocyte markers; *Abca8a*, *ald1a1*, and *Vim* are representative Müller glia markers; and *Nrl* and *Rom1* are representative photoreceptor markers. *Rpe65, Calb2, Prkca*, and *Lim2* each individually representative markers for RPE, amacrine, bipolar, and horizontal cells, respectively.

The XFC series of cells consist of XFC-2 and XFC-3 cells, which were isolated from independent 6-day differentiated RSC cell populations using MACS. Similarly, the XFC_m series cells consist of XFC_m-2 and XFC_m-4 cells, which were isolated from independent 14-day differentiated RSC cell populations using MACS. An alternative method of isolation using FACS was also evaluated on 6-day differentiated RSCs for comparison, which resulted in XFC_{facs} cells. Gene expression was profiled by quantifying target gene mRNA copies expressed from target cells, and a threshold of 20 mRNA copies was considered as positive mRNA expression with high confidence.

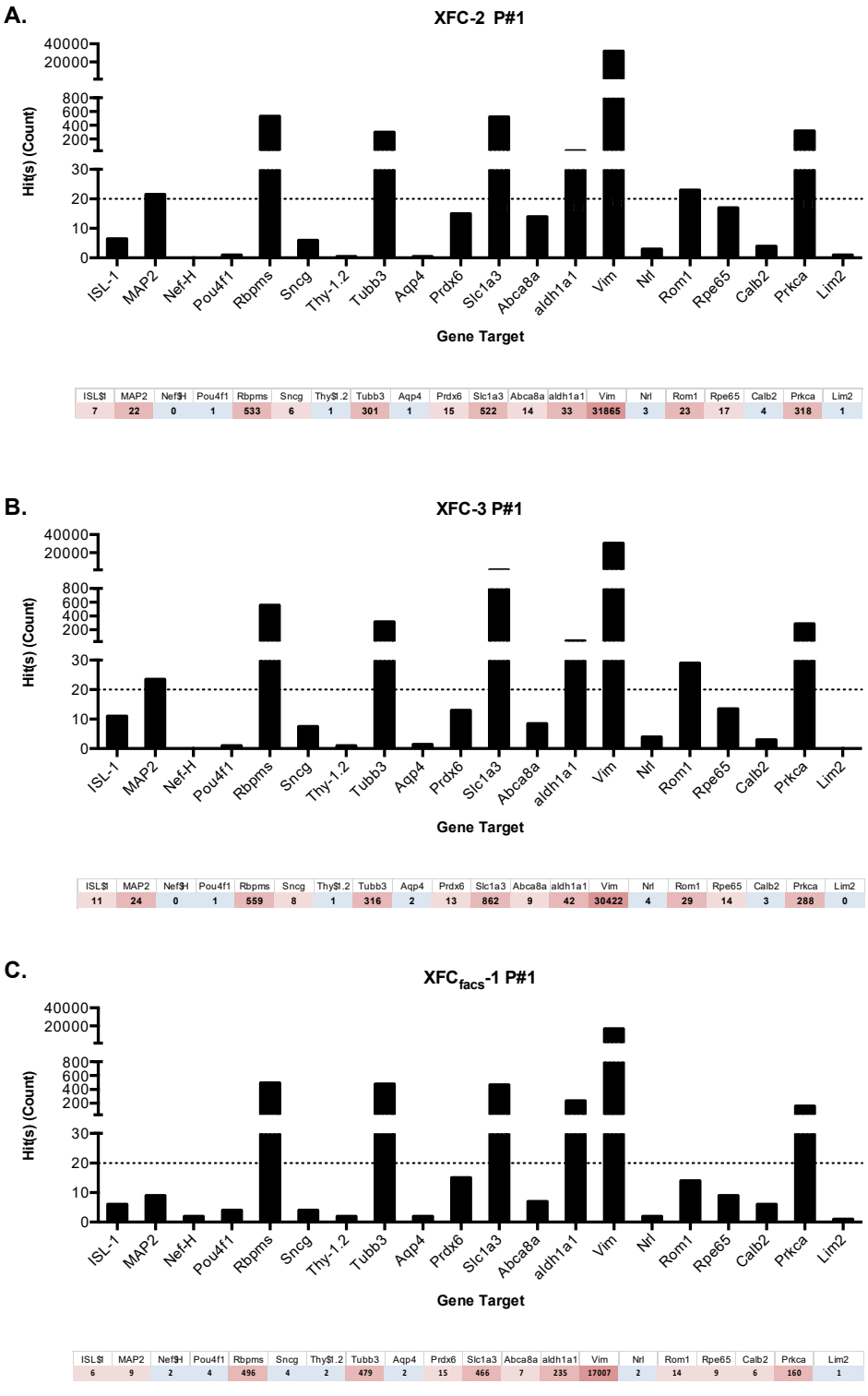

Figure 4.2 Retinal biomarker mRNA expression profile of XFC-2 (A), XFC-3 (B), and XFC_{facs}-1 (C) cells. Horizontal dotted line represents threshold level where n>20 indicates positive gene expression

Six-day differentiated and isolated XFC cells demonstrated multiple retinal biomarker gene expression, including RGC biomarkers (Figure 4.2). Amongst twenty different retinal biomarkers in this panel, XFC-2 cells were found to positively express eight biomarkers *Map-2*, *Rbpms, Tubb3*, *Slc1a3*, *Aldh1al, Vim, Rom1, and Prkca*, three of which are representative of RGCs. An additional five other biomarkers detected in low threshold copy number were *Isl-1*, *Sncg*, *Prdx6*, *Abca8a*, and *Rpe65*. XFC-3 cells were also found to have a highly similar expression profile, with minor differences in copy numbers compared to XFC-2 cells. XFC_{facs} cells yielded similar gene expression profile with a few differences compared to XFC cells. XFC_{facs}-1 cells were found to positively express six biomarkers from the panel including *Rbpms*, *Tubb3, Slc1a3, Aldh1al*, *Vim,* and *Prkca*. An additional seven biomarkers were detected but in low levels, and that did not meet threshold copy number.

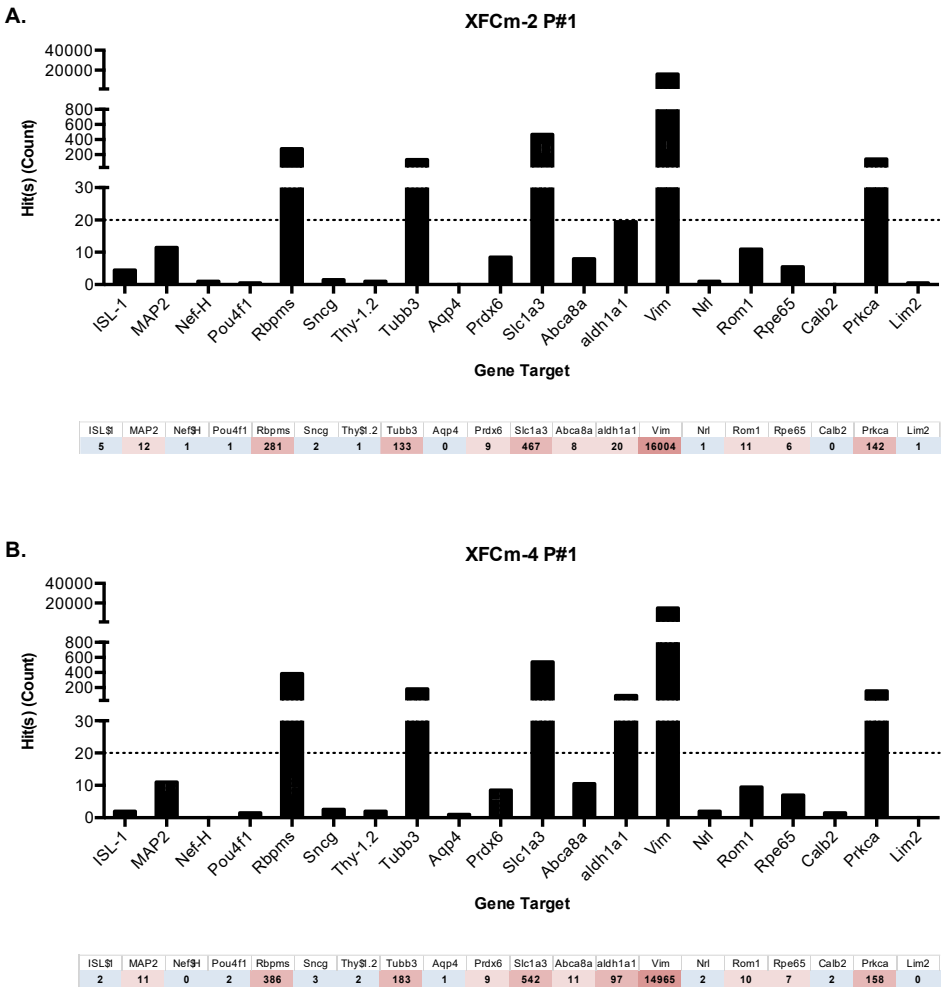

Figure 4.3 Retinal biomarker mRNA gene expression profile of XFC_m-2 (A) and XFC_m-4 (B) cells. Horizontal dotted line represents threshold level where n>20 indicates positive gene expression

RGC-like cells isolated from a 14-day differentiated stem cell population, XFC_m-2 and XFC_m-4 cells, also expressed RGC biomarkers (Figure 4.3). Expression profile for XFC_m-2 cells showed the expression of six retinal biomarkers *Rbpms, Tubb3, Slc1a3, Aldh1al, Vim, and Prkca*, two of which were representative of RGCs. Additional five biomarkers detected at low levels were *Map-2*, *Prdx6*, *Abca8a*, *Rom1*, and *Rpe65*. XFC_m-4 was a biological replicate of XFC_m-2 cells and showed a similar level of gene expression profile.

The XFC and XFC_m cells had similar gene expression profiles with slight fluctuations in the copy number over three passages (Figure 4.4). For example, in the third passage of XFC-3 cells, RGC biomarkers *Map-2* showed a 4-fold increase in mRNA copy number, while *Tubb3* expression exhibited a slight decrease by 0.35-fold compared to the first passage. Additional retinal biomarkers such as *Slc1a3* and *Aldh1al* exhibited an increase of 0.64-fold and *8.71-fold*, while *Vim* and *Prkca* exhibited a decrease of 0.43-fold and 0.29-fold compared to the first passage, respectively. For XFC_m-2 cells, RGC biomarker *Map-2* was found to exhibit a 2.92-fold increase compared to the first passage, a biomarker that was not expressed at a high enough level in the first passage to be considered as a positive expression. Expression of the two other RGC biomarkers *Rbpms* and *Tubb3* both exhibited an increase of 1.09-fold and 2.57-fold compared to the first passage, respectively. Additional retinal biomarkers such as *Vim*, and *Prkca* all exhibited a 0.26-fold and 0.25-fold increase compared to the first passage, respectively.

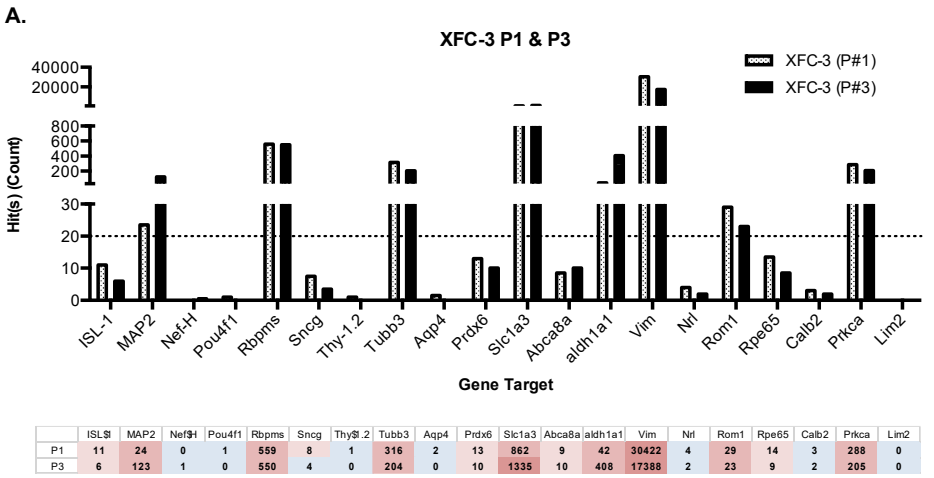

	ISL1	MAP2	Nef3H	Pou4f1	Rbpms	Sncg	Thy1.2	Tubb3	Aqp4	Prdx6	Slc1a3	Abca8a	aldh1a1	Vim	Nrl	Rom1	Rpe65	Calb2	Prkca	Lim2
P1	11	24	0	1	559	8	1	316	2	13	862	9	42	30422	4	29	14	3	288	0
P3	6	123	1	0	550	4	0	204	0	10	1335	10	408	17388	2	23	9	2	205	0

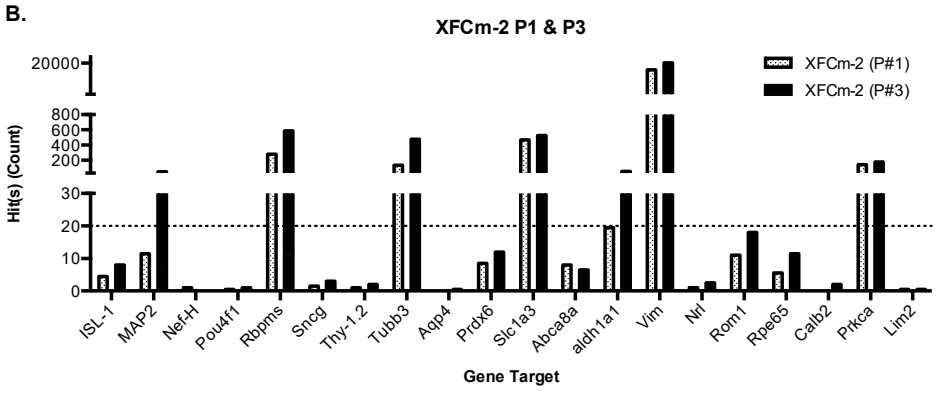

	ISL1	MAP2	Nef3H	Pou4f1	Rbpms	Sncg	Thy1.2	Tubb3	Aqp4	Prdx6	Slc1a3	Abca8a	aldh1a1	Vim	Nrl	Rom1	Rpe65	Calb2	Prkca	Lim2
P1	5	12	1	1	281	2	1	133	0	9	467	8	20	16004	1	11	6	0	142	1
P3	8	47	0	1	588	3	2	475	1	12	524	7	52	20301	3	18	12	2	178	1

Figure 4.4 Comparative analysis of XFC-3 cells (A) and XFC_m-2 cells (B) retinal biomarker mRNA gene expression profile at passage 1 and passage 3. Horizontal dotted line represents threshold level where n>20 indicates positive gene expression

To gain a better understanding of the gene expression profile of cells *in vivo* and to serve as controls, the gene expression profile of retina and primary mouse RGCs isolated using MACS were analyzed (Figure 4.5). Primary mouse RGC expresses all the RGC biomarkers in the panel, but also express biomarkers representing other retinal cell types.

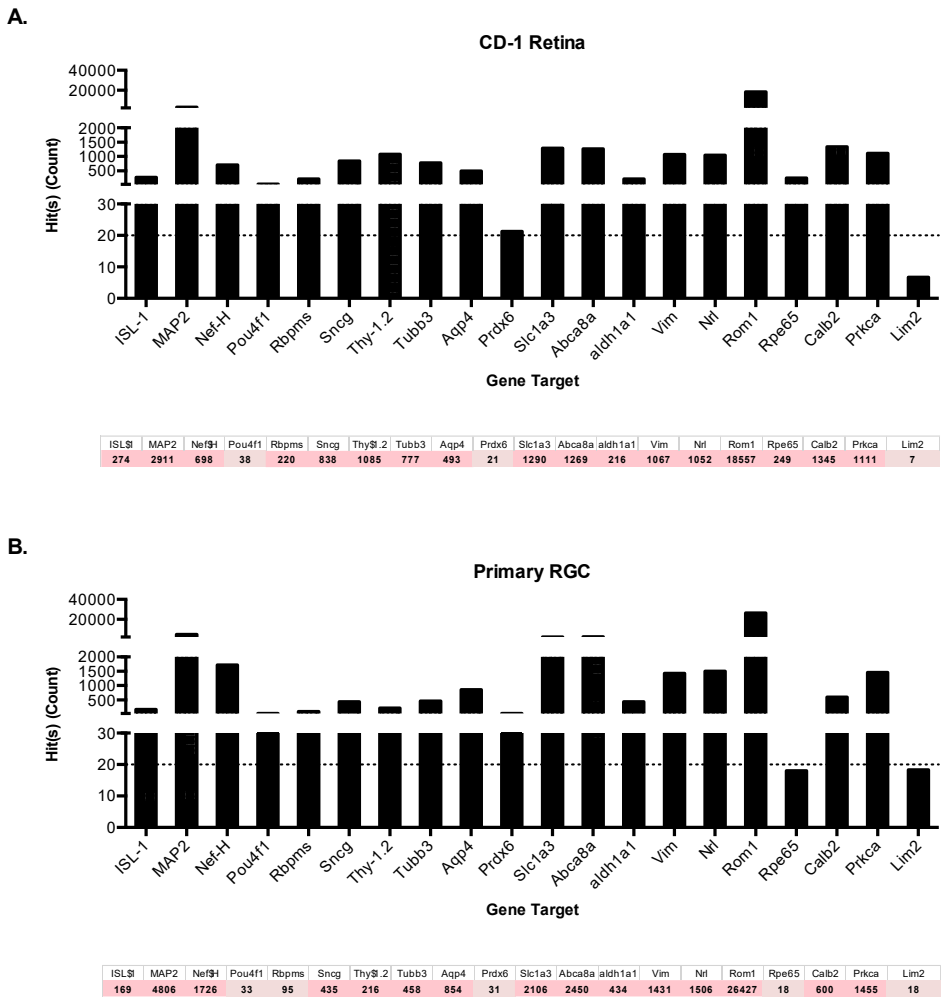

Figure 4.5 Comparative analysis of retinal biomarker mRNA gene expression profile of mouse primary cells: CD-1 retina (A) and isolated primary RGCs (B). Horizontal dotted line represents threshold level where n>20 indicates positive gene expression

4.4.4 XFC-3 neurites can be extended upon stimuli activation

From the various XFC, XFC_m and XFC_{facs} cells generated, XFC-3 cells were selected for further validation for neuronal characteristics and RGC-like stimuli-dependent neurite extension responses using NF and RKI such as BDNF, CNTF, Y-27632, and their combinations, as follows: 20 ng of BDNF protein alone; 20 ng of CNTF protein alone; 10 μM of Y-27632 RKI alone; combination of 20 ng of BDNF protein with 10 μM of Y-27632 RKI (BDNF+Y-27632);

combination of 20 ng of CNTF protein with 10 μM of Y-27632 RKI (CNTF+Y27632); or combination of 20 ng of BDNF protein with 20 ng of CNTF protein and 10 μM of Y-27632 RKI (BDNF+CNTF+Y-27632).

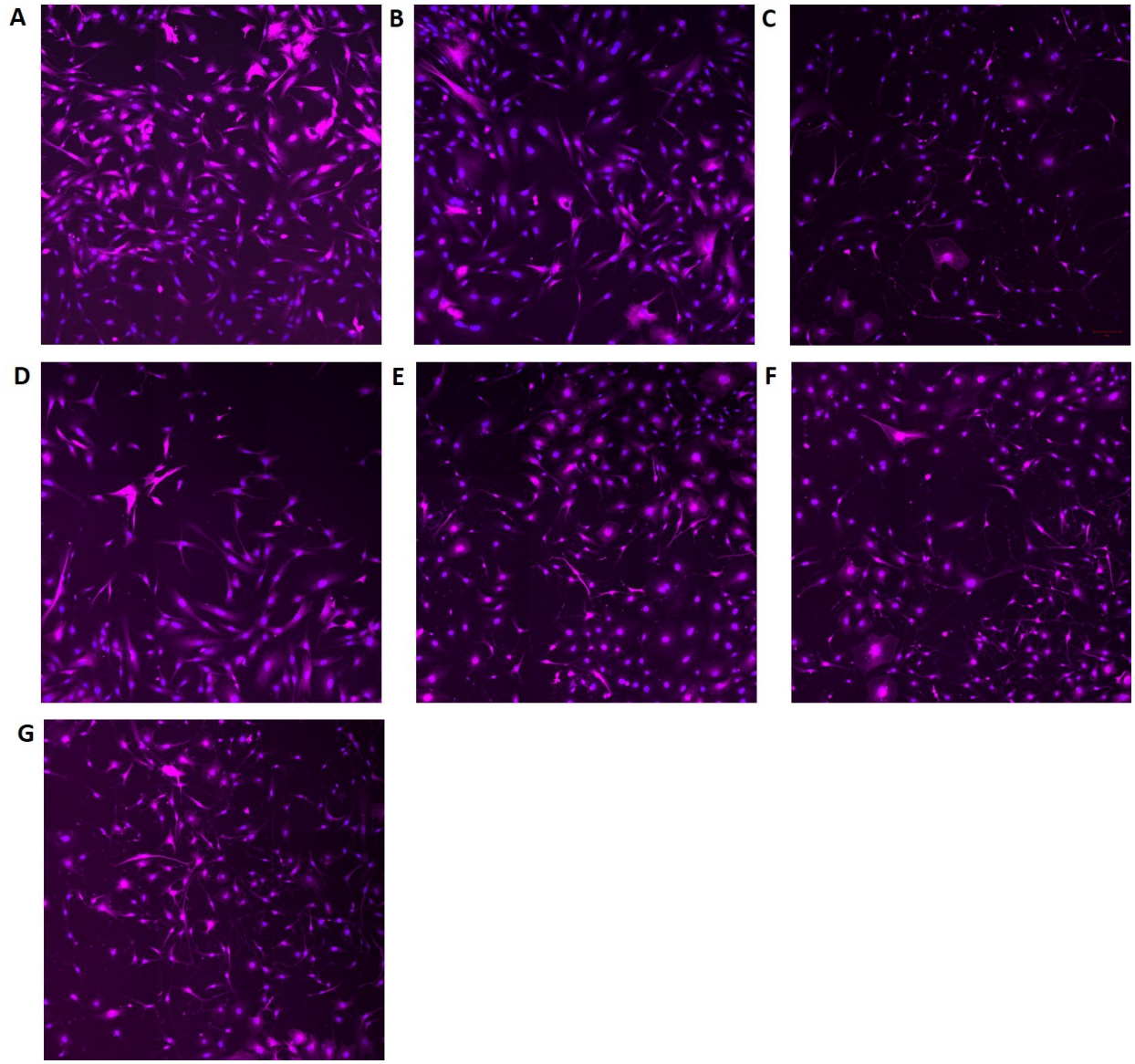

Figure 4.6 XFC-3 cells after 24 hours of stimuli exposure. Cells were stained with Beta-Tubulin AF647 (purple) and Syto™16 nuclei stain (blue). Images were captured using a 20x objective with tile scan function (area 3x3). XFC-3 cells treated with A) untreated; B) BDNF protein (20 ng); C) BDNF protein (20 ng) and Y-27632 (10 μM); D) CNTF (20 ng); E) CNTF (20 ng) + Y-27632 (10 μM; F) Y-27632 (10 μM); and G) BDNF (20 ng) + CNTF (20 ng) + Y-27632 (10 μM)

Analysis of XFC-3 cells treated with BDNF, CNTF, Y-27632, and their combinations showed that the cells have neurites that can be extended extend upon activation, evident by the elongated neurites seen in Figure 4.6. Further neurite length distribution profiling was carried out by neurite length tracing and quantitation (Figure 4.7), which showed increased number of neurites with longer neurite lengths in XFC-3 cells treated with stimuli compared to untreated XFC-3 cells.

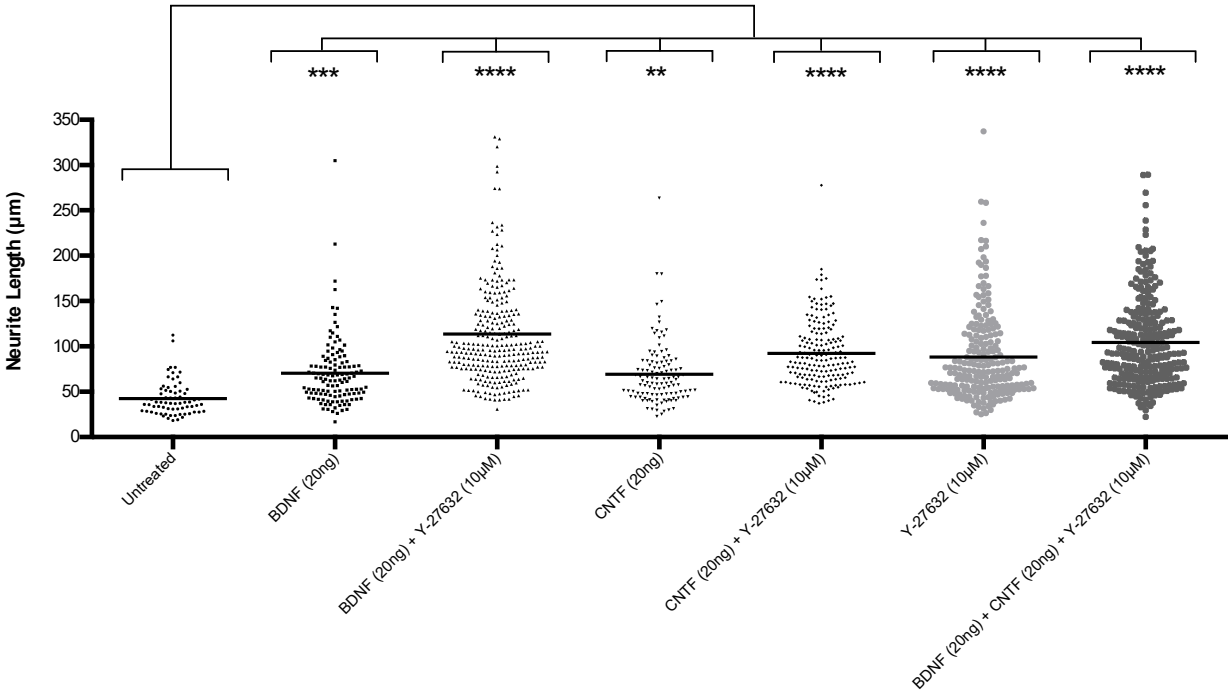

Figure 4.7 Total neurite length distribution profiling of XFC-3 cells in response to BDNF, CNTF, and Y-27632 activation. Values expressed as mean ± s.d., n=3. ** $p<0.01$; *** $p<0.001$; **** $p<0.0001$

Further neurite length categorization (Figure 4.8) showed that XFC-3 cells treated with BDNF+Y-27632 and BDNF+CNTF+Y-27632 demonstrated the highest degree of neurite extensions ($p<0.0001$), followed by Y-27632 alone ($p<0.001$) and CNTF+Y-27632 ($p<0.01$). XFC-3 cells treated with BDNF+CNTF+Y-27632 and BDNF+Y-27632, where XFC-3 cells exhibit 38 and 43.7 times more neurites that were 100 µm compared to untreated XFC-3 cells. XFC-3 cells treated with either Y-27632 alone or CNTF+Y-27632 were both able to induce 21.7

times more neurites with length greater than 100 µm compared to untreated condition. XFC-3 cells treated with either BDNF or CNTF alone also demonstrated evidence of neurite extension as the number of neurites with length greater than 100 µm were 4.7 and 4 times higher compared to the untreated control.

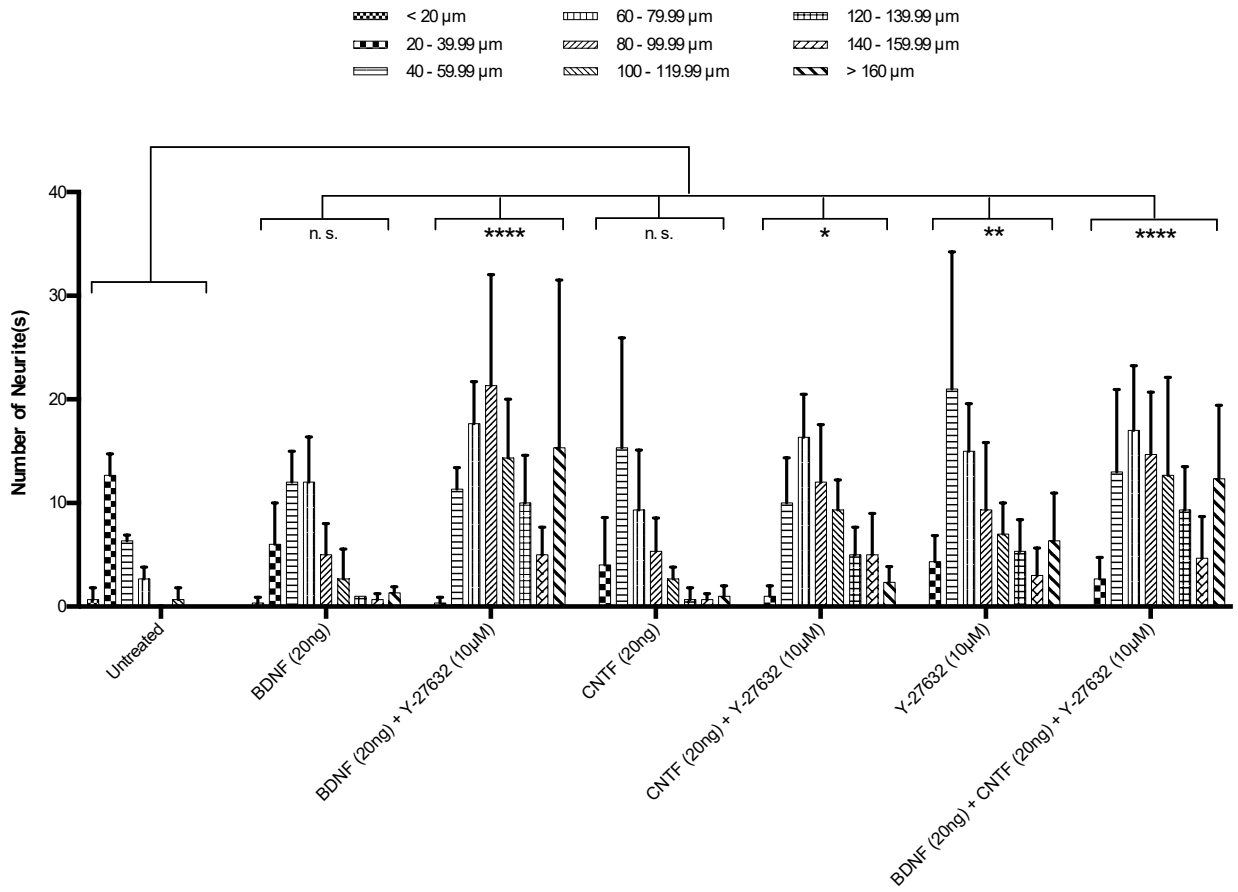

Figure 4.8 Neurite length category analysis of XFC-3 cells in response to BDNF, CNTF, and Y-27632 activation. Values expressed as mean ± s.d., n=3. * $p<0.05$; ** $p<0.01$; **** $p<0.0001$; n.s. = not significant

4.4.5 Integration of XFC-3 cells into the 3D co-culture bioassay

As XFC-3 cells have shown to exhibit neurite extension in response to activation, in particular BDNF protein, XFC-3 cells were integrated into the 3D co-culture bioassay for NF gene delivery system evaluation established in the previous study to demonstrate the application of the cell model [122]. Using XFC-3 cells as BDNF-responsive retinal cells, an A7-XFC-3 co-culture

setup was structured (Figure 4.9). Two main co-culture conditions were established to evaluate the suitability of XFC-3 cells as BDNF-responsive cell candidate in the 3D co-culture bioassay system: 1) untransfected A7 cells co-cultured with XFC-3 cells (A7/XFC-3; Top:A7 / Bot:XFC-3), and 2) BDNF-transfected A7 cells (trA7) co-cultured with XFC-3 cells (trA7/XFC-3; Top:trA7 / Bot:XFC-3). Examination of the traced mean neurite length and length distribution showed no significant differences between the two conditions as they exhibited highly similar neurite length distribution profiles. As XFC-3 cells were shown to exhibit low levels of neurite extension in response to 20 ng/mL of BDNF protein, it is perhaps that the amount of BDNF secreted by trA7 in 24 hours was insufficient to induce neurite extension on XFC-3 cells.

The second approach evaluated was to determine whether Y-27632-pretreated XFC-3 cells would be more responsive to BDNF detection (XFC-3-rki) in the co-culture setup. Thus, two co-culture conditions were evaluated: 1) untransfected A7 cells co-cultured with Y-27632-pretreated XFC-3 cells (A7/XFC-3-rki; Top:A7 / Bot:XFC-3-rki); and 2) BDNF-transfected A7 cells co-cultured with Y-27632-pretreated XFC-3 cells (trA7/XFC-3-rki; Top:trA7 / Bot:XFC-3-rki). Examinations of neurite length distribution profiles showed that XFC-3 cells in trA7/XFC-3-rki exhibited overall 2.78 times more neurites compared to A7/XFC-3-rki. Moreover, the number of neurites longer than 50 μm in trA7/XFC-3-rki was found to be on average 2.3 times higher than that of A7/XFC-3rki. These findings suggest that perhaps Y-27632-pretreated XFC-3 cells may have an elevated BDNF sensitivity compared to untreated XFC-3 cells, a characteristic that may be employed for BDNF bioactivity evaluation application in the A7/XFC-3-rki co-culture setup.

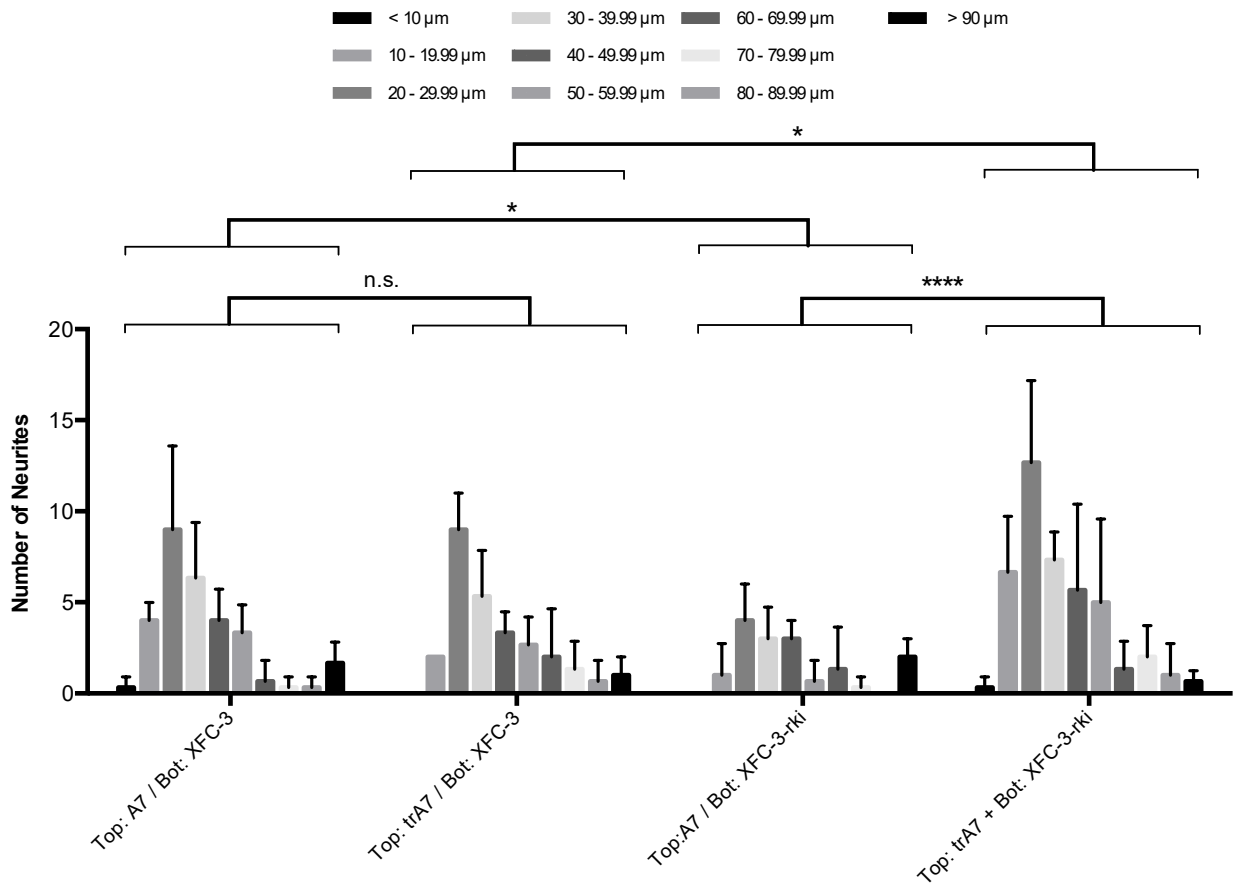

Figure 4.9 Neurite length distribution profile of XFC co-culture with BDNF-transfected A7 cells or untransfected cells after 24 hours. XFC cells cultured at the bottom layer were either untreated or treated with Y-27632 rki. Values expressed as mean ± s.d., n=3. *p<0.05; **** p<0.0001; n.s. = not significant

4.4.6 XFC-3 cells as gene delivery target

An aspect of gene therapy development involves the identification of a representative cell line for gene delivery system transfection evaluations. Hence, XFC-3 cells were evaluated for their transfectability using non-viral gene delivery systems. Three different types of non-viral gene delivery systems were evaluated in this study: 18-7NH-18 GL-NP, *f*-ptSWNT-pDNA, and K2-NP (Figure 4.10).

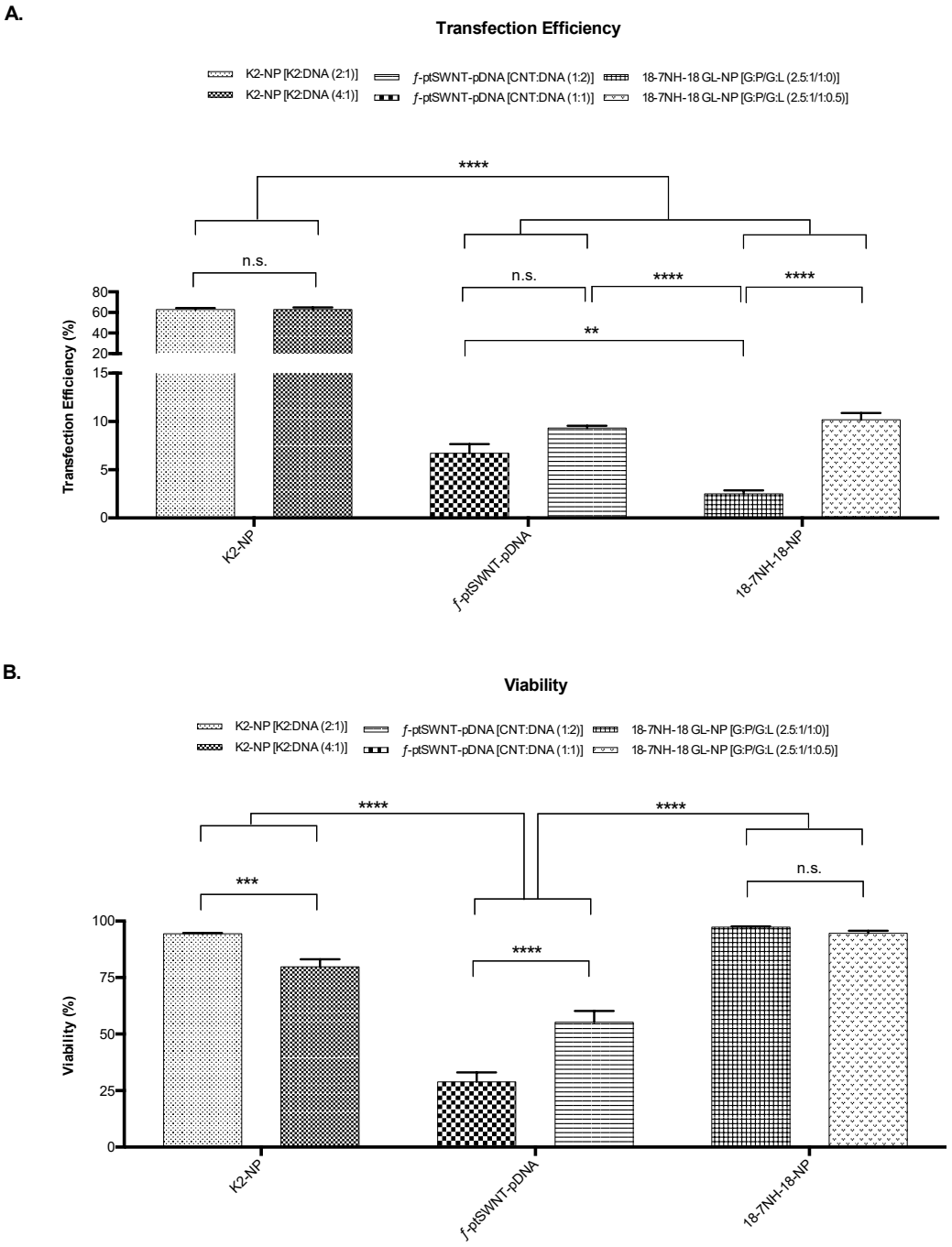

Figure 4.10 Transfection efficiency (A) and viability (B) evaluation of XFC-3 cells transfected with three non-viral gene delivery systems: K2-NP, GL-NP, and *f*-ptSWNT-pDNA. Two different formulations of each non-viral system were tested. Values expressed as mean ± s.d., n=3. ** $p<0.01$; *** $p<0.001$; **** $p<0.0001$; n.s. = not significant

K2-NPs showed the highest level of TE at 63.1±1.4% with 2μL:1μg K2:DNA ratio, and 62.9±1.9% with 4μL:1μg K2:DNA ratio and the highest cell viability at 94.4±0.4% and 79.7±3.4%, respectively. The *f*-ptSWNT-pDNA complexes were able to transfect XFC-3 cells at relatively low levels with a TE of 6.7±1.0% with the 1:1 w/w CNT:DNA ratio, and 9.3±0.2% with the 0.5:1 w/w CNT:DNA ratio. The *f*-ptSWNT-pDNA complex also induced a relatively high level of toxicity that resulted in viability of 28.8±4.17% and 55.2±5.0%, respectively. The 18-7NH-18 GL-NPs were also able to transfect XFC-3 cells and showed a TE of 2.25±0.36% using G:P/G:L ratios of 2.5:1/1:0, and 10.2±0.7% with G:P/G:L ratios of 2.5:1/1:0.5. Cell viability remained high with 97.3±0.4% and 94.5±1.2% for the two formulations of GL-NPs.

As XFC-3 cells were found to be transfectable by non-viral gene delivery systems, they were also evaluated for their ability to serve as gene delivery "medic" cells to produce and secrete BDNF proteins to induce neurite extension on the receiving XFC-3 cells. To achieve this, XFC-3/XFC-3 co-culture was established by integration of XFC-3 cells into the "therapeutic protein-producing" layer of the co-culture bioassay model (Figure 4.11). Thus, four conditions were evaluated: 1) untransfected XFC-3 cells co-cultured with XFC-3 cells (XFC-3/XFC-3; Top:XFC-3 / Bot:XFC-3); 2) BDNF-transfected XFC-3 cells (trXFC-3) co-cultured with XFC-3 cells (trXFC-3/XFC-3; Top:trXFC-3 / XFC-3); 3) untransfected XFC-3 cells co-cultured with Y-27632-pretreated XFC-3 cells (XFC-3/XFC-3-rki; Top:XFC-3 / Bot:XFC-3-rki); and 4) BDNF-transfected XFC-3 cells co-cultured with Y-27632-pretreated XFC-3 cells (trXFC-3/XFC-3-rki; Top:trXFC-3 / Bot:XFC-3-rki). A comparison of the neurite length distribution profiles of the four co-culture conditions showed that there were little differences in neurite counts and length distribution between XFC-3/XFC-3 and trXFC-3/XFC-3 co-cultures.

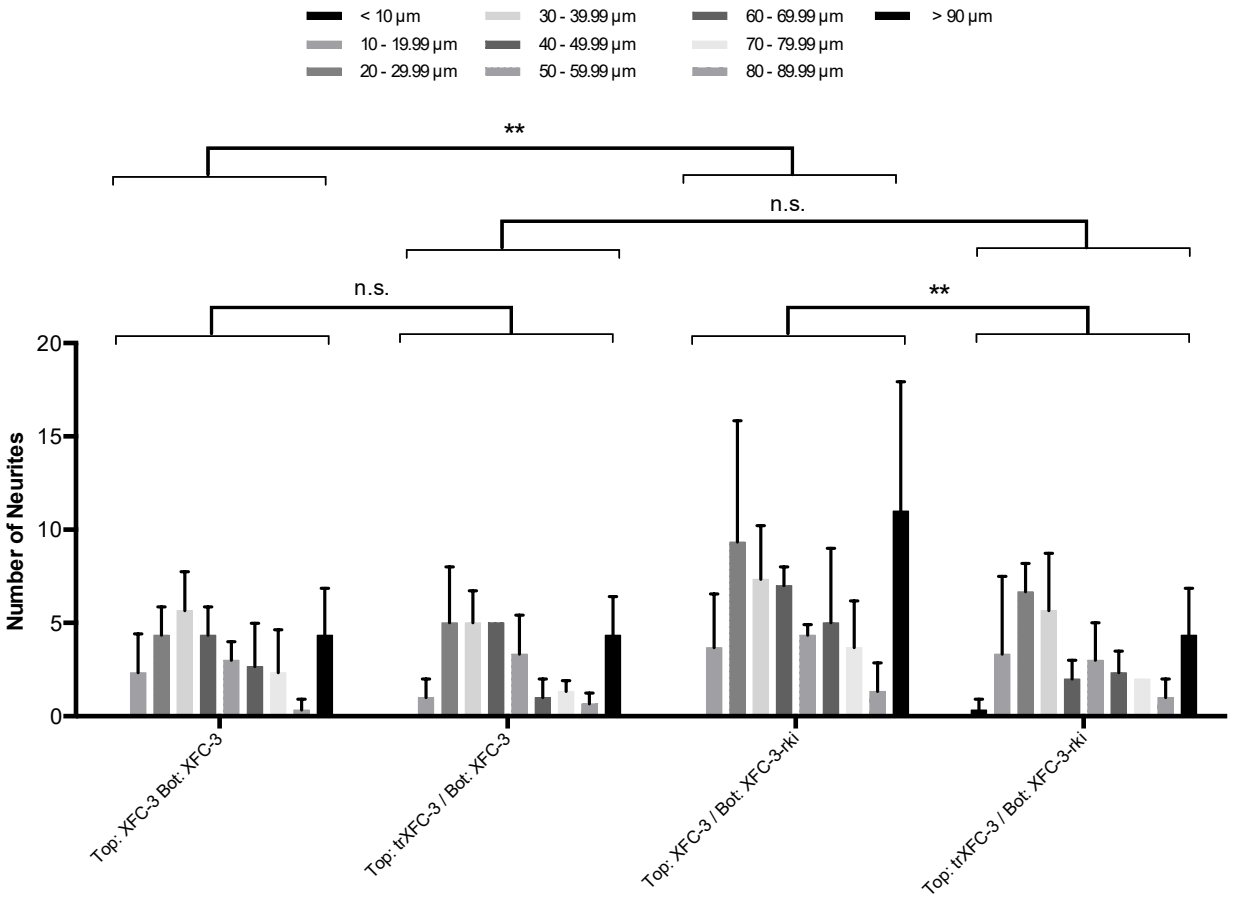

Figure 4.11 Neurite length distribution profile of XFC-3 cells co-culture with BDNF-transfected XFC-3 cells and untransfected cells after 24 hours. XFC-3 cells cultured at the bottom layer were either untreated or treated with Y-27632 rki. Values expressed as mean ± s.d., n=3. ** $p<0.01$; n.s. = not significant

Similarly, a comparison of the two Y-27632-pretreated XFC-3 cells co-culture conditions (XFC-3/XFC-3-rki and trXFC-3/XFC-3rki) showed that the number of neurites shorter than 90 µm was similar amongst the two conditions, but the number of neurites longer than 90 µm was approximately 2 times higher in XFC-3/XFC-3-rki compared to trXFC-3/XFC-3-rki. The results suggest that while XFC-3 cells can be transfected with non-viral gene delivery systems, the level of subsequent protein production efficiency may perhaps be lower in XFC-3 cells and requires further characterization on the secreted protein bioavailability.

4.5 Discussion

In this investigation, we have developed stem cell-derived RGC-like cells with key molecular and physiological characteristics resembling that of RGCs. More specifically, a particular cell isolate, XFC-3 cells, expressed three key RGC biomarkers *Map-2*, *Rbpms*, and *Tubb3*, and exhibited neurite extension upon activation by BDNF, CNTF, Y-27632, and their combinations. Given these molecular and physiological characteristics that XFC-3 cells displayed, we have integrated XFC-3 cells into the 3D co-culture model as BDNF-responsive cells, towards the generation of an astrocyte-RGC co-culture model. Furthermore, the co-culture setup A7/XFC-3-rki have demonstrated that XFC-3 cells in A7/XFC-3rki conditions were able to confirm the bioactivity of BDNF proteins secreted from trA7 by exhibiting neurite extension. Together, these finding demonstrated the potential of XFC-3 cells as model RGCs for preclinical development of ganglion cell therapeutics. Moreover, the applicability of XFC-3 cells in the A7/XFC-3-rki co-culture model demonstrated their potential in screening applications, such as a tool for NF gene delivery systems screening.

Utilizing stem cells to generate difficult-to-culture cells *in vitro* is a promising avenue to create useful cell models that can fuel the process of therapeutic discovery. The use of multipotent stem cells has an advantage in the application of differentiating target tissue specific cell types, as their differentiation diversity is limited to the predetermined cellular lineage. In the application of RGCs generation, RSC is one of the most promising stem cell candidates. Mammalian RSCs were first described by Tropepe et al. in 2000, where it was shown that the RSCs isolated from ciliary epithelium (CE) of the mouse eye expressed stem cell characteristics and was able to differentiate into multiple retinal cell types [125]. The work was then followed by the finding of Coles et al., who identified human RSCs from the CE of human eyes [126]. The RSCs used in this study were

isolated from the retina in the absence of CE as described by Li et al. [121]. The high expression of Müller glia biomarkers such as *Vim* and *aldh1a1* in undifferentiated CD1-4 cells and XFC cells suggest that these cells may have a Müller glial origin as Müller glial cells have been shown in various studies to possess stem cell characteristics [127-129]. Moreover, it was demonstrated in different studies that they could differentiate into RGCs [130-132]. Bhatia et al. have further suggested that Müller glia has spontaneous proliferative and neuronal marker expression capacity that fulfills the characteristics of a true stem cell [133]. On the other hand, while there were reports of stem cell-derived RGCs derived from other stem cell types such as embryonic stem cells [134-137] and induced pluripotent stem cells [136, 138-141]. While primary RGCs remain a possible RGC cell source for *in vitro* investigations, the low abundance of RGCs in commonly used mouse strains for glaucoma research such as C57/BL6 and DBA2 peaks at roughly 80,000 cells per eye at 9 months old rodents [142]. Coupled with the low efficiency of RGC isolation and spontaneous degeneration once isolated, the combination of factors limits the versatility of primary RGCs for *in vitro* investigations.

Characterization of neurite extension capacity provides further support for the similarities between XFC-3 cells and primary RGCs. Stimuli such as BDNF [143-146], CNTF [143, 147], and Y-27632 [147] have shown in various studies for their ability to promote neurite extension in RGCs. In this paper, we have shown that XFC-3 cells also exhibit neurite extension in response to the same stimuli, thus demonstrated neurite response similarities to RGCs.

The development of XFC-3 cells has the potential to enhance the cellular aspects of the 3D co-culture model as XFC-3 cells express key RGC biomarkers and neurite extension ability in response to BDNF. The resultant A7/XFC-3 co-culture demonstrated feasibility for assessing BDNF bioactivity as 2.3 times more neurites longer than 50 μm were detected in XFC-3 cells in

trA7/XFC-3-rki compared to XFC-3 cells in A7/XFC-3-rki condition. Y-27632-pretreated XFC-3 cells exhibited enhanced sensitivity to BDNF, which could be explained by the role of rho-kinase inhibitors where factors that limit neurite extension were suppressed as a result [148].

In addition to utilization of XFC-3 cells as BDNF-responsive cells, XFC-3 cells were also investigated as BDNF-producing cells in the 3D co-culture system. The results showed that XFC-3 cells in either XFC-3/XFC-3-rki or XFC-3/XFC-3 conditions did not result in overall higher or longer neurite distribution profile compared to the controls. This observation may perhaps be attributed to the level of bioavailability of BDNF secreted from trXFC-3 cells, and this will require further characterization.

A number of RGC biomarkers have been used for identification and characterization of RGCs, such as *Thy-1* (CD90) [149], *Rbpms* [150], *ISL-1* [151], *Nef-H*, *Map-2*, *Brn3b* [152], γ-synuclein (Sncg) [153], and *β-tubulin-III* (Tubb3) [154]. However, the proportion of RGCs that expresses Sncg+ or Brn3+ can vary [155]. Moreover, *Sncg* was shown to be downregulated with decreased retrograded transport of fluorogold from the superior colliculus to RGCs as a result of retrograded transport obstruction [156]. Thy-1 is a surface glycoprotein that was identified as a key biomarker of RGCs [149]. However, it was suggested that this biomarker was also expressed amongst other retinal cell types [157, 158]. Furthermore, the *Thy-1* marker was found to be expressed dynamically as its expression was downregulated after optic nerve crush-induced IOP elevation [159, 160]. Collectively, these findings suggested that the expression of biomarkers is dynamic and complex, and these considerations need to be considered in the characterization of RGCs since it is arguable that a RGCs could be lacking a particular RGC biomarker (i.e. *Thy-1*) but possess an RGC identity depending on the cellular state and condition. Beyond the dynamic expression of biomarkers, further considerations in RGC characterization are required. For

example, is the presence of a single molecular biomarker sufficient for identification of RGCs? Given the number of different RGC biomarkers described in the literature, is one biomarker more representative or important than the other biomarkers? Another aspect of biomarker expression is whether there should be a defined level of threshold for a biomarker to be considered "positive" expression.

The misidentification of RGC-5 cell line was a major setback in RGC-related biomedical research [118, 119]. With more than 200 publications generated using the cell line in the time between the original discovery [161] and the realization of the misidentification, the urgent need for an RGC cell model is apparent in the field. The stem cell-derived XFC-3 cells described in this paper serve as a promising cell model to bridge the gap in the field of RGC-related therapeutic discovery.

4.6 Conclusion

The lack of representative RGC models to facilitate effective and efficient *in vitro* screening remains an important obstacle that needs to be addressed. In this paper, we described the development of an RGC cell model, XFC-3, that expresses key RGC biomarkers and neurite extension capacity. Furthermore, we have demonstrated its application using the previously described co-culture model suitable for bioactivity and bioavailability assays of NFs. Overall, XFC-3 cells hold great promise as a useful model for preclinical screening and therapeutic discovery applications.

4.7 Acknowledgement

We thank Monika Sharma and Neil Winegarden of the Princess Margaret Genomic Centre for their help with NanoString analysis.

Chapter 5 Development of retinal multipotent stem cell-derived "MiEye" 3D retinal neurosphere model

Majority of this chapter are reflective of an original manuscript published in the journal Precision Nanomedicine.

Chen, D.W. and Foldvari, M. (2018). Retinal multipotent stem cell derived "MiEye" spheroid 3D culture model for preclinical screening of non-viral gene delivery systems. *Precision Nanomedicine*. July;1(2):106-123 DOI:10.29016/180711.1

Author Contribution: DWC and MF developed the concept and designed the experiments. DWC performed the experiments. DWC and MF analyzed the data and prepared the manuscript.

5.1 Rationale and objective

In a non-viral approach of delivering therapeutic nucleic acids for glaucoma management, a significant challenge lies in efficiently delivering genes into target retinal cells. Majority of non-viral gene delivery systems that have shown highly effective gene transfer capacity in 2D monolayer transfection have failed to translate to comparable levels of gene delivery efficiency *in vivo*. The gap, in part, is a consequence of the lack of correlation of the results generated from current standards of TE screening to *in vivo* feasibility. Recognizing such deficiency, a "mini-retina" neurosphere model composed of major retinal cell types arranged in a three-dimensional tissue-like architecture aimed to bridge *in vitro-in vivo* gap was developed. The MiEye retinal neurospheres aim to serve as a retinal model for the rapid screening of transfection capacity of NP systems to retinal cells, towards the generation of *in vitro* results with higher *in vivo* translatability.

5.2 Background

Glaucoma is a neurodegenerative disease of the retina characterized by multifactorial pathophysiology that ultimately results in the loss of retinal ganglion cells (RGCs) [65]. A gene therapy approach such as NF gene therapy has the potential to provide extrinsic neurotrophic support that can rescue and protect glaucomatous stressed RGCs [162, 163]. Non-viral approaches

to deliver therapeutic genes to the retinal cells to carry out therapeutic action for stressed RGCs provides many advantages compared to viral approaches such as lower risk of immunogenicity and mutagenesis, as well as better patient compliance and large-scale manufacturing feasibility [104]. Despite the large number of NP systems that have demonstrated high levels of TE *in vitro,* very few demonstrated effectiveness *in vivo*. An aspect of this is disconnect between *in vitro* and *in vivo* TE screening, suggesting that current standards of *in vitro* models do not sufficiently predict *in vivo* performance and feasibility of NPs. The current standards of *in vitro* NP gene delivery evaluation rely on the assessment of TE in cells cultured in 2D monolayers, which include two major pitfalls in cellular modeling from a gene delivery perspective: 1) a lack of multicellular tissue spatial architecture; and 2) suboptimal representation of NP biodistribution and kinetics.

In retinal degenerative diseases such as glaucoma, cell-cell interactions play an important role in the pathogenesis through various mechanical and molecular factors near the trabecular meshwork and optic nerve head [164-167]. Thus, tissue models such as organotypic explant cultures could greatly benefit the understanding of glaucoma pathogenesis and facilitate gene therapy development using representative models *in vivo*. Organotypic explants of the retina were explored by various groups to study pathogenesis and drug development applications [168-170]. However, preparation of retinal explant culture is difficult. While cultivatable for up to two weeks *ex vivo*, retinal explants spontaneously undergo degeneration upon isolation. 3D retinal models generated from stem cells can yield various retinal cell types along with cellular arrangements similar to the retina [171, 172]. The ability of stem cells to differentiate autonomously and form the optic cup structure in 3D culture model was first demonstrated by Eiraku et al. using mouse embryonic stem cells [173, 174]. Following that, there have also been various attempts to generate

retinal organotypic cultures [175-177]. Maekawa et al. have generated retinal organotypic cultures from mouse embryonic stem cells utilizing mouse and human embryonic stem cells [178].

Another approach in the construction of 3D models was explored using bioprinting technologies, in which cells were printed based on the desired cellular arrangement. Lorber et al. have demonstrated that RGCs and glial cells of the retina can be printed using 3D printing technology while maintaining viability and neurite outgrowth capacity for both cell types [179]. More recently, a study conducted by Kador et al. demonstrated that by combining 3D printing with radial electrospun scaffolds, they were able to 3D print RGCs onto electrospun surfaces with precise distribution and positioning of RGCs as found in the retina [180]. From a spatial arrangement standpoint, 3D printing-based techniques theoretically possess a comparative advantage as they allow for more control in dictating cellular location on a tissue-like arrangement by "printing" specific cells at specific locations. While the spatial arrangement of the cells cultured in 3D culture is either dependent on the resultant conformation from self-aggregation or the conformation dictated by the scaffold onto which the cells adhere. While these various advancements in different tissue modeling approaches are pivotal in developing *in vivo*-like models for many biological and physiological studies, a relatively simpler 3D model is needed for rapid and more predictive screening of non-viral gene delivery systems.

The mouse multipotent retinal stem cells (CD1-4 RSCs) used in this project have previously been described to differentiate into all major retinal cell types in 2D monolayers [121]. In this paper, we describe the engineering of 3D spheroids, termed "MiEye" under different culture conditions using the CD1-4 RSCs. The RSCs can be seeded into 96-well plates and differentiated into multiple retinal cell types while forming spheroids providing an easily scalable model for retinal gene delivery assessment.

5.3 Materials and methods

5.3.1 CD1-4 RSC culture

CD1-4 RSCs isolated from 4-8 weeks old CD-1 mouse were kindly gifted by Dr. Ting Xie, Stower Institute for Medical Research and University of Kansas. The purified CD1-4 RSCs were cultured in 12-well plates coated with 0.2% gelatin for 3 hours at 37°C and maintained in RSCCM media. Culturing medium for CD1-4 (RSCCM) was composed of advanced DMEM/F12 (Gibco, Thermo Fisher Scientific, Waltham, MA, USA) media with addition of 1.0 g/L glucose (Sigma-Aldrich, St. Louis, MO, USA), 1.0 g/L lactose (Sigma-Aldrich), 1.0 g/L BSA (Sigma-Aldrich), 0.045 g/L proline (Sigma-Aldrich), 2 mM nicotinamide (Sigma-Aldrich), 2 mM L-glutamate (Gibco), 1% penicillin/streptomycin (Hyclone), 1% insulin-transferrin-supplement (Gibco), 5% knockout serum replacement (Gibco), 20 ng/mL EGF (Gibco), and 20 ng/mL bFGF protein (Gibco). Differentiation medium (RSCDM-1) was composed of advanced DMEM/F12 (Gibco) with 2% B-27 supplement (Gibco), 1% L-Glutamine (Gibco) and 10 ng/mL bFGF protein (Gibco). RSCDM-1 containing 1% N-2 supplement (Gibco) was named RSCDM-2. Maturation medium was formulated with 2 mM L-Glutamine (Gibco), 2% B-27 supplement (Gibco), 1% N-2 supplement (Gibco), 10 ng/mL bFGF protein (Gibco), and 100 ng/mL BDNF protein (Peprotech), 10 ng/mL glial-derived neurotrophic factor protein (Gibco), and 10 ng/mL insulin growth factor protein (Gibco) in advanced DMEM/F12, with (RGCMM-3) or without (RGCMM-4), 2% fetal bovine serum (Thermo Fisher Scientific).

CD1-4 RSCs were cultured on 0.2% gelatin (Sigma-Aldrich) coated 12-well tissue-culture treated plate for 3 hours at 37 °C. For maturation of retinal neurospheres, culture surfaces were coated with either Matrigel™ (Corning Incorporated, Corning, NY, USA), or combination of poly-L-ornithine (PLO) (EMD Millipore, Billerica, MA, USA) and laminin (EMD Millipore). For PLO-

laminin coating, 0.015 mg/mL of PLO were prepared in sterile water and applied on to the glass-bottom surface of multi-well plates overnight at room temperature. PLO was removed, and laminin was coated at a concentration of 2 μg/cm^2 overnight at 4 °C. For Matrigel™ coating, 7.6 mg/mL of Matrigel™ (Corning) was coated on the culture surface at 100 μL/cm^2 volume, and allowed for gel formation for an hour at 37°C.

5.3.2 Generation of MiEye retinal neurospheres

The retinal neurospheres model was established through differentiation of CD1-4 RSCs in commercially available force-floating three-dimensional 96-well ultra-low adhesive (ULA) microplates (Corning). For differentiation of CD1-4 RSCs, 15,000 cells (best seeding density compared to 5,000 and 10,000 cells/well) were seeded into each well of the ULA microplate, and differentiation was carried out using various protocols consisting of different combinations of media, schedules, or surface coating, resulting in the generation of 11 different retinal neurosphere types termed MiEye (1-11) with 2-4 spheres for each. MiEye 1-4 were 24-day differentiated retinal neurospheres, first initiated through differentiation in RSCDM-1 media for 3 days, which was then switched into RSCDM-2 media for 7 more days. Following 10 days of differentiation, spheres were transferred onto either PLO-Laminin- or Matrigel™-coated surface for maturation using either RGCMM-3 or RGCMM-4 media. MiEye5 was an 18-day differentiated retinal neurosphere, first initiated through differentiation in RSCDM-1 media for the first 4 days, followed by differentiation in RSCDM-2 for 14 more days. MiEye7 retinal neurosphere was generated by further maturating the 18-day differentiated spheres on PLO-Laminin-coated surface for 3 days in RGCMM-4. MiEye8 retinal neurospheres were 6-day differentiated spheres, which were initiated by differentiating in RSCDM-1 for 2 days. After 2 days of differentiation, the differentiated

spheres were changed to RSCDM-2 media for 4 more days. MiEye10 was generated by subjecting MiEye8 to further maturation on PLO-Laminin for 4 days in RGCMM-4 media.

5.3.3 NanoString Analysis

RNA was isolated using a commercially available silica column-based RNA isolation kit, PicoPure® RNA Isolation Kit (Arcturus, Thermo Fisher Scientific, Waltham, MA, USA), based on the manufacturer's suggested protocol. Isolated RNA was subjected to gene expression profiling for retinal cell biomarkers using the NanoString nCounter Analysis system, a highly sensitive and reproducible multiplexed mRNA gene expression quantitation method (NanoString, Seattle, Washington, USA). The technology enables direct hybridization of mRNA to its sequence-specific target reporter and capture probe, which allows for the quantitation of mRNA copy number for multiple (up to 800) mRNA sequences simultaneously with high sensitivity for the generation of a gene expression profile. Retinal biomarker gene expression analysis was performed using a custom code set containing 25 target genes representative of most retinal cell types and housekeeping genes as controls. The panel of target genes includes biomarkers representing major retinal cell types. *ISL-1, Map-2, Nef-H, Pou4f1, Rbpms, Sncg, Thy-1.2,* and *Tubb3* are representative RGC biomarkers; *Aqp4, Prdx6* and *Slcla3* are representative astrocyte biomarkers; *Abca8a*, *ald1a1*, and *Vim* are representative Müller glia biomarkers; and *Nrl* and *Rom1* are representative photoreceptor biomarkers. *Rpe65, Calb2, Prkca*, and *Lim2* each individually represent RPE, amacrine, bipolar and horizontal cell biomarkers, respectively. Each reaction was analyzed with 100 ng of RNA in a 5µL loading volume, mixed with capture probe and reporter probe. The gene profiling experiment was carried out at the Princess Margaret Genomics Centre (Toronto, Ontario, Canada).

5.3.4 Preparation of K2-NPs

K2-NPs were formulated by complexing the K2® lipopolyamine-based proprietary transfection reagent (Biontex Laboratories GmBH, München, Germany) with gWiz™ GFP plasmid (Aldevron, Fargo, ND, USA) at various ratios for 30 minutes prior to transfection. K2-DNA v/w ratios from 1:1 to 10:1, DNA dose ranged from 1 to 10µg were formulated and evaluated for TE on the retinal neurospheres. Transfection was carried out by first adding 25µL of K2® Multiplier into each well for 2 hours. After 2 hours, complexed K2-NPs were added into wells. Nine different K2-NPs formulations (F1-F9) composed of various combinations of K2® transfection reagent and DNA concentrations were prepared for transfection evaluation (Table 5.1).

Table 5.1 K2-NPs formulated for transfection in MiEye8 retinal neurosphere model

Formulation	K2:DNA ratio (µL: µg)	Empirical K2:DNA ratio (µL: µg)	K2® reagent (µL)	DNA (µg)
F1	1:1	1:1	1	1
F2	2:1	2:1	2	1
F3	4:1	4:1	4	1
F4	10:1	10:1	10	1
F5	20:2.5	8:1	20	2.5
F6	30:5	6:1	30	5
F7	10:2	5:1	10	2
F8	20:5	4:1	20	5
F9	30:10	3:1	30	10

5.3.5 Confocal laser scanning microscopy

Retinal neurospheres were counterstained with either 5µM Syto™ 62 nuclear stain (Thermo Fisher Scientific, Waltham, MA, USA) or 5µM DRAQ5™ nuclear stain (Thermo Fisher Scientific) for 30 minutes at 37°C prior to imaging. Neurospheres were imaged using a Zeiss LSM710 confocal laser scanning microscope (Carl Zeiss AG, Oberkochen, Baden-Wü, Germany) with 20x

objective. Three-dimensional images of the spheres were captured using the Z-stack functionality in the Zen 2009 software, each constituting 20 optical slices of images through the observable thickness of the retinal neurospheres. Transfection was measured by the detection of GFP expression in the retinal neurospheres. Combined mean fluorescence intensity (cMFI) of the retinal neurospheres were obtained by calculating the average of all individual MFI of optical sections of the neurospheres captured using z-stack. The cMFI of transfected neurospheres was normalized to the MFI of the untreated control neurosphere (background fluorescence). Co-localization between GFP expression and nuclei staining were also assessed using Mander's Overlap Coefficient (MOC) for each optical slice.

5.4 Results

5.4.1 Generation and characterization of MiEye retinal neurospheres

The initial studies showed that undifferentiated CD1-4 RSCs themselves were able to form stem cell spheres in 3D culture conditions when seeded at cell densities of 5,000, 10,000 and 15,000 cells in ULA spheroid plates. Spheroids were formed within 24 hours and their morphology was maintained for at least 12 days (Figure 5.1).

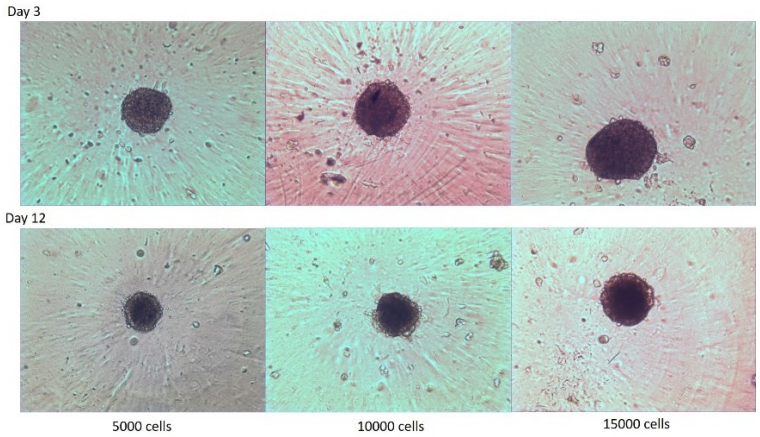

Figure 5.1 Undifferentiated RSC derived retinal neurosphere cultured in ultra-low adhesive spheroid plate at day 3 and 12. Images were captured with 10x objective using light microscopy

Using a similar approach, retinal neurospheres were initiated by seeding CD1-4 RSCs suspended in differentiation medium in ULA plates. Eleven different MiEye retinal neurospheres were prepared using various protocols. A representative workflow of differentiation and maturation is illustrated in Figure 5.2A-B. After culturing of the RSCs for 6-10 days, the formed differentiated neurospheres were allowed to mature on the coated surface (i.e. PLO-Laminin) to evaluate the possibility of inducing the formation of morphological features such as neurite extensions. The effect of various combinations of parameters such as retinal neurosphere population (5,000, 10,000, and 15,000 cells per sphere), maturation medium (serum / no serum), and surface coating (PLO-Laminin/Matrigel™) were evaluated on the structural integrity of the spheres. First, a decrease in seeding cell density from 15,000 cells to 5,000 cells resulted in a decrease in retinal neurosphere structural stability after 2 days of maturation (Figure 5.3A). Furthermore, the decreased structural stability was more obvious in the presence of Matrigel™ coating and serum. A decrease in structural stability was evident from size reduction and deformation of the spheres, along with increased monolayer cell attachment on the coated surface surrounding the sphere. Retinal neurospheres were least structurally stable when maturation was

taking place in serum containing maturation media, coupled with Matrigel™-coated surface, where retinal neurospheres were completely deformed by day 6 (Figure 5.3B). Seeding density played an important role in the sphere structural stability as retinal neurospheres constructed with only 5,000 cells exhibited complete structural deformation across all culturing conditions by day 6. The retinal neurospheres made with 10,000 cells matured in serum-containing medium on either PLO-Laminin or Matrigel™-coated surface also showed significant deformation. However, retinal neurospheres matured in medium without serum on either PLO-Laminin- or Matrigel™-coated surface showed greater structural stability. The retinal neurospheres made with 15,000 cells maintained the highest structural integrity after 6 days of maturation on various coated surface and media.

Matrigel™- and PLO-Laminin-coated surfaces produced significantly different effect on retinal neurosphere integrity profile over 6 days. Maturation on Matrigel™ resulted in four out of six retinal neurospheres showing significant structural stability decline with significant deformation and size reduction after 2 days. By day 6, five out of six maturation conditions resulted in near-complete deformation of retinal neurospheres. On the other hand, PLO-Laminin-coated surfaces support retinal neurosphere structural stabilization with all six retinal neurosphere maturation conditions showing no sign of structural destabilization after 2 days.

A)

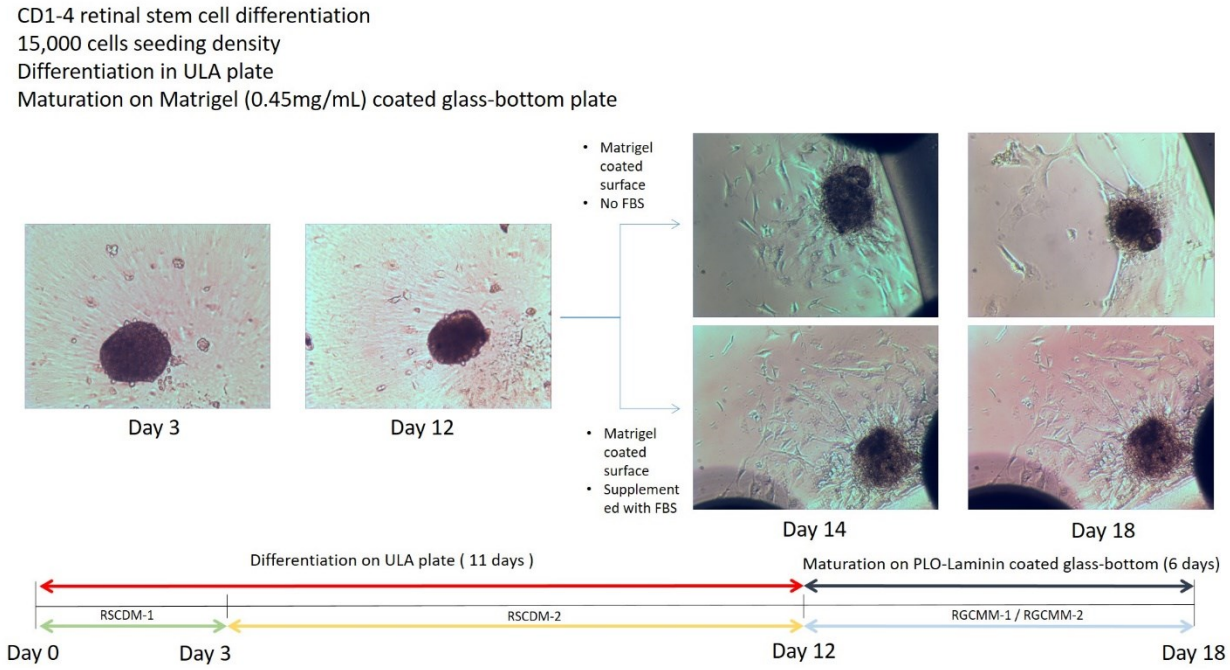

B)

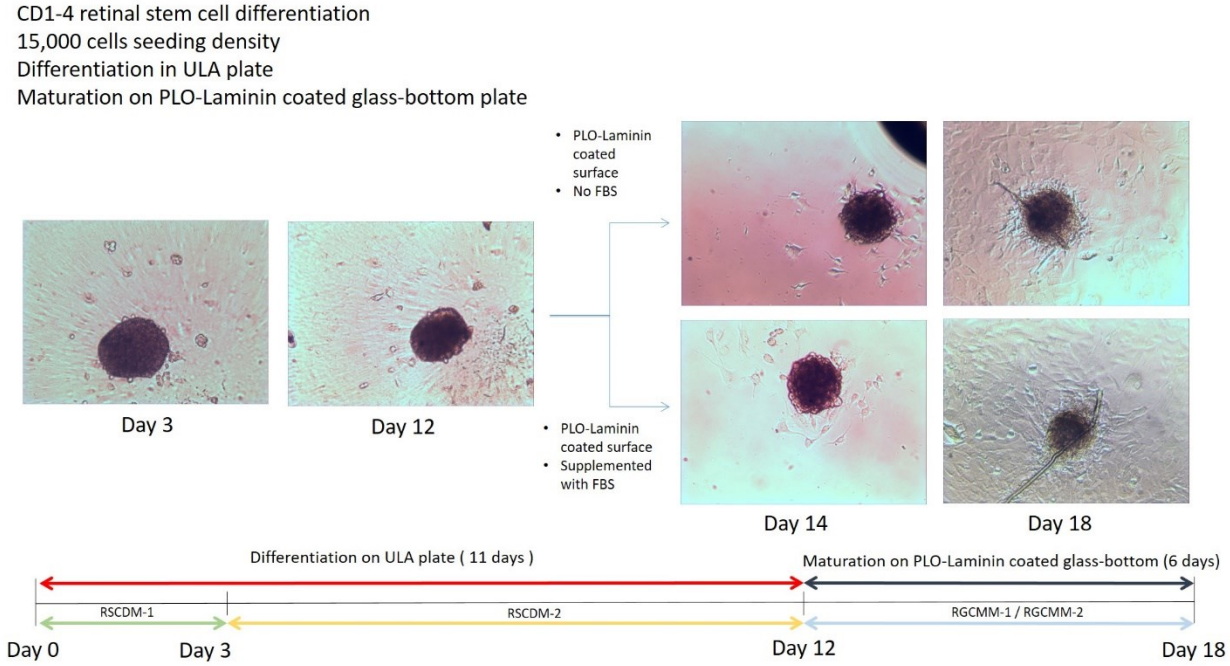

Figure 5.2 Representative differentiation and maturation process of RSCs towards the generation of differentiated retinal neurosphere on Matrigel™- (A) and PLO-Laminin-coated surface (B). Images were captured with 10x objective using light microscopy

A)

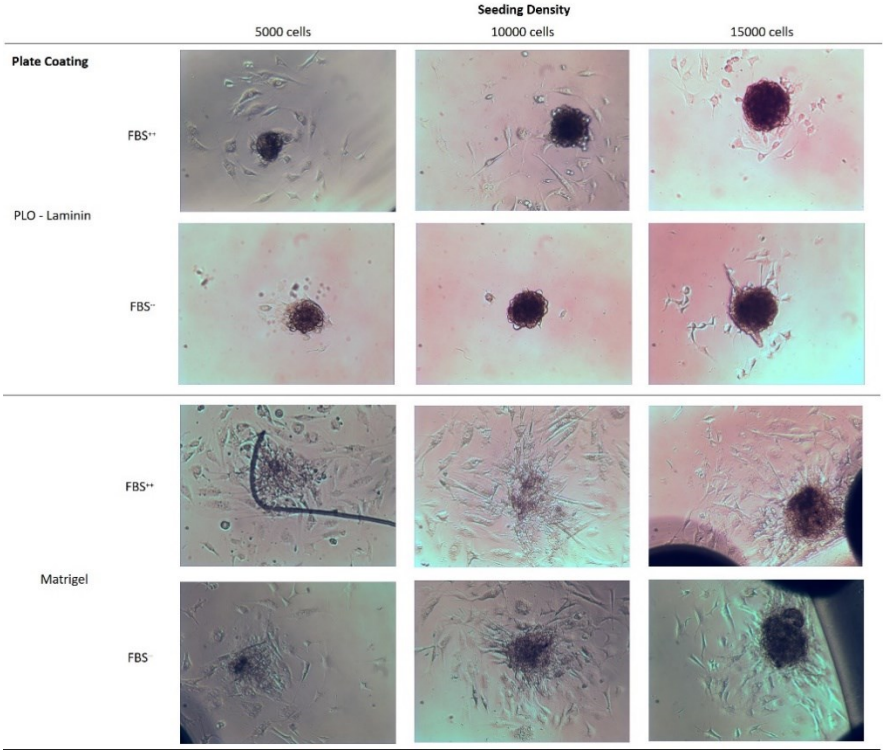

B)

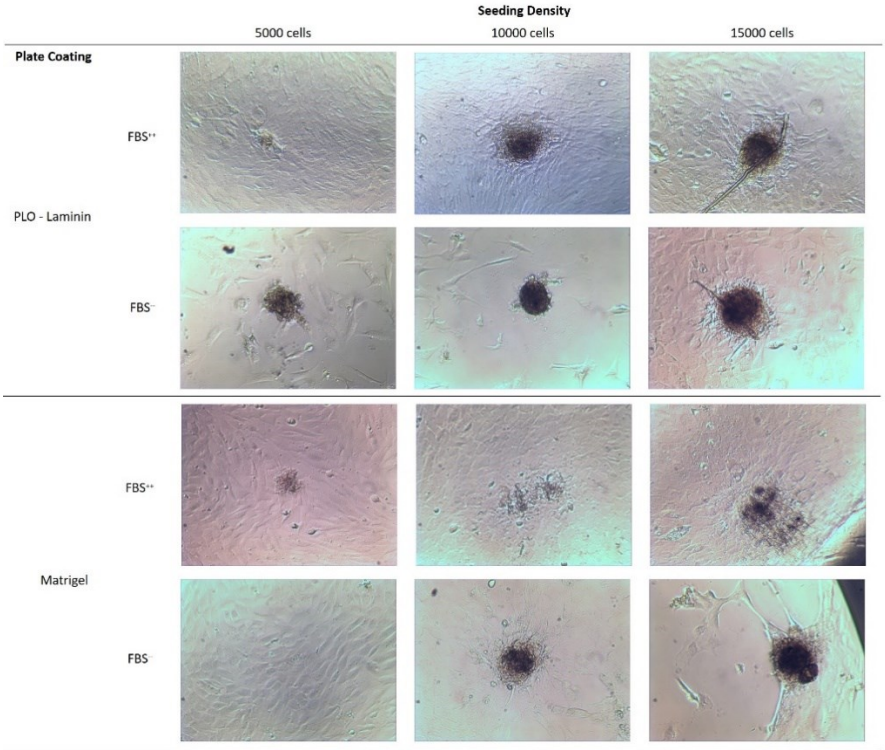

Figure 5.3 Effect of neurosphere size on the maintenance of structural integrity during the maturation process on PLO-Laminin- and Matrigel™-coated surfaces, with or without serum for 2 days (A) and 6 days (B). Images were captured with 10x objective using light microscopy

Furthermore, four of the six maturation conditions showed minimal structural de-stabilization after 6 days. As it was determined that retinal neurospheres with 15,000 cells were able to provide the highest morphological integrity, downstream experimentations and evaluations were carried out using 15,000 cell seeding density, and eight MiEye retinal neurospheres (MiEye1, MiEye2, MiEye3, MiEye4, MiEye5, MiEye7, MiEye8, MiEye10) were considered viable from the various combinations of differentiation and maturation conditions (Table 5.2).

Table 5.2 Overview of MiEye retinal neurosphere differentiation and maturation parameters

Name	Description	Differentiation		Maturation		
		Days	Media	Days	Media	Surface
MiEye1	24-day differentiation – protocol#2	10	RSCDM-1 (D0-3) RSCDM-2 (D3-10)	12	RGCMM-3	PLO-Laminin
MiEye2	24-day differentiation – protocol#2	10	RSCDM-1 (D0-3) RSCDM-2 (D3-10)	12	RGCMM-4	PLO-Laminin
MiEye3	24-day differentiation – protocol#2	10	RSCDM-1 (D0-3) RSCDM-2 (D3-10)	12	RGCMM-3	Matrigel™
MiEye4	24-day differentiation – protocol#2	10	RSCDM-1 (D0-3) RSCDM-2 (D3-10)	12	RGCMM-4	Matrigel™
MiEye5	18-day differentiation – protocol#3	18	RSCDM-1 (D0-4) RSCDM-2 (D4-18)	-	-	-
MiEye6	21-day differentiation – protocol #3	18	RSCDM-1 (D0-4) RSCDM-2 (D4-18)	3	RGCMM-3	PLO-Laminin
MiEye7	21-day differentiation – protocol #3	18	RSCDM-1 (D0-4) RSCDM-2 (D4-18)	3	RGCMM-4	PLO-Laminin
MiEye8	6-day differentiation – protocol #4	6	RSCDM-1 (D0-2) RSCDM-2 (D2-6)	-	-	-
MiEye9	6-day differentiation – protocol #5	6	RSCDM-2 (D0-6)	-	-	-
MiEye10	10-day differentiation – protocol#4	6	RSCDM-1 (D0-2) RSCDM-2 (D2-6)	4	RGCMM-4	PLO-Laminin
MiEye11	10-day differentiation – protocol #5	6	RSCDM-2 (D0-6)	4	RGCMM-4	PLO-Laminin

Based on biomarker mRNA gene expression profiling, retinal neurospheres *MiEye1, MiEye2, MiEye3 and MiEye4,* positively expressed multiple biomarkers that represent seven different retinal cell types (Table 5.3). Several target genes were expressed across the four retinal neurospheres such as *Rbpms, Slc1a3*1, *Aldh1a1*, *Vim*, *Rom*, and *Prkca*. Selective biomarker such as *Tubb3* was also positively expressed in MiEye 1 (Figure 5.4A) and MiEye3 (Figure 5.4C), but not in MiEye2 (Figure 5.4B) and MiEye4 (Figure 5.4D). *Abca8a* was positively expressed in MiEye1, MiEye3 and MiEye4, but not in MiEye2. *Rpe65 and Prdx6,* were detected to be expressed at low levels but did not meet the 20 copies thresholds in MiEye1, MiEye2, MiEye3, MiEye4, respectively. All four retinal neurospheres positively expressed eight different markers including *Rbpms, Tubb3.* Based on the gene expression profile results, these four differentiated populations expressed the markers for most of the retinal cell types such as RGC, astrocyte, Müller glia, photoreceptor, RPE, amacrine and bipolar cells, suggesting the possibility that the retinal neurospheres contained all these major retinal cell types.

MiEye5 (Figure 5.4E) was an 18-day differentiated retinal neurosphere, and MiEye7 (Figure 5.4F) was differentiated with the 18-day differentiation protocol with an additional 3-day protocol on PLO-Laminin surface. Both retinal neurospheres showed very different expression profiles. MiEye5 positively expressed six gene targets with differential mRNA copies of *Rbpms, Slc1a3, Abca8a, Aldh1al, Vim* and *Prkca*. On the other hand, MiEye7 positively expressed only four gene targets, *Rbpms*, *Slc1a3*, *Vim*, and *Prkca*, with relatively lower copy numbers.

MiEye8 (Figure 5.4G) was a 6-day differentiated retinal neurosphere, and MiEye10 (Figure 5.4H) was generated from the same 6-day differentiation protocol with an additional 4 days of maturation process on PLO-Laminin surface. MiEye8 positively expressed six target genes *Rbpms*,

Slc1a3, *Abca8a*, *Aldh1a1*, *Vim*, and *Prkca*. On the other hand, MiEye10 positively expressed only three target genes, *Rbpms, Slc1a3,* and *Vim,* at relatively lower expression levels.

Table 5.3 Retinal biomarker mRNA expression profile summary for MiEye retinal neurospheres. Heat map categorizes gene expression into three major categories: no expression (n<5; blue), semi-positive expression (5<n<20; pink), and positive expression (n>20; red)

Gene Specificity	Gene Name	6-days Differentiated CD1-4	MiEye1	MiEye2	MiEye3	MiEye4	MiEye5	MiEye7	MiEye8	MiEye10
RGC	CD48	5	7	2	1	3	2	4	5	2
	ISL-1	6	3	8	1	9	5	3	7	2
	MAP2	2	4	1	2	8	0	0	0	0
	Nef-H	0	1	0	3	1	1	0	4	1
	Pou4f1	2	2	5	2	1	0	2	7	2
	Rbpms	527	675	620	606	855	362	120	601	120
	Sncg	3	0	2	3	5	2	0	2	1
	Thy-1.2	2	3	0	1	0	1	0	1	0
	Tubb3	40	25	17	61	10	1	3	4	4
Astrocyte	Aqp4	1	1	0	3	2	3	2	1	2
	Prdx6	4	9	12	11	10	7	1	11	3
	Slc1a3	272	925	762	734	724	162	24	268	54
Müller	Abca8a	7	36	15	41	34	28	1	31	4
	aldh1a1	31	204	166	157	200	44	9	40	12
	Vim	16544	14115	16081	16150	18974	3865	2583	3860	1519
Photoreceptor	Nrl	1	0	2	1	3	0	0	0	0
	Rom1	30	23	25	29	33	13	2	17	4
RPE	Rpe65	9	8	5	10	11	14	10	3	9
Amacrine	Calb2	5	5	5	3	5	5	3	1	3
Bipolar	Prkca	104	140	152	120	151	32	32	53	14
Horizontal	Lim2	0	0	0	2	0	0	0	5	1

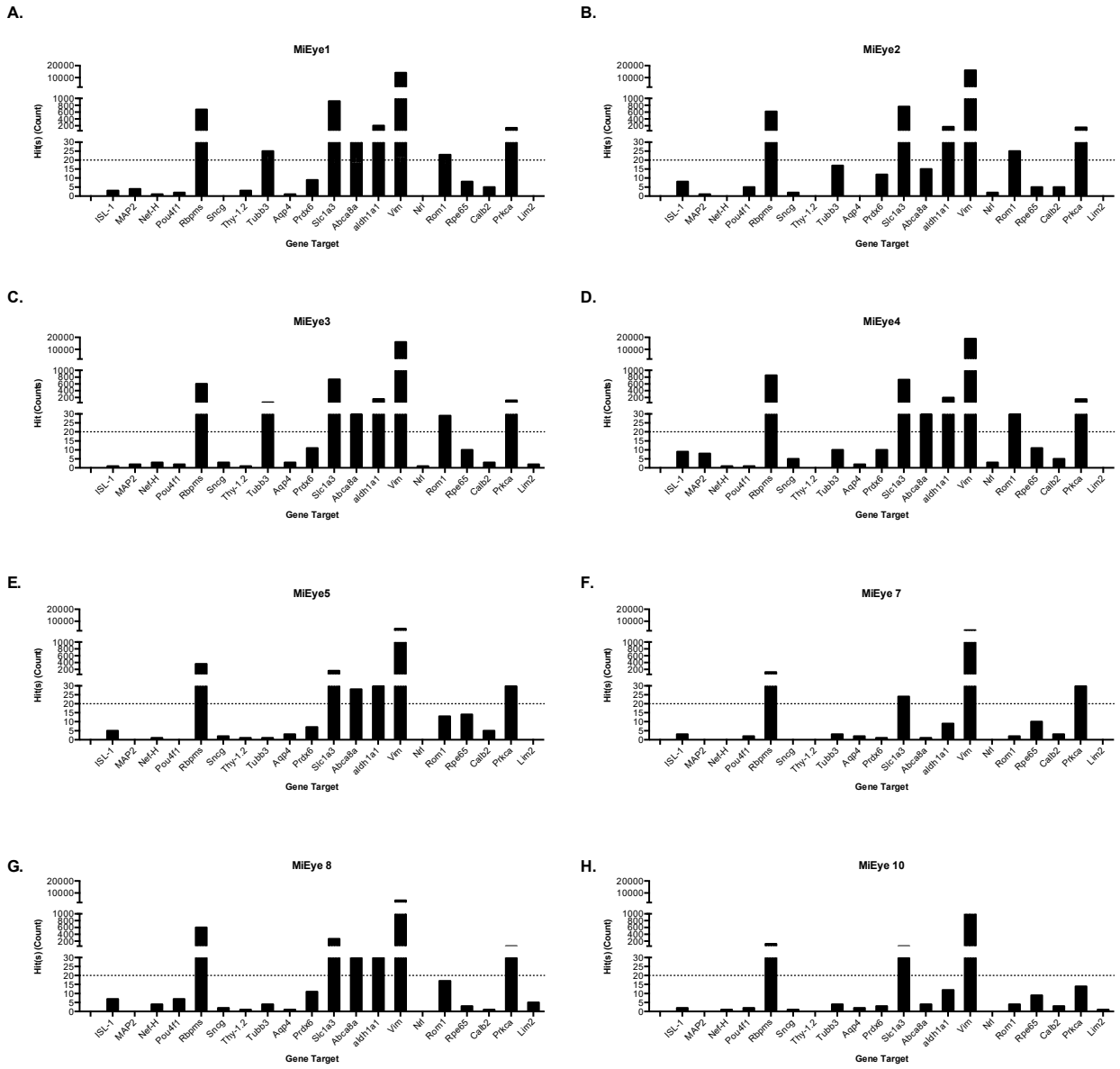

Figure 5.4 Retinal biomarker mRNA gene expression profiles of retinal neurospheres MiEye1 (A), MiEye2 (B), MiEye3 (C), MiEye4 (D), MiEye5 (E), MiEye7 (F), MiEye8 (G), and MiEye10 (H). Threshold indicator (dotted lines) at n=20 is indicative of the threshold for positive expression

Amongst the retinal neurospheres generated, MiEye8 retinal neurosphere was chosen as a model retinal neurosphere to demonstrate the proof of concept for transfection studies as it showed similarities in differentiated retinal cell type compositions compared to the 6-day differentiated CD1-4 RSCs in monolayers that was described in previously published work [121]. From

biomarker expression profile perspective, both 6-day differentiated CD1-4 cells in monolayer and 6-day differentiated CD1-4 in 3D (MiEye8) showed they consists of multiple target cell types such as astrocyte, Müller glial, RGC, and bipolar cells as they both expresses retinal target genes *Rbpms*, *Slc1a3*, *aldh1a1*, *Vim*, and *Prkca* at similar levels (Figure 5.5). *Tubb3*, *Rom1,* genes, *Abca8a* biomarkers were expressed at different levels between 2D and neurosphere, with 10-fold, 1.8-fold, and 4.4-fold differences, respectively.

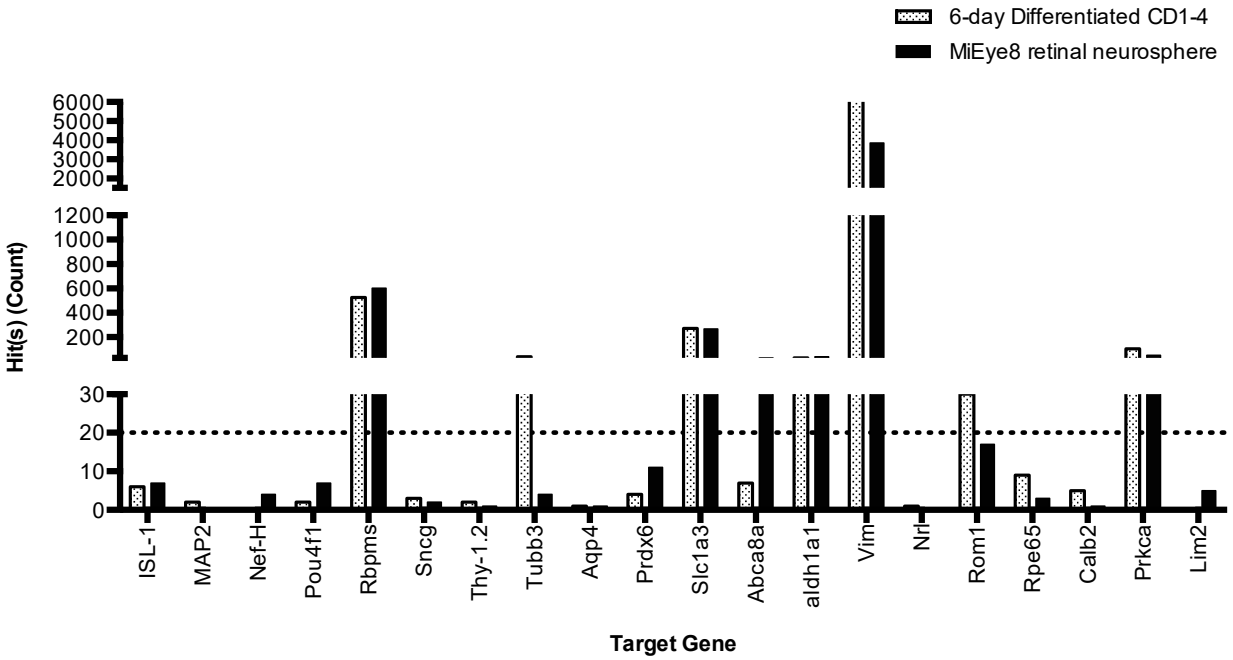

Figure 5.5 Comparative mRNA gene expression profile analysis of 6-day differentiated CD1-4 stem cells in monolayers and MiEye8 retinal neurospheres

5.4.2 Transfection screening of K2-NP non-viral gene delivery systems in MiEye retinal neurospheres

Transfection of MiEye8 retinal neurospheres was carried out using K2-NPs, a non-viral gene delivery system shown to have high TE in astrocytes and RGCs cultured in monolayer in our previous studies [122]. Nine formulations of K2-NPs were prepared and screened in the MiEye8 retinal neurospheres. Amongst the different treatments, neurospheres transfected with F3 (4:1 v/w K2:DNA ratio) and F4 (10:1 v/w K2:DNA Ratio) K2-NPs were able to transfect the neurospheres

as demonstrated by confocal microscopic observations of GFP expression (Table 5.4). Transfection was further assessed by quantitative evaluation of MFI captured in the GFP channel throughout the thickness of retinal neurospheres.

Table 5.4 Transfection screening of a panel of K2-NP formulations in MiEye8 retinal neurosphere, CD1-4 derived RGC monolayer and A7 astrocyte monolayer

	Retinal Cell Models					
	MiEye8 Retinal Neurosphere		**CD1-4 derived RGC monolayer (Chapter 4)**		**A7 astrocyte monolayer [122]**	
K2-NP Formulation	**cMFI of GFP channel* (normalized to baseline)**	**Observed toxicity**	**Transfection Efficiency****	**Cell viability**	**Transfection Efficiency****	**Cell viability**
F1	-	+	n/a	n/a	-	n/a
F2	-	+	63.1±1.4%	94.4±0.4	15.8±2.6%	76.2±1.7
F3	36.0±55.7	+	62.9±1.9%	79.7±3.3	31.3±1.5%	44.8±2.2
F4	91.9±30.5	++	n/a	n/a	n/a	n/a
F5	-	++	n/a	n/a	n/a	n/a
F6	-	++	n/a	n/a	n/a	n/a
F7	-	+++	n/a	n/a	n/a	n/a
F8	-	+++	n/a	n/a	n/a	n/a
F9	-	+++	n/a	n/a	n/a	n/a

Transfection efficiency evaluations:
* combined (c)MFI = average of the individual MFI of all optical sections of the neurospheres (n=9-12; number of sections vary depending on the exact size of each sphere)
** data from flow cytometry measurements (mean ± s.d.; n=3) - no transfection
Observed toxicity evaluations:
+ low toxicity level with minimal debri
++ medium toxicity level with some debri near neurosphere
+++ significant toxicity level with lots of debri and noticeable disintegration of neurosphere

In untreated retinal neurospheres, all cells remained intact and no detached cells or cell aggregates were found outside of the neurospheres. Following treatment with K2-NPs using increasing concentrations of K2® reagent, increasing number of detached cells and cell debris were present around neurospheres, which we have interpreted as increasing levels of toxicity (Table 5.4).

In the MiEye8 retinal neurosphere transfected with F3, localized gene expression was observed in the superficial layers of the neurosphere (Figure 5.6A). This was also evident through analysis of z-stack optical slices (Figure 5.6B), where GFP expression was visible between optical slices 4 to 9. The MFI profile for specific regions of interest, as shown in Figure 5.6C-D, illustrates presence of GFP-expressing cells. Quantitative analysis of optical slices 4-9 indicated that the cMFI of F3-transfected neurosphere were up to 7-fold higher compared to the control neurosphere (Figure 5.6E). The cMFI throughout the thickness of the F3-transfected neurosphere was 36.0±55.7.

Retinal neurospheres transfected with F4 (10:1 v/w K2:DNA ratio) showed a widely scattered GFP expression pattern on the surface of the retinal neurosphere (Figure 5.7A). Analysis of z-stack optical slices show that GFP expressions was observed scattered across the sphere in optical slices 4 to 11 (Figure 5.7B). MFI analysis showed that the neurosphere transfected with F4 consistently have higher MFI (up to 1.71-fold) compared to untreated control. The cMFI throughout the thickness of the neurosphere was 91.9±30.5. Similarly, MFI profiling in a selected region of interest shows peaks corresponding to GFP expressing cells along the line (Figure 5.7C-D).

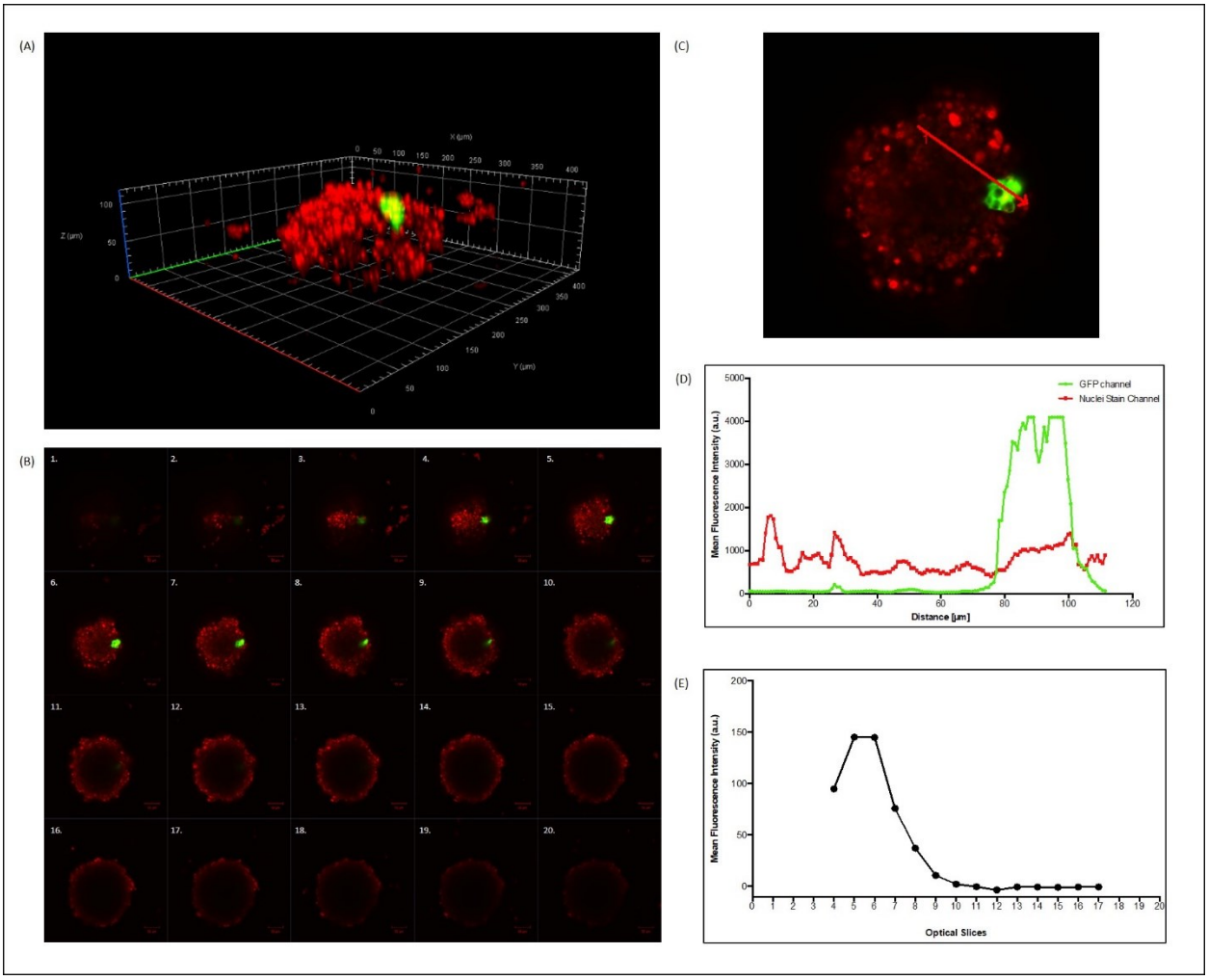

Figure 5.6 Z-stack analysis of MiEye8 retinal neurosphere at 120 hours post treatment with F3 K2-NP (4µL:1µg). MiEye8 retinal neurosphere was counterstained with 5µM of DRAQ5™ nuclei stain (red). Successful transfection is indicated by GFP expression (green). A) 3D reconstruction of the MiEye8 retinal neurosphere demonstrating GFP expression in the neurosphere surface layer. B) 20 z-stack optical slices captured across the observable thickness of the retinal neurosphere showing visible GFP expression in slices 4 to 9. C) Representative illustration MFI analysis on GFP and nuclei stain channels through a region of interest (red arrow) on an optical section (slice 6) of the neurosphere. Blunt end of the arrow marks the start of the path (0 µm) and the tip of the arrow marks the end of the path (111 µm). The corresponding GFP (green) and nuclei stain (red) channel MFI through the path of interest is shown in (D). E) Normalized average GFP channel MFI of the neurosphere in each optical section throughout the z-stack.

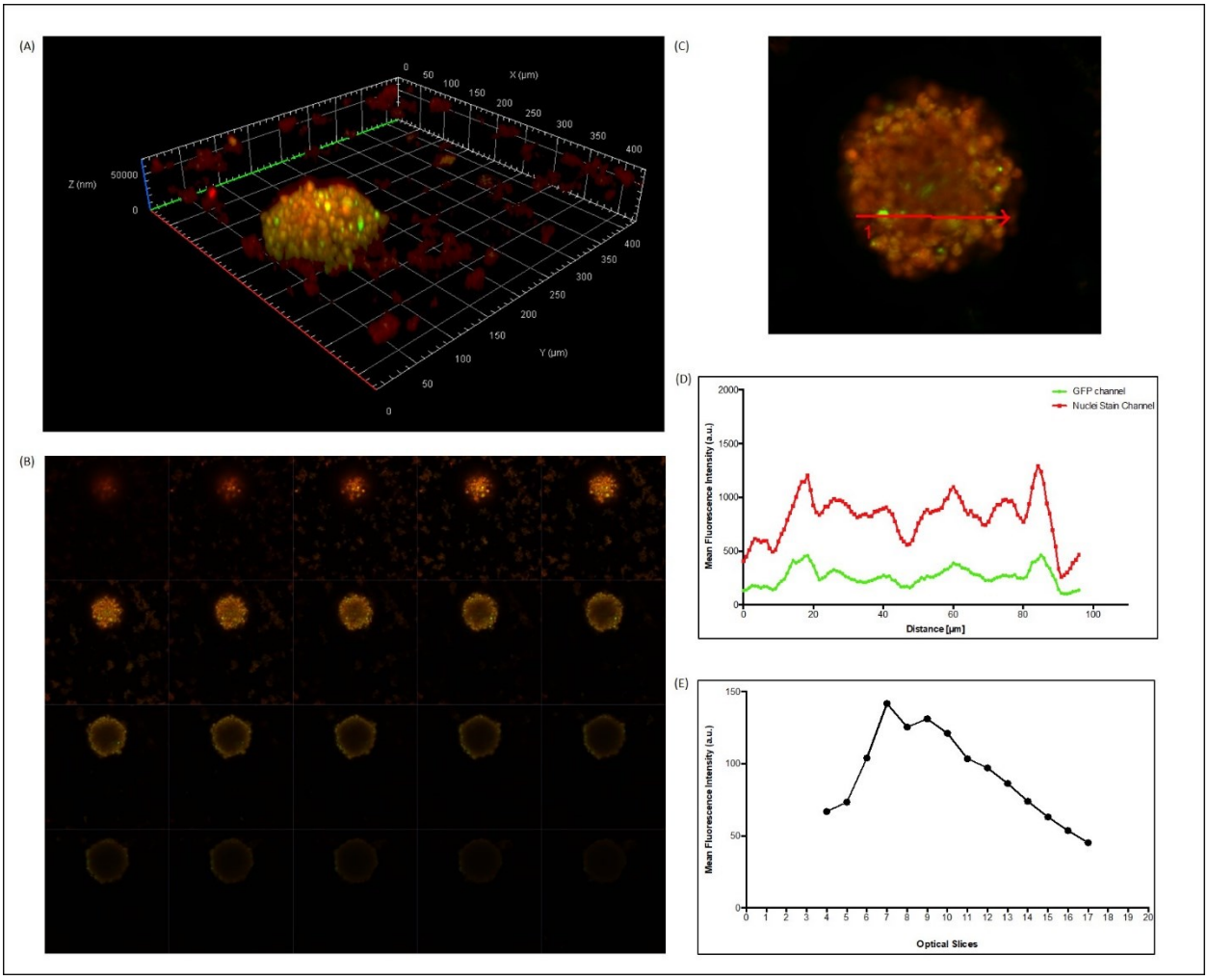

Figure 5.7 Z-stack analysis of MiEye8 retinal neurosphere at 120 hours post treatment with F4 K2-NP (10µL:1µg). MiEye8 retinal neurosphere was counterstained with 5µM of Syto™62 nuclei stain (red). Successful transfection is indicated by GFP expression (green). A) 3D reconstruction of the MiEye8 retinal neurosphere demonstrating GFP expression on neurosphere surface. B) 20 z-stack optical slices captured across the observable thickness of the retinal neurosphere showing visible GFP expression in slices 4 to 9. C) Representative illustration MFI analysis on GFP and nuclei stain channels through the region of interest (red arrow) on an optical section (slice 7) of neurosphere. Blunt end of the arrow marks the start of the path (0 µm) and the tip of the arrow marks the end of the path (96 µm). The corresponding GFP (green) and nuclei stain (red) channel MFI through the path of interest is shown in (D). E) Normalized average GFP channel MFI of the neurosphere in each optical section throughout the z-stack.

5.5 Discussion

Eight retinal neurospheres with distinct retinal gene expression profiles were generated using various differentiation procedures. Through gene expression profiling, it was evident that CD1-4 RSCs were able to differentiate in 3D culture, generating retinal neurospheres composed of various retinal cell types including RGCs, astrocytes, Müller glial and photoreceptor cells, depending on the differentiation procedure. Of particular interest, the 6-day differentiated CD1-4 RSCs in either 2D or 3D showed similar diversity of cells through gene expression profiles as both expresses key biomarkers for astrocytes, Müller glial, astrocyte, and bipolar cells at similar levels. The presence of mixed cell types in retinal neurosphere cultures may allow for versatile downstream gene delivery system assessment options such as transfection, infiltration, and targeting efficiencies. Using the MiEye8, a 6-day differentiated retinal neurosphere expressing markers of RGC, astrocyte, Müller glial, photoreceptor and bipolar cells, K2-NPs with various compositions were screened. The K2-NP system was a highly effective gene delivery reagent in 2D monolayers as demonstrated in our previous work, where K2-NP formulation with K2:DNA ratio of 4:1 at 1 μg pDNA per dose showed 60% TE in monolayer XFC retinal ganglion cells (Table 5.4) [122]. In MiEye8, K2-NPs with the same K2:DNA ratios of 4:1 at 1 μg pDNA per dose (F3) showed lower TE and the transfection was localized to the surface cellular layers of the neurosphere. K2-NP formulation (F4) with K2:DNA ratios of 10:1 at 1 μg pDNA per dose also showed lower transfection compared to cells in monolayers, but with a more uniformly scattered pattern across the surface of the neurosphere. In both cases, transfected cells were localized on the surface of the sphere with very limited signs of gene expression in the interior of the spheres. Increasing the K2:DNA ratio and DNA per dose did not improve the TE, however, toxicity increased. More specifically, higher concentrations of K2® transfection reagent resulted in higher

toxicity, as observed by the increasing amounts of cellular debris around the spheres. Differences in NP toxicity profile was also observed between 3D neurosphere and 2D cell monolayers as neurospheres appears to have higher resistance to NP toxicity compared to cells cultured in 2D monolayers. For example, in the case of F3 K2-NP transfection, CD1-4 derived RGCs and A7 cells culture in 2D monolayer were more susceptible to toxicity compared to MiEye8 neurosphere.

Assessment of the gene delivery capacity of NPs through evaluation of the cMFI of neurospheres is an alternative approach to flow cytometry of individual cells from 2D cultures as it measures the relative level of a reporter protein that is produced by transfected cells. Utilizing fluorescence intensity and cMFI as a means of evaluating neurospheres in this paper has allowed the characterization of transfection by K2-NPs. Such evaluation of TE analysis could also be applied in other forms of tissue-like cultures and *in vivo* to approximate TE, where dissociation of tissue structure into individual cells for single-cell transfection analysis is inefficient and challenging.

As expected, TE of cells in 3D were significantly lower (~2~4%) compared to cell 2D monolayer (15-63%) in cells transfected with the same NP system, which could be attributed to several factors. One of the major differences in a 3D culture-based assay is the architectural and spatial properties. From a cell-nano exposure perspective, traditional 2D monolayer culture allows for higher cell-nano exposure, where cell populations are distributed across the culture surface and can be exposed to NPs more uniformly. In 3D culture, on the other hand, lower cell-nano exposure can be attributed to the tissue-like cellular arrangement, where the outermost cell layers have the highest cell-nano contact with gradual decrease with increasing depth towards the center of the sphere. Aside from architectural and spatial factors, cell proliferation factors could also influence transfection. Majority of the commonly used cell lines for *in vitro* studies were immortalized cell

lines that proliferate at a high rate in cell culture, while primary cells and cells found *in vivo* either do not proliferate or typically proliferate at a much lower rate. Various studies over the years have shown that cell cycle plays a role in gene delivery, particularly for non-viral based NPs that lack the efficient transduction machinery unlike viruses [181]. Moreover, the difficult part of transfection is not necessarily cellular entry, but rather translocation of pDNA to the nucleus [181]. Delivery of pDNA before mitosis was suggested to increase the level of transgene expression [182, 183], and was suggested that transfection during cell division results in significantly higher level of expression in part due to nuclear envelope split, thus assisting pDNA in nuclear entry [184]. As cells in MiEye8 constitute tissue-like multicellular arrangement coupled with limited proliferation capacity compared to immortalized cell lines that divide indefinitely, it therefore captures key characteristics of cells *in vivo*, in an *in vitro* modality. Altogether, the combinations of various *in vivo* relevant structural and cellular properties, retinal neurospheres such as MiEye8 have the potential to serve as a tool for predicting *in vivo* performance of NPs. It is recognized that a 3D retinal model that consists of a complete representation of the retinal cell type diversity, arrangements, and functions of the retina could be an important tool for the understanding of retinal biology and retinal therapeutic discovery. The significance of the MiEye retinal model described in this paper is two-fold: 1) the model is an important first step towards the generation of a complete retina model; and 2) the model demonstrates the potential towards the generation of a more *in vivo* translatable preclinical screening model for NP-mediated gene delivery.

5.6 Conclusion

In summary, in this paper the development of a 3D retinal neurosphere model was demonstrated. Among neurospheres grown in eleven different culture conditions, a 6-day differentiated neurosphere, MiEye8, have shown value as a "mini-retina"-like model that contains the major retinal cell types and can be used towards a more *in vivo*-relevant screening of non-viral gene delivery systems.

5.7 Acknowledgement

We thank Monika Sharma and Neil Winegarden of the Princess Margaret Genomic Centre for their help with NanoString analysis.

Chapter 6 Gemini surfactant NP system physicochemical property optimization

6.1 Rationale and objective

Previous work utilized regular plasmid (RP) as the vector to encode therapeutic protein sequences and for GL-NP systems construction. However, MC offers significant advantages such as longer transgene expression and lower risk of inflammatory response resulting from the absence of bacterial sequences normally found in RP vector backbone. In this study, the effect of pDNA construct size has on the physicochemical properties of NPs was investigated using RP and MC pDNA. Furthermore, optimization of NP physicochemical properties was also explored through incorporation of sonication and TNPC in the manufacturing process.

6.2 Background

A pDNA vector consists of two major components: a vector backbone and a transgene expression cassette. In a traditional RP, significant portion of the vector backbone are encoded with bacterial sequences and antibiotic resistance gene(s) used in the production and selection of pDNA in prokaryotic manufacturing system, but such sequences are non-essential and undesirable in mammalian cells. The presence of bacterial sequences such as CpG in pDNA was shown to contribute to inflammatory immune responses, whereas CpG-free pDNA was shown to have significantly reduced inflammatory risks [185]. Furthermore, bacterial sequences have also been shown to shorten the duration of gene expression in mammalian cells as a consequence of transcription silencing associated with histone modification mechanisms [186]. MC is a novel type of pDNA construct that is free of non-essential bacterial sequences in the vector backbone, which can effectively reduce construct size while maintaining the target sequence expression capacity [187]. Studies have shown that MC have a significant role in pDNA gene therapy as it results in

longer and persistent transgene expression in various gene transfer studies [188-191]. Elevated levels of transgene expressions resulted from MC compared to RP have been suggested due to improved active chromatin and transcription activity compared to RP [192]. In this chapter, the main objective was to evaluate whether MC can also improve the physicochemical properties of NP systems formulated with MC. In addition, whether the incorporation of sonication and TNPC in the manufacturing process can further improve the physicochemical properties of NP systems.

6.3 Materials and methods

6.3.1 RP and MC pDNA constructs production

Different nucleic acid constructs were used as model RPs such as pEF1-BDNF-IRES-GFP, pEF1-TNFR-IRES-GFP, pCMV-TNFR-IRES-GFP, and gWiz™ GFP. pEF1-BDNF-IRES-GFP, pEF1-TNFR-IRES-GFP, and pCMV-TNFR-IRES-GFP constructs were prepared through cloning of either BDNF or tumor necrosis factor receptor (TNFR) sequences into MN530A-1 or MN501A vector (System Biosciences, Palo Alto, CA, USA), which serve as parent plasmids for MC production. A commercially available construct gWiz™ GFP reporter vector was also used as a model RP construct (Aldevron, Fargo, ND, USA). MC constructs mcEF1-BDNF-IRES-GFP, mcEF1-TNFR-IRES-GFP, and mcCMV-TNFR-IRES-GFP were produced by first transforming the respected cloned parent plasmids pEF1-BDNF-IRES-GFP, pEF1-TNFR-IRES-GFP, and pCMV-TNFR-IRES-GFP into ZYCY10P352T *E.coli*. Transformed *E.coli* were grown until desired optical density according to manufacturer's protocol. Initiation of MC production in the transformed *E.coli* was activated through arabinose-activated endonuclease activity for 5 hours at 30ºC. MCs were extracted at the end of the arabinose induction period. Plasmid design, construction, and scale-up were performed by Dr Nafiseh Nafissi. A commercially available vector pUMVC1 reporter plasmid (Aldevron) was used as a model MC in selective studies.

6.3.2 Cy®5 labeling of RP and MC

pDNA used in FCS were labelled using Label IT® Cy®5 nucleic acid labeling kit (Mirus Bio LCC, Madison, WI, USA) according to manufacturer's protocol. Labelled pDNAs were purified by ethanol precipitation followed by membrane filtration using Amicon 3kDa centrifugal filters (EMD Millipore, Billerica, MA, USA). Labeling density was calculated using the base:dye following formula:

$$base{:}\,dye = \frac{A_{base} * \varepsilon_{dye}}{A_{dye} * \varepsilon_{base}}$$

The extinction coefficient of nucleic acid bound dye (ε_{dye}) for Cy®5 used is 250,000. The extinction coefficient of nucleic acid (ε_{base}) for double stranded DNA is 6,600.

6.3.3 NP preparation

K2-NP was prepared according to the manufacturer's protocol. Briefly, K2-NP were formulated by complexing one of the RP or MC pDNA with K2® transfection agent (Biontex Laboratories GmBH, München, Germany) at ratios of 2 µL of K2® per 1 µg of pDNA. GL-NPs were prepared by a two-step formulation process. First, gemini-pDNA (GP) complex was formed by combining GS and pDNA at 10:1 charge ratio, and incubated for 15 minutes at room temperature, followed by addition of desired ratios of 1,2-Dioleoyl-sn-glycero-3-phosphoethanolamine (DOPE; Avanti Polar Lipids, Alabaster, AL, USA) vesicles, forming the final GL-NPs upon incubation of 30 minutes at room temperature. DOPE vesicles were prepared by first dissolving 1mM DOPE in 9.25% w/v sucrose solution (pH 9) with brief bath sonication, followed by processing of DOPE solution through the LV1 Microfluidizer (Microfluidics Inc., Newton, MA, USA) for three-passes.

6.3.4 Dynamic light scattering

Size distribution analysis was performed using Zetasizer Nano ZS (Malvern Instruments, United Kingdom). Three separate measurements were taken using 50 µL samples. Size distribution was recorded, and the z-average was taken as average size with 10 runs per measurement. Zeta potential analysis was performed by a combination method of phase analysis light scattering (PALS) and a patented mixed-mode measurement technique (M3) using Zetasizer Nano ZS (Malvern Instruments). Each sample was diluted using ultrapure water at a 1:20 (v/v) ratio and measured using capillary cell.

6.3.5 Fluorescent correlation spectroscopy

FCS measurements were performed on a Zeiss LSM 710 confocal laser scanning microscope with Confocor 3 systems (Carl Zeiss AG). NPs were prepared with Cy®5-labelled gWiz™ GFP and pUMVC1 pDNA. Free Cy®5 or Cy®5-labelled pDNA was excited using 633nm He-Ne laser and reflected by a dichroic beam splitter (488/633), which is focused 200 µm into the sample through Apochromat NA 1.2 water-immersion 40x objective lens. Emission spectra were collected through a 580 nm long-pass filter and recorded by an avalanche photodiode detector. FCS measurements were performed in 200 µL volumes of GL-NPs in a CELLview 4-well chamber with glass-bottom coverslip (Grenier-Bio One, Frickenhausen, DE). All samples were measured in triplicates. Stokes-Einstein equation was used in particle size calculation:

$$d_H = \frac{kT}{3\pi\eta D}$$

6.4 Results

6.4.1 Effects of pDNA size and particle physicochemical properties: a case study using commercial NP system

A systematic study to evaluate the effect of pDNA construct lengths on NP properties were initially investigated using K2® nanoparticle system formulated with seven different pDNA constructs. The constructs fall into three major sizes categories: small (4.4 – 4.7kb), medium (8.4 – 8.5kb), and large (>14kb) (Table 6.1), where MCs fit into the "small" category, while RPs fits into the "medium" category, and a "large" construct with 14kbs was incorporated for comparison. Each MC used in this study was derived from its corresponding RP (i.e. pEF1-BDNF-IRES-GFP is the RP of mcEF1-BDNF-IRES-GFP).

Table 6.1 Physicochemical properties of K2-NP formulated with seven different plasmid constructs that varies in construct size. Values expressed as mean ± s.d., n=3

Size Category	Construct	Size (kbp)	Z-average (nm)	PDI	Zeta Potential (mV)
Small	mcEF1-BDNF-IRES-GFP	4.7	86.2 ± 0.5	0.19	53.3 ± 0.4
	mcEF1-TNFR-IRES-GFP	4.5	78.6 ± 0.6	0.19	48.5 ± 0.4
	mcCMV-TNFR-IRES-GFP	4.4	83.2 ± 1.8	0.16	52.2 ± 1.8
Medium	pEF1-BDNF-IRES-GFP	8.7	102.5 ± 1.0	0.18	52.9 ±0.8
	pEF1-TNFR-IRES-GFP	8.5	109.6 ± 3.2	0.25	45.3 ± 2.9
	pCMV-TNFR-IRES-GFP	8.4	93.9 ± 1.0	0.16	51.6 ± 1.3
Large	phTERT	14.0	122.4 ± 6.4	0.28	53.8 ± 3.2

The results showed a positive correlation between nucleic acid construct size and particle size of K2-NPs systems (Figure 6.1). K2-NPs constructed with three different MCs (mcEF1-BDNF-IRES-GFP, mcEF1-TNFR-IRES-GFP, and mcCMV-TNFR-IRES-GFP) resulted in particles with an average size of 82.7±3.47 nm. In comparison, K2-NP formulated with the three corresponding RPs (pEF1-BDNF-IRES-GFP, pEF1-TNFR-IRES-GFP, and pCMV-TNFR-IRES-GFP) resulted in particles with an average size of 102.0±7.0 nm. Particles formulated with the 14kb phTERT construct resulted in particle size of 122.4±6.4 nm.

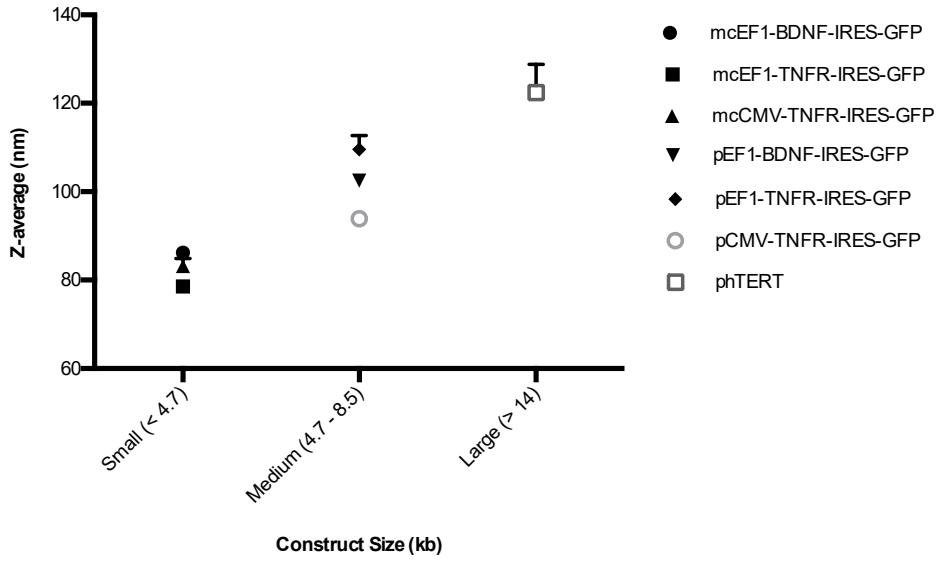

Figure 6.1 Effect of construct size have on the particle size of K2-NP. Construct size falls in three main size ranges: small, medium, and large. Values expressed as mean ± s.d., n=3

Particle size comparison showed that NPs formulated with the MC version of the same expression cassette also consistently resulted in smaller NPs compared to its RP counterparts in K2-NP system (Figure 6.2).

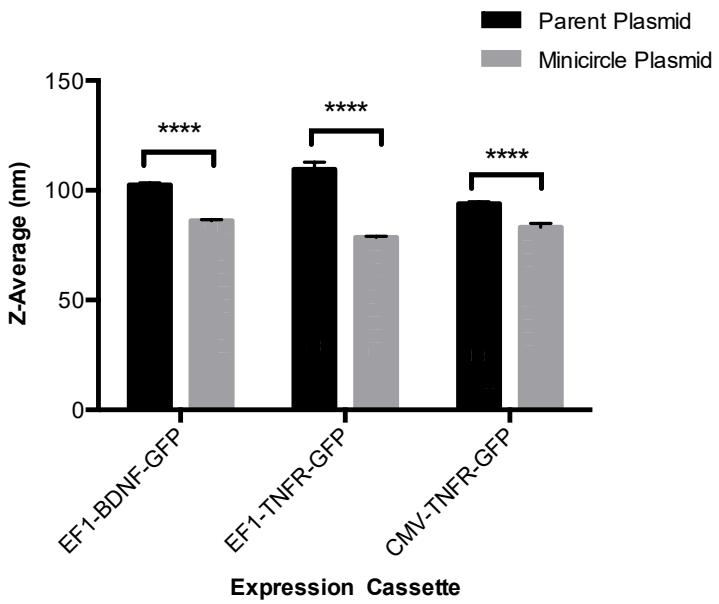

Figure 6.2 Particle size comparison between K2-NPs formulated with either RPs or its corresponding MCs. Values expressed as mean ± s.d., n=3

6.4.2 Effect of pDNA construct size on GL-NP physicochemical properties

To evaluate the impact MCs have on the physicochemical properties of GL-NPs, two sets of GL-NPs were constructed for evaluation: 18-3-18 and 16-3-16 GL-NPs formulated with either RP (gWiz™ GFP; 5.7kb) or with MC (pUMVC1; 4.0kb). 18-3-18 GL-NPs formulated with either RP or MC both resulted in similar particle sizes of 140.4±1.1 nm and 151.3±0.8 nm, respectively (Figure 6.3). Similarly, 16-3-16 GL-NPs formulated with either RP or MC resulted in similar particle sizes of 136.3±1.3 nm and 143.6±1.1 nm, respectively. Particle size uniformity amongst the particles were consistently high amongst the GP complexes and GL-NPs, and largely remained highly similar between RP and MC counterparts with the exception of 16-3-16 GL-NPs, where a larger difference of PDI were observed between RP and MC containing NPs, with values of 0.025 and 0.25, respectively.

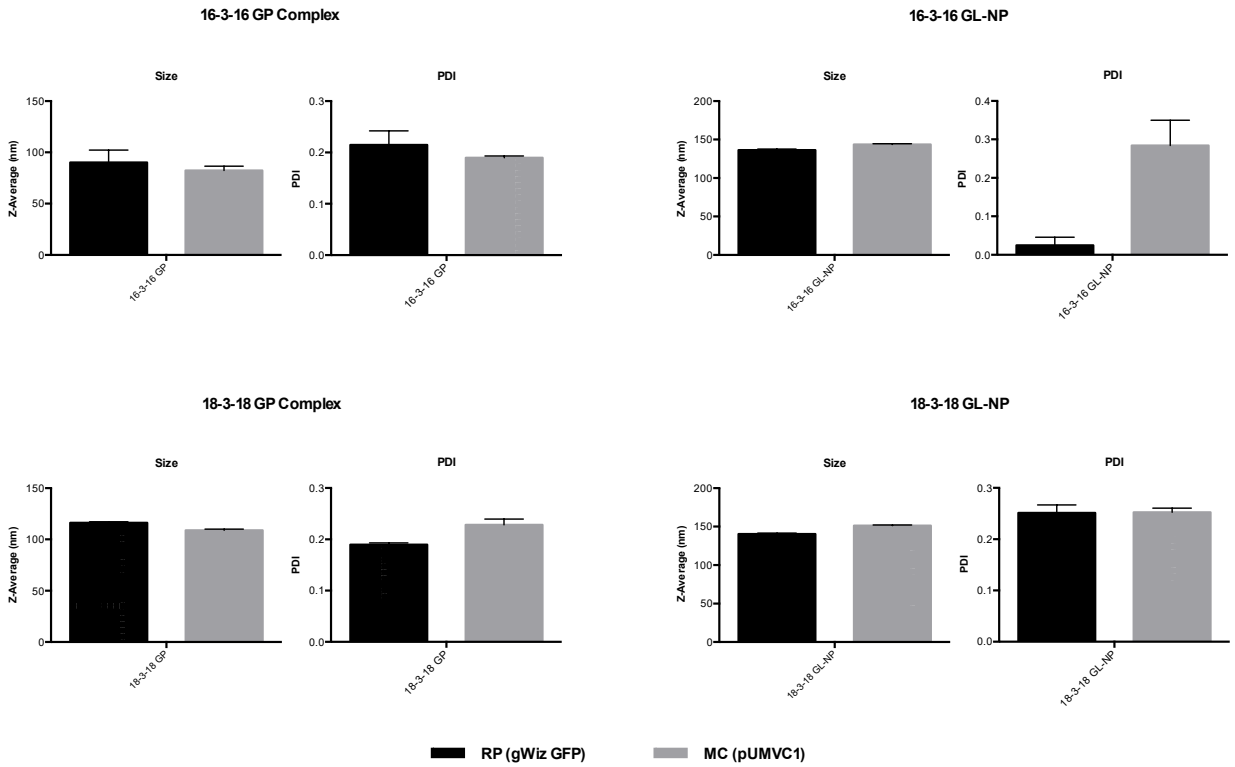

Figure 6.3 Particle size and PDI analysis of 16-3-16 and 18-3-18 GL-NPs formulated with either RP or MC plasmids. Values expressed as mean ± s.d., n=3

6.4.3 Assessment of pDNA in GL-NPs using fluorescence correlation spectroscopy

GL-NPs formulated with either RPs or MCs were further characterized for number of pDNA copy number per particle by FCS between the types of GL-NPs. As FCS utilizes a fluorescence-based spectroscopy technique, the pDNA used in the construction of GL-NPs in this set of experiment were substituted with Cy®5-labelled RP (gWiz GFP-Cy5) and MC (pUMVC1-Cy5). A comparison of RP-containing and MC-containing GP complexes and GL-NPs demonstrated differences in autocorrelation curves (ACC) (Figure 6.4). More specifically, the ACC of MC-containing 16-3-16 GL-NPs indicated a downward shift relative to RP-containing 16-3-16 GL-NPs, suggesting higher number of fluorophores per particle were present in MC-containing GL-NPs compared to RP-containing GL-NPs. On the other hand, the ACC for MC-

and RP-containing 18-3-18 GL-NPs indicated no shifting of the curve, suggesting that differences in the number of fluorophores per particle were not detectable.

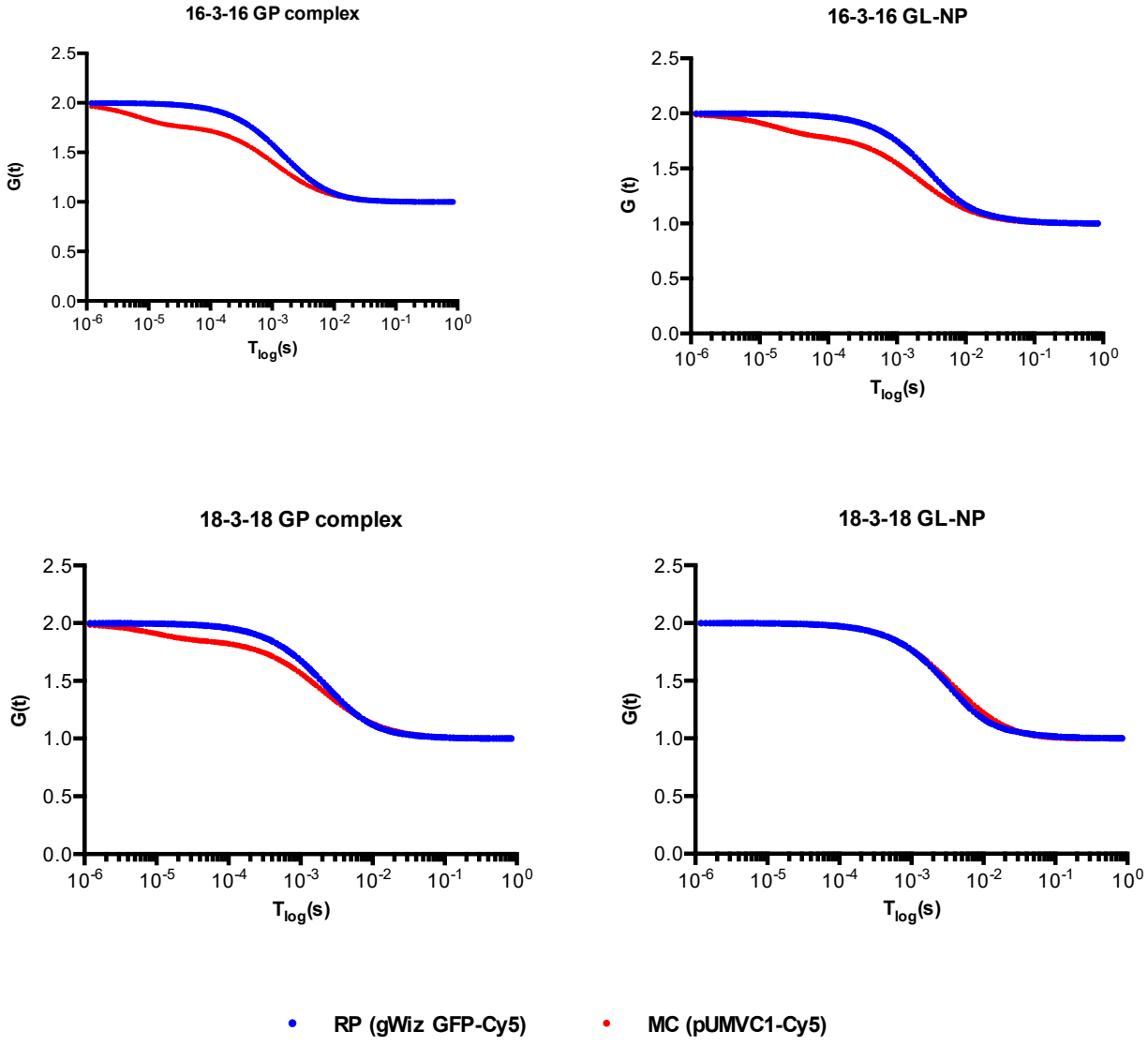

Figure 6.4 Autocorrelation curve analysis of RP- and MC-containing 16-3-16 and 18-3-18 GP complexes and GL-NPs

An analysis of counts per particle (kHz) measurements for free Cy®5 and Cy®5-labelled RP- and MC-containing GL-NPs indicated that 16-3-16 GL-NPs contained 1-8 copies of RPs or 1-6 copies of MCs (Table 6.2). On the other hand, 18-3-18 GL-NPs contained 1-10 copies of RPs and 1-9 copies of MCs. A further analysis of the distribution of plasmid copy number per particle of GL-NPs showed that specific GL-NPs such as MC-containing GL-NPs may result in particles with more homogenous pDNA copy number per particle compared to RP-containing GL-NPs (Figure 6.5). For example, 84% of MC-containing 18-3-18 GL-NPs contained 1 to 3 copies of MCs per particle, and only 16% of particles contained more than 3 copies of MCs per particle. On the other hand, only 51% of RP-containing 18-3-18 GL-NPs contained between 1 to 3 copies of RPs, and 49% of particles contained more than 3 copies of RPs.

Table 6.2 Estimation of the number of pDNA per GL-NPs from FCS data. Averages are expressed as mean ± s.d., n=3

		16-3-16 GL-NP gWiz™ GFP-Cy®5 (RP)	**16-3-16 GL-NP pUMVC1-Cy®5 (MC)**	**18-3-18 GL-NP gWiz™ GFP-Cy®5 (RP)**	**18-3-18 GL-NP pUMVC1-Cy®5 (MC)**
Plasmid copy per particle	Minimum	1	1	1	1
	Maximum	7	6	10	9
	Average	2.33±1.35	1.61±0.88	3.77±2.05	2.23±1.54

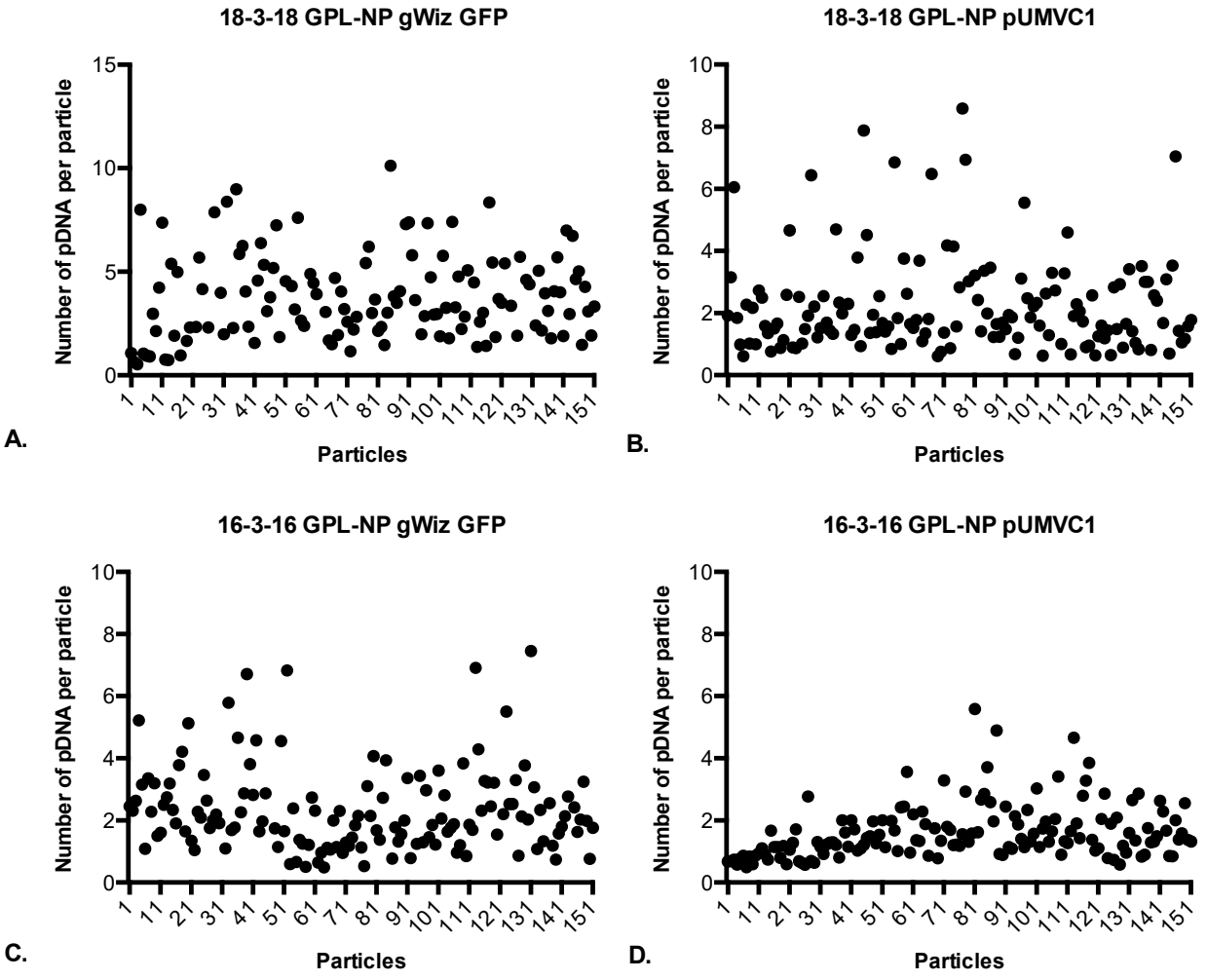

Figure 6.5 Estimation of number of pDNA copy number per RP- (A,C) or MC- (B, D) containing 18-3-18 GL-NPs and 16-3-16 GL-NPs based on average individual counts per particle (kHz)

Using GL-NP diffusion time and diffusion coefficient to derive particle size through Stokes-Einstein equation, hydrodynamic radius for RP- and MC-containing 18-3-18 GL-NPs were estimated to be 878.0 nm and 495.7 nm, respectively (Table 6.3). The hydrodynamic radius of RP- and MC-containing 16-3-16 GL-NPs were 832.9 nm and 377.7 nm, respectively. Interestingly, the calculated hydrodynamic radius showed that RP-containing 16-3-16 and 18-3-18 GL-NP were consistently larger than the MC-containing 16-3-16 and 18-3-18 GL-NP, which correlated with the larger number of RPs found in GL-NPs. The FCS-derived hydrodynamic radius for these particles were larger than the actual measure particle sizes by zetasizer.

Table 6.3 16-3-16 and 18-3-18 GL-NPs particle size calculation extrapolated from FCS measurements using Stokes-Einstein equation

Nanoparticle	Diffusion time (µs)	Mean diffusion coefficient (10^{-11} m^2/s)	Hydrodynamic radius (nm)
16-3-16 GL-NP gWiz™ GFP-Cy®5	5330.109	2.93E-12	832.9
16-3-16 GL-NP puMVC1-Cy®5	2417.128	6.46E-12	377.7
18-3-18 GL-NP gWiz™ GFP-Cy®5	5619.077	2.78E-12	878.0
18-3-18 GL-NP pUMVC1-Cy®5	3172.176	4.93E-12	495.7

6.4.4 GL-NP formulation optimization by sonication

The currently used GL-NP formulation protocols in our laboratory (see section 4.3.3) yields NPs with average particle sizes and PDIs, in ranges of 100-500 nm and 0.2-0.6, respectively, depending on composition. However, improvement of size distribution and reduction of aggregation still would be useful. Hence, sonication and high-pressure homogenization were tested to determine whether better particle uniformity can be achieved. Various sonication and homogenization conditions were evaluated to determine the optimum conditions. Using 12-3-12 GL-NPs as the model GL-NP system, bath sonication for 15, 30, and 60 minutes, or high-pressure

homogenization (one- or two-passes) were evaluated (Figure 6.6). Based on the results, 15-minutes sonication was the optimal sonication time as it reduced 12-3-12 GL-NP particle size by 60%, from 415.6±20.2nm to 167.1±1.2 nm, compared to non-sonicated particles. The homogeneity of particle size distribution has also improved after 15-minutes of sonication as PDI was reduced by about 40%, from 0.36±0.05 to 0.22±0.01, compared to non-sonicated particles. While extending the durations into 30- or 60-minutes sonication periods still resulted in smaller particle sizes compared to non-sonicated GL-NPs, the particle size and particle size heterogeneity have increased compared to particles sonicated for 15 minutes. Sonication for 30 or 60 minutes resulted in particle size of 194.4±4.9 nm and 226.5±6.5 nm, which was 16 % and 36% larger than the particle size of GL-NPs sonicated for 15 minutes. PDI also increased from 0.22±0.01 to 0.33±0.03 and 0.37±0.01 for 30- and 60-minutes-sonicaed particles, which increased by approximately 49% and 71% compared to 15-minutes sonicated particles.

High-pressure homogenization had little benefit to improve particle size and particle size homogeneity as one-pass and two-pass homogenization resulted in particle size of 348.6±13.0 nm and 3030.0±251.7 nm, respectively. Corresponding PDI values also increased from 0.36±0.05 to 0.38±0.02 and 0.43±0.18 after one-pass and two-pass high-pressure homogenization, respectively. The results demonstrated that particle size heterogeneity increased after high-pressure homogenization.

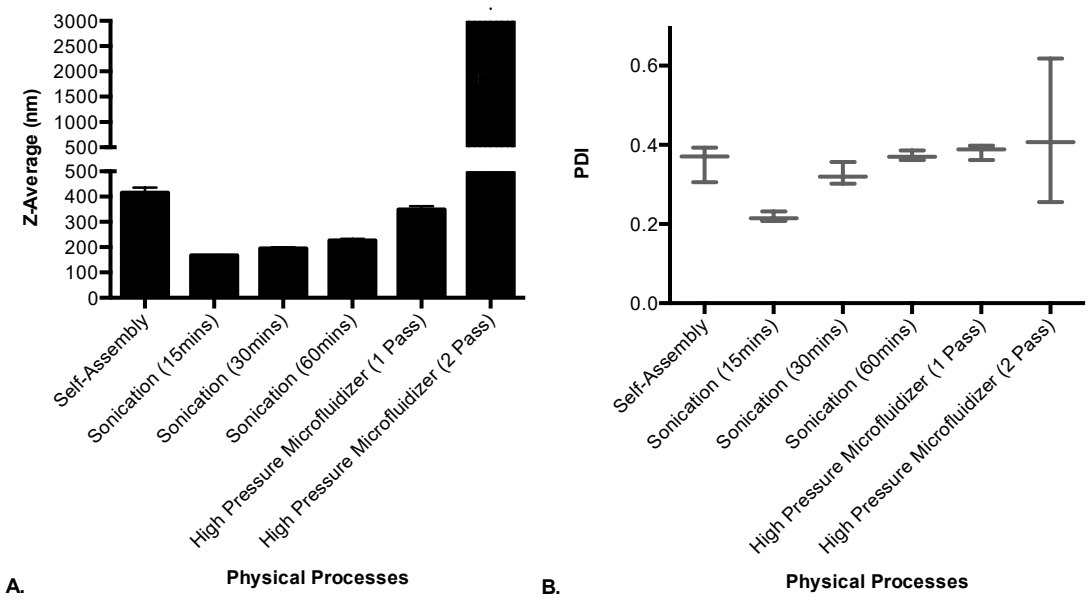

Physical Processes	Z-average (nm)	PDI
Self-Assembly	415.5±20.2	0.36±0.05
Sonication (15 minutes)	167.1±1.2	0.22±0.01
Sonication (30 minutes)	194.4±4.9	0.33±0.03
Sonication (60 minutes)	226.5±6.5	0.37±0.01
High-Pressure Homogenization (one-pass)	348.6±13.0	0.38±0.02
High-Pressure Homoegnization (two-passes)	3030.0±251.7	0.43±0.18

Figure 6.6 12-3-12 GL-NP treated with either sonication or high-pressure microfluidic homogenization 1-hour post self-assembly. Values expressed as mean ± s.d., n=3

An analysis on the particle size polydispersity index (Figure 6.7) showed the change in GL-NP population size distribution after sonication and homogenization. Prior to any further processing, self-assembled GL-NPs showed bimodal population distribution with peaks at 601.2 nm (83%) and 140.4 nm (16%). Upon 15 minutes of sonication, the bimodal distribution resulted in unimodal distribution with a single peak presented at 224.9 nm, which demonstrated a rather homogenous population. Further induction of sonication for a total of 30 minutes resulted in a shift of the unimodal distribution towards bimodal distribution with the rise of a secondary peak, with a new distribution profile of two peaks at 232.7 nm (95%) and 4717.0 nm (5%). Sonication for a total duration of 60-minutes resulted in the bimodal distribution profile with similar proportions

compared to 30-minutes sonication. Collectively, it was evident that 15-minutes sonicated 12-3-12 GL-NPs was the most optimal condition to generate optimal particle size and particle size homogeneity amongst the conditions tested.

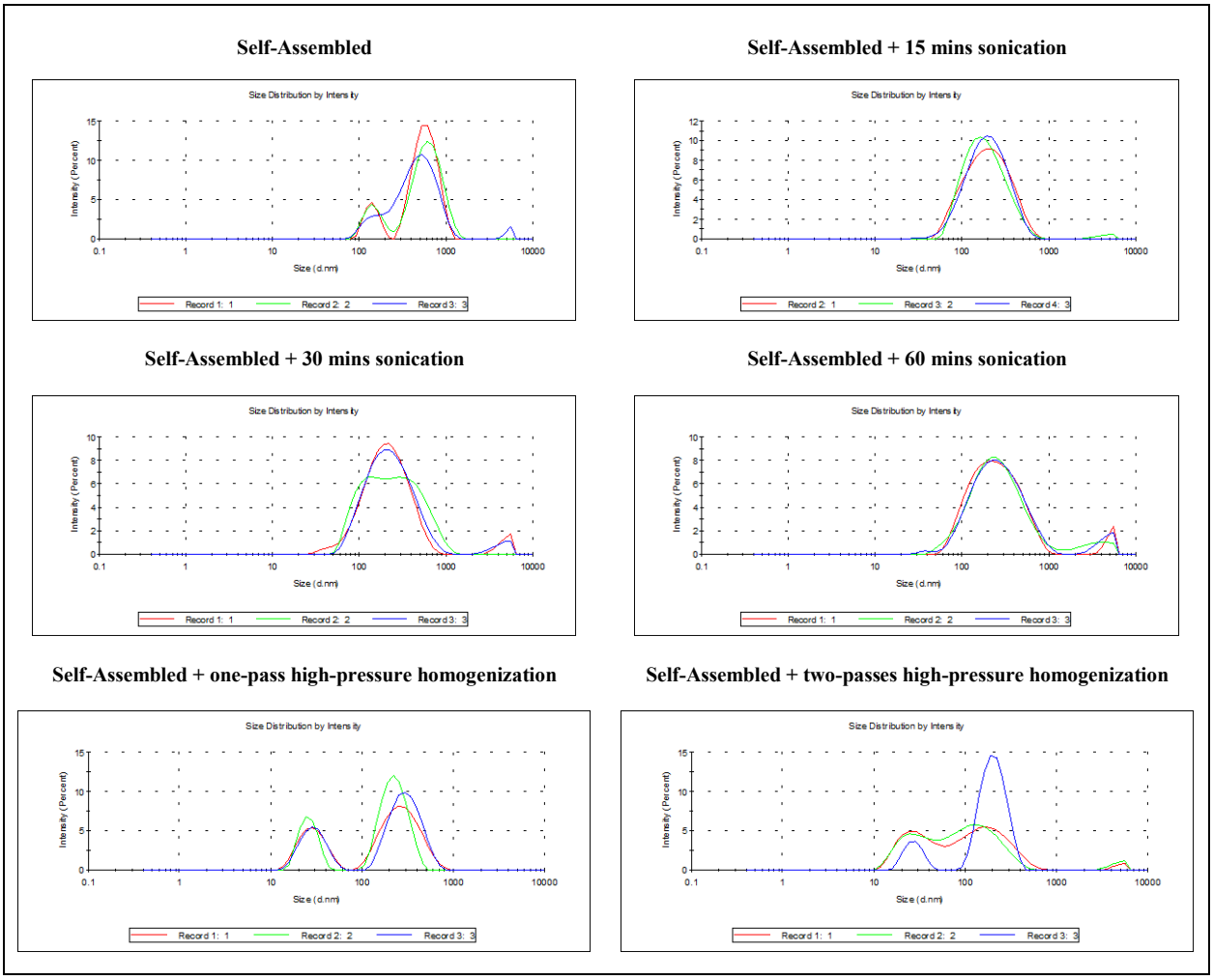

Figure 6.7 Particle size distribution profile for 12-3-12 GL-NPs after sonication or homogenization

6.4.5 GL-NP optimization by TNPC

The effect of TNPC per unit volume on NP physicochemical properties was also evaluated as different concentrations of NP formulations are often needed to accommodate the administration volume limitation that are specific to the route of administration. Furthermore, it also allows for the determination of optimal NP concentrations that can be utilized in the manufacturing process to generate GL-NPs with optimal physicochemical properties through concentration adjustments. In order to evaluate the effect of TNPC have on the NP physicochemical properties, RP- and MC-containing 12-3-12 and 16-3-16 GL-NPs with two different GL-NP concentrations (1X [= routinely used concentration] or 2X [= two times the routinely used starting concentration of all components]) were formulated. Thus, resulting in 1X-TNPC and 2X-TNPC particles for each of the following GL-NPs: RP-containing 12-3-12 GL-NPs, MC-containing 12-3-12 GL-NPs, RP-containing 16-3-16 GL-NPs, and MC-containing 16-3-16 GL-NPs.

Based on the results, GL-NPs formulated with 2X-TNPC consistently generated smaller 12-3-12 GL-NPs and 16-3-16 GL-NPs (Figure 6.8). For example, both 2X-TNPC RP-containing 12-3-12 GL-NPs and 16-3-16 GL-NPs resulted in smaller particle size compared to 1X-TNPC RP-containing 12-3-12 GL-NPs and 16-3-16 GL-NPs with differences of 33.3% and 63.0%, respectively. Similarly, 2X-TNPC MC-containing 12-3-12 GL-NPs and 16-3-16 GL-NPs resulted in smaller particle size compared to 1X-TNPC MC-containing 12-3-12 GL-NPs and 16-3-16 GL-NPs, with average differences of 20.4% and 22.3%, respectively. The particle size distribution for 2X- and 1X- TNPC GL-NPs resulted in similar levels of homogenous particle size distribution as described by unimodal particle size distribution (Figure 6.9) and PDI ranged between 0.20 and 0.28.

In terms of particle surface charge, zeta potential measurements showed increase in zeta potential in GL-NPs constructed at 2X-TNPC compared to GL-NPs constructed at 1X-TNPC. More specifically, 2X-TNPC RP-containing 12-3-12 GL-NPs and 16-3-16 GL-NPs resulted in higher zeta potential compared to 1X-TNPC RP-containing 12-3-12 GL-NPs and 16-3-16 GL-NPs with differences of 19.5% and 12.8%, respectively. Similarly, 2X-TNPC RP-containing 16-3-16 GL-NPs and 2X-TNPC MC-containing 16-3-16 GL-NPs resulted in higher particle surface charge compared to their respected 1X-TNPC counterparts. Altogether, these findings showed that changes in GL-NP concentration could result in changes in the physicochemical properties of GL-NPs. Furthermore, 2X-TNPC GL-NPs could result in the generation of GL-NPs with smaller particle size and higher surface charge amongst different GL-NP systems.

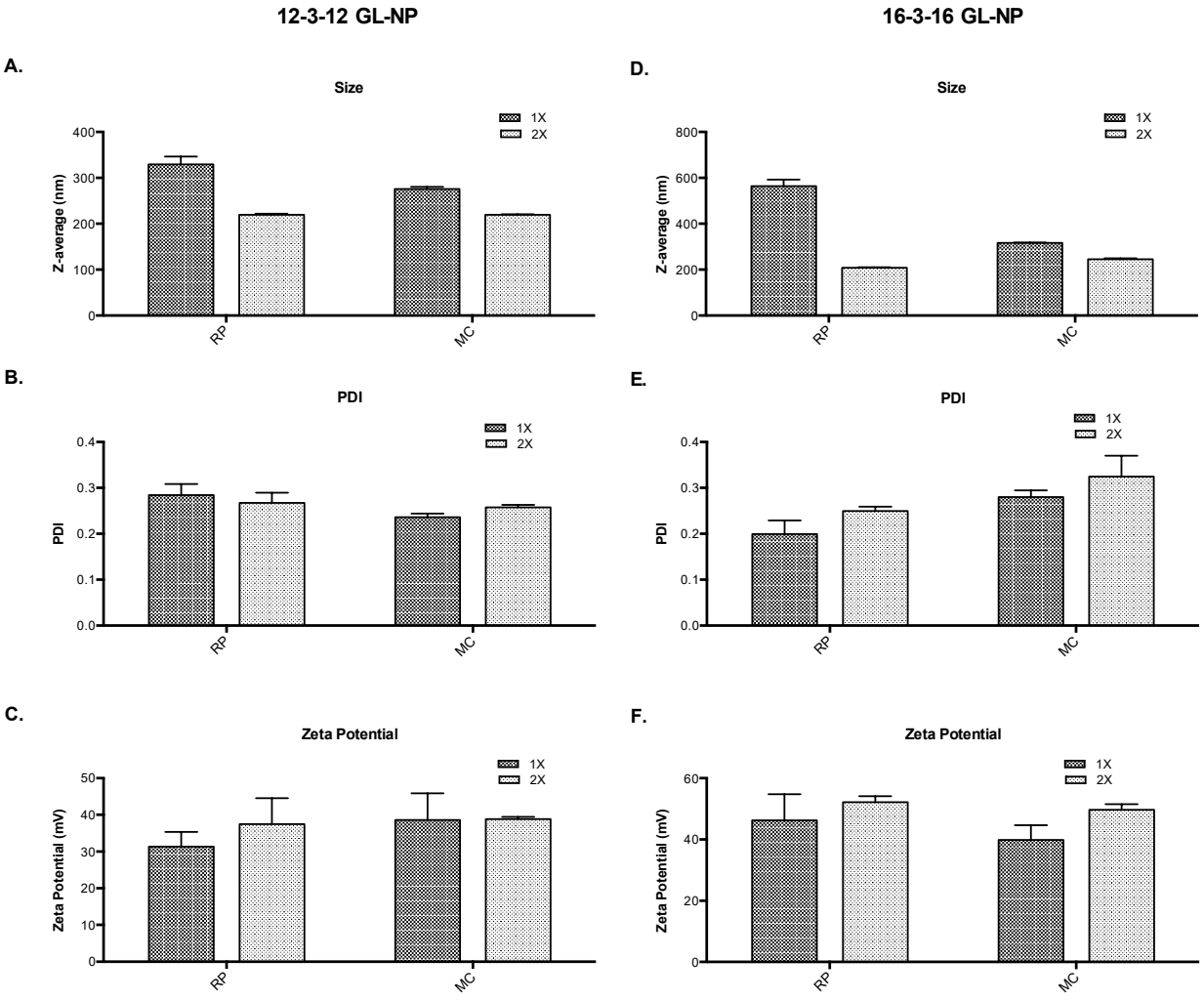

Figure 6.8 Physicochemical characterization of 12-3-12 (A-C) and 16-3-16 (D-F) GL-NPs formulated at 1X-TNPC or 2X-TNPC with either RP or MC. Values expressed as mean ± s.d., n=3

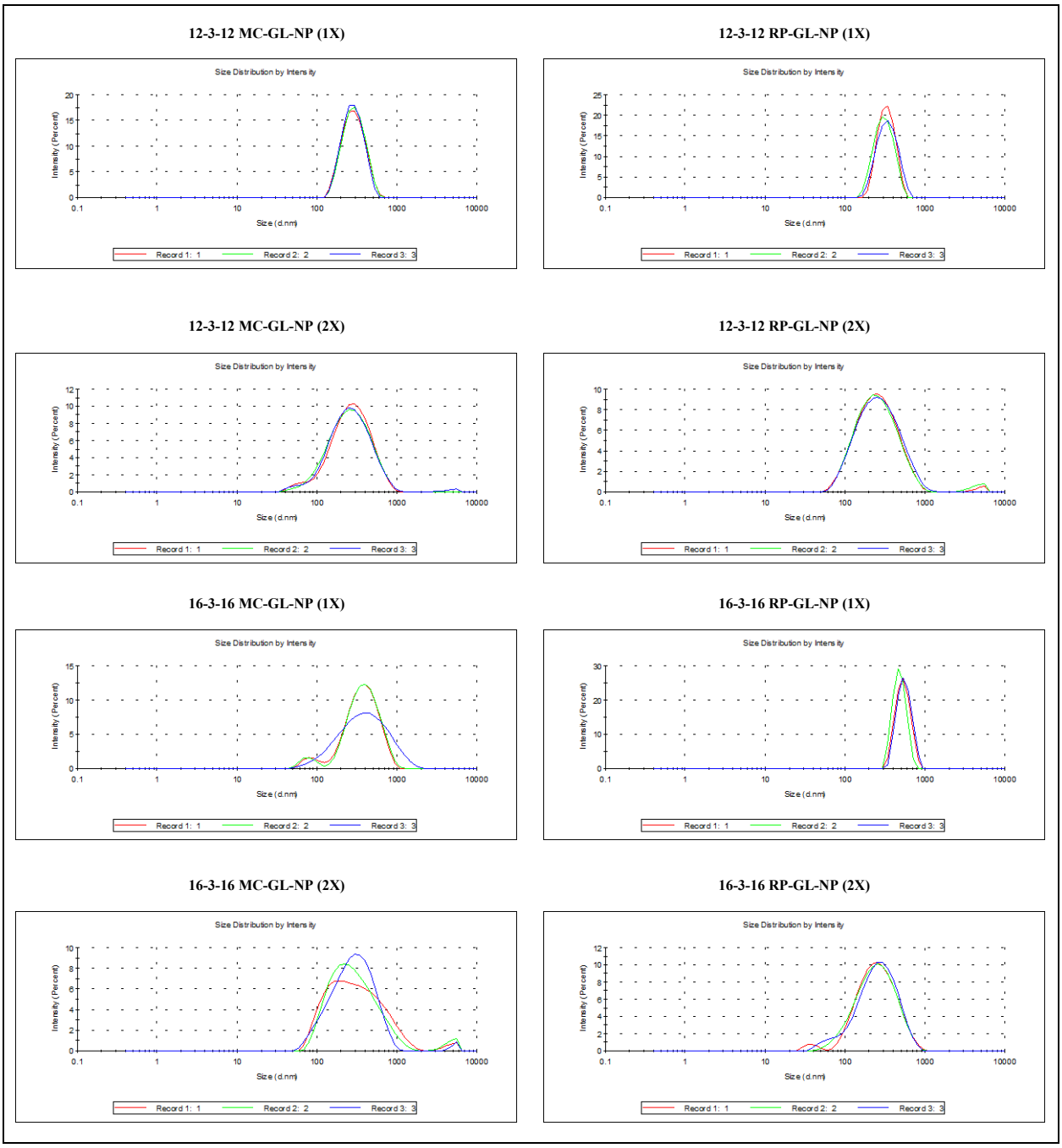

Figure 6.9 Particle size distribution analysis of 12-3-12 and 16-3-16 GL-NPs formulated at 1X-TNPC or 2X-TNPC with either RP or MC

6.4.6 GL-NP optimization by combination of sonication and TNPC

Based on the earlier investigation of sonication and TNPC effects on GL-NP physicochemical properties, it was evident that these processes could be evaluated for a variety of GL-NPs. A panel of first-generation and second-generation GL-NPs were generated: 12-3-12, 12-4-12, 12-6-12, 12-8-12, 12-10-12, 12-12-12, 12-16-12, 16-3-16, 18-3-18, 12-7NH-12, 12-7N-12, and Py-3-12. The twelve different GL-NPs were formulated at two concentrations (1X-TNPC and 2X-TNPC), and 15 minutes of sonication processing.

Nine out of twelve GL-NPs formulated at 2X-TNPC compared to 1X-TNPC GL-NPs resulted in smaller particle size (Figure 6.10). More specifically, the 12-*m*-12 series GL-NPs (with the exception of 12-7NH-12) formulated at 2X-TNPC consistently resulted in smaller particle size. In contrast, 16-3-16, 18-3-18, and 12-7NH-12 GL-NPs all exhibited a larger particle size. In addition to particle size, the particle size homogeneity was also found to have increased in eight out of twelve GL-NPs prepared in 2X-TNPC (Figure 6.12), evident from reduction of PDI and the presence of unimodal particle size distribution pattern compared to 1X-TNPC (Figure 6.11). Except for selected GL-NPs such as 12-8-12, 12-7NH-12, and Py-3-12 GL-NPs, PDI was found to have increased instead. In terms of particle surface charge, an increase in particle surface charge was observed in GL-NPs prepared by 2X-TNPC compared to 1X-TNPC in ten out of twelve GL-NPs, except for 12-7NH-12 and 12-7N-12 GL-NPs, where a decrease in zeta potential was detected.

Table 6.4 Physicochemical characterization of GL-NP (1X- or 2X- TNPC) formulated with 12-s-12, m-3-m, and Py-3-12 using RP. Z-average (A), PDI (B), and zeta potential (C). Values expressed as mean ± s.d., n=3

Conditions/Properties		**GL-NPs**						
TNPC	**Properties**	**12-3-12**	**12-4-12**	**12-6-12**	**12-8-12**	**12-10-12**	**12-12-12**	**12-16-12**
1X	Z-average (nm)	275.8±7.2	194.8±1.6	250.9±5.0	240.1±2.9	233.7±1.5	233.4±3.1	228.0±3.4
	PDI	0.38±0.01	0.37±0.01	0.28±0.01	0.37±0.02	0.39±0.01	0.38±0.01	0.30±0.02
	Zeta Potential (mV)	31.1±1.2	21.8±0.5	28.1±2.7	13.6±0.8	32.8±4.5	36.3±1.1	40.2±2.6
2X	Z-average (nm)	173.0±0.8	185.4±0.7	130.1±0.6	175.5±1.2	172.2±2.2	174.9±1.1	159.9±1.1
	PDI	0.16±0.00	0.22±0.01	0.26±0.00	`0.42±0.00	0.31±0.01	0.36±0.04	0.28±0.00
	Zeta Potential (mV)	46.0±1.6	29.3±6.4	39.1±4.4	44.1±1.3	46.8±5.1	53.2±4.5	57.1±2.9
Conditions/Properties		**GL-NPs**						
TNPC	**Properties**	**16-3-16**	**18-3-18**	**12-7NH-12**	**12-7N-12**	**Py-3-12**	-	-
1X	Z-average (nm)	135.9±3.3	433.2±126.8	204.7±1.5	222.8±1.8	168.8±2.3	-	-
	PDI	0.20±0.01	0.35±0.16	0.16±0.02	0.14±0.02	0.20±0.01	-	-
	Zeta Potential (mV)	36.7±0.4	55.5±4.3	39.9±2.1	41.2±5.9	34.6±0.1	-	-
2X	Z-average (nm)	166.1±6.2	439.9±38.3	242.3±4.5	204.6±3.2	131.6±1.6	-	-
	PDI	0.13±0.03	0.26±0.08	0.19±0.05	0.10±0.04	0.26±0.00	-	-
	Zeta Potential (mV)	57.3±3.8	56.1±0.5	22.1±2.3	31.7±9.5	38.5±6.9	-	-

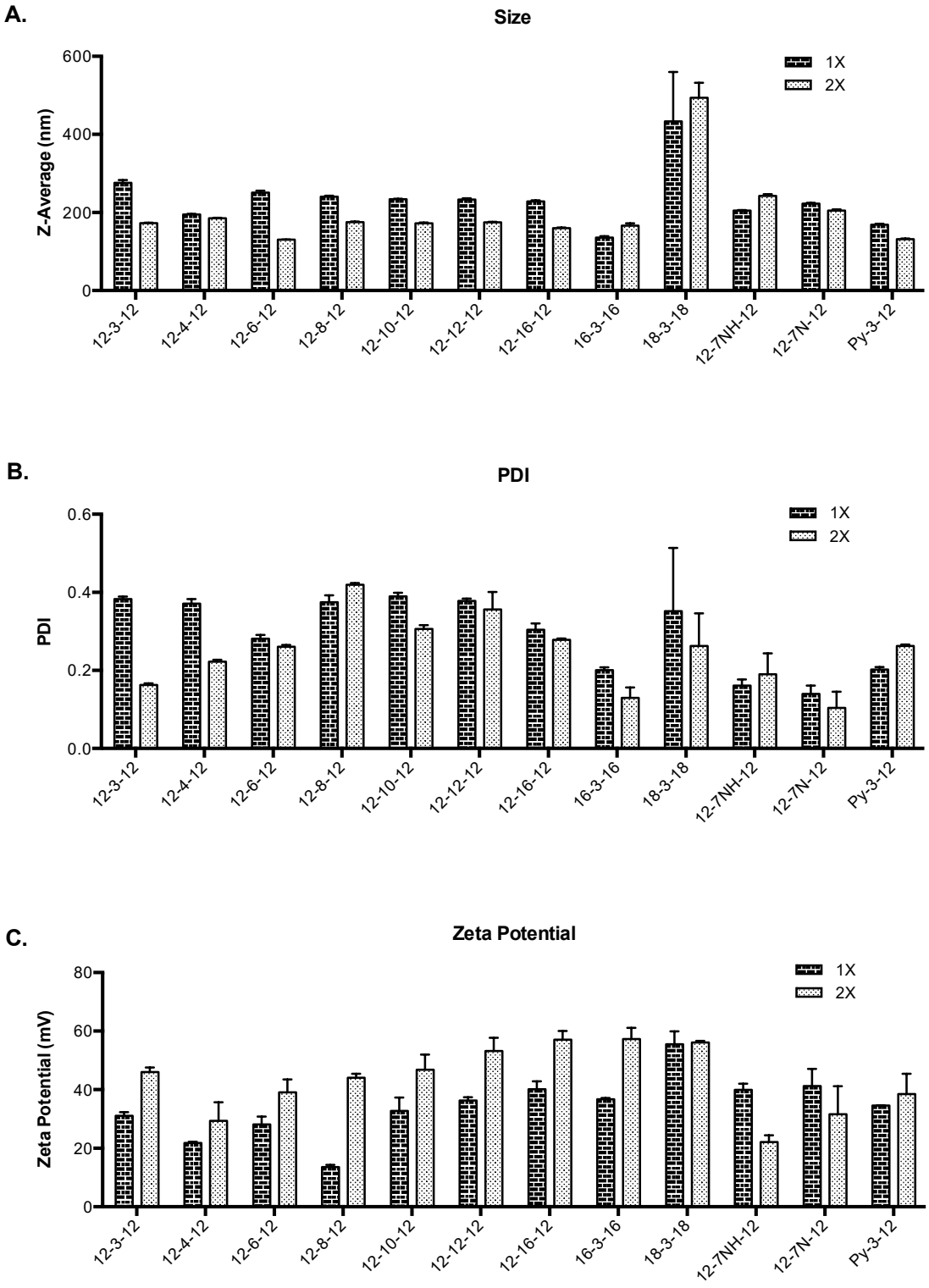

Figure 6.10 Physicochemical characterization of RP-GL-NPs formulated with 12-s-12, m-3-m, and Py-3-12 at either 1X- or 2X- TNPC. Z-average (A), PDI (B), and zeta potential (C). Values expressed as mean ± s.d., n=3

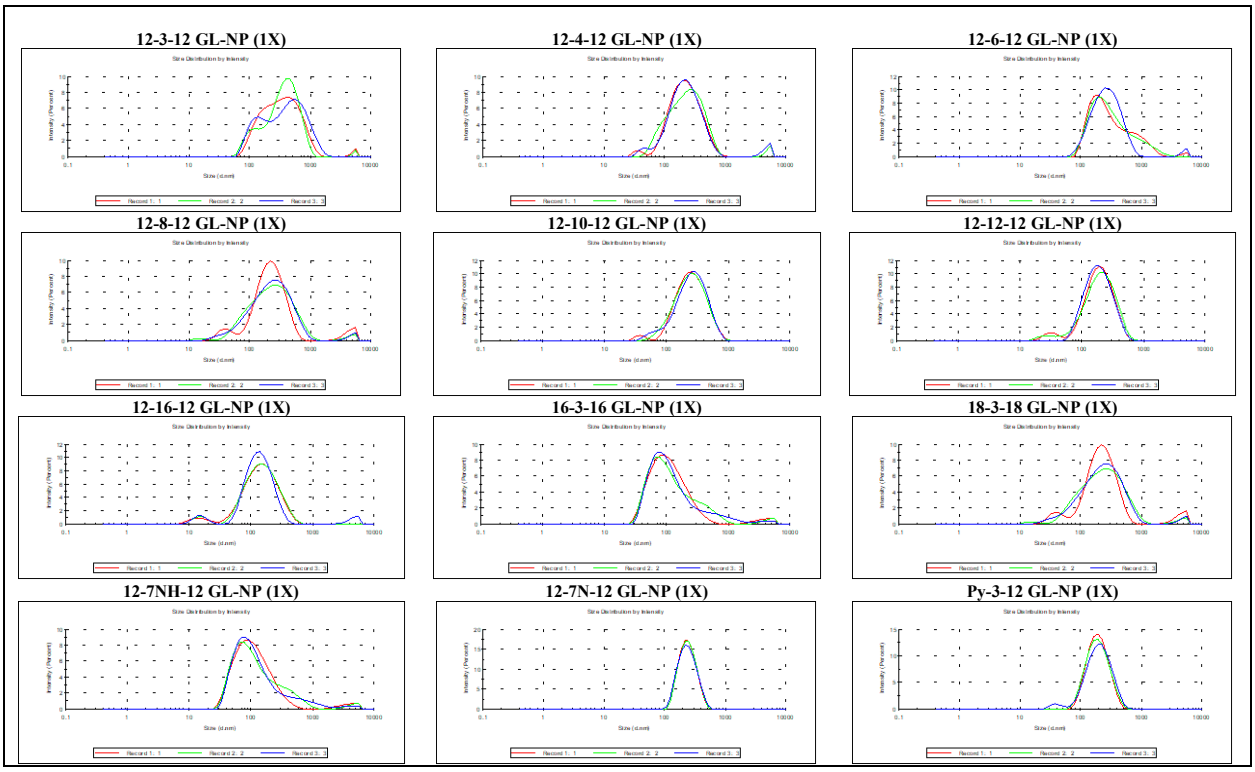

Figure 6.11 Particle size distribution profile of GL-NPs formulated with 12-s-12, m-3-m, and Py-3-12 at 1X-TNPC

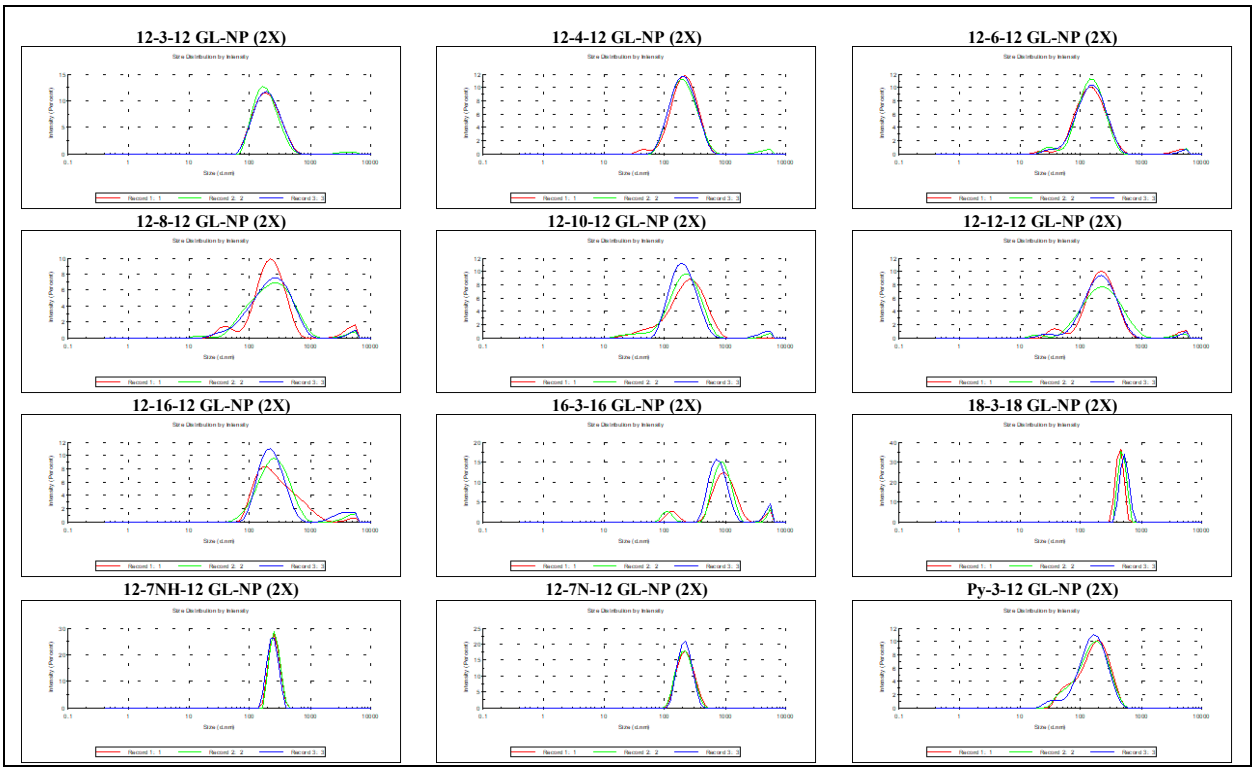

Figure 6.12 Particle size distribution profile of GL-NPs formulated with 12-s-12, m-3-m, and Py-3-12 at 2X-TNPC

6.5 Discussion

The incorporation of MC in NPs is a promising approach towards the development of more efficient gene therapy systems as MC can provide a safer and more effective means of encoding therapeutic protein sequences for pDNA gene therapy applications. The absence of the bacterial backbone not only decreases overall construct size, but it also reduces the risk of unwanted immunogenic responses. Aside from this, another important aspect of MC is the potential improvement of the physicochemical properties of NPs. As shown in the results, MC incorporation resulted in smaller K2-NPs and improved the TE when compared to its RP counterparts. Furthermore, GL-NPs constructed with MC were able to generate more GL-NPs with more homogenous pDNA copy number per particle. Interestingly, it was found that RP-containing GL-NPs have more plasmid per particle on average compared to MC-containing GL-NPs. One explanation could be the influence of Cy®5 (M.W.= 761.38g/mol) labelling on pDNA, where the presence of Cy®5 fluorophores on pDNA could have resulted in differences in nucleic acid coiling and pDNA-GS electrostatic interaction in the GL-NP system. Moreover, the number of Cy®5 present on gWiz GFP-Cy5 (n=10.930±0.605 fluorophores per plasmid) and pUMVC1-Cy5 (n=47.215±7.693 fluorophores per plasmid), could also contributed to changes in GL-NP complexation properties. A higher pDNA copy number per particle in RP-containing GL-NPs further correlates with the finding that the particle size of RP-containing GL-NPs is larger than MC-containing GL-NPs. Nonetheless, the estimated number of plasmids in the GL-NPs was found to be in the range between 1 to 10 pDNA, which falls in the range of plasmid number count reported by Dong et al. [193]. Future pDNA quantitation could focus on optimizing Cy®5 labelling efficiency down to single Cy®5 per pDNA in order to generate a more representative modeling and estimation of plasmid construct copies in GL-NPs.

pDNA copy number was suggested in many studies to be associated with the outcome of transgene expression in gene transfer. Nuclear pDNA copy number was suggested to influence the level of transgene expression in a study that investigated the copy number required for successful transgene expression using lipid-based (Lipofectamine™) and polymer-based (PEI) NPs [194]. This study showed that on average, each transfected nucleus contained 75 to 50,000 copies of pDNA. Furthermore, it was suggested that there might be a pDNA copy threshold within the nucleus for transgene expression as pDNA copy numbers beyond 3,000 copies per nucleus only marginally elevated subsequent gene expression. A subsequent comparison showed that 2817 and 876 copies of pDNA per nucleus was found in high-expressing and low-expressing cells, respectively, where high-expressing cells expressed 2-fold more proteins than the low-expression population [194]. Intracellular trafficking studies have suggested that dissociation of pDNA from the cationic polymer complexes is not a necessity for nuclear entry [195]. Furthermore, one possible mechanisms of nuclear entry may be associated with the anionic groups of phospholipid or lysosomal membrane that may have complexed with pDNA or NP components throughout the process prior to nuclear entry [195]. As smaller constructs may result in smaller NPs, it is also possible that particles could dissociate into smaller pDNA-nanomaterial (pDNA-nano) complexes, which may improve nuclear entry through the nuclear pores or nuclear membrane fusion capacity. In a recent study, it was found that most of the pDNA delivered with NPs were localized in cytoplasm, and the majority of pDNA remained bound to components of the NPs, which suggests that a significant number of pDNA entering the nucleus were bound to some amounts of nanomaterial. Dissociated pDNA-nano complexes that are less than 26 nm may improve the nuclear entry of pDNA into the nucleus [184].

Previous studies in our laboratory have investigated the physicochemical properties of GL-NPs with different assembly order of pDNA, GS, and lipids. The rationale behind the approach of sonicating assembled GL-NPs was to introduce external forces that may possible results in the formation of smaller particle. Based on the shift in particle size distribution profile from a bimodal distribution to a unimodal distribution shown in the results, it suggests that sonication may induce a systematic structural rearrangement of the GL-NP systems. Further sonication beyond 15 minutes resulted in the formation of macroaggregated populations, which indicates that excess sonication is deleterious to optimal complexation and colloid stabilization. In addition, the finding that NP formulation concentration could improve the physicochemical properties of GL-NPs shows that TNPC is an important factor of consideration in GL-NP manufacturing.

6.6 Conclusion

In summary, the results have shown that pDNA construct size can also improve the physicochemical properties of GL-NPs. Furthermore, it was identified that sonication and TNPC were two parameters that could improve GL-NP physicochemical properties, which could be considered for incorporation into future GL-NP formulation development.

Chapter 7 Development of GS-functionalized carbon nanotube for pDNA delivery to retinal cells

7.1 Rationale and objective

In addition to GL-NP systems development, our laboratory also concurrently explores other novel nanomaterial entities that may have the potential to be utilized as gene delivery vehicles. CNTs are one of the candidate nanomaterials that are capable of binding nucleic acids and could be utilized in gene delivery applications.

7.2 Background

CNTs are a novel class of carbon-based nanomaterials with unique electronic, mechanical, and optical properties that can be utilized for a wide range of biomedical and pharmaceutical applications [196, 197]. CNTs can be broadly divided into two main types based on the number of graphene layers that constitute the cylindrical tube structure of CNTs into single-wall carbon nanotubes (SWNT) and multi-wall carbon nanotubes (MWNT) [198]. CNTs were explored for a variety of pharmaceutical and biomedical applications [199-206]. In the scope of gene therapy applications, CNTs have also been heavily explored as promising candidate gene delivery systems in studies that demonstrated their ability to interact with and compact nucleic acids [207-209], provide protection to nucleic acids from enzymatic degradation [210], and achieve cellular delivery for transgene expression [211].

Given the hydrophobic nature of CNTs, one of the main areas of development for pharmaceutical applications involves solubilizing nanotubes into solution, in order to complex with therapeutic molecules and carry out therapeutic action. Solubilization can be achieved through surface modifications of CNTs, which can result in functionalized carbon nanotubes (f-CNTs) containing moieties that reduce the hydrophobicity and aid solubilization. The use of

surfactants to functionalize and solubilize CNTs were explored using various non-ionic, cationic, anionic, and mixed surfactants [212-218]. Of particular interest in our laboratory, cationic gemini surfactant (GS) are effective in dispersing CNTs through hydrophobic interactions between the carbon alkyl chain and CNT walls. The cationic nature of the GS may provide an enhanced interaction between *f*-CNT and nucleic acid through electrostatic interactions.

In this study, ptSWNTs was utilized as the CNT candidate and it was found that the SWNTs could be dispersed by non-covalent functionalization with GSs, generating GS-functionalized ptSWNTs (*f*-ptSWNTs) that were able to complex with pDNA. Furthermore, the preliminary results demonstrated the potential of a *f*-ptSWNT gene delivery system for retinal gene therapy applications.

7.3 Materials and methods

7.3.1 Carbon nanotube dispersion and *f*-ptSWNT formulation

PureTubes™ SWNTs (ptSWNT), surfactant-eliminated, was purchased from NanoIntegris Inc (Raymor Industries Inc., Boisbriand, QC, Canada). A 0.1% w/v 12-3-12 surfactant solution was prepared by dissolving 12-3-12 GS in sterile nuclease-free water at a concentration of 1 mg/mL and sonicated. *f*-ptSWNTs were prepared by dispersing ptSWNTs in 0.1% w/v 12-3-12 GS solution at 10 μg/mL and sonicated using a Branson bath sonicator at 40 kHz frequency (Branson Ultrasonics Corporation, Danbury, CT, USA). *f*-ptSWNT-pDNA complexes were constructed by complexing *f*-ptSWNT with gWiz™ GFP pDNA (Aldevron, Fargo, ND, USA) at desired concentrations and ratios for 15 minutes at room temperature.

7.3.2 Transfection of A7 astrocyte cells

A7 rat astrocytes (a gift from Dr Jeremy Sivak, University of Toronto; [109, 110]) were cultured in DMEM/high glucose media (HyClone, GE Healthcare Life Sciences, Logan, Utah,

USA) supplemented with 10% FBS and 1% Pen/Strep at 37 °C in a 95% air and 5% carbon dioxide atmosphere. *f*-ptSWNT-pDNA complexes were first evaluated and optimized in monolayer cultures of A7 astrocytes. Cells were seeded at seeding density of 50,000 cells/well (n=3 each) into clear 24-well culture plates (Grenier Bio-One, Monore, NC, USA) and transfected using *f*-ptSWNT-pDNA complexes. TE and viability was assessed after 24 hours of incubation using the Attune Flow Cytometer (Applied Biosystems, Thermo Fisher Scientific, Waltham, MA, USA). TE was measured based on GFP expression and viability was measured based using a mitochondrial activity dye Mitotracker™ Deep Red (Invitrogen™, Thermo Fisher Scientific).

7.4 Results

7.4.1 Dispersion and characterization of ptSWNT in 0.1% 12-3-12 GS solution

ptSWNTs were SWNTs with a mean diameter and length of 1.4 nm and 1 μm, respectively. ptSWNTs, like most CNTs, are hydrophobic as a result of the non-polar aromatic carbon structure. Hence, dispersion of CNTs often involves surface modification of CNTs through addition of polar functionalization. In this experiment, four concentrations of 12-3-12 GS solution (0.1%, 0.05%, 0.01%, 0.005% w/v) were explored for dispersion of ptSWNT 10 μg/mL (0.001% w/v). GS concentration-dependent dispersion was observed with distinct characteristics of dispersion and aggregation (Figure 7.1). Dispersion of ptSWNTs using 0.1% 12-3-12 GS solution was the most effective with no signs of visible particles. In addition, centrifugation and sedimentation tests also demonstrated the absence of aggregates and or sedimentation of *f*-ptSWNTs. Dispersion of ptSWNTs with 0.05% 12-3-12 GS solution produced partially dispersed ptSWNTs. The dispersion was grey with visible ptSWNT particles distributed across the volume. The 0.01% and 0.005% GS solutions were ineffective at dispersing ptSWNTs.

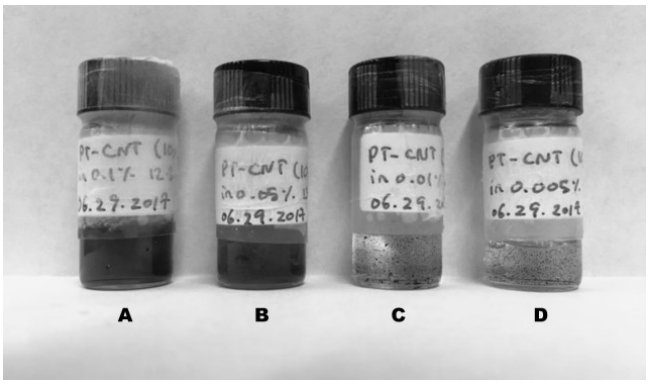

Figure 7.1 ptSWNT dispersions in 0.1% (A), 0.05% (B), 0.01% (C), and 0.005% (D) 12-3-12 GS solution

As ptSWNTs dispersed most optimally using 0.1% w/v 12-3-12 GS solution at 10 µg/mL compared to the other three concentrations tested, further characterization and studies were carried out using *f*-ptSWNTs generated from this condition.

7.4.2 Implications of *f*-ptSWNT-pDNA mediated gene delivery to retinal astrocytes

To evaluate gene delivery capacity of *f*-ptSWNT-pDNA complexes to retinal cells, a series of *f*-ptSWNT-pDNA complexes with different combinations of CNT:DNA ratios were formulated (Figure 7.2). Three measurements were collected in this study: percentage of viable population, TE of the cells in viable population, and metabolic active cells in viable population. Percentage of *viable population* measures the percentage of A7 cells that remained viable and attached on the culture surface after *f*-ptSWNT-pDNA complex treatment. *TE of the viable population* measures the percentage of cells from the viable population that were transfected by *f*-ptSWNT-pDNA complexes. *Metabolically active cells of the viable population* measures the percentage of cells that are metabolically active from the viable population. The reporting of the percentage of viable cells is important in this investigation as it was found that treatment with *f*-ptSWNT-pDNA complexes could result in significant reduction of viable A7 cell population (i.e. cells lost / disintegrated).

In the 1 μg pDNA per dose evaluation, four ratios of *f*-ptSWNT-pDNA complexes were evaluated and it was found that while *f*-ptSWNT-pDNA complexes constructed with a CNT:DNA ratio of 1:1 were able to demonstrate highest level of TE, it also resulted highest level of toxicity (Figure 7.2A). The percentage of viable population was found to be only 25.2±4.6%, demonstrating a toxicity that resulted in approximately 75% A7 cell loss. Amongst the cells that remained viable and attached on culture surface, where 85.3±8.6% of cells were transfected and 83.8±2.7% of cells were metabolically active. Evaluation of *f*-ptSWNT-pDNA complexes constructed with increasing CNT:DNA ratios of 1:2, 1:3, and 1:4 resulted in increasing viable population, and decreasing TE of the viable population. Amongst the 4 ratios, transfection using *f*-ptSWNT-pDNA complexes constructed with CNT:DNA ratio of 1:4 resulted in the highest viable population of 39.1±8.8%, but lowest TE level of 2.1±1.5%.

In the 3 μg pDNA per dose evaluation, the results showed that *f*-ptSWNT-pDNA complexes constructed with increasing CNT:DNA ratios of 1:3, 1:6, 1:9, and 1:12 resulted in increasing viable population from 37.4±8.9% to 54.1±2.5%, but resulted in decreasing TE of the viable population from 54.7±2.6% to 34.4±5.0% (Figure 7.2B). Moreover, the percentage of metabolically active cells from viable population remained in range between 76.7±1.9% and 65.5±3.2%. Interestingly, *f*-ptSWNT-pDNA complexes constructed with CNT:DNA ratios of 1:15 and 1:30 were not able to transfect A7 cells.

In the 5 μg pDNA per dose evaluation, it was found that *f*-ptSWNT-pDNA complexes constructed with increasing CNT:DNA ratios at 1:5, 1:10, 1:15, and 1:20 resulted in increasing viable population between 32.5±5.0% and 65.3±3.3%, with TE of viable population between 55.5±3.5% and 44.5±2.0% (Figure 7.2C). Interestingly, *f*-ptSWNT-pDNA complexes constructed with CNT:DNA ratios of 1:25, 1:50, 1:67 and 1:100 did not transfect the viable cell population.

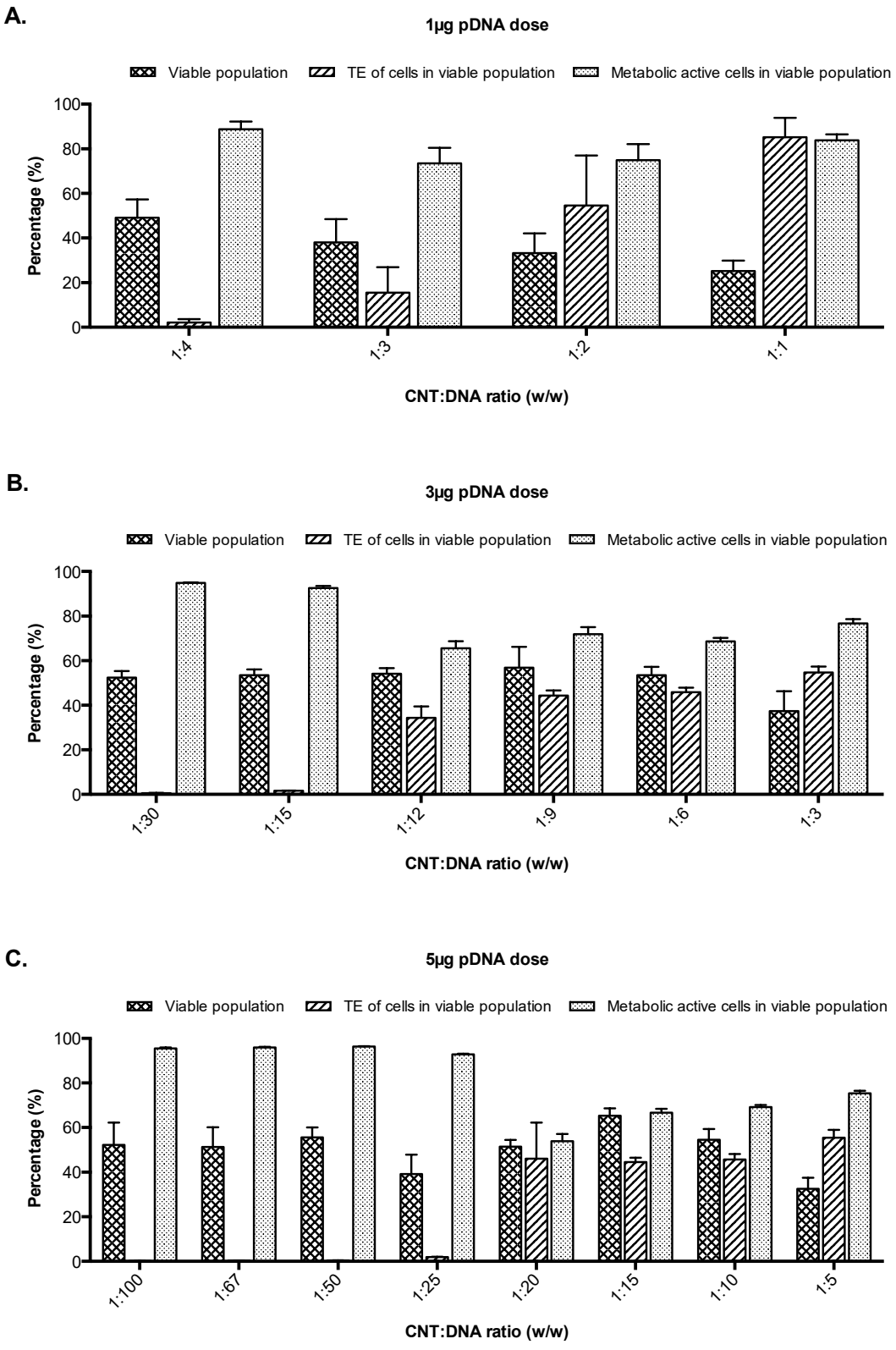

Figure 7.2 TE and viability of A7 astrocytes following transfection with *f*-ptSWNT-pDNA constructed with either 1, 3 and 5 µg pDNA after 24 hours. Values expressed as mean ± s.d., n=3

7.5 Discussion

In this study, the results showed that ptSWNTs can be stably dispersed in 0.1% 12-3-12 GS solution to generate *f*-ptSWNTs, which can be further developed into *f*-ptSWNT-pDNA complexes upon complexation with pDNA. High aspect ratio gene delivery systems such as *f*-ptSWNT-pDNA complex possess a unique mode of cellular interaction that differs from the low aspect ratio spherical NP systems, where additional geometrical considerations such as tube length and angle of entry as part of nano-cell interaction are to be taken into consideration. Shi et al. has suggested that MWNTs enters the cell tip-first, with favorable entry angle between 45 to 90 degrees [219]. Consistent with these findings, Huang et al. also suggested in a simulation study involving free energy analysis of the geometry of NP uptake that high aspect ratio materials that are initially in a laying-down horizontal position with the length of nanotube parallel to the cell surface would undergo rotation to a standing-up position until the completion of endocytic pathway [220]. The possibilities for passive entry of CNTs also exist as it was demonstrated that using MWNTs attached to an AFM probe to execute controlled CNT piercing of the cellular membrane does not cause membrane or cellular damages [221].

Toxicity is a major obstacle in CNT development. Some studies have suggested a contribution to toxicity from disrupted endocytosis due to length-dependency that was particularly amplified in cells transfected with CNTs through tip-first entry mechanism [219]. Recent studies by Zhu et al. suggested that the length and the stiffness of CNTs play a role in inducing lysosomal damage in cells as there exists a critical length that can be entrapped within the lysosome before the induction of cell death from lysosome damage [222]. As a result, longer and stiffer CNT entities (i.e.1μm long and rigid MWNTs) were shown to penetrate through the lysosomal membrane, while shorter and flexible MWNTs were found to be entrapped within cytoplasmic vesicles [222]. As

CNTs in this study consisted of wide range of CNT lengths that may include lengths in the micrometer range, this may be a contributing factor to the toxicity. While sonication could have reduced CNT length, the resulting CNT length has yet to be characterized. Shorter CNTs may have showed for better viability coupled with enhanced gene delivery capacity. A study by Geng et al. showed that SWNTs with length between 10 and 30 nm can be integrated into mammalian cell membranes, forming rigid CNT porins that mimic the electrical conductance of native lipid membrane and capable of transmembrane transport of ion and DNA [223].

A critical aspect of CNT formulation for biomedical application lies in the dispersion of CNTs as it requires surface functionalization for dispersion in water-based aqueous solution. The lowest GS solution concentration for CNT dispersion was 0.1% w/v 12-3-12 GS amongst the conditions evaluated. While effective for dispersion, the free (unbound) GS in the effective CNT:DNA ratio was consequently high, which could have further contributed to the toxicity of the cells exposed [178].

7.6 Conclusion

Overall, results in this study showed that CNT-based gene delivery system *f*-ptSWNT-pDNA complex can deliver pDNA to A7 cells *in vitro*. However, the significant amount of toxicity due to free GS in the A7 cells treated with *f*-ptSWNT-pDNA is a concern that needs to be addressed to resolve the issues surrounding toxicity. Moreover, investigation is needed to identify the most optimal parameter by investigating the effect of various GS with different alkyl chain lengths and optimal binding properties for more effective CNT dispersion.

Chapter 8 Summary, perspectives, and future directions

Portions of this chapter are reflective of an original manuscript published in the journal Neural Regeneration Research.

Foldvari, M. and **Chen, D.W**., 2016. The intricacies of neurotrophic factor therapy for retinal ganglion cell rescue in glaucoma: a case for gene therapy. *Neural Regeneration Research*, *11*(6), p.875.

Author Contributions: MF and DWC developed the concept and prepared the manuscript.

8.1 Summary

Research described in this dissertation aimed to contribute to the development of retinal non-viral gene therapy through developments of *in vitro* screening modalities and non-viral gene delivery systems. The concurrent developments in the two areas aimed to provide synergism to drive the overall development of non-viral NF gene therapy for glaucoma.

In vitro models are an integral part of therapeutic development as libraries of therapeutic compounds and entities are typically screened using *in vitro* models prior to downstream development and optimization *in vivo*. Effective *in vitro* models that can facilitate *in vivo* efficacy and translatability are therefore an important avenue of innovation. Research in Chapter 3, Chapter 4 and Chapter 5 present advancements of three *in vitro* models that address multiple levels ofdeficiencies.

Chapter 3 addresses the need for an *in vitro* co-culture that can model cell-to-cell interactions required for the proposed NF supplementation approach of RGC rescue through pDNA gene therapy. Unlike direct drug-receptor interactions of target cells in conventional small molecule therapeutics to induce therapeutic action, the proposed pDNA gene therapeutic approach is a two-stage process that involves an intermediary "*medic*" cell population that serves to produce therapeutic proteins *in situ* required to carry out therapeutic actions. Hence, two parameters that

may be useful in assessing therapeutic potential of a system are the bioavailability and bioactivity of therapeutic proteins that can be produced by *medic* cell. To address this issue, a co-culture bioassay platform as an essential tool for the assessment of gene delivery systems was developed. Using transwell insert setup, it demonstrated that the co-culture setup allows for effective culturing of two cell populations in separate compartments within a well, communicable through a membrane with pores that allows for molecule passage, simulating "*medic*" and "*stressed*" cell microenvironment. The co-culture setup provides a controlled environment to demonstrate therapeutic effects that are induced by therapeutic proteins produced from "medic" cells, eliminating the possibility of direct cell-to-cell interactions. A gap bridged by culture medium between the two cell layers is also an added advantage in demonstrating that therapeutic proteins secreted from the "*medic*" cells are transported through the medium to "*stressed*" cells. Dosing is another complex question in the pDNA therapy: 1) the optimum pDNA and NP dose required to carry out efficient transfection of "*medic*" cells upon administration, and 2) the controllability of therapeutic protein dose secreted from the transfected "*medic*" cells to carry out therapeutic action on "*stressed*" cells. Assessments incorporated in this *in vitro* bioassay facilitate the quantitationof the therapeutic protein and confirmation of its bioactivity produced by transfected cells. The bioactivity of the secreted therapeutic protein assessed through measuring the level of neurite extension exhibited by the "*stressed*" cell, which is represented by the neurite extension activity of SH-SY5Y in this modality. Altogether, this co-culture modality was demonstrated to be a feasible and versatile system that can be incorporated into the process of *in vitro* evaluation of gene delivery systems. Moreover, the versatility of the described system enables the utilization of different cellular combinations through the substitution of either "*medic*" or "*stressed*" according to the specific research question. For example, "*medic*" cell population can be substituted with

other retinal cell types to evaluate their capacity to serve as "*medic*" cell candidates in the retina. Similarly, "*stressed*" cells can be substituted with representative RGC cell models such as stem cell-derived RGCs described in Chapter 4.

Lack of a representative RGC cell model remains a major hindrance for RGC-aimed therapeutic development. While the co-culture model presented in Chapter 3 utilized an alternative model cell line, SH-SY5Y cells, for neurite extension study based on its BDNF responsiveness, the need for a RGC cell model is a requirement for the evaluation of specific neuroprotective effect and efficacy on RGCs. One possible approach is to utilize primary RGCs isolated from rodents or even post-mortem human retinas to serve as model cells, but the low abundance of RGCs, the difficulty for efficient isolation, and more importantly, the short viability of isolated primary RGCs limit the range of applications. For close to a decade, RGC-5 cells were thought to be a model RGC cell line until it was officially announced to be misidentified in 2013 [119]. As a result, a reliable RGC cell model is urgently needed, which have thus inspired scientists to explore innovative ways to generate model RGCs such as using stem cells. The use of stem cells and directing them to RGC fate opens a wide range of possibilities such as the generation of mitotic or immortalized RGCs. Research presented in Chapter 4 described the generation of a stem cell-derived RGC-like cells from multipotent RSCs isolated from CD-1 mouse retina (termed XFC-3), which displays major characteristics of RGCs. First, through multiplexed gene expression profiling, XFC-3 cells demonstrated the expression of three key RGC biomarkers *Map-2, Rbpms, and Tubb3*. Secondly, XFC-3 cells have neurites that can extend upon activation by BDNF, CNTF, Y-27632 and their combinations. While promising, this cell model requires further characterizations to confirm its representativeness compared to RGCs *in vivo.* An important question that one must ask in the characterization of RGCs is what characteristics are required to

be defined as a representative RGC model? Genetic heterogeneity in human population and diseases are one of the major contributors to disease complexity and subsequent treatment outcome variability. Likewise, heterogeneity also exists within the RGC population. A recent paper published by Sanes and Masland describe the existence of at least 30 different types of RGCs, which are heterogeneous morphologically, physiologically, molecularly and functionally [63]. Moreover, different subtypes of RGCs respond to stressors differently [224]. For example, a study that compared the level of survival amongst eleven different subtypes of RGCs following optic nerve transection showed that five subtypes had a significantly higher capacity to withstand optic nerve transection [225]. Knowing such heterogeneity exist within the ganglion cell population, the criterion of characterization must be defined with care.

In Chapter 5, the main objective was to bridge the disconnects between *in vitro* and *in vivo* in the context of gene delivery screening as many promising NP systems tested *in vitro* fail to translate comparable levels of gene delivery efficiency *in vivo*. By harnessing the differentiation capacity of multipotent RSCs, a "mini-retina" MiEye model that consists of multiple retinal cell types arranged in tissue-like arrangement to serve as a more *in vivo*-like preclinical gene delivery screening platform was developed. Using a commercial gene delivery system, the application of the MiEye system towards the generation of more *in vivo* translatable gene delivery system screening results was demonstrated. Additionally, there are other benefits as well to using such organotypic-like cultures for more advanced screening of NP properties such as targeting efficiency and tissue infiltration capacity. Furthermore, in-depth evaluation will be needed to characterize the distribution and arrangements of retinal cell types in the MiEye model. Collectively, the three aspects of *in vitro* modalities (Chapters 3-5) developed as tools aim to facilitate future developments in RGC NF gene therapy systems.

Concurrently with the development of *in vitro* models, research in the optimization of non-viral gene delivery systems were also explored. In Chapter 6, research that aimed to expand our knowledge of the GL-NP gene delivery systems was described, with an emphasis to optimize the physicochemical properties of the NP systems by incorporating MC and manufacturing considerations. Through a series of physicochemical studies, it was shown that NPs formulated with MCs can have smaller size, smaller particle size distribution, and higher homogeneity in terms of the number of pDNA per particle. On the other hand, GL-NP physicochemical properties were also shown to be improvable by manufacturing processes, specifically through sonication and TNPC considerations. The incorporation of a 15-minute sonication step and 2X TNPC was able to reduce particle size, particle size distribution, and zeta potential. Altogether, these findings contribute to our understanding and manufacturing of GL-NP systems.

In Chapter 7, an investigation on the application of CNTs for retinal gene delivery was described. In this work, non-covalent functionalization of SWNT was optimized using GS and eighteen different ratios of *f*-ptSWNT-pDNA complexes were subsequently formulated and tested for retinal cell gene delivery. Screening of *f*-ptSWNT-pDNA complexes in A7 astrocytes demonstrated that the CNT-based gene delivery system has the capacity to provide high gene delivery efficiency, however, the level of toxicity was high. Nonetheless, the results suggest that if the toxicity concern can be resolved, *f*-ptSWNT-pDNA system would be a promising gene delivery system for the retina.

8.2 Perspectives and future directions

8.2.1 Neuroprotection therapy for RGC in glaucoma

The neuroprotective therapeutic approach depicted in this research aims to deliver gene therapy locally to the retina, for a localized retinal cell transfection and subsequent localized NF production and supplementation action. As optic nerve extends into the brain, it may be beneficial to consider the site of optic nerve innervation as a secondary therapeutic target site to explore additional means of enhancing RGC survival. A recent study in a cat model with mild optic nerve crush demonstrated that when BDNF protein was administered in both the eyes and the brain, RGC survival was enhanced compared to RGCs that were only treated in the eyes [73]. Delivering NFs to the site of axon innervation have two implications towards axonal repair. Firstly, in a situation where TrkB receptors in the retina are downregulated and axoplasmic transport is not compromised, TrkB receptors that are present in the axons at the site of innervation can internalize exogenous BDNF and retrogradely transport it to the retina. In addition to supporting RGC survival, BDNF may also play a role in the maintenance of axonal innervation to LGN. While an attractive concept, delivering NFs to the innervation site in the brain would be even more challenging than delivery to the retina. Recent studies achieved gene expression in the retina after local administration of viral and non-viral gene delivery systems in the eye through injection and topical administrations [42, 76]. However, controlled delivery to areas of the brain is much more complicated due to the presence of complex barriers such as the blood-brain barrier. Potential routes of administration for delivery to sites of the brain may utilize intraocular and intranasal routes of administration as delivery through either routes have shown potential to access the brain [21].

While NF gene therapy is a promising strategy to overcome NF deficiency-mediated pathogenesis, it is important to keep in mind that glaucoma is a multifactorial disease that consists of other contributing factors towards the pathogenesis. As a result, a therapeutic approach that aims to address multiple stressors simultaneously may yield synergistic therapeutic outcomes. For example, glial-mediated tissue remodeling at the lamina cribrosa (LC) under glaucomatous stress could greatly influence the degree of optic nerve regeneration and remyelination. LC is one of the initial sites of glaucomatous damage as thickening of the prelaminar tissue, bowing of the LC and changes to the extracellular matrices collectively inflict stress on the optic nerve. Glial cells also play an important role in the pathogenesis as the activated form of glial cells secrete various extracellular matrix proteins that contribute to the formation of scarring, which may impede the restructuring of the optic nerve [226]. In this context, gene silencing strategies to suppress fibrotic genes could be used as an add-on treatment to overcome glial scar formation. Glial cells are traditionally known for their supportive roles in the CNS, however, reactive glial cells in glaucoma were shown to play mixed roles. Despite these mixed implications, it is important not to overlook the potential benefit that glial cells could provide. A recent study found that an intraocularly injected population of genetically modified neural stem cells overexpressing CNTF preferentially differentiated into astrocytes and were neuroprotective to RGCs [227]. Taken together, NFs and glial cells can both play important roles in the regeneration of the optic nerve axons.

8.2.2 Tissue-like *in vitro* modalities for glaucoma drug discovery

The pathophysiology of glaucoma is known to be multifactorial and its development is attributed to multiple molecular and mechanical factors throughout the eye, with emphasis at sites of trabecular meshwork, LC, and retina. Limitations in the modeling of key clinical features *in vitro* is a significant hindrance in deciphering the precise cause and effect interactions as intricate

cellular and molecular mechanisms are often difficult to control and discern directly *in vivo.* In addition to the modalities described in the earlier chapters, studies in recent years have shown promising advancements in 3D culture and its ability to produce more representative models that are able to better describe key molecular and structural events found *in vivo.* For example, Dautriche et al. have developed a 3D Schlemm's canal model by culturing primary cells on SU-8 synthetic scaffold [228]. It was shown that the 3D cultured primary human Schlemm's canal cells had *in vivo*-like physiology and expression profile through features of human Schlemm's canal pore formation and VE-cadherin and PECAM1 gene expression. As a result, this model serves as a tool for *in vitro* screening of human Schlemm's canal-based mechanism or drug discovery. Torrejon et al. have also utilized SU-80 synthetic scaffold to generate an ocular three-dimensional culture. More specifically, they have created a three-dimensional human trabecular model by culturing human trabecular meshwork cells on the SU-80 scaffold [229]. The 3D cultured trabecular meshwork was reported to exhibit trabecular meshwork physiology and expression of markers such as alpha-smooth muscle actin, myocillin, and alpha-beta-crystallin. This model was further modified to establish a steroid-induced glaucoma disease model of trabecular meshwork with characteristics of ECM overproduction and outflow resistance [230]. Thus, it can be utilized as an *in vitro* model for trabecular meshwork mechanism characterization and therapeutic development. Osmond et al. also developed a trabecular meshwork 3D culture model, but utilized collagen and collagen-chondroitin scaffold to improve the SU-80 scaffold based 3D culture through the incorporation of key ECMs found in trabecular meshwork such as collagen and collagen-chondroitin sulfate [231]. Together, these ocular 3D cultures demonstrated to be a gateway towards modeling key *in vivo* mechanical physiology and cellular interactions *in vitro.*

A different approach in the construction of 3D models was explored using bioprinting technologies, in which cells could be printed based on desired cellular arrangements. Utilizing 3D bioprinting techniques, Lorber et al. showed that RGCs and glial cells of the retina can be printed using 3D while maintaining its viability and neurite outgrowth capacity [179]. More recently, a study conducted by Kador et al. showed that by combining 3D printing with radial electrospun scaffolds, they were able to 3D print RGCs onto an electrospun surface with precise distribution and positioning of RGCs as found in the retina [180]. From a spatial arrangement standpoint, 3D printing-based techniques theoretically possess a comparative advantage as they allow for more control in dictating cellular positioning on a tissue-like arrangement by "printing" specific cells at a specific location. While the spatial arrangement of the cells cultured in 3D culture is either dependent on the resultant conformation from self-aggregation or the conformation dictated by the scaffold in which the cells adhere. However, much remains to be investigated in terms of feasibility and functionality of the resulting printed tissue-like structures. Nonetheless, the concurrent advancements with the two main approaches in constructing tissue-like structures *in vitro* demonstrates the possibility for such advanced culture system to be useful part in the modeling of intricate cell interactions found *in vivo.*

8.2.3 Understanding protein corona in ocular biological fluids

Using NPs as vehicles to deliver therapeutic genes to target cells encompass great promises in the future of therapeutic landscape and there are many aspects that need to be investigated to unleash the full potential. The presence of protein corona (PC) on NP, a phenomenon first described by Cedervall et al. in 2007 [232], is perhaps one of the most significant, yet overlooked factor that is limiting the therapeutic potential of NPs *in vivo.* PC formation is a dynamic process that occurs spontaneously on NP surfaces in the biological system, where biomolecules in the

biological system undergo dynamic surface modifications. Studies of PCs to date have primarily investigated using blood as the model biological medium [232-236], but little is known about the characteristics of PCs in other biological fluid medium. A more comprehensive understanding of PCs in different biological fluids may greatly improve the design of NPs and facilitate the clinical translation of nanomedicine. In the context of ocular nanomedicine, the three main biological fluids of the eye are tear film, aqueous humour, and vitreous humour. *Tear film* is the ocular fluid that lines the surface of cornea, preventing the entry of foreign entities into the eye while maintaining the hydration of the corneal surface. In a tear film protein study, Zhou et al. have identified 1543 proteins in human tear, in which selective proteins such as lysozyme, lactoferrin, secretory IgA, and lipocalin had the highest abundance [237]. *Aqueous humour* is the ocular fluid that occupies the anterior segment of the eye between the lens and cornea. In a study conducted by Chowdhury et al., they reported an identification of 676 proteins in human aqueous humour, which were largely composed of albumin, transferrin, antitrypsin, haploglobin, fibrinogen, IgG, and IgA [238]. Likewise, Murthy et al. reported similar levels of proteins identified in human aqueous humour in their study [239]. *Vitreous humour* is the ocular fluid that occupies the posterior segment of the eye between the lens and the retina. In a human vitreous proteomics analysis Murthy et al. reported 1205 proteins in the human vitreous [240]. In a more recent analysis, Mirzaei et al. described 4984 proteins in the vitreous humour [241], which are mainly composed of albumin, collagen, hyaluronic acid, and hyalocyte. Majority of the PC characterizations to date utilizes blood as the model biological medium as protein source, but studies that compare the differences in blood and tear film proteome, for example by Farrah et al., showed that approximately only 28% of the proteins found in blood are also found in tear film [242]. As PCs are from the available proteins in the biological medium, the significant differences between blood and tear film

proteome suggest the possibility that PC fingerprints can be significantly different in blood compared to tear film for the same NP. Both tear film and vitreous are the first biological medium of contact for NPs administered either topically or intravitreally. Thus, a more specific characterization of PCs tailored to the route of administration may improve NP *in vivo* efficacy. To add an additional layer of complexity in the understanding of PC, a disease-state based change in PCs would be an important avenue of investigation as differences in proteomic expression were reported between healthy human subject and glaucoma patient in aqueous humour [243-246] and vitreous [241]. Nonetheless, a more in-depth understanding of the PCs with focus on the first biological fluid medium that NPs may be in contact with upon administration is an important avenue for a more effective NP design and formulation for *in vivo* success.

8.3 Concluding remarks

Glaucoma is a neurodegenerative disease that can greatly affect the quality of life of individuals and families affected. While multifactorial, loss of visual function in glaucoma is a result of RGC cell death. Hence, therapeutic approach that can directly improve the health of RGCs could have the possibility to directly impede, or even reverse the continuous degeneration of damaged RGCs. Therapies, such as NF gene therapy, possess the potential to achieve such possibility through a localized supplementation of NF to stressed RGCs and rescue them from a degenerative condition. Moreover, such therapy could particularly benefit individuals who are suffering from NTG or continuous vision loss after IOP reduction treatments. The research and perspectives iterated in this dissertation were developed with the goal to facilitate research in NF gene therapy development, and as well reflect on the challenges that need to be overcome to bring forth nanomedicine gene therapy treatments to the clinic.

Letter of copyright permission

Chen, D.W. and Foldvari, M., 2016. *In vitro* bioassay model for screening non-viral neurotrophic factor gene delivery systems for glaucoma treatment. *Drug Delivery and Translational Research*, *6*(6), pp.676-685.

License Number	4364530825690
License date	Jun 08, 2018
Licensed Content Publisher	Springer Nature
Licensed Content Publication	Drug Delivery and Translational Research
Licensed Content Title	In vitro bioassay model for screening non-viral neurotrophic factor gene delivery systems for glaucoma treatment
Licensed Content Author	Ding Wen Chen, Marianna Foldvari
Licensed Content Date	Jan 1, 2016
Licensed Content Volume	6
Licensed Content Issue	6
Type of Use	Thesis/Dissertation
Requestor type	academic/university or research institute
Format	print and electronic
Portion	full article/chapter
Will you be translating?	no
Circulation/distribution	<501
Author of this Springer Nature content	yes
Title	Development of In Vitro 3D Model Systems For Screening Non-Viral Neurotrophic Factor Gene Therapies In Retina
Instructor name	Dr. Marianna Foldvari
Institution name	University of Waterloo
Expected presentation date	Jul 2018
Requestor Location	Ding-Wen Chen 212 Westfield Place

Chen D.W., Pauloff K. and Foldvari M., 2018. Three-dimensional co-culture bioassay for screening of retinal gene delivery systems. Methods in Molecular Biology (MiMB) series; In: "Retinal Gene Therapy: Methods and Protocols" ed. Wijnholds J. (Springer) 1715:79-88.

License Number	4359701412306
License date	May 31, 2018
Licensed Content Publisher	Springer Nature
Licensed Content Publication	Springer eBook
Licensed Content Title	Three-Dimensional Co-Culture Bioassay for Screening of Retinal Gene Delivery Systems
Licensed Content Author	Ding Wen Chen, Kathleen Pauloff, Marianna Foldvari
Licensed Content Date	Jan 1, 2018
Type of Use	Thesis/Dissertation
Requestor type	academic/university or research institute
Format	print and electronic
Portion	full article/chapter
Will you be translating?	no
Circulation/distribution	<501
Author of this Springer Nature content	yes
Title	Development of In Vitro 3D Model Systems For Screening Non-Viral Neurotrophic Factor Gene Therapies In Retina
Instructor name	Dr. Marianna Foldvari
Institution name	University of Waterloo
Expected presentation date	Jul 2018
Requestor Location	Ding-Wen Chen 212 Westfield Place

Reference

[1] J. Raty, J. Pikkarainen, T. Wirth, S. Yla-Herttuala, Gene therapy: the first approved gene-based medicines, molecular mechanisms and clinical indications, Current molecular pharmacology, 1 (2008) 13-23.
[2] J.M. Wilson, Gendicine: The first commercial gene therapy product; Chinese translation of editorial, Human gene therapy, 16 (2005) 1014-1015.
[3] G.-x. Chen, S. Zhang, X.-h. He, S.-y. Liu, C. Ma, X.-P. Zou, Clinical utility of recombinant adenoviral human p53 gene therapy: current perspectives, OncoTargets and therapy, 7 (2014) 1901.
[4] N. Miller, Glybera and the future of gene therapy in the European Union, Nature Reviews Drug Discovery, 11 (2012) 419-419.
[5] S. Ylä-Herttuala, Endgame: glybera finally recommended for approval as the first gene therapy drug in the European union, in, Nature Publishing Group, 2012.
[6] I. Perrault, J.-M. Rozet, S. Gerber, I. Ghazi, C. Leowski, D. Ducroq, E. Souied, J.-L. Dufier, A. Munnich, J. Kaplan, Leber congenital amaurosis, Molecular genetics and metabolism, 68 (1999) 200-208.
[7] F. Simonelli, C. Ziviello, F. Testa, S. Rossi, E. Fazzi, P.E. Bianchi, M. Fossarello, S. Signorini, C. Bertone, S. Galantuomo, Clinical and molecular genetics of Leber's congenital amaurosis: a multicenter study of Italian patients, Investigative ophthalmology & visual science, 48 (2007) 4284-4290.
[8] C. A Montiel-Equihua, A. J Thrasher, H. Bobby Gaspar, Gene therapy for severe combined immunodeficiency due to adenosine deaminase deficiency, Current gene therapy, 12 (2012) 57-65.
[9] A. Aiuti, M.G. Roncarolo, L. Naldini, Gene therapy for ADA-SCID, the first marketing approval of an ex vivo gene therapy in Europe: paving the road for the next generation of advanced therapy medicinal products, EMBO Molecular Medicine, (2017) e201707573.
[10] B.M. Kuehn, The Promise and Challenges of CAR-T Gene Therapy, JAMA, (2017).
[11] F. Mingozzi, K.A. High, Immune responses to AAV vectors: overcoming barriers to successful gene therapy, Blood, 122 (2013) 23-36.
[12] A.K. Zaiss, D.A. Muruve, Immune responses to adeno-associated virus vectors, Current gene therapy, 5 (2005) 323-331.
[13] A. Follenzi, L. Santambrogio, A. Annoni, Immune responses to lentiviral vectors, Current gene therapy, 7 (2007) 306-315.
[14] C.E. Thomas, A. Ehrhardt, M.A. Kay, Progress and problems with the use of viral vectors for gene therapy, Nature Reviews Genetics, 4 (2003) 346-358.
[15] S. Nayak, R.W. Herzog, Progress and prospects: immune responses to viral vectors, Gene therapy, 17 (2010) 295-304.
[16] N. Bessis, F. GarciaCozar, M. Boissier, Immune responses to gene therapy vectors: influence on vector function and effector mechanisms, Gene therapy, 11 (2004) S10-S17.
[17] H.H. Wong, N.R. Lemoine, Y. Wang, Oncolytic viruses for cancer therapy: overcoming the obstacles, Viruses, 2 (2010) 78-106.
[18] V. Louis Jeune, J.A. Joergensen, R.J. Hajjar, T. Weber, Pre-existing anti–adeno-associated virus antibodies as a challenge in AAV gene therapy, Human gene therapy methods, 24 (2013) 59-67.

[19] D.T. Teachey, S.F. Lacey, P.A. Shaw, J.J. Melenhorst, S.L. Maude, N. Frey, E. Pequignot, V.E. Gonzalez, F. Chen, J. Finklestein, D.M. Barrett, S.L. Weiss, J.C. Fitzgerald, R.A. Berg, R. Aplenc, C. Callahan, S.R. Rheingold, Z. Zheng, S. Rose-John, J.C. White, F. Nazimuddin, G. Wertheim, B.L. Levine, C.H. June, D.L. Porter, S.A. Grupp, Identification of Predictive Biomarkers for Cytokine Release Syndrome after Chimeric Antigen Receptor T-cell Therapy for Acute Lymphoblastic Leukemia, Cancer discovery, 6 (2016) 664-679.
[20] J.N. Brudno, J.N. Kochenderfer, Toxicities of chimeric antigen receptor T cells: recognition and management, Blood, 127 (2016) 3321-3330.
[21] Z. Han, S.M. Conley, R. Makkia, J. Guo, M.J. Cooper, M.I. Naash, Comparative analysis of DNA nanoparticles and AAVs for ocular gene delivery, PLoS One, 7 (2012) e52189.
[22] A. Kent, J. Spink, Will rising prices and budget constraints prevent patients from accessing novel gene therapies?, Gene therapy, 24 (2017) 542-543.
[23] S.H. Orkin, P. Reilly, Paying for future success in gene therapy, Science, 352 (2016) 1059-1061.
[24] S.-d. Li, L.-y. Huang, Nonviral gene therapy: promises and challenges, Gene therapy, 7 (2000) 31.
[25] H. Yin, R.L. Kanasty, A.A. Eltoukhy, A.J. Vegas, J.R. Dorkin, D.G. Anderson, Non-viral vectors for gene-based therapy, Nature Reviews Genetics, 15 (2014) 541-555.
[26] F. Menger, C. Littau, Gemini surfactants: a new class of self-assembling molecules, Journal of the American Chemical Society, 115 (1993) 10083-10090.
[27] F.M. Menger, J.S. Keiper, Gemini surfactants, Angewandte Chemie International Edition, 39 (2000) 1906-1920.
[28] S.D. Wettig, R.E. Verrall, M. Foldvari, Gemini surfactants: a new family of building blocks for non-viral gene delivery systems, Current gene therapy, 8 (2008) 9-23.
[29] A.J. Kirby, P. Camilleri, J.B. Engberts, M.C. Feiters, R.J. Nolte, O. Söderman, M. Bergsma, P.C. Bell, M.L. Fielden, C.L. García Rodríguez, Gemini surfactants: new synthetic vectors for gene transfection, Angewandte Chemie International Edition, 42 (2003) 1448-1457.
[30] M. Donkuru, I. Badea, S. Wettig, R. Verrall, M. Elsabahy, M. Foldvari, Advancing nonviral gene delivery: lipid-and surfactant-based nanoparticle design strategies, Nanomedicine, 5 (2010) 1103-1127.
[31] M. Donkuru, S.D. Wettig, R.E. Verrall, I. Badea, M. Foldvari, Designing pH-sensitive gemini nanoparticles for non-viral gene delivery into keratinocytes, Journal of Materials Chemistry, 22 (2012) 6232-6244.
[32] J. Singh, P. Yang, D. Michel, R. E Verrall, M. Foldvari, I. Badea, Amino acid-substituted gemini surfactant-based nanoparticles as safe and versatile gene delivery agents, Current drug delivery, 8 (2011) 299-306.
[33] S.D. Wettig, I. Badea, M. Donkuru, R.E. Verrall, M. Foldvari, Structural and transfection properties of amine-substituted gemini surfactant-based nanoparticles, The journal of gene medicine, 9 (2007) 649-658.
[34] S.D. Wettig, C. Wang, R.E. Verrall, M. Foldvari, Thermodynamic and aggregation properties of aza-and imino-substituted gemini surfactants designed for gene delivery, Physical Chemistry Chemical Physics, 9 (2007) 871-877.
[35] I. Badea, C. Virtanen, R. Verrall, A. Rosenberg, M. Foldvari, Effect of topical interferon-γ gene therapy using gemini nanoparticles on pathophysiological markers of cutaneous scleroderma in Tsk/+ mice, Gene therapy, 19 (2012) 978-987.

[36] I. Badea, N. Shaterian, M. Foldvari, Topical gene delivery in mice using gemini surfactant-lipid nanoparticles with and without tape electrode electroporation, Drug Delivery Letters, 1 (2011) 62-66.
[37] I. Badea, S. Wettig, R. Verrall, M. Foldvari, Topical non-invasive gene delivery using gemini nanoparticles in interferon-γ-deficient mice, European journal of pharmaceutics and biopharmaceutics, 65 (2007) 414-422.
[38] I. Badea, R. Verrall, M. Baca-Estrada, S. Tikoo, A. Rosenberg, P. Kumar, M. Foldvari, In vivo cutaneous interferon-γ gene delivery using novel dicationic (gemini) surfactant–plasmid complexes, The journal of gene medicine, 7 (2005) 1200-1214.
[39] D. Calderon-Nieva, K.B. Goonewardene, S. Gomis, M. Foldvari, Veterinary vaccine nanotechnology: pulmonary and nasal delivery in livestock animals, Drug Delivery and Translational Research, 7 (2017) 558-570.
[40] S. Alqawlaq, J.T. Huzil, M.V. Ivanova, M. Foldvari, Challenges in neuroprotective nanomedicine development: progress towards noninvasive gene therapy of glaucoma, Nanomedicine, 7 (2012) 1067-1083.
[41] S. Alqawlaq, J.M. Sivak, J.T. Huzil, M.V. Ivanova, J.G. Flanagan, M.A. Beazely, M. Foldvari, Preclinical development and ocular biodistribution of gemini-DNA nanoparticles after intravitreal and topical administration: towards non-invasive glaucoma gene therapy, Nanomedicine: Nanotechnology, Biology and Medicine, 10 (2014) 1637-1647.
[42] S. Alqawlaq, J.M. Sivak, J.T. Huzil, M.V. Ivanova, J.G. Flanagan, M.A. Beazely, M. Foldvari, Preclinical development and ocular biodistribution of gemini-DNA nanoparticles after intravitreal and topical administration: Towards non-invasive glaucoma gene therapy, Nanomedicine: Nanotechnology, Biology, and Medicine, 10 (2014) 1637-1647.
[43] D.C. Wallace, G. Singh, M.T. Lott, J.A. Hodge, T.G. Schurr, A. Lezza, L.J. Elsas, E.K. Nikoskelainen, Mitochondrial DNA mutation associated with Leber's hereditary optic neuropathy, Science, 242 (1988) 1427-1430.
[44] V. Carelli, A. Ghelli, L. Bucchi, P. Montagna, A. De Negri, V. Leuzzi, C. Carducci, G. Lenaz, E. Lugaresi, M. Degli Esposti, Biochemical features of mtDNA 14484(ND6/m 64 V) point mutation associated with Leber's hereditary optic neuropathy, Annals of neurology, 45 (1999) 320-328.
[45] S. Ghosh, E. Fahy, I. Bodis-Wollner, J. Sherman, N. Howell, Longitudinal study of a heteroplasmic 3460 Leber hereditary optic neuropathy family by multiplexed primer-extension analysis and nucleotide sequencing, American journal of human genetics, 58 (1996) 325.
[46] S. Ellouze, S. Augustin, A. Bouaita, C. Bonnet, M. Simonutti, V. Forster, S. Picaud, J.-A. Sahel, M. Corral-Debrinski, Optimized allotopic expression of the human mitochondrial ND4 prevents blindness in a rat model of mitochondrial dysfunction, The American Journal of Human Genetics, 83 (2008) 373-387.
[47] H. Cwerman-Thibault, S. Augustin, C. Lechauve, J. Ayache, S. Ellouze, J.-A. Sahel, M. Corral-Debrinski, Nuclear expression of mitochondrial ND4 leads to the protein assembling in complex I and prevents optic atrophy and visual loss, Molecular Therapy-Methods & Clinical Development, 2 (2015) 15003.
[48] C.T. Leffler, S.G. Schwartz, F.M. Giliberti, M.T. Young, D. Bermudez, What was Glaucoma Called Before the 20th Century?, Ophthalmology and Eye Diseases, 7 (2015) 21-33.
[49] Y.-C. Tham, X. Li, T.Y. Wong, H.A. Quigley, T. Aung, C.-Y. Cheng, Global prevalence of glaucoma and projections of glaucoma burden through 2040: a systematic review and meta-analysis, Ophthalmology, 121 (2014) 2081-2090.

[50] R.N. Weinreb, P.T. Khaw, Primary open-angle glaucoma, The Lancet, 363 (2004) 1711-1720.
[51] H.A. Quigley, D.S. Friedman, N.G. Congdon, Possible mechanisms of primary angle-closure and malignant glaucoma, J. Glaucoma, 12 (2003) 167-180.
[52] M. Sarfarazi, I. Stoilov, Molecular genetics of primary congenital glaucoma, Eye, 14 (2000) 422-428.
[53] M.C. Leske, A. Connell, S.-Y. Wu, L.G. Hyman, A.P. Schachat, Risk factors for open-angle glaucoma: the Barbados Eye Study, Archives of ophthalmology, 113 (1995) 918-924.
[54] A. Sommer, J.M. Tielsch, J. Katz, H.A. Quigley, J.D. Gottsch, J. Javitt, K. Singh, Relationship between intraocular pressure and primary open angle glaucoma among white and black Americans: the Baltimore Eye Survey, Archives of ophthalmology, 109 (1991) 1090-1095.
[55] M. Almasieh, A.M. Wilson, B. Morquette, J.L.C. Vargas, A. Di Polo, The molecular basis of retinal ganglion cell death in glaucoma, Progress in retinal and eye research, 31 (2012) 152-181.
[56] A. Sommer, N.R. Miller, I. Pollack, A.E. Maumenee, T. George, The nerve fiber layer in the diagnosis of glaucoma, Archives of ophthalmology, 95 (1977) 2149-2156.
[57] J.E. Pederson, D.R. Anderson, The mode of progressive disc cupping in ocular hypertension and glaucoma, Archives of Ophthalmology, 98 (1980) 490-495.
[58] Y.H. Kwon, J.H. Fingert, M.H. Kuehn, W.L. Alward, Primary open-angle glaucoma, New England Journal of Medicine, 360 (2009) 1113-1124.
[59] M.A. Kass, D.K. Heuer, E.J. Higginbotham, C.A. Johnson, J.L. Keltner, J.P. Miller, R.K. Parrish, M.R. Wilson, M.O. Gordon, The Ocular Hypertension Treatment Study: a randomized trial determines that topical ocular hypotensive medication delays or prevents the onset of primary open-angle glaucoma, Archives of ophthalmology, 120 (2002) 701-713.
[60] G. Tezel, Oxidative stress in glaucomatous neurodegeneration: mechanisms and consequences, Progress in retinal and eye research, 25 (2006) 490-513.
[61] M.P. Murphy, How mitochondria produce reactive oxygen species, Biochemical Journal, 417 (2009) 1-13.
[62] C.N.-T.G.S. Group, The effectiveness of intraocular pressure reduction in the treatment of normal-tension glaucoma, American journal of ophthalmology, 126 (1998) 498-505.
[63] J.R. Sanes, R.H. Masland, The types of retinal ganglion cells: current status and implications for neuronal classification, Annual review of neuroscience, 38 (2015) 221-246.
[64] C.G.J.J.o.g. De Moraes, Anatomy of the visual pathways, 22 (2013) S2-S7.
[65] M. Almasieh, A.M. Wilson, B. Morquette, J.L. Cueva Vargas, A. Di Polo, The molecular basis of retinal ganglion cell death in glaucoma, Prog Retin Eye Res, 31 (2012) 152-181.
[66] D.R. Kaplan, F.D. Miller, Neurotrophin signal transduction in the nervous system, Current opinion in neurobiology, 10 (2000) 381-391.
[67] M. Hetman, K. Kanning, J.E. Cavanaugh, Z. Xia, Neuroprotection by brain-derived neurotrophic factor is mediated by extracellular signal-regulated kinase and phosphatidylinositol 3-kinase, Journal of Biological Chemistry, 274 (1999) 22569-22580.
[68] S.V. Bhave, L. Ghoda, P.L. Hoffman, Brain-derived neurotrophic factor mediates the anti-apoptotic effect of NMDA in cerebellar granule neurons: signal transduction cascades and site of ethanol action, Journal of Neuroscience, 19 (1999) 3277-3286.
[69] H. Chen, A.J. Weber, BDNF enhances retinal ganglion cell survival in cats with optic nerve damage, Investigative ophthalmology & visual science, 42 (2001) 966-974.
[70] L. Domenici, N. Origlia, B. Falsini, E. Cerri, D. Barloscio, C. Fabiani, M. Sansò, L. Giovannini, Rescue of retinal function by BDNF in a mouse model of glaucoma, PLoS ONE, 9 (2014).

[71] G. Rovere, F.M. Nadal-Nicolás, J. Wang, J.M. Bernal-Garro, N. García-Carrillo, M.P. Villegas-Pérez, M. Agudo-Barriuso, M. Vidal-Sanz, Melanopsin-Containing or Non-Melanopsin–Containing Retinal Ganglion Cells Response to Acute Ocular Hypertension With or Without Brain-Derived Neurotrophic Factor NeuroprotectionAOH Induces RGC Loss, Permanent Rescue With BDNF, Investigative ophthalmology & visual science, 57 (2016) 6652-6661.
[72] M.C. Sanchez-Migallon, F.J. Valiente-Soriano, F.M. Nadal-Nicolas, M. Vidal-Sanz, M. Agudo-Barriuso, Apoptotic Retinal Ganglion Cell Death After Optic Nerve Transection or Crush in Mice: Delayed RGC Loss With BDNF or a Caspase 3 Inhibitor, Invest Ophthalmol Vis Sci, 57 (2016) 81-93.
[73] A.J. Weber, S. Viswanáthan, C. Ramanathan, C.D. Harman, Combined application of BDNF to the eye and brain enhances ganglion cell survival and function in the cat after optic nerve injury, Investigative ophthalmology & visual science, 51 (2010) 327-334.
[74] K.R. Martin, H.A. Quigley, D.J. Zack, H. Levkovitch-Verbin, J. Kielczewski, D. Valenta, L. Baumrind, M.E. Pease, R.L. Klein, W.W. Hauswirth, Gene therapy with brain-derived neurotrophic factor as a protection: retinal ganglion cells in a rat glaucoma model, Investigative ophthalmology & visual science, 44 (2003) 4357-4365.
[75] R. Ren, Y. Li, Z. Liu, K. Liu, S. He, Long-term rescue of rat retinal ganglion cells and visual function by AAV-mediated BDNF expression after acute elevation of intraocular pressure, Investigative ophthalmology & visual science, 53 (2012) 1003-1011.
[76] A. Di Polo, L.J. Aigner, R.J. Dunn, G.M. Bray, A.J. Aguayo, Prolonged delivery of brain-derived neurotrophic factor by adenovirus-infected Müller cells temporarily rescues injured retinal ganglion cells, Proceedings of the National Academy of Sciences, 95 (1998) 3978-3983.
[77] S. Isenmann, N. Klöcker, C. Gravel, M. Bähr, Protection of axotomized retinal ganglion cells by adenovirally delivered BDNF in vivo, European Journal of Neuroscience, 10 (1998) 2751-2756.
[78] X. Mo, A. Yokoyama, T. Oshitari, H. Negishi, M. Dezawa, A. Mizota, E. Adachi-Usami, Rescue of axotomized retinal ganglion cells by BDNF gene electroporation in adult rats, Investigative ophthalmology & visual science, 43 (2002) 2401-2405.
[79] L. Feng, Z. Puyang, H. Chen, P. Liang, J.B. Troy, X. Liu, Overexpression of Brain-Derived Neurotrophic Factor Protects Large Retinal Ganglion Cells After Optic Nerve Crush in Mice, eNeuro, 4 (2017).
[80] A. Carrel, On The Permanent Life of Tissue Outside Of The Organism, The Journal of Experimental Medicine, 15 (1912) 516-528.
[81] A. Abbott, Cell culture: biology's new dimension, Nature, 424 (2003) 870-872.
[82] M. Bokhari, R.J. Carnachan, N.R. Cameron, S.A. Przyborski, Culture of HepG2 liver cells on three dimensional polystyrene scaffolds enhances cell structure and function during toxicological challenge, Journal of Anatomy, 211 (2007) 567-576.
[83] G.N. Li, L.L. Livi, C.M. Gourd, E.S. Deweerd, D. Hoffman-Kim, Genomic and morphological changes of neuroblastoma cells in response to three-dimensional matrices, Tissue engineering, 13 (2007) 1035-1047.
[84] D.J. Maltman, S.A. Przyborski, Developments in three-dimensional cell culture technology aimed at improving the accuracy of in vitro analyses, Biochemical Society transactions, 38 (2010) 1072-1075.
[85] M.M. Bercu, H. Arien-Zakay, D. Stoler, S. Lecht, P.I. Lelkes, S. Samuel, R. Or, A. Nagler, P. Lazarovici, U. Elchalal, Enhanced survival and neurite network formation of human umbilical cord blood neuronal progenitors in three-dimensional collagen constructs, Journal of molecular neuroscience : MN, 51 (2013) 249-261.

[86] A. Desai, W.S. Kisaalita, C. Keith, Z.Z. Wu, Human neuroblastoma (SH-SY5Y) cell culture and differentiation in 3-D collagen hydrogels for cell-based biosensing, Biosensors & bioelectronics, 21 (2006) 1483-1492.
[87] A.C. Erickson, J.R. Couchman, Still more complexity in mammalian basement membranes, Journal of Histochemistry & Cytochemistry, 48 (2000) 1291-1306.
[88] F. Rosso, A. Giordano, M. Barbarisi, A. Barbarisi, From cell–ECM interactions to tissue engineering, Journal of cellular physiology, 199 (2004) 174-180.
[89] K.J. Price, A. Tsykin, K.M. Giles, R.T. Sladic, M.R. Epis, R. Ganss, G.J. Goodall, P.J. Leedman, Matrigel basement membrane matrix influences expression of microRNAs in cancer cell lines, Biochemical and biophysical research communications, 427 (2012) 343-348.
[90] B. Chevallay, D. Herbage, Collagen-based biomaterials as 3D scaffold for cell cultures: applications for tissue engineering and gene therapy, Medical and Biological Engineering and Computing, 38 (2000) 211-218.
[91] S.-A. Oh, H.-Y. Lee, J.H. Lee, T.-H. Kim, J.-H. Jang, H.-W. Kim, I. Wall, Collagen three-dimensional hydrogel matrix carrying basic fibroblast growth factor for the cultivation of mesenchymal stem cells and osteogenic differentiation, Tissue Engineering Part A, 18 (2012) 1087-1100.
[92] T.A. Ahmed, E.V. Dare, M. Hincke, Fibrin: a versatile scaffold for tissue engineering applications, Tissue Engineering Part B: Reviews, 14 (2008) 199-215.
[93] H. Hall, Modified fibrin hydrogel matrices: both, 3D-scaffolds and local and controlled release systems to stimulate angiogenesis, Current pharmaceutical design, 13 (2007) 3597-3607.
[94] H. Hong, J.P. Stegemann, 2D and 3D collagen and fibrin biopolymers promote specific ECM and integrin gene expression by vascular smooth muscle cells, Journal of Biomaterials Science, Polymer Edition, 19 (2008) 1279-1293.
[95] I. Brito, C. Silva, A. Duarte, I. Lima, G. Rodrigues, R. Rossetto, A. Sales, C. Lobo, M. Bernuci, A. Rosa-e-Silva, Alginate hydrogel matrix stiffness influences the in vitro development of caprine preantral follicles, Molecular reproduction and development, 81 (2014) 636-645.
[96] J.A. Rowley, G. Madlambayan, D.J. Mooney, Alginate hydrogels as synthetic extracellular matrix materials, Biomaterials, 20 (1999) 45-53.
[97] A. Balgude, X. Yu, A. Szymanski, R. Bellamkonda, Agarose gel stiffness determines rate of DRG neurite extension in 3D cultures, Biomaterials, 22 (2001) 1077-1084.
[98] A. Di Martino, M. Sittinger, M.V. Risbud, Chitosan: a versatile biopolymer for orthopaedic tissue-engineering, Biomaterials, 26 (2005) 5983-5990.
[99] Y.N. Wei, Q.Q. Wang, T.T. Gao, M. Kong, K.K. Yang, Y. An, S.Y. Jiang, J. Li, X.J. Cheng, X.G. Chen, 3-D culture of human umbilical vein endothelial cells with reversible thermosensitive hydroxybutyl chitosan hydrogel, Journal of Materials Science: Materials in Medicine, 24 (2013) 1781-1787.
[100] E. Knight, B. Murray, R. Carnachan, S. Przyborski, Alvetex®: polystyrene scaffold technology for routine three dimensional cell culture, 3D Cell Culture: Methods and Protocols, (2011) 323-340.
[101] J.-H. Shim, J.Y. Kim, M. Park, J. Park, D.-W. Cho, Development of a hybrid scaffold with synthetic biomaterials and hydrogel using solid freeform fabrication technology, Biofabrication, 3 (2011) 034102.
[102] N.E. Timmins, L.K. Nielsen, Generation of multicellular tumor spheroids by the hanging-drop method, Tissue Engineering, (2007) 141-151.

[103] Y.-C. Tung, A.Y. Hsiao, S.G. Allen, Y.-s. Torisawa, M. Ho, S. Takayama, High-throughput 3D spheroid culture and drug testing using a 384 hanging drop array, Analyst, 136 (2011) 473-478.
[104] M. Foldvari, D.W. Chen, N. Nafissi, D. Calderon, L. Narsineni, A. Rafiee, Non-viral gene therapy: Gains and challenges of non-invasive administration methods, Journal of Controlled Release, (2015).
[105] H.V. Danesh-Meyer, Neuroprotection in glaucoma: recent and future directions, CURR. OPIN. OPHTHALMOL., 22 (2011) 78-86.
[106] B. Castillo, M. Del Cerro, X. Breakefield, D. Frim, C. Barnstable, D. Dean, M. Bohn, Retinal ganglion cell survival is promoted by genetically modified astrocytes designed to secrete brain-derived neurotrophic factor (BDNF), Brain research, 647 (1994) 30-36.
[107] E. Vecino, F.D. Rodriguez, N. Ruzafa, X. Pereiro, S.C. Sharma, Glia–neuron interactions in the mammalian retina, Progress in retinal and eye research, (2015).
[108] N.M. Radio, W.R. Mundy, Developmental neurotoxicity testing in vitro: models for assessing chemical effects on neurite outgrowth, Neurotoxicology, 29 (2008) 361-376.
[109] H. Geller, M. Dubois-Dalcq, Antigenic and functional characterization of a rat central nervous system-derived cell line immortalized by a retroviral vector, The Journal of cell biology, 107 (1988) 1977-1986.
[110] M. Noble, K. Murray, Purified astrocytes promote the in vitro division of a bipotential glial progenitor cell, The EMBO journal, 3 (1984) 2243.
[111] J. Schindelin, I. Arganda-Carreras, E. Frise, V. Kaynig, M. Longair, T. Pietzsch, S. Preibisch, C. Rueden, S. Saalfeld, B. Schmid, J.-Y. Tinevez, D.J. White, V. Hartenstein, K. Eliceiri, P. Tomancak, A. Cardona, Fiji: an open-source platform for biological-image analysis, Nat Meth, 9 (2012) 676-682.
[112] C.F. Burgoyne, J. Crawford Downs, A.J. Bellezza, J.K. Francis Suh, R.T. Hart, The optic nerve head as a biomechanical structure: A new paradigm for understanding the role of IOP-related stress and strain in the pathophysiology of glaucomatous optic nerve head damage, Progress in Retinal and Eye Research, 24 (2005) 39-73.
[113] H.A. Quigley, S.J. McKinnon, D.J. Zack, M.E. Pease, L.A. Kerrigan-Baumrind, D.F. Kerrigan, R.S. Mitchell, Retrograde axonal transport of BDNF in retinal ganglion cells is blocked by acute IOP elevation in rats, Investigative Ophthalmology and Visual Science, 41 (2000) 3460-3466.
[114] S. Iwabe, N.A. Moreno-Mendoza, F. Trigo-Tavera, C. Crowder, G.A. García-Sánchez, Retrograde axonal transport obstruction of brain-derived neurotrophic factor (BDNF) and its TrkB receptor in the retina and optic nerve of American Cocker Spaniel dogs with spontaneous glaucoma, Veterinary ophthalmology, 10 (2007) 12-19.
[115] A. Weber, C. Harman, S. Viswanathan, Effects of optic nerve injury, glaucoma, and neuroprotection on the survival, structure, and function of ganglion cells in the mammalian retina, The Journal of physiology, 586 (2008) 4393-4400.
[116] L. Benowitz, Y. Yin, Rewiring the injured CNS: lessons from the optic nerve, Experimental neurology, 209 (2008) 389-398.
[117] L.I. Benowitz, Y. Yin, Optic nerve regeneration, Archives of ophthalmology, 128 (2010) 1059-1064.
[118] N.J. Van Bergen, J.P. Wood, G. Chidlow, I.A. Trounce, R.J. Casson, W.-K. Ju, R.N. Weinreb, J.G. Crowston, Recharacterization of the RGC-5 retinal ganglion cell line, Investigative ophthalmology & visual science, 50 (2009) 4267-4272.

[119] R.R. Krishnamoorthy, A.F. Clark, D. Daudt, J.K. Vishwanatha, T. Yorio, A forensic path to RGC-5 cell line identification: lessons learned, Invest Ophthalmol Vis Sci, 54 (2013) 5712-5719.
[120] D.W. Chen, K. Pauloff, M. Foldvari, Three-Dimensional Co-Culture Bioassay for Screening of Retinal Gene Delivery Systems, in: Retinal Gene Therapy, Springer, 2018, pp. 79-88.
[121] T. Li, M. Lewallen, S. Chen, W. Yu, N. Zhang, T. Xie, Multipotent stem cells isolated from the adult mouse retina are capable of producing functional photoreceptor cells, Cell research, 23 (2013) 788-802.
[122] D.W. Chen, M. Foldvari, In vitro bioassay model for screening non-viral neurotrophic factor gene delivery systems for glaucoma treatment, Drug delivery and translational research, 6 (2016) 676-685.
[123] M. Donkuru, S.D. Wettig, R.E. Verrall, I. Badea, M.J.J.o.M.C. Foldvari, Designing pH-sensitive gemini nanoparticles for non-viral gene delivery into keratinocytes, 22 (2012) 6232-6244.
[124] J.T. Huzil, E. Saliaj, M.V. Ivanova, M. Gharagozloo, M.J. Loureiro, C. Lamprecht, A. Korinek, D.W. Chen, M. Foldvari, Selective nuclear localization of siRNA by metallic versus semiconducting single wall carbon nanotubes in keratinocytes, Future Science OA, (2015) 1-15.
[125] V. Tropepe, B.L. Coles, B.J. Chiasson, D.J. Horsford, A.J. Elia, R.R. McInnes, D. van der Kooy, Retinal stem cells in the adult mammalian eye, Science, 287 (2000) 2032-2036.
[126] B.L. Coles, B. Angénieux, T. Inoue, K. Del Rio-Tsonis, J.R. Spence, R.R. McInnes, Y. Arsenijevic, D. van der Kooy, Facile isolation and the characterization of human retinal stem cells, Proceedings of the National Academy of Sciences of the United States of America, 101 (2004) 15772-15777.
[127] F. Doetsch, The glial identity of neural stem cells, Nature neuroscience, 6 (2003) 1127-1134.
[128] R.L. Bernardos, L.K. Barthel, J.R. Meyers, P.A. Raymond, Late-stage neuronal progenitors in the retina are radial Müller glia that function as retinal stem cells, Journal of Neuroscience, 27 (2007) 7028-7040.
[129] J.M. Lawrence, S. Singhal, B. Bhatia, D.J. Keegan, T.A. Reh, P.J. Luthert, P.T. Khaw, G.A. Limb, MIO-M1 Cells and Similar Müller Glial Cell Lines Derived from Adult Human Retina Exhibit Neural Stem Cell Characteristics, Stem cells, 25 (2007) 2033-2043.
[130] S. Singhal, B. Bhatia, H. Jayaram, S. Becker, M.F. Jones, P.B. Cottrill, P.T. Khaw, T.E. Salt, G.A. Limb, Human Müller glia with stem cell characteristics differentiate into retinal ganglion cell (RGC) precursors in vitro and partially restore RGC function in vivo following transplantation, Stem cells translational medicine, 1 (2012) 188-199.
[131] W.-t. Song, X.-y. Zhang, X.-b. Xia, Atoh7 promotes the differentiation of Müller cells-derived retinal stem cells into retinal ganglion cells in a rat model of glaucoma, Experimental Biology and Medicine, 240 (2015) 682-690.
[132] W. Song, X. Zhang, X. Xia, Atoh7 promotes the differentiation of retinal stem cells derived from Müller cells into retinal ganglion cells by inhibiting Notch signaling, Stem Cell Research & Therapy, 4 (2013) 94.
[133] B. Bhatia, H. Jayaram, S. Singhal, M.F. Jones, G.A. Limb, Differences between the neurogenic and proliferative abilities of Müller glia with stem cell characteristics and the ciliary epithelium from the adult human eye, Experimental eye research, 93 (2011) 852-861.
[134] K.P. Gill, S.S. Hung, A. Sharov, C.Y. Lo, K. Needham, G.E. Lidgerwood, S. Jackson, D.E. Crombie, B.A. Nayagam, A.L. Cook, A.W. Hewitt, A. Pebay, R.C. Wong, Enriched retinal ganglion cells derived from human embryonic stem cells, Sci Rep, 6 (2016) 30552.

[135] V.M. Sluch, C.H. Davis, V. Ranganathan, J.M. Kerr, K. Krick, R. Martin, C.A. Berlinicke, N. Marsh-Armstrong, J.S. Diamond, H.Q. Mao, D.J. Zack, Differentiation of human ESCs to retinal ganglion cells using a CRISPR engineered reporter cell line, Sci Rep, 5 (2015) 16595.
[136] T. Tanaka, T. Yokoi, F. Tamalu, S. Watanabe, S. Nishina, N. Azuma, Generation of Retinal Ganglion Cells With Functional Axons From Mouse Embryonic Stem Cells and Induced Pluripotent Stem Cells, Invest Ophthalmol Vis Sci, 57 (2016) 3348-3359.
[137] B. Jagatha, M.S. Divya, R. Sanalkumar, C.L. Indulekha, S. Vidyanand, T.S. Divya, A.V. Das, J. James, In vitro differentiation of retinal ganglion-like cells from embryonic stem cell derived neural progenitors, Biochemical and Biophysical Research Communications, 380 (2009) 230-235.
[138] K. Li, X. Zhong, S. Yang, Z. Luo, K. Li, Y. Liu, S. Cai, H. Gu, S. Lu, H. Zhang, Y. Wei, J. Zhuang, Y. Zhuo, Z. Fan, J. Ge, HiPSC-derived retinal ganglion cells grow dendritic arbors and functional axons on a tissue-engineered scaffold, Acta Biomaterialia, 54 (2017) 117-127.
[139] P. Teotia, M.J. Van Hook, C.S. Wichman, R. Allingham, M.A. Hauser, I. Ahmad, Modeling Glaucoma: Retinal Ganglion Cells Generated from Induced Pluripotent Stem Cells of Patients with SIX6 Risk Allele Show Developmental Abnormalities, STEM CELLS, 35 (2017) 2239-2252.
[140] S.K. Ohlemacher, A. Sridhar, Y. Xiao, A.E. Hochstetler, M. Sarfarazi, T.R. Cummins, J.S. Meyer, Stepwise Differentiation of Retinal Ganglion Cells from Human Pluripotent Stem Cells Enables Analysis of Glaucomatous Neurodegeneration, Stem Cells, 34 (2016) 1553-1562.
[141] B.B. Xie, X.M. Zhang, T. Hashimoto, A.H. Tien, A. Chen, J. Ge, X.J. Yang, Differentiation of retinal ganglion cells and photoreceptor precursors from mouse induced pluripotent stem cells carrying an Atoh7/Math5 lineage reporter, PLoS One, 9 (2014) e112175.
[142] J. Danias, K.C. Lee, M.-F. Zamora, B. Chen, F. Shen, T. Filippopoulos, Y. Su, D. Goldblum, S.M. Podos, T. Mittag, Quantitative analysis of retinal ganglion cell (RGC) loss in aging DBA/2NNia glaucomatous mice: comparison with RGC loss in aging C57/BL6 mice, Investigative ophthalmology & visual science, 44 (2003) 5151-5162.
[143] J.L. Goldberg, J.S. Espinosa, Y. Xu, N. Davidson, G.T. Kovacs, B.A. Barres, Retinal ganglion cells do not extend axons by default: promotion by neurotrophic signaling and electrical activity, Neuron, 33 (2002) 689-702.
[144] H. Sawai, D.B. Clarke, P. Kittlerova, G.M. Bray, A.J. Aguayo, Brain-derived neurotrophic factor and neurotrophin-4/5 stimulate growth of axonal branches from regenerating retinal ganglion cells, Journal of Neuroscience, 16 (1996) 3887-3894.
[145] A. Cohen, G. Bray, A. Aguayo, Neurotrophin-4/5 (NT-4/5) increases adult rat retinal ganglion cell survival and neurite outgrowth in vitro, Developmental Neurobiology, 25 (1994) 953-959.
[146] A. Bosco, R. Linden, BDNF and NT-4 differentially modulate neurite outgrowth in developing retinal ganglion cells, Journal of neuroscience research, 57 (1999) 759-769.
[147] Z. Ahmed, M. Berry, A. Logan, ROCK inhibition promotes adult retinal ganglion cell neurite outgrowth only in the presence of growth promoting factors, Mol Cell Neurosci, 42 (2009) 128-133.
[148] Y. Fujita, T.J.F.i.n. Yamashita, Axon growth inhibition by RhoA/ROCK in the central nervous system, 8 (2014) 338.
[149] C. Barnstable, U. Dräger, Thy-1 antigen: a ganglion cell specific marker in rodent retina, Neuroscience, 11 (1984) 847-855.

[150] A.R. Rodriguez, S. Müller, L. Pérez, N.C. Brecha, The RNA binding protein RBPMS is a selective marker of ganglion cells in the mammalian retina, Journal of Comparative Neurology, 522 (2014) 1411-1443.
[151] F. Wu, T.J. Kaczynski, S. Sethuramanujam, R. Li, V. Jain, M. Slaughter, X. Mu, Two transcription factors, Pou4f2 and Isl1, are sufficient to specify the retinal ganglion cell fate, Proceedings of the National Academy of Sciences, 112 (2015) E1559-E1568.
[152] L. Pan, M. Deng, X. Xie, L. Gan, ISL1 and BRN3B co-regulate the differentiation of murine retinal ganglion cells, Development, 135 (2008) 1981-1990.
[153] I. Surgucheva, A.D. Weisman, J.L. Goldberg, A. Shnyra, A. Surguchov, γ-Synuclein as a marker of retinal ganglion cells, (2008).
[154] S.-M. Jiang, L.-P. Zeng, J.-H. Zeng, L. Tang, X.-M. Chen, X. Wei, β-III-Tubulin: a reliable marker for retinal ganglion cell labeling in experimental models of glaucoma, Int. J. Ophthalmol., 8 (2015) 643.
[155] V. Senatorov, I. Malyukova, R. Fariss, E.F. Wawrousek, S. Swaminathan, S.K. Sharan, S. Tomarev, Expression of mutated mouse myocilin induces open-angle glaucoma in transgenic mice, Journal of Neuroscience, 26 (2006) 11903-11914.
[156] I. Soto, E. Oglesby, B.P. Buckingham, J.L. Son, E.D. Roberson, M.R. Steele, D.M. Inman, M.L. Vetter, P.J. Horner, N. Marsh-Armstrong, Retinal ganglion cells downregulate gene expression and lose their axons within the optic nerve head in a mouse glaucoma model, Journal of Neuroscience, 28 (2008) 548-561.
[157] V. Perry, R. Morris, G. Raisman, Is Thy-1 expressed only by ganglion cells and their axons in the retina and optic nerve?, Journal of neurocytology, 13 (1984) 809-824.
[158] B.A. Barres, B.E. Silverstein, D.P. Corey, L.L. Chun, Immunological, morphological, and electrophysiological variation among retinal ganglion cells purified by panning, Neuron, 1 (1988) 791-803.
[159] C.L. Schlamp, E.C. Johnson, Y. Li, J.C. Morrison, R.W. Nickells, Changes in Thy1 gene expression associated with damaged retinal ganglion cells, Mol Vis, 7 (2001) 192-201.
[160] W. Huang, J. Fileta, Y. Guo, C.L. Grosskreutz, Downregulation of Thy1 in retinal ganglion cells in experimental glaucoma, Current eye research, 31 (2006) 265-271.
[161] R.R. Krishnamoorthy, P. Agarwal, G. Prasanna, K. Vopat, W. Lambert, H.J. Sheedlo, I.H. Pang, D. Shade, R.J. Wordinger, T. Yorio, A.F. Clark, N. Agarwal, Characterization of a transformed rat retinal ganglion cell line, Brain Res Mol Brain Res, 86 (2001) 1-12.
[162] K.R.G. Martin, H.A. Quigley, D.J. Zack, H. Levkovitch-Verbin, J. Kielczewski, D. Valenta, L. Baumrind, M.E. Pease, R.L. Klein, W.W. Hauswirth, Gene Therapy with Brain-Derived Neurotrophic Factor As a Protection: Retinal Ganglion Cells in a Rat Glaucoma Model, Investigative Opthalmology & Visual Science, 44 (2003) 4357.
[163] A. Wilson, A. Di Polo, Gene therapy for retinal ganglion cell neuroprotection in glaucoma, Gene therapy, 19 (2012) 127-136.
[164] J.C. Downs, M.D. Roberts, I.A. Sigal, Glaucomatous cupping of the lamina cribrosa: a review of the evidence for active progressive remodeling as a mechanism, Experimental eye research, 93 (2011) 133-140.
[165] A.F. Clark, The cell and molecular biology of glaucoma: biomechanical factors in glaucoma, Investigative ophthalmology & visual science, 53 (2012) 2473-2475.
[166] M.R. Hernandez, H. Miao, T. Lukas, Astrocytes in glaucomatous optic neuropathy, Progress in brain research, 173 (2008) 353-373.

[167] E.C. Johnson, J.C. Morrison, Friend or foe? Resolving the impact of glial responses in glaucoma, J. Glaucoma, 18 (2009) 341.
[168] N. Bull, T. Johnson, K. Martin, Organotypic explant culture of adult rat retina for in vitro investigations of neurodegeneration, neuroprotection and cell transplantation, Protoc exch, (2011).
[169] S. Gustmann, N. Dünker, In vivo-like organotypic murine retinal wholemount culture, Journal of visualized experiments: JoVE, (2010).
[170] T.V. Johnson, K.R. Martin, Development and characterization of an adult retinal explant organotypic tissue culture system as an in vitro intraocular stem cell transplantation model, Investigative ophthalmology & visual science, 49 (2008) 3503-3512.
[171] J.S. Meyer, R.L. Shearer, E.E. Capowski, L.S. Wright, K.A. Wallace, E.L. McMillan, S.-C. Zhang, D.M. Gamm, Modeling early retinal development with human embryonic and induced pluripotent stem cells, Proceedings of the National Academy of Sciences, 106 (2009) 16698-16703.
[172] J.S. Meyer, S.E. Howden, K.A. Wallace, A.D. Verhoeven, L.S. Wright, E.E. Capowski, I. Pinilla, J.M. Martin, S. Tian, R. Stewart, Optic vesicle-like structures derived from human pluripotent stem cells facilitate a customized approach to retinal disease treatment, Stem cells, 29 (2011) 1206-1218.
[173] M. Eiraku, N. Takata, H. Ishibashi, M. Kawada, E. Sakakura, S. Okuda, K. Sekiguchi, T. Adachi, Y. Sasai, Self-organizing optic-cup morphogenesis in three-dimensional culture, Nature, 472 (2011) 51-56.
[174] T. Nakano, S. Ando, N. Takata, M. Kawada, K. Muguruma, K. Sekiguchi, K. Saito, S. Yonemura, M. Eiraku, Y. Sasai, Self-Formation of Optic Cups and Storable Stratified Neural Retina from Human ESCs, Cell Stem Cell, 10 (2012) 771-785.
[175] H.Y. Chen, K.D. Kaya, L. Dong, A. Swaroop, Three-dimensional retinal organoids from mouse pluripotent stem cells mimic in vivo development with enhanced stratification and rod photoreceptor differentiation, Mol. Vision, 22 (2016) 1077.
[176] M. Völkner, M. Zschätzsch, M. Rostovskaya, R.W. Overall, V. Busskamp, K. Anastassiadis, M.O. Karl, Retinal organoids from pluripotent stem cells efficiently recapitulate retinogenesis, Stem cell reports, 6 (2016) 525-538.
[177] A.W. Browne, C. Arnesano, N. Harutyunyan, T. Khuu, J.C. Martinez, H.A. Pollack, D.S. Koos, T.C. Lee, S.E. Fraser, R.A. Moats, Structural and Functional Characterization of Human Stem-Cell-Derived Retinal Organoids by Live Imaging, Investigative Ophthalmology & Visual Science, 58 (2017) 3311-3318.
[178] Y. Maekawa, A. Onishi, K. Matsushita, N. Koide, M. Mandai, K. Suzuma, T. Kitaoka, A. Kuwahara, C. Ozone, T. Nakano, Optimized culture system to induce neurite outgrowth from retinal ganglion cells in three-dimensional retinal aggregates differentiated from mouse and human embryonic stem cells, Current eye research, 41 (2016) 558-568.
[179] B. Lorber, W.-K. Hsiao, I.M. Hutchings, K.R. Martin, Adult rat retinal ganglion cells and glia can be printed by piezoelectric inkjet printing, Biofabrication, 6 (2013) 015001.
[180] K.E. Kador, S.P. Grogan, E.W. Dorthé, P. Venugopalan, M.F. Malek, J.L. Goldberg, D.D. D'lima, Control of retinal ganglion cell positioning and neurite growth: Combining 3D printing with radial electrospun scaffolds, Tissue Engineering Part A, 22 (2016) 286-294.
[181] J. Zabner, A.J. Fasbender, T. Moninger, K.A. Poellinger, M.J. Welsh, Cellular and molecular barriers to gene transfer by a cationic lipid, Journal of Biological Chemistry, 270 (1995) 18997-19007.

[182] W.-C. Tseng, F.R. Haselton, T.D. Giorgio, Mitosis enhances transgene expression of plasmid delivered by cationic liposomes, Biochimica et Biophysica Acta (BBA)-Gene Structure and Expression, 1445 (1999) 53-64.
[183] I. Mortimer, P. Tam, I. MacLachlan, R. Graham, E. Saravolac, P. Joshi, Cationic lipid-mediated transfection of cells in culture requires mitotic activity, Gene therapy, 6 (1999).
[184] M. Männistö, M. Reinisalo, M. Ruponen, P. Honkakoski, M. Tammi, A. Urtti, Polyplex-mediated gene transfer and cell cycle: effect of carrier on cellular uptake and intracellular kinetics, and significance of glycosaminoglycans, The journal of gene medicine, 9 (2007) 479-487.
[185] S.C. Hydes, I.A. Pringle, S. Abdullah, A.E. Lawton, L.A. Davies, A. Varathalingam, G. Nunez-Alonso, A.-M. Green, R.P. Bazzani, S.G. Sumner-Jones, CpG-free plasmids confer reduced inflammation and sustained pulmonary gene expression, Nature biotechnology, 26 (2008) 549-552.
[186] E. Riu, Z.-Y. Chen, H. Xu, C.-Y. He, M.A. Kay, Histone modifications are associated with the persistence or silencing of vector-mediated transgene expression in vivo, Molecular Therapy, 15 (2007) 1348-1355.
[187] Z.-Y. Chen, C.-Y. He, A. Ehrhardt, M.A. Kay, Minicircle DNA vectors devoid of bacterial DNA result in persistent and high-level transgene expression in vivo, Molecular therapy, 8 (2003) 495-500.
[188] Z.-Y. Chen, C.-Y. He, M.A. Kay, Improved production and purification of minicircle DNA vector free of plasmid bacterial sequences and capable of persistent transgene expression in vivo, Human gene therapy, 16 (2005) 126-131.
[189] W.M. Dietz, N.E. Skinner, S.E. Hamilton, M.D. Jund, S.M. Heitfeld, A.J. Litterman, P. Hwu, Z.-Y. Chen, A.M. Salazar, J.R. Ohlfest, Minicircle DNA is superior to plasmid DNA in eliciting antigen-specific CD8+ T-cell responses, Molecular Therapy, 21 (2013) 1526-1535.
[190] M.J. Osborn, R.T. McElmurry, C.J. Lees, A.P. DeFeo, Z.-Y. Chen, M.A. Kay, L. Naldini, G. Freeman, J. Tolar, B.R. Blazar, Minicircle DNA-based gene therapy coupled with immune modulation permits long-term expression of α-L-iduronidase in mice with mucopolysaccharidosis type I, Molecular Therapy, 19 (2011) 450-460.
[191] M.M. Munye, A.D. Tagalakis, J.L. Barnes, R.E. Brown, R.J. McAnulty, S.J. Howe, S.L. Hart, Minicircle DNA provides enhanced and prolonged transgene expression following airway gene transfer, Scientific reports, 6 (2016) 23125.
[192] L.E.G. Maniar, J.M. Maniar, Z.-Y. Chen, J. Lu, A.Z. Fire, M.A. Kay, Minicircle DNA vectors achieve sustained expression reflected by active chromatin and transcriptional level, Molecular Therapy, 21 (2013) 131-138.
[193] C. Dong, I. Badea, M. Poorghorban, R. Verrall, M. Foldvari, Impact of phospholipids on plasmid packaging and toxicity of gemini nanoparticles, Journal of Materials Chemistry B, 3 (2015) 8806-8822.
[194] R.N. Cohen, M.A. van der Aa, N. Macaraeg, A.P. Lee, F.C. Szoka, Quantification of plasmid DNA copies in the nucleus after lipoplex and polyplex transfection, Journal of Controlled Release, 135 (2009) 166-174.
[195] W. Godbey, K.K. Wu, A.G. Mikos, Tracking the intracellular path of poly (ethylenimine)/DNA complexes for gene delivery, Proceedings of the National Academy of Sciences, 96 (1999) 5177-5181.
[196] M. Foldvari, M. Bagonluri, Carbon nanotubes as functional excipients for nanomedicines: I. Pharmaceutical properties, Nanomedicine: Nanotechnology, Biology and Medicine, 4 (2008) 173-182.

[197] M. Foldvari, M. Bagonluri, Carbon nanotubes as functional excipients for nanomedicines: II. Drug delivery and biocompatibility issues, Nanomedicine: Nanotechnology, Biology and Medicine, 4 (2008) 183-200.
[198] R.H. Baughman, A.A. Zakhidov, W.A. De Heer, Carbon nanotubes--the route toward applications, science, 297 (2002) 787-792.
[199] A. Bianco, K. Kostarelos, M. Prato, Applications of carbon nanotubes in drug delivery, Current opinion in chemical biology, 9 (2005) 674-679.
[200] J. Chen, S. Chen, X. Zhao, L.V. Kuznetsova, S.S. Wong, I. Ojima, Functionalized single-walled carbon nanotubes as rationally designed vehicles for tumor-targeted drug delivery, Journal of the American Chemical Society, 130 (2008) 16778-16785.
[201] A.A. Bhirde, V. Patel, J. Gavard, G. Zhang, A.A. Sousa, A. Masedunskas, R.D. Leapman, R. Weigert, J.S. Gutkind, J.F. Rusling, Targeted killing of cancer cells in vivo and in vitro with EGF-directed carbon nanotube-based drug delivery, ACS nano, 3 (2009) 307-316.
[202] Z. Liu, K. Chen, C. Davis, S. Sherlock, Q. Cao, X. Chen, H. Dai, Drug delivery with carbon nanotubes for in vivo cancer treatment, Cancer research, 68 (2008) 6652-6660.
[203] H. Huang, Q. Yuan, J. Shah, R. Misra, A new family of folate-decorated and carbon nanotube-mediated drug delivery system: synthesis and drug delivery response, Advanced drug delivery reviews, 63 (2011) 1332-1339.
[204] Z. Liu, X. Sun, N. Nakayama-Ratchford, H. Dai, Supramolecular chemistry on water-soluble carbon nanotubes for drug loading and delivery, ACS nano, 1 (2007) 50-56.
[205] N.W. Shi Kam, T.C. Jessop, P.A. Wender, H. Dai, Nanotube molecular transporters: internalization of carbon nanotube− protein conjugates into mammalian cells, Journal of the American Chemical Society, 126 (2004) 6850-6851.
[206] M. Prato, K. Kostarelos, A. Bianco, Functionalized carbon nanotubes in drug design and discovery, Accounts of chemical research, 41 (2007) 60-68.
[207] M. Zheng, A. Jagota, E.D. Semke, B.A. Diner, R.S. Mclean, S.R. Lustig, R.E. Richardson, N.G. Tassi, DNA-assisted dispersion and separation of carbon nanotubes, Nature materials, 2 (2003) 338-342.
[208] E.N. Primo, P. Cañete-Rosales, S. Bollo, M.D. Rubianes, G.A. Rivas, Dispersion of bamboo type multi-wall carbon nanotubes in calf-thymus double stranded DNA, Colloids and Surfaces B: Biointerfaces, 108 (2013) 329-336.
[209] S.N. Kim, Z. Kuang, J.G. Grote, B.L. Farmer, R.R. Naik, Enrichment of (6, 5) single wall carbon nanotubes using genomic DNA, Nano letters, 8 (2008) 4415-4420.
[210] Y. Wu, J.A. Phillips, H. Liu, R. Yang, W. Tan, Carbon nanotubes protect DNA strands during cellular delivery, ACS nano, 2 (2008) 2023-2028.
[211] D. Pantarotto, R. Singh, D. McCarthy, M. Erhardt, J.-P. Briand, M. Prato, K. Kostarelos, A. Bianco, Functionalized Carbon Nanotubes for Plasmid DNA Gene Delivery, Angewandte Chemie International Edition, 43 (2004) 5242-5246.
[212] X. Gong, J. Liu, S. Baskaran, R.D. Voise, J.S. Young, Surfactant-assisted processing of carbon nanotube/polymer composites, Chemistry of materials, 12 (2000) 1049-1052.
[213] S. Cui, R. Canet, A. Derre, M. Couzi, P. Delhaes, Characterization of multiwall carbon nanotubes and influence of surfactant in the nanocomposite processing, Carbon, 41 (2003) 797-809.
[214] T.H. Kim, C. Doe, S.R. Kline, S.M. Choi, Water-Redispersible Isolated Single-Walled Carbon Nanotubes Fabricated by In Situ Polymerization of Micelles, Advanced Materials, 19 (2007) 929-933.

[215] M.S. Strano, V.C. Moore, M.K. Miller, M.J. Allen, E.H. Haroz, C. Kittrell, R.H. Hauge, R. Smalley, The role of surfactant adsorption during ultrasonication in the dispersion of single-walled carbon nanotubes, Journal of Nanoscience and Nanotechnology, 3 (2003) 81-86.
[216] B. Sohrabi, N. Poorgholami-Bejarpasi, N. Nayeri, Dispersion of carbon nanotubes using mixed surfactants: experimental and molecular dynamics simulation studies, The Journal of Physical Chemistry B, 118 (2014) 3094-3103.
[217] A.J. Blanch, C.E. Lenehan, J.S. Quinton, Optimizing surfactant concentrations for dispersion of single-walled carbon nanotubes in aqueous solution, The Journal of Physical Chemistry B, 114 (2010) 9805-9811.
[218] L. Vaisman, H.D. Wagner, G. Marom, The role of surfactants in dispersion of carbon nanotubes, Advances in colloid and interface science, 128 (2006) 37-46.
[219] X. Shi, A. von Dem Bussche, R.H. Hurt, A.B. Kane, H. Gao, Cell entry of one-dimensional nanomaterials occurs by tip recognition and rotation, Nature nanotechnology, 6 (2011) 714-719.
[220] C. Huang, Y. Zhang, H. Yuan, H. Gao, S. Zhang, Role of nanoparticle geometry in endocytosis: laying down to stand up, Nano letters, 13 (2013) 4546-4550.
[221] X. Chen, A. Kis, A. Zettl, C.R. Bertozzi, A cell nanoinjector based on carbon nanotubes, Proceedings of the National Academy of Sciences, 104 (2007) 8218-8222.
[222] W. Zhu, A. von dem Bussche, X. Yi, Y. Qiu, Z. Wang, P. Weston, R.H. Hurt, A.B. Kane, H. Gao, Nanomechanical mechanism for lipid bilayer damage induced by carbon nanotubes confined in intracellular vesicles, Proceedings of the National Academy of Sciences, 113 (2016) 12374-12379.
[223] J. Geng, K. Kim, J. Zhang, A. Escalada, R. Tunuguntla, L.R. Comolli, F.I. Allen, A.V. Shnyrova, K.R. Cho, D. Munoz, Y.M. Wang, C.P. Grigoropoulos, C.M. Ajo-Franklin, V.A. Frolov, A. Noy, Stochastic transport through carbon nanotubes in lipid bilayers and live cell membranes, Nature, 514 (2014) 612-615.
[224] L. Della Santina, D.M. Inman, C.B. Lupien, P.J. Horner, R.O. Wong, Differential progression of structural and functional alterations in distinct retinal ganglion cell types in a mouse model of glaucoma, The Journal of Neuroscience, 33 (2013) 17444-17457.
[225] X. Duan, M. Qiao, F. Bei, I.-J. Kim, Z. He, J.R. Sanes, Subtype-specific regeneration of retinal ganglion cells following axotomy: effects of osteopontin and mTOR signaling, Neuron, 85 (2015) 1244-1256.
[226] D.M. Wallace, C.J. O'brien, The role of lamina cribrosa cells in optic nerve head fibrosis in glaucoma, Experimental eye research, 142 (2016) 102-109.
[227] K. Flachsbarth, K. Kruszewski, G. Jung, W. Jankowiak, K. Riecken, L. Wagenfeld, G. Richard, B. Fehse, U. Bartsch, Neural Stem Cell–Based Intraocular Administration of Ciliary Neurotrophic Factor Attenuates the Loss of Axotomized Ganglion Cells in Adult MiceNS Cell–Based Intraocular Administration of CNTF, Investigative ophthalmology & visual science, 55 (2014) 7029-7039.
[228] C.N. Dautriche, D. Szymanski, M. Kerr, K.Y. Torrejon, M. Bergkvist, Y. Xie, J. Danias, W.D. Stamer, S.T. Sharfstein, A biomimetic Schlemm's canal inner wall: A model to study outflow physiology, glaucoma pathology and high-throughput drug screening, Biomaterials, 65 (2015) 86-92.
[229] K.Y. Torrejon, D. Pu, M. Bergkvist, J. Danias, S.T. Sharfstein, Y. Xie, Recreating a human trabecular meshwork outflow system on microfabricated porous structures, Biotechnology and bioengineering, 110 (2013) 3205-3218.

[230] K.Y. Torrejon, E.L. Papke, J.R. Halman, J. Stolwijk, C.N. Dautriche, M. Bergkvist, J. Danias, S.T. Sharfstein, Y. Xie, Bioengineered glaucomatous 3D human trabecular meshwork as an in vitro disease model, Biotechnology and bioengineering, 113 (2016) 1357-1368.
[231] M. Osmond, S.M. Bernier, M.B. Pantcheva, M.D. Krebs, Collagen and collagen-chondroitin sulfate scaffolds with uniaxially aligned pores for the biomimetic, three dimensional culture of trabecular meshwork cells, Biotechnology and bioengineering, 114 (2017) 915-923.
[232] T. Cedervall, I. Lynch, S. Lindman, T. Berggård, E. Thulin, H. Nilsson, K.A. Dawson, S. Linse, Understanding the nanoparticle–protein corona using methods to quantify exchange rates and affinities of proteins for nanoparticles, Proceedings of the National Academy of Sciences, 104 (2007) 2050-2055.
[233] H. Zhang, K.E. Burnum, M.L. Luna, B.O. Petritis, J.S. Kim, W.J. Qian, R.J. Moore, A. Heredia-Langner, B.J.M. Webb-Robertson, B.D. Thrall, Quantitative proteomics analysis of adsorbed plasma proteins classifies nanoparticles with different surface properties and size, Proteomics, 11 (2011) 4569-4577.
[234] S. Tenzer, D. Docter, J. Kuharev, A. Musyanovych, V. Fetz, R. Hecht, F. Schlenk, D. Fischer, K. Kiouptsi, C. Reinhardt, K. Landfester, H. Schild, M. Maskos, S.K. Knauer, R.H. Stauber, Rapid formation of plasma protein corona critically affects nanoparticle pathophysiology, Nat Nanotechnol, 8 (2013) 772-781.
[235] M.P. Monopoli, D. Walczyk, A. Campbell, G. Elia, I. Lynch, F. Baldelli Bombelli, K.A. Dawson, Physical− chemical aspects of protein corona: relevance to in vitro and in vivo biological impacts of nanoparticles, Journal of the American Chemical Society, 133 (2011) 2525-2534.
[236] M. Lundqvist, J. Stigler, G. Elia, I. Lynch, T. Cedervall, K.A. Dawson, Nanoparticle size and surface properties determine the protein corona with possible implications for biological impacts, Proceedings of the National Academy of Sciences, 105 (2008) 14265-14270.
[237] L. Zhou, S.Z. Zhao, S.K. Koh, L. Chen, C. Vaz, V. Tanavde, X.R. Li, R.W. Beuerman, In-depth analysis of the human tear proteome, Journal of proteomics, 75 (2012) 3877-3885.
[238] U.R. Chowdhury, B.J. Madden, M.C. Charlesworth, M.P. Fautsch, Proteome Analysis of Human Aqueous Humor, Investigative Ophthalmology & Visual Science, 51 (2010) 4921-4931.
[239] K.R. Murthy, P. Rajagopalan, S.M. Pinto, J. Advani, P.R. Murthy, R. Goel, Y. Subbannayya, L. Balakrishnan, M. Dash, A.K. Anil, Proteomics of human aqueous humor, Omics: a journal of integrative biology, 19 (2015) 283-293.
[240] K.R. Murthy, R. Goel, Y. Subbannayya, H.K. Jacob, P.R. Murthy, S.S. Manda, A.H. Patil, R. Sharma, N.A. Sahasrabuddhe, A. Parashar, B.G. Nair, V. Krishna, T.K. Prasad, H. Gowda, A. Pandey, Proteomic analysis of human vitreous humor, Clinical Proteomics, 11 (2014) 29.
[241] M. Mirzaei, V.B. Gupta, J.M. Chick, T.M. Greco, Y. Wu, N. Chitranshi, R. Vander Wall, E. Hone, L. Deng, Y. Dheer, Age-related neurodegenerative disease associated pathways identified in retinal and vitreous proteome from human glaucoma eyes, Scientific reports, 7 (2017) 12685.
[242] T. Farrah, E.W. Deutsch, G.S. Omenn, D.S. Campbell, Z. Sun, J.A. Bletz, P. Mallick, J.E. Katz, J. Malmström, R. Ossola, A high-confidence human plasma proteome reference set with estimated concentrations in PeptideAtlas, Molecular & cellular proteomics, 10 (2011) M110. 006353.
[243] A. Izzotti, M. Longobardi, C. Cartiglia, S. Sacca, Proteome alterations in primary open angle glaucoma aqueous humor, Journal of proteome research, 9 (2010) 4831-4838.
[244] A. Bagnis, A. Izzotti, M. Centofanti, S. Sacca, Aqueous humor oxidative stress proteomic levels in primary open angle glaucoma, Experimental eye research, 103 (2012) 55-62.

[245] X. Duan, P. Xue, N. Wang, Z. Dong, Q. Lu, F. Yang, Proteomic analysis of aqueous humor from patients with primary open angle glaucoma, Mol. Vision, 16 (2010) 2839.
[246] R.A. Bouhenni, S. Al Shahwan, J. Morales, B.T. Wakim, A.M. Chomyk, F.S. Alkuraya, D.P. Edward, Identification of differentially expressed proteins in the aqueous humor of primary congenital glaucoma, Experimental eye research, 92 (2011) 67-75.

Appendices

Appendix A Method development to study the neuroprotective effect of BDNF expressed by non-virally transfected RGCs on oxidatively stressed RGCs

The objective was to evaluate different three-dimensional culture formats for its feasibility and suitability for downstream retinal co-culture model development and therapeutic evaluation. At the beginning of the project, RGC-5 cell line was used as a model cell line and considerable work was done to develop healthy RGC/oxidatively stressed RGC co-culture in 3D culture to test the effect of BDNF on rescuing oxidatively stressed RGC. Subsequently, the false identity of the RGC-5 cell line was discovered and therefore further work with this cell line was discontinued. The results presented here; however, demonstrate methodology development and support the incorporation of the new RGC cell line generated from retinal stem cells.

Hydrogen peroxide mediated oxidative stress decreases RGC-5 viability in a dose-dependent manner

RGC-5 cells were exposed with five different concentrations of hydrogen peroxide (300μM - 700μM) over 24 hours, it was found that there is a dose-dependent response between the level of hydrogen peroxide and the viability of RGC-5 where increasing concentration of hydrogen peroxide decreases the viability of RGC-5. The effective concentration (EC_{50}) of hydrogen peroxide after 24 hours hydrogen peroxide exposure is approximately 400μM.

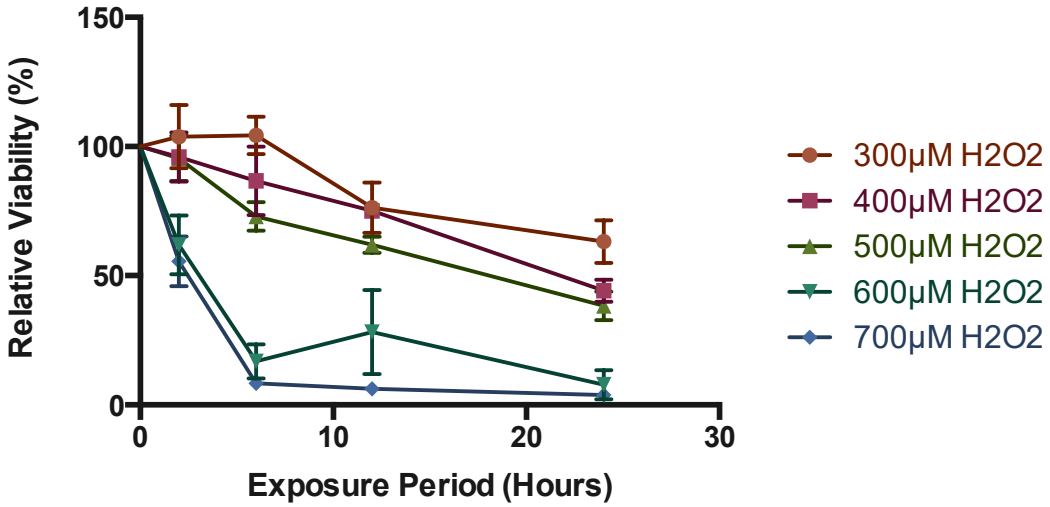

RGC-5 viability over 24 hours of hydrogen peroxide exposure at concentrations (300μM – 700μM) in traditional monolayer

Development of "mini-retinas" model in three-dimensional cell culture system

NF gene therapy, a therapeutic approach that is achieved through the delivery of NF encoded pDNA such as BDNF to targeted cell candidates, NP-transfected cells would be genetically modified to produce BDNF proteins. BDNF-transfected cell population is given the name of "medic cell" due to its role in the production and delivery of the therapeutic gene to the stressed cells. To evaluate the neuroprotective effect of BDNF in a more *in vivo*-like condition with *in vitro* model, three types of retinal model were developed.

Contact-dependent model was developed using RAFT® 3D culture system, where the stressed and medic populations are cultured in their independent layers that are right on top of each other. Contact-independent model was developed using the Alvetex 3D culture scaffold. Both medic cells and stressed cell populations are cultured in their independent polystyrene scaffold matrix that is separated by the well-insert. The delivery of NF is achieved as both

populations are cultured in the same media. The mini-eye neurosphere model is created using the Perfecta hanging-drop culture system, where retinal cells are cultured in the form of spheroids.

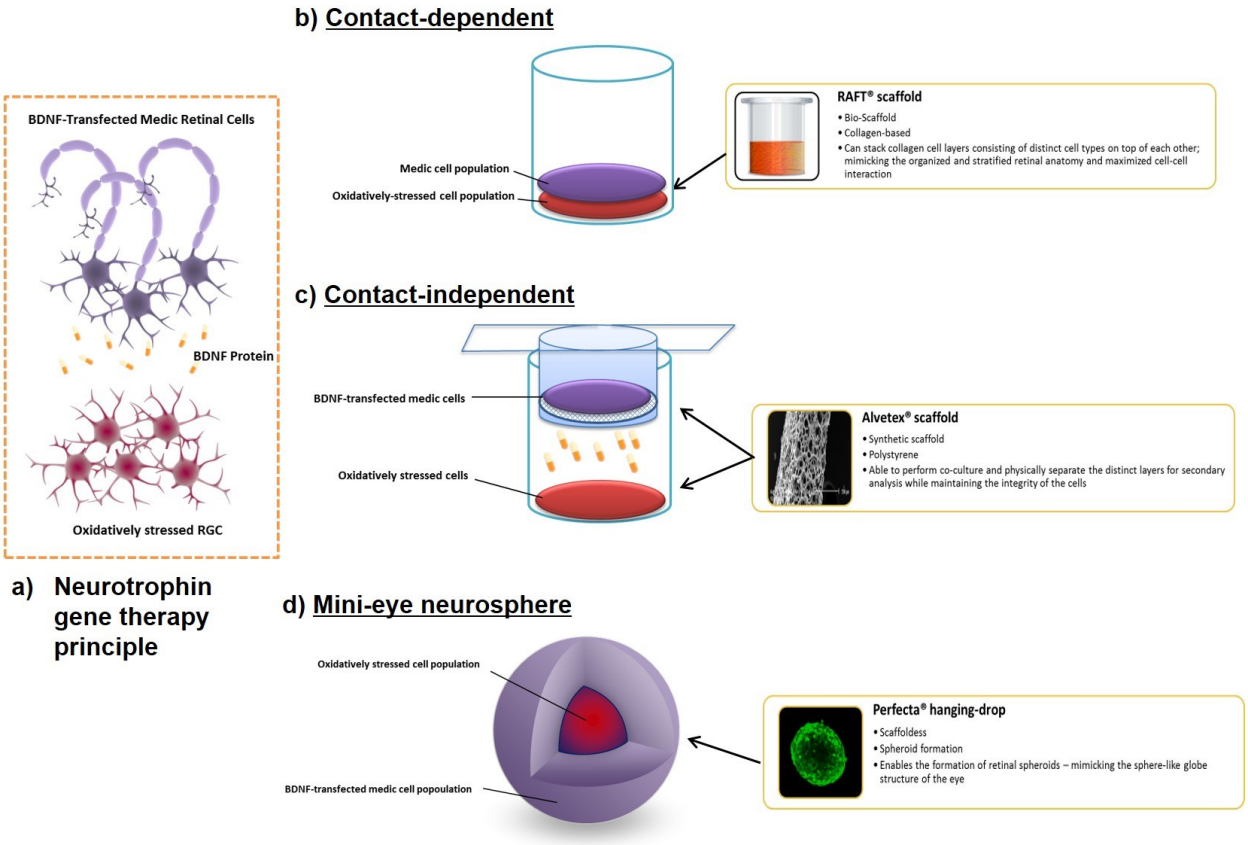

Modeling of three different types of "mini-retinas" for various *in vitro* evaluation of gene therapy mediated rescue on the RGC. A) Illustrates the principle of NF gene therapy. B) Contact-dependent model established using bioscaffold-based system. C) Contact-independent model established using polystyrene-based system. D) Mini-eye neurosphere model established using hanging-drop method system.

Hydrogen peroxide induced oxidative stress also observed in RGC-5 cultured in three-dimensional cell culture

The susceptibility of the RGC-5 cultured in 3D culture in response to hydrogen peroxide RGC-5 hydrogen was evaluated, and it was found that RGCs cultured in the RAFT® 3D cell culture system showed a dose-dependent decrease in viability of RGC-5 cells in response to increasing levels of hydrogen peroxide concentration over 48 hours period.

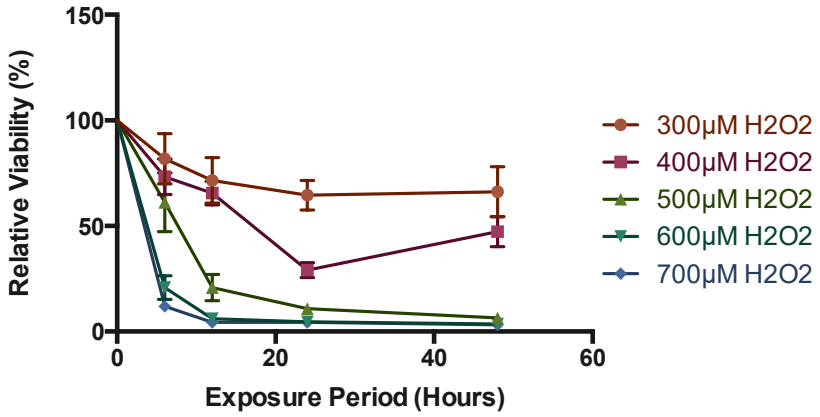

RGC-5 viability over 24 hours of hydrogen peroxide exposure at various concentrations (300µM – 700µM) cultured in 3D cell culture using RAFT® culture system.

Optimization, characterization of "mini-retina" neurosphere culture and bioassay for cellular health

The seeding density plays a critical role in the formation of neurosphere with proper size and morphology. RGC-5 were seeded in the hanging drop at various initial population from 100, 200, 500, 1000, 1500, 2000, and 25000 cells and the cells were monitored daily for spheroid formation progress and the images were taken on day 1 and day 3. A seeding density between 200 cells to 1000 cells demonstrated to be the most optimal for generating neurosphere with controllable morphology and size.

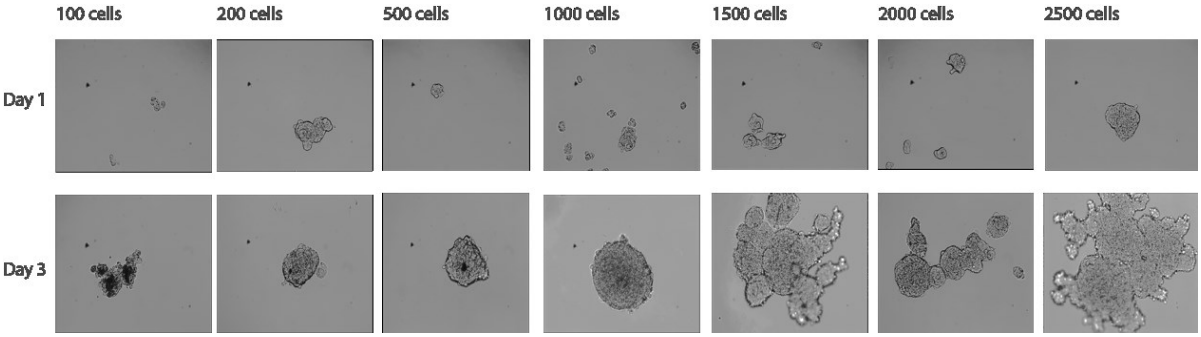

Neurosphere formation after one and three days culturing at 37ºC in Perfecta 3D® 96-well hanging drop plate. Optimization of the seeding density was necessary since neurosphere formation is dependent on the seeding density and it differs from cell line

Viability of the neurosphere was by staining the neurosphere with Calcein AM and viewed with confocal microscopy with Z-stack option. The viability of the neurosphere across the thickness of the neurosphere was evaluated with positive viability profile.

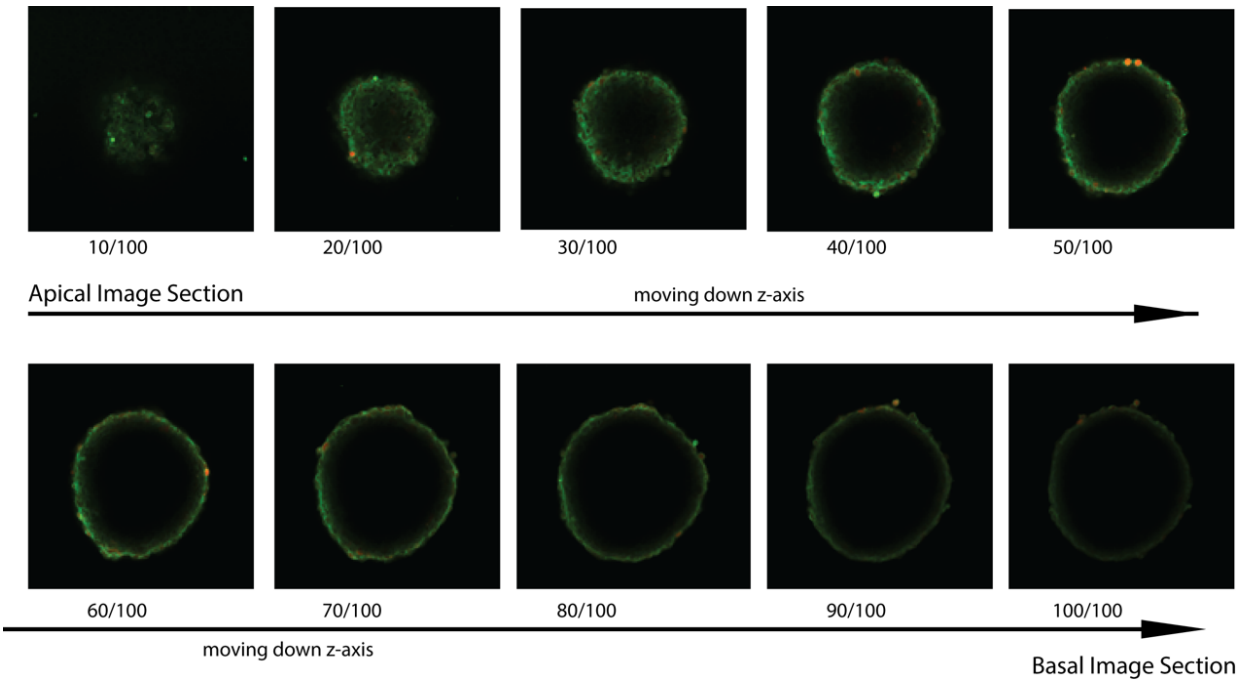

Images of a neurosphere sections organized from the apical layer and descending to its basal layer. The neurosphere was imaged with 100 sections where 0 is the most apical section while 100 was the basal section

Appendix B Retinal biomarker mRNA gene expression profile

Retinal biomarker gene expression profiles for RGC-5 and 661W cells

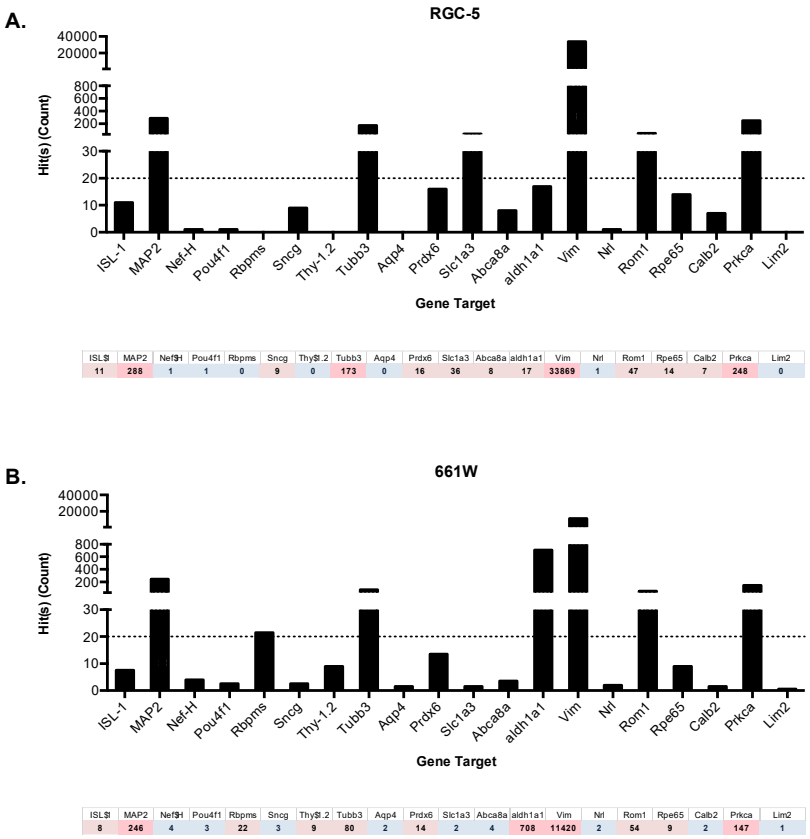

Retinal biomarker mRNA gene expression profile of RGC-5 (A) and 661W (B) cells. Horizontal dotted line represents threshold level where n>20 indicates positive gene expression.

Retinal biomarker gene expression profiles for 6-day and 14-day differentiated RSCs

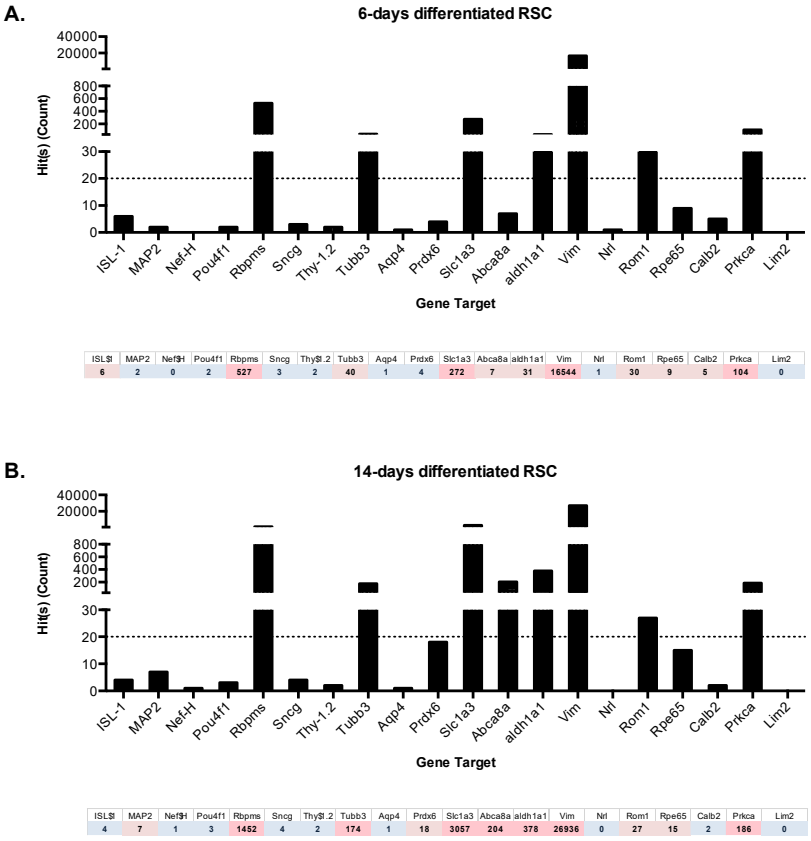

Retinal biomarker mRNA gene expression profile of 6-day differentiated RSCs (A) and 14-day differentiated RSCs (B). Horizontal dotted line represents threshold level where n>20 indicates positive gene expression.

Appendix C Transfection of MiEye8 retinal neurospheres

MiEye8 retinal neurospheres transfected with various formulations of K2-NPs

Control MiEye8 retinal neurospheres

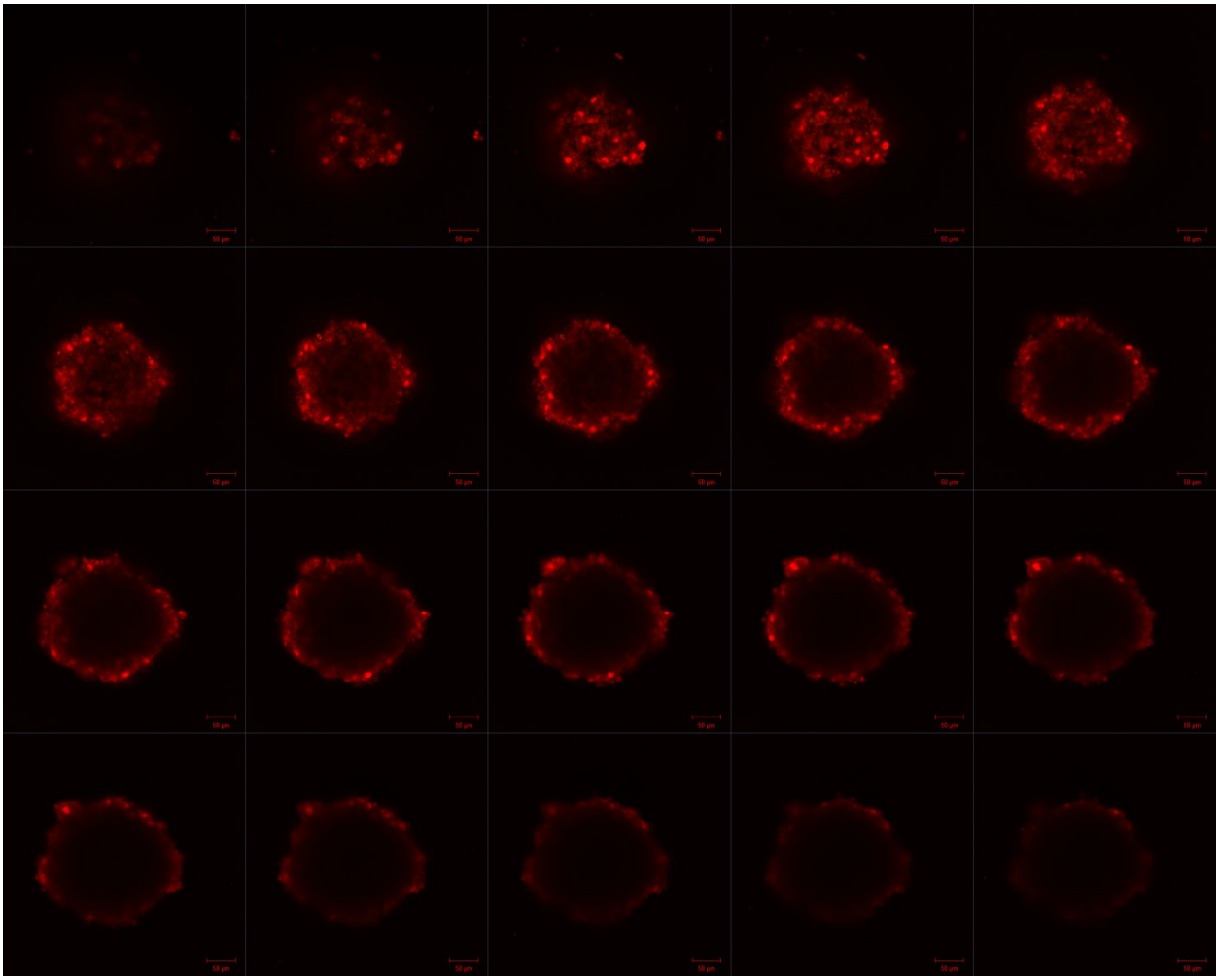

Z-stack of MiEye8 control (untreated) at 120 hours post treatment. 20 slices of images were captured across the observable thickness of the retinal neurosphere. MiEye8 retinal neurosphere were counterstained with 5µM of Syto™62 nuclei stain (red). Successful transfection is indicated by GFP expression (green).

MiEye8 retinal neurospheres transfected with F2 K2-NPs

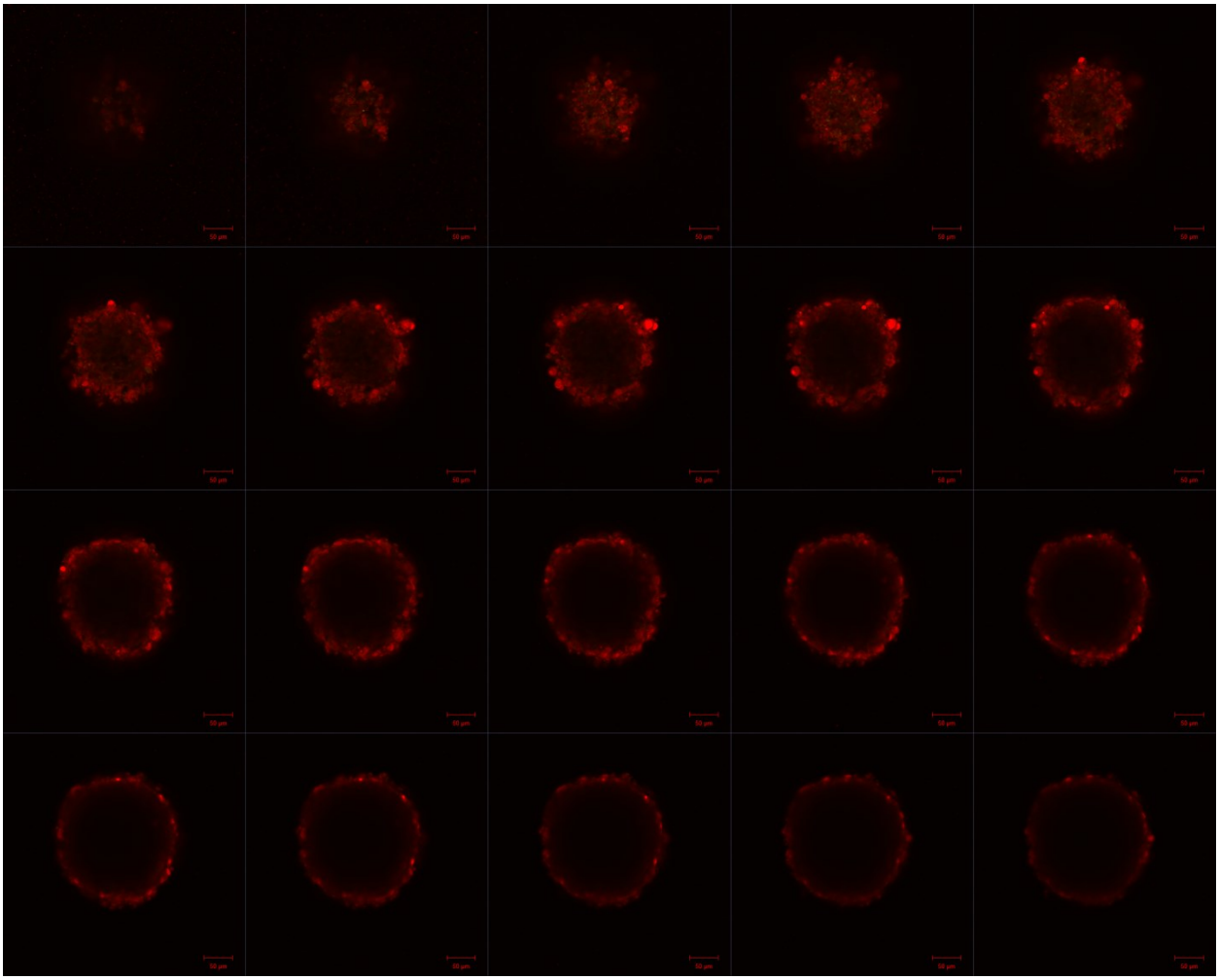

Z-stack of MiEye8 at 120 hours post treatment with K2-NP (2µL:1µg). 20 slices of images were captured across the observable thickness of the retinal neurosphere. MiEye8 retinal neurosphere were counterstained with 5µM of Syto™62 nuclei stain (red). Successful transfection is indicated by GFP expression (green).

MiEye8 retinal neurospheres transfected with F5 K2-NPs

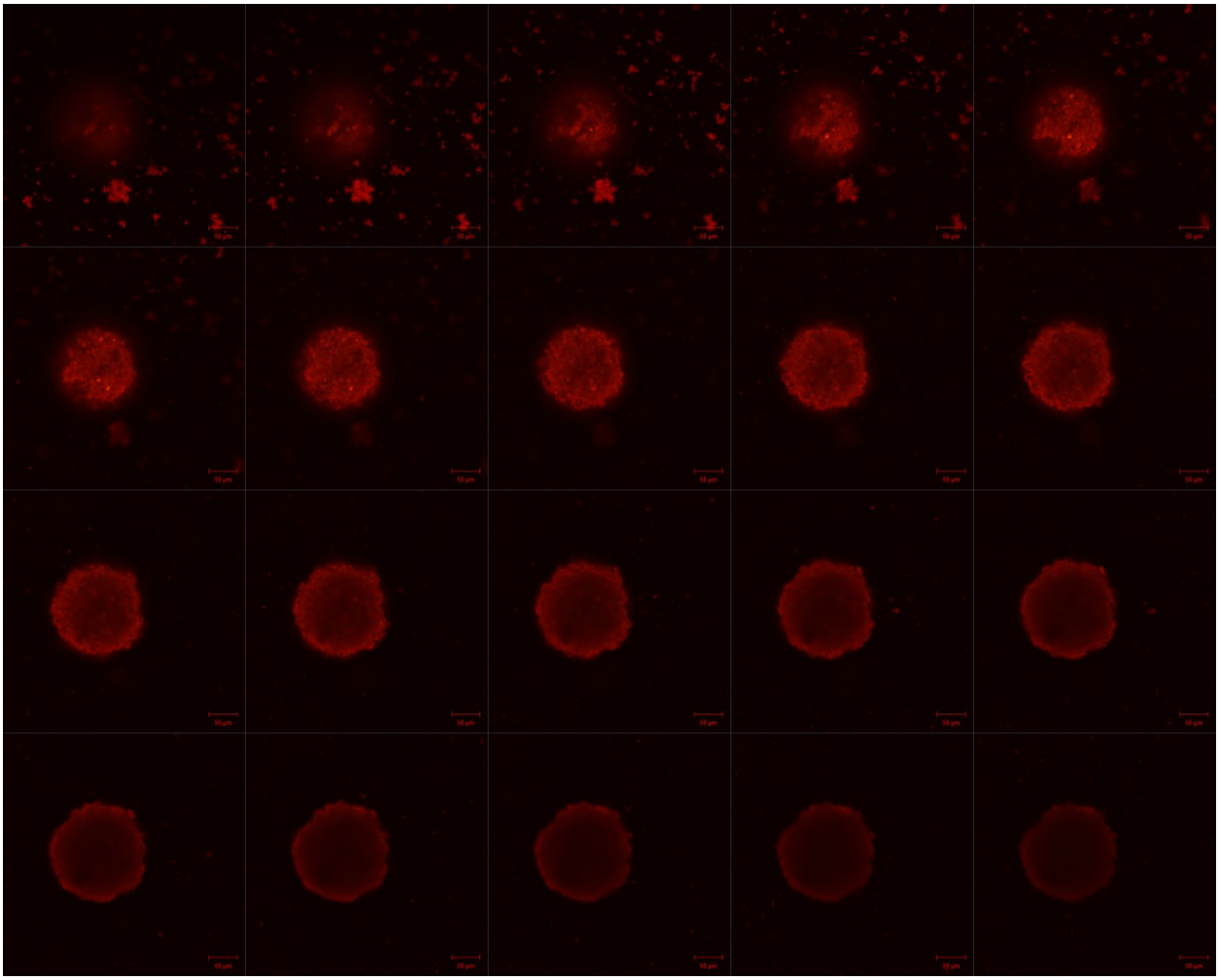

Z-Stack of MiEye8 retinal neurosphere at 120 hours post treatment with K2-NP (20µL:2.5µg). 20 slices of images were captured across the observable thickness of the retinal neurosphere. MiEye8 retinal neurosphere were counterstained with 5µM of Syto™62 nuclei stain (red). Successful transfection is indicated by GFP expression (green).

MiEye8 retinal neurospheres transfected with F6 K2-NPs

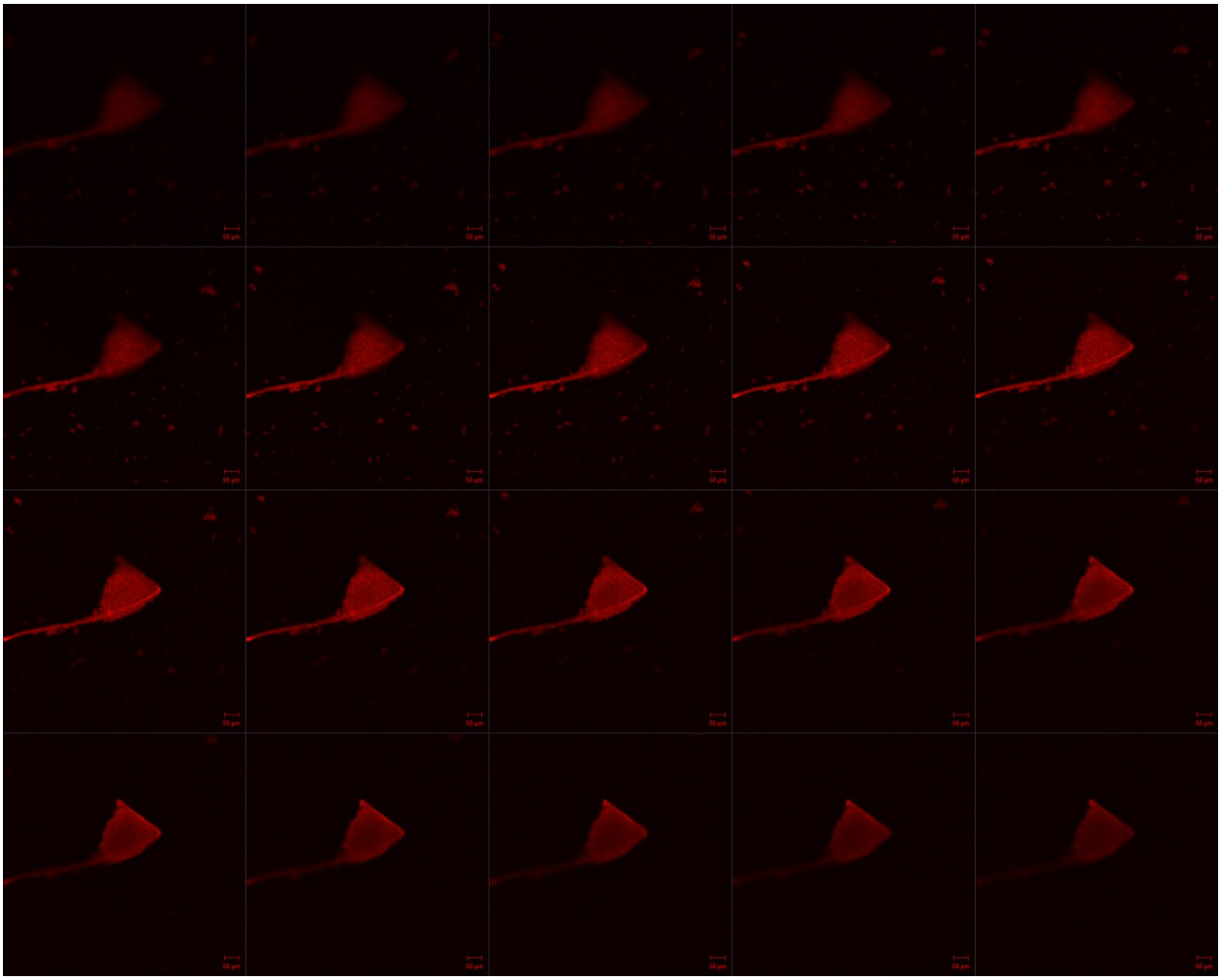

Z-Stack of MiEye8 retinal neurosphere at 120 hours post treatment with K2-NP (30µL:5µg). 20 slices of images were captured across the observable thickness of the retinal neurosphere. MiEye8 retinal neurosphere were counterstained with 5µM of Syto™62 nuclei stain (red). Successful transfection is indicated by GFP expression (green). The object surrounding the retinal neurosphere is a fiber.

MiEye8 retinal neurospheres transfected with F7 K2-NPs

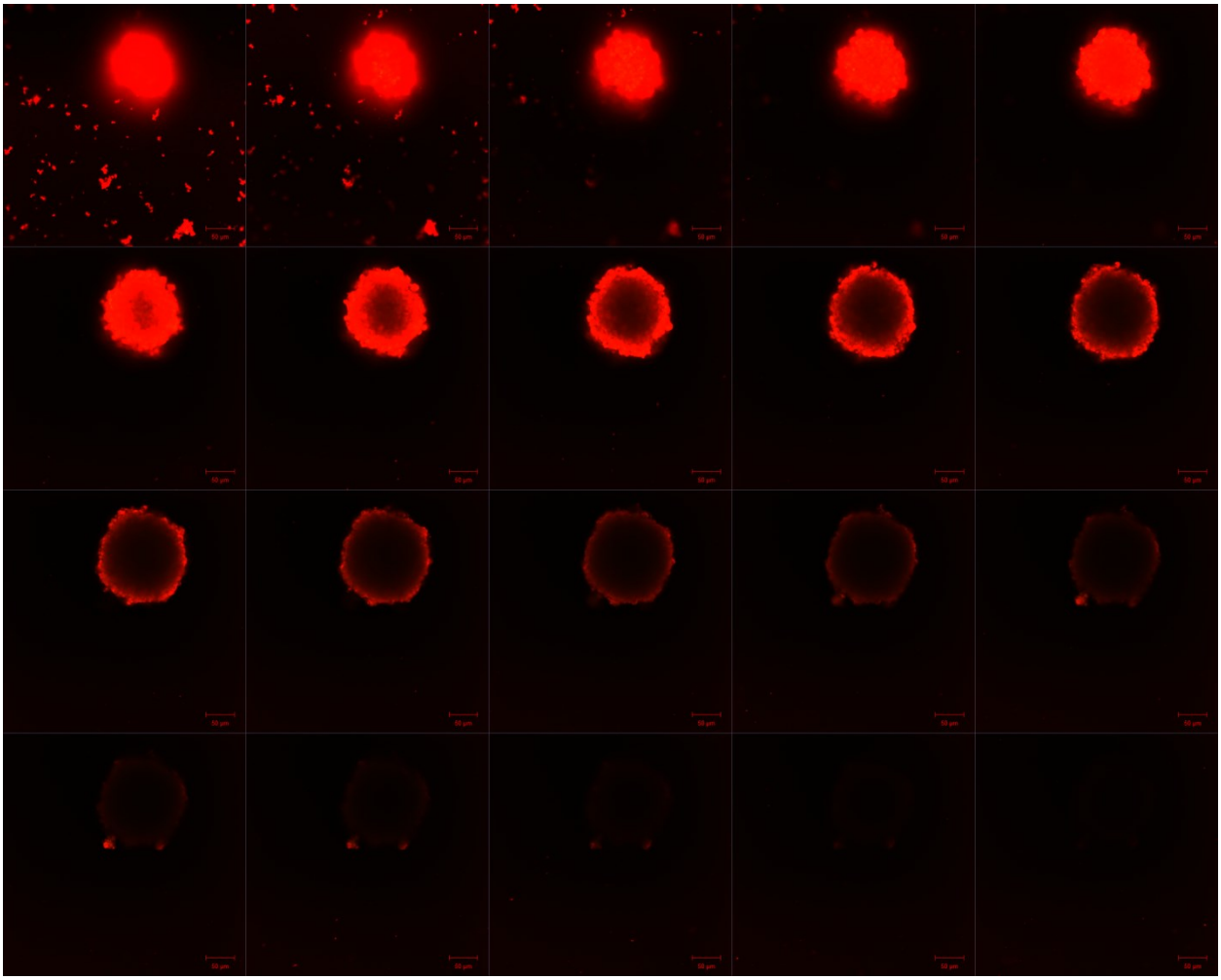

Z-Stack of MiEye8 retinal neurosphere at 120 hours post treatment with K2-NP (10µL:2µg). 20 slices of images were captured across the observable thickness of the retinal neurosphere. MiEye8 retinal neurosphere were counterstained with 5µM of Syto™62 nuclei stain (red). Successful transfection is indicated by GFP expression (green).